# DISCOVERY OF NEW INORGANIC METAL HALIDE PEROVSKITE SCINTILLATORS FOR HOMELAND SECURITY APPLICATIONS

A Dissertation Presented for the

Doctor of Philosophy

Degree

The University of Tennessee, Knoxville

Kimberly S. Pestovich

May 2025

*“Crystal growth is as much an art as it is a science.”*

*-My crystal growth mentor*

*“Don’t wallow in the paint.”*

*-My art teacher*

## ACKNOWLEDGEMENTS

I would like to express my sincere gratitude to my advisor, Dr. Mariya Zhuravleva, and committee members, Dr. Chuck Melcher, Dr. Veerle Keppens, Dr. Jason Hayward, and Dr. Edgar van Loef, for their expertise, guidance, and feedback. I have been fortunate to work within an incredibly supportive network at the University of Tennessee (UT), with the Nuclear Science and Security Consortium (NSSC), and in collaboration with Radiation Monitoring Devices, Inc. (RMD). Special thanks to Dr. Michael Koehler, Dr. Xianfei Wen, Ketaki Joshi, and Luke Harrill at UT and Dr. Lakshmi Pandian, Dr. Pijush Bhattacharya, and Nicholas Anastasi at RMD for their technical contributions to this work. Furthermore, I am grateful for the friendship and scientific discussions shared with my lab mates at the Scintillation Materials Research Center (SMRC). My thanks to the SMRC would not be complete without recognizing Dr. Luis Stand, whose advice has been invaluable. Special thanks to the contributions of undergraduate researchers as well, in particular Megan Gillespie.

X-ray diffraction (XRD), including high temperature XRD, was performed at the Institute for Advanced Materials & Manufacturing (IAMM) Diffraction Facility, located at the University of Tennessee, Knoxville.

This material is based upon work supported by the U.S. Department of Homeland Security under Grant Award Number 20CWDARI00036-01-00. The views and conclusions contained in this document are those of the authors and should not be interpreted as necessarily representing the official policies, either expressed or implied, of the U.S. Department of Homeland Security.

This material is based upon work supported by the Department of Energy National Nuclear Security Administration through the Nuclear Science and Security Consortium under Award Number DE-NA0003996. This report was prepared as an account of work sponsored by an agency of the United States Government. Neither the United States Government nor any agency thereof, nor any of their employees, makes any warranty, express or implied, or assumes any legal liability or responsibility for the accuracy, completeness, or usefulness of any information, apparatus, product, or process disclosed, or represents that its use would not infringe privately owned rights. Reference herein to any specific commercial product, process, or service by trade name, trademark, manufacturer, or otherwise does not necessarily constitute or imply its endorsement, recommendation, or favoring by the United States Government or any agency

thereof. The views and opinions of authors expressed herein do not necessarily state or reflect those of the United States Government or any agency thereof.

In reference to IEEE copyrighted material which is used with permission in this dissertation, the IEEE does not endorse any of University of Tennessee's products or services. Internal or personal use of this material is permitted. If interested in reprinting/republishing IEEE copyrighted material for advertising or promotional purposes or for creating new collective works for resale or redistribution, please go to http://www.ieee.org/publications_standards/publications/rights/rights_link.html to learn how to obtain a License from RightsLink.

## ABSTRACT

Discovery of new scintillation materials supports a number of applications related to public health and safety, like medical imaging and homeland security. Among several complementary homeland security technologies for radiation detection, high energy (0.5-9 MeV) X-ray radiography enables the high throughput and non-invasive screening of cargo entering the United States. Current systems primarily use $CdWO_4$ [cadmium tungstate] inorganic scintillation crystals, as well as CsI:Tl [cesium iodide doped with thallium]. These scintillators have performance and practical limitations that encourage research for alternative detector materials.

Due to interesting structure-property relationships and advancements in photoconversion efficiency, halide perovskite and related compositional families have recently garnered significant attention for photovoltaics as well as radiation detection. However, many of these compounds have only been synthesized as nanocrystals or thin films, and they suffer from chemical and functional stability. In radiation detection applications, several inorganic metal halide perovskite and perovskite-derivative scintillators containing cesium and potassium have shown excellent light yield, greater than 50,000 photons per MeV, and energy resolution, less than 4 percent at 662 keV, which makes them well-suited for gamma ray spectroscopy applications. However, there are few reports on rubidium-based halide perovskite compounds and scintillators, in addition to effects of radiation damage.

The goals of this work were to discover new inorganic metal halide perovskite and perovskite-like scintillators and investigate their suitability for homeland security applications. The compositional space focused on rubidium-based scintillators in $RbBX_3$, $RbB_2X_5$ and $Rb_4BX_6$ compositional families, where $B^{2+}$ = Sr, Ca, Ba, Eu, Yb and $X^-$ = Cl, Br, I, as well as the cubic perovskite $CsCaCl_3$(Eu, Tl) [cesium calcium chloride]. These new scintillator compositions were grown from the melt via the Vertical Bridgman method, and their physical and scintillation properties were tested. For the most promising scintillators, scale up of crystal growth was pursued (22 mm diameter) and the X-ray afterglow using a pulsed X-ray source was measured, as was the temperature stability of the light yield. Finally, the effects of radiation damage (10 Mrad with Co-60 and 9 MV X-rays) were investigated.

## TABLE OF CONTENTS


CHAPTER 1 INTRODUCTION ..... 1

1.1 Inorganic Scintillators ..... 1

1.2 Applications for Inorganic Scintillators ..... 4

1.3 Metal Halide Perovskites: Materials with Promising Optoelectronic Properties ..... 8

1.4 Vertical Bridgman Crystal Growth ..... 13

CHAPTER 2 SCOPE AND OBJECTIVES ..... 15

CHAPTER 3 METHODOLOGY ..... 16

3.1 Materials Selection & Doping Studies ..... 16

3.2 Crystal Growth ..... 18

3.3 Physical Properties Characterization ..... 20

3.4 Optical, Luminescence & Scintillation Characterization ..... 22

CHAPTER 4 $ABX_3$ COMPOSITIONS ..... 26

4.1 Rubidium Calcium Bromide with $Eu^{2+}$ and $Yb^{2+}$ Dopants ($RbCaBr_3$) ..... 29

4.2 Cesium Calcium Chloride with $Eu^{2+}$ and $Tl^{+}$ Dopants ($CsCaCl_3$) ..... 35

4.3 Rubidium Strontium Iodide with $Eu^{2+}$ and $Yb^{2+}$ Dopants ($RbSrI_3$) ..... 45

CHAPTER 5 $AB_2X_5$ COMPOSITIONS ..... 54

5.1 Rubidium Strontium Iodide and Rubidium Strontium Bromide ($RbSr_2I_5$, $RbSr_2Br_5$) ..... 57

5.2 Rubidium Strontium Iodide with $Ce^{3+}$ dopant ($RbSr_2I_5$:Ce) ..... 69

5.3 Rubidium Strontium-Barium Iodide Mixed Scintillators ($Rb(Sr,Ba)_2I_5$) ..... 71

CHAPTER 6 $A_4BX_6$ COMPOSITIONS ..... 80

6.1 Rubidium Calcium Bromide with $Eu^{2+}$ and $Yb^{2+}$ Dopants ($Rb_4CaBr_6$) ..... 82

6.2 Rubidium Calcium Iodide with $Eu^{2+}$ and $Yb^{2+}$ Dopants ($Rb_4CaI_6$) ..... 89

CHAPTER 7 SCALE UP OF CRYSTAL GROWTH ..... 97

7.1 Rubidium Calcium Bromide ($RbCaBr_3$:Eu) ..... 100

7.2 Rubidium Strontium Iodide ($RbSrI_3$:Eu) ..... 105

7.3 Rubidium Strontium Bromide, Rubidium Strontium Iodide ($RbSr_2Br_5$:Eu, $RbSr_2I_5$:Eu) 110

7.4 Rubidium Calcium Iodide ($Rb_4CaI_6$:Eu) ..... 119

CHAPTER 8 RADIATION DAMAGE ..... 121

8.1 Irradiation Effects ..... 121

8.2 Methodology ..... 123
8.3 Rubidium Calcium Bromide ($RbCaBr_3$ and $Rb_4CaBr_6$) ..... 126
8.4 Cesium Calcium Chloride ($CsCaCl_3$:(Eu, Tl)) – 100 krad and 1 Mrad, Co-60 ..... 127
8.5 Rubidium Strontium Iodide ($RbSrI_3$) – 100 krad to 10 Mrad, Co-60 and X-ray linac ..... 129
8.6 Rubidium Strontium Bromide ($RbSr_2Br_5$) – 2 Mrad, 10 Mrad, Co-60 ..... 132
8.7 Rubidium Strontium Iodide ($RbSr_2I_5$) – 2 Mrad, 10 Mrad, Co-60 and X-ray linac ..... 133
8.8 Rubidium Calcium Iodide ($Rb_4CaI_6$) – 100 krad and 1 Mrad, Co-60 ..... 134
CHAPTER 9 SUMMARY AND OUTLOOK ..... 136
LIST OF REFERENCES ..... 140
APPENDICES ..... 162
VITA ..... 167

## LIST OF TABLES

Table 1. Scintillator properties for high energy X-ray radiography ..... 7
Table 2. Scintillator compositions explored in this work. ..... 17
Table 3. Comparison of ionic radii of dopant and host matrix species..... 17
Table 4. Crystal growth parameters. ..... 19
Table 5. Properties of $ABX_3$ Scintillators. ..... 28
Table 6. Properties of $AB_2X_5$ Scintillators. ..... 56
Table 7. Lattice Parameters from Rietveld Refinement..... 59
Table 8. Afterglow intensity of $RbSr_2Br_5$ and $RbSr_2I_5$ crystals. ..... 66
Table 9. Lattice parameters of $Rb(Sr,Ba)_2I_5$:Eu compared to $RbSr_2I_5$ and $RbBa_2I_5$..... 74
Table 10. X-ray afterglow of $Rb(Sr,Ba)_2I_5$:Eu crystals compared to $SrI_2$:Eu and $CdWO_4$. ..... 79
Table 11. Properties of $A_4BX_6$ Scintillators ..... 81
Table 12. Summary of Properties for 22 mm Crystals ..... 99
Table 13. Comparison of purity and cost of RbBr and $CaBr_2$ raw materials..... 102
Table 14. Coefficient of Thermal Expansion of $RbSrI_3$ ..... 106
Table 15. Linear and volumetric coefficients of thermal expansion of $RbSr_2Br_5$ and $RbSr_2I_5$ compared to other scintillators. ..... 112
Table 16. Properties of select scintillators from this work compared to requirements for high energy X-ray radiography. ..... 139
Table 17. New scintillators with synthesis or performance limitations..... 166
Table 18. Unstable compositions or compositions without radioluminescence ..... 166

## LIST OF FIGURES

Figure 1. The proabability of different interactions with matter according to atomic number Z and incident gamma ray energy (hv), adapted from [7]..... 2
Figure 2. Simple depiction of the scintillation process, involving dopant/activator states, reproduced from [4]. ..... 3
Figure 3. Drive through X-ray inspection system and comparison of radiographs acquired with dual energy X-rays (DE) and dual species (DS) inspection system using X-rays and neutrons. Adapted from [22]..... 6
Figure 4. Effect of structural dimensionality on the band gap of cesium lead bromide. Adapted from [48]. ..... 10
Figure 5. Sample preparation for Vertical Bridgman crystal growth. ..... 19
Figure 6. Apparatus and sample holder for testing temperature dependence of scintillator light yield..... 24
Figure 7. Experiments to maximize light collection and improve pulse height spectra for LSO:Ce collected at room temperature..... 25
Figure 8. Backlit photos of $RbCaBr_3$ crystals 7 mm in diameter size. ..... 29
Figure 9. A) Powder XRD Rietveld refinement, B) structure projection and C) DSC heat flow curves obtained for $RbCaBr_3$ © 2023 IEEE..... 31
Figure 10. Hygroscopicity evaluation of $RbCaBr_3$ including A-B) Dynamic Vapor Sorption measurements and C) pulse height spectra measurements. ..... 31
Figure 11. Absorbance and transmittance of $RbCaBr_3$ and Tauc plot to determine band gap. .... 32
Figure 12. Photoluminescence and radioluminescence of A) undoped, europium doped and B) ytterbium doped $RbCaBr_3$..... 33
Figure 13. A) Cs-137 pulse height spectra of $RbCaBr_3$ crystals and B) Gaussian fit to determine energy resolution of $RbCaBr_3$:7 mol% Eu..... 34
Figure 14. Scintillation decay and B) X-ray afterglow of $RbCaBr_3$:Eu crystals. ..... 34
Figure 15. $CsCaCl_3$ crystals with $Eu^{2+}$ and $Tl^{+}$ dopants. The black color at the cone is surface residue from the carbon coated growth ampoule. B) $Eu^{2+}$ doped crystal under UV light. D) close up of the textured surface of $CsCaCl_3$:Eu, Tl. E) quartz ampoule after growth. F) backlit photo of cross sectional sample of undoped $CsCaCl_3$..... 37

Figure 16. A) Optical transmittance and absorbance of $CsCaCl_3$. B) Tauc plot showed that $CsCaCl_3$ had a direct band gap of 5.47 eV..... 37
Figure 17. $CsCaCl_3$:(Eu, Tl) A) Photoluminescence excitation and emission spectra. The inset graphs show the y-axis in log scale. B) Photoluminescence decay time. ..... 39
Figure 18. $CsCaCl_3$:(Eu, Tl) A) Radioluminescence emission spectra, B) scintillation decay time, and C) X-ray afterglow. ..... 42
Figure 19. $CsCaCl_3$:(Eu, Tl) pulse height spectra (Cs-137)..... 42
Figure 20. A) Pulse shape discrimination scatter plot obtained with $CsCaCl_3$:Tl doped sample under $^{241}$Am/Be neutrons. B) FOM plot generated from the scatter plot shows excellent separation between gamma-rays and fast neutron captures in $^{35}$Cl. The fast neutron capture events that produce protons and alphas can also be separated. C) Scintillation decay profiles (average of several traces) of gamma events and fast neutron capture events in ..... 44
Figure 21. A) Ø7 mm crystals of $RbSrI_3$ and B) Improvements in quality of separate Ø7 mm $RbSrI_3$ crystals by reducing translation rate (left) and cooling rate (right)..... 46
Figure 22. Dynamic Vapor Sorption curves comparing moisture sensitivity of $RbSrI_3$ with $SrI_2$:Eu and NaI:Tl. The photos show the sample shortly after the start of the measurement compared to the end. ..... 46
Figure 23. A) Powder XRD Rietveld refinement results and B) Differential Scanning Calorimetry heat flow curves for $RbSrI_3$. ..... 47
Figure 24. A) Optical transmittance and absorbance measurements of 2 mm thick undoped $RbSrI_3$ and B) determination of band gap using the Tauc method. ..... 47
Figure 25. A) Photoluminescence and B) radioluminescence of $RbSrI_3$..... 49
Figure 26. Scintillation decay time profiles for $RbSrI_3$. ..... 49
Figure 27. X-ray Afterglow of $RbSrI_3$ . $RbSrI_3$:5 mol% Eu had an afterglow of 1.8% at 2 ms. .. 50
Figure 28. $RbSrI_3$ pulse height spectra (Cs-137) and light yield and energy resolution as a function of europium dopant concentration. ..... 52
Figure 29. Relative light yield of $RbSrI_3$:Eu as a function of temperature. The data is represented as a percent change in the 662 keV centroid position from room temperature. ..... 52

Figure 30. X-ray radioluminescence intensity of $RbSrI_3$:Eu as a function of temperature compared to relative light yield. Wavelength-resolved radioluminescence of $RbSrI_3$:Eu collected as a function of temperature. ..... 53
Figure 31. Backlit photos of $RbSr_2Br_5$:Eu and $RbSr_2I_5$:Eu single crystals grown via the Vertical Bridgman method in a 7 mm diameter size. ..... 58
Figure 32. Photographs of Ø7, 4 mm cross-sections from $RbSr_2Br_5$:Eu 5% (A) and $RbSr_2I_5$:Eu 5% (B) crystals in mineral oil. Image conditions are as follows: (I) Ambient lighting, (II) Optical microscope backlighting, (III) Optical microscope polarized light, (IV) Optical microscope with flashlights illuminating the sides of the samples. ..... 58
Figure 33. Powder X-ray Diffraction patterns and Rietveld refinements with GSASII showed the $RbSr_2I_5$ and $RbSr_2Br_5$ crystals to be phase pure. ..... 59
Figure 34. Dynamic Vapor Sorption moisture curves and pulse height spectra acquired to assess hygroscopicity of $RbSr_2I_5$:Eu and $RbSr_2Br_5$:Eu scintillators. ..... 60
Figure 35. A) Optical absorbance and B) transmittance of $RbSr_2Br_5$ and $RbSr_2I_5$, and C) Tauc plots to determine optical band gap. ..... 61
Figure 36. A-B) Photoluminescence excitation and emission spectra for $RbSr_2Br_5$:Eu and $RbSr_2I_5$:Eu crystals. C-D) Radioluminescence of $RbSr_2Br_5$:Eu and $RbSr_2I_5$:Eu redshifted with increased europium concentration. The inset shows the spectra in log scale. ..... 62
Figure 37. A-B) Light yield and energy resolution (at 662 keV) of $RbSr_2I_5$ and $RbSr_2Br_5$ as a function of europium dopant concentration. Samples were Ø7, 4 mm in size. An asterisk (*) marks data reproduced from [69]. C) Pulse height spectra collected for samples from different sections of the boule, showing good uniformity. ..... 64
Figure 38. Scintillation decay time curves for $RbSr_2Br_5$ and $RbSr_2I_5$ crystals. ..... 66
Figure 39. X-ray induced afterglow of $RbSr_2Br_5$ and $RbSr_2I_5$ crystals. The inset figures show the first 10 ms after X-rays were shut off. ..... 66
Figure 40. Testing repeatability of light yield measurements vs temperature with a $RbSr_2I_5$:Eu crystal. Relative light yield was determined by the change in channel number of the 662 keV photopeak centroid from room temperature. ..... 67
Figure 41. Temperature dependent light yield of $RbSr_2Br_5$:Eu and $RbSr_2I_5$:Eu was determined by the change in channel number of the 662 keV photopeak from room temperature. ..... 68

Figure 42. $RbSr_2I_5$:0.5 mol% Ce: Ø7 mm crystal and scintillation properties. ..... 70
Figure 43. A) Backlit photos of $Rb(Sr,Ba)_2I_5$:Eu crystals. The transparency worsened with more than 50% barium concentration. B) Under the optical microscope, small bubbles were visible inside of the $Rb(Sr_{0.5}, Ba_{0.5})_2I_5$:Eu crystal. C) $RbBa_2I_5$:Eu crystal became translucent on cooling..... 72
Figure 44. A) Cross-section sample of $Rb(Sr_{0.5}, Ba_{0.5})_2I_5$:Eu crystal used for measurements, photographed with ambient lighting. B) Optical transmittance and absorbance spectra..... 72
Figure 45. DSC curves and comparison of $Rb(Sr,Ba)_2I_5$:Eu melting points. ..... 74
Figure 46. DVS curves used to study moisture sensitivity of $Rb(Sr,Ba)_2I_5$:Eu crystals. The sample's surface became pale yellow in color and there was a slight increase in mass (~7%) over time. ..... 75
Figure 47. Photoluminescence and radioluminescence of $Rb(Sr,Ba)_2I_5$:Eu crystals..... 75
Figure 48. Pulse height spectra measured with a Cs-137 gamma source and light yield proportionality measured with a set of gamma sources for $Rb(Sr,Ba)_2I_5$:Eu crystals. ..... 77
Figure 49. A) Scintillation decay time and B) X-ray afterglow of $Rb(Sr,Ba)_2I_5$:Eu crystals..... 79
Figure 50. $Rb_4CaBr_6$ crystals grown in a Ø7 mm size at 0.5 mm/hr. ..... 83
Figure 51. $Rb_4CaBr_6$:Eu 5 mol% crystal grown at 1 mm/hr shows decreased transparency and. 83
Figure 52. Optical absorbance and transmittance of $Rb_4CaBr_6$ and the Tauc plot ..... 83
Figure 53. A) Powder XRD Rietveld refinement, B) Structure projection and C) DSC heat flow curves for $Rb_4CaBr_6$..... 84
Figure 54. A) Dynamic Vapor Sorption (DVS) curves and B) pulse height spectra acquired under ambient conditions for $Rb_4CaBr_6$. The inset figures show the sample during the DVS measurement. ..... 85
Figure 55. Photoluminescence and radioluminescence of $Rb_4CaBr_6$. ..... 86
Figure 56. Pulse height spectra (Cs-137) measured witth $Rb_4CaBr_6$ crystals, showing differences between the seed end and tail end of the crystals. ..... 88
Figure 57. A) Scintillation decay time profiles and B) X-ray afterglow of $Rb_4CaBr_6$ crystals.... 88
Figure 58. Ø7 mm $Rb_4CaI_6$ crystals in the transparent furnace and backlit after cooling. ..... 91
Figure 59. A) Powder XRD Rietveld refinement and B) DSC heat flow curves for $Rb_4CaI_6$..... 91

Figure 60. Hygroscopicity evaluation of $Rb_4CaI_6$: Dynamic Vapor Sorption measurements and pulse height spectra acquired under ambient conditions. ..... 92
Figure 61. Optical absorbance and transmittance of $Rb_4CaI_6$, and the Tauc plot. ..... 92
Figure 62. A-B) Photoluminescence and B) Radioluminescence of $Rb_4CaI_6$ crystals. ..... 94
Figure 63. Light yield and energy resolution of $Rb_4CaI_6$ crystals. ..... 94
Figure 64. Scintillation decay profiles of $Rb_4CaI_6$ crystals. ..... 96
Figure 65. X-ray afterglow of $Rb_4CaI_6$ crystals. ..... 96
Figure 66. Growth of Ø22 mm $RbCaBr_3$:5 mol% Eu. A) shows crystal in ampoule, b) shows crystal extracted from ampoule, C) shows a cut and polished Ø22, 25 thick cylinder used for scintillation characterization. ..... 101
Figure 67. Light yield and scintillation decay time measured for a Ø22, 25 mm cylinder of $RbCaBr_3$:5 mol% Eu. ..... 101
Figure 68. Treatment of RbBr by a single pass in a Bridgman furnace and its qualitative impact on polycrystalline $Rb_4CaBr_6$ samples. This method also worked for batches of 10-100 g of RbI and RbBr raw materials, though it did not seem to work well for $CaBr_2$. ..... 103
Figure 69. Melt-filtering of a 22 g charge of 99.5% pure anhydrous $CaBr_2$ powder led to recovery of ~18 g of material. ..... 104
Figure 70. 12 mm diameter $RbCaBr_3$:Eu crystal grown using melt-filtered $CaBr_2$ and treated RbBr raw materials. ..... 104
Figure 71. A) Peaks shifted to lower $2\theta$ with increased temperature. B) Lattice parameters and C) Cell volume as a function of temperature. ..... 106
Figure 72. Ø12 mm $RbSrI_3$:5 mol% Eu crystal shown with ambient light and backlighting. ..... 106
Figure 73. Scintillation properties of Ø12 mm $RbSrI_3$:5 mol% Eu crystal. ..... 108
Figure 74. Cracking in Ø22 mm $RbSrI_3$:Eu crystals was observed during cooldown, regardless of translation rate, capillary type, cooling time, and use of a carbon coated ampoule. ..... 108
Figure 75. A) Melt filtering and B) zone refining of 99% pure RbI powder from the company Strem. ..... 108
Figure 76. RbI from APL turned brown/grey after drying under vacuum. The Ø22 mm $RbSrI_3$:Eu crystal grown from 99.9% pure Sigma-Aldrich material purifed in-house is labeled (1), and

the crystal grown from 99.9% pure anhydrous RbI material is labled (2). There was no evidence of impurites in the DSC measurement of RbI. ..... 110
Figure 77. A) High temperature X-ray diffraction apparatus and sample. B) Diffraction patterns from 25°C-400°C for $RbSr_2I_5$ and $RbSr_2Br_5$ and C) Changes in lattice parameter and unit cell volume. ..... 112
Figure 78. Ø22 mm $RbSr_2Br_5$:1% Eu and $RbSr_2I_5$:1% Eu crystals grown at 0.5 mm/hr: (a, e) backlit in the quartz growth ampoule after cooling, (b, f) under UV light excitation, and (c) after extraction from the ampoule with ambient lighting. (d) Small vertical trails of bubbles inside of the $RbSr_2Br_5$:1% Eu were seen. ..... 113
Figure 79. When adhered to the ampoule wall, black impurities in the melt destabilized the solid liquid interface, resulting in a poor-quality crystal. However, these impurities typically floated to the surface of the melt. ..... 114
Figure 80. A) The crystal was directly coupled to the PMT with mineral oil to measure light yield. B-C) show the Ø22, 35 mm crystals measured and the associated pulse height spectra for $RbSr_2Br_5$:Eu and $RbSr_2I_5$:Eu. ..... 116
Figure 81. Pulse height spectra acquired for a Ø7 mm, 3 mm thick crystal versus a Ø22, 35 mm crystal of $RbSr_2I_5$:1% Eu, showing the intrinsic radioactive background from Rb-87. ..... 116
Figure 82. Ø22, 35 mm $RbSr_2Br_5$:Eu and $RbSr_2I_5$:Eu crystals had two-component scintillation decays, with a primary component of 1.2 μs and a longer secondary component ~6 μs.... 116
Figure 83. High quality Ø7 mm $RbSr_2I_5$:1% Eu crystals could be grown with fast translation rates of 1, 2, and 5 mm/hr. The crystals are shown backlit (left) and glowing under UV light (right). There was little variation in the scintillation properties of the samples from different portions of the boules, indicating uniformity. ..... 118
Figure 84. Ø22 mm crystals of $RbSr_2I_5$:1% Eu could be grown with fast translation rates. The isodiametric section of the boules was ~35 mm tall. The off-set photos of (a-c) show close ups of unique observations from each crystal. (D) shows the crystal grown at 1.5 mm/hr under ambient lighting on grid paper. (E) shows the same crystal under UV light. ..... 118
Figure 85. Growth of Ø22 mm $Rb_4CaI_6$:5 mol% Eu at 0.25 mm/hr. ..... 120
Figure 86. A) Pulse height spectra and 2) scintillation decay of a Ø22, 20 mm $Rb_4CaI_6$:5 mol% Eu cylindrical crystal. ..... 120

Figure 87. Transmittance of $CdWO_4$ and CsI:Tl vs dose with Co-60. Adapted from [28, 237]. 122
Figure 88. Samples in front of the linac in a vacuum sealed bag. ..... 124
Figure 89. Mass attenuation versus energy for different scintillators calculated with the NIST XCOM Photon Cross Section Database [242]. $RbSr_2I_5$ and $RbSrI_3$ were nearly equivalent, so only $RbSr_2I_5$ is shown here. ..... 125
Figure 90. A) $RbCaBr_3$ crystals and B) $Rb_4CaBr_6$ crystals before and after irradiation with Co-60 to 100 krad and 1 Mrad. ..... 126
Figure 91. Changes in visual appearance of $CsCaCl_3$:(Eu, Tl) crystals after exposure to 100 krad ($10^5$ rad or 1 x $10^3$ Gy) and 1 Mrad ($10^6$ rad or 1 x $10^4$ Gy) dose points. ..... 127
Figure 92. Changes in optical transmittance (top) and pulse height spectra (bottom) with dose (pre-irradiation in black, 100 krad in blue, and 1 Mrad in red) for $CsCaCl_3$ crystals..... 128
Figure 93. Comparison between pulse height spectra acquired with $RbSrI_3$ scintillators before irradiation and after irradiation with 100 krad and 1 Mrad doses (Co-60). Eu-doping appears to improve radiation hardness of $RbSrI_3$. ..... 129
Figure 94. Characterization of $RbSrI_3$:Eu crystals before and after 10 Mrad Co-60 irradiation at the Gamma Cave, including A) visual inspection of the crystals, B) optical transmittance measurements, and C) light yield as a function of dose point. ..... 130
Figure 95. Eu-doped $RbSrI_3$ crystals before and after 2 and 10 Mrad doses with the Varian M9A linear accelerator. Immediately after irradiation, they had a dim blue color that faded after a few minutes. ..... 131
Figure 96. A) Pulse height spectra acquired approximately 24 hours after linac irradiation showed activation of the crystals at both dose points. B) After 3 weeks, this activation had decreased significantly. ..... 131
Figure 97. Characterization of $RbSr_2Br_5$:Eu crystals before and after Co-60 irradiation at the Gamma Cave, including A) visual inspection of the crystals under the optical microscope, B) optical transmittance measurements, and C) pulse height spectra measurements. ..... 132
Figure 98. Characterization of $RbSr_2I_5$:Eu crystals before and after Co-60 irradiation at the Gamma Cave, including A) visual inspection of the crystals under the optical microscope, B) optical transmittance measurements, and C) pulse height spectra measurements ..... 133

Figure 99. $RbSr_2I_5$:1% Eu crystals before and after 2 and 10 Mrad doses with the Varian M9A linear accelerator. ..... 134
Figure 100. Backlit photos of $Rb_4CaI_6$ before and after irradiation. ..... 135
Figure 101. Optical absorbance and pulse height spectra measured for $Rb_4CaI_6$ crystals before and after 100 krad and 1 Mrad doses (Co-60). ..... 135

# CHAPTER 1 INTRODUCTION

## 1.1 Inorganic Scintillators

Inorganic scintillation materials, including their synthesis and their properties, have been studied for over a century for use in a variety of radiation detection applications. Scintillators are materials that absorb and convert ionizing radiation into visible light. When paired with photodetector and associated electronics, the scintillation light is processed as an electrical signal. Because of their ability to detect radiation of different types, scintillators are used in a diverse set of ever-evolving applications that service a broad variety of fields including medical imaging, nuclear security, high energy physics, space exploration, and oil-well logging [1-6].

The starting point of the scintillation process is interaction of the crystal with ionizing radiation. There are three important interactions of gamma rays with matter, which lead to partial or complete transfer of the gamma ray photon energy to electron energy: photoelectric absorption, Compton scattering, and pair production [7]. These three interactions are highly dependent on the incident energy (Eγ) as well as the atomic number of the absorber, which is shown in **Figure 1**. For radiation detection, scintillators with high atomic numbers (Z) are highly favorable. A common formula for the effective atomic number of a compound or mixture was defined by Murty as follows [8]:

$$Z_{eff} = \sqrt[2.94]{f_1 \times (Z_1)^{2.94} + f_2 \times (Z_2)^{2.94} + \cdots + f_n \times (Z_n)^{2.94}}$$

where $f_n$ is the fraction of the total number of electrons associated with each element and $Z_n$ is the atomic number of each element.

During photoelectric absorption, a photon transfers all its energy to an electron. This photoelectron is then ejected from the atom. Materials with high Z have a much greater photoelectric absorption probability ($\tau \propto Z^4/E\gamma^{3.5}$). In Compton scattering, the incident gamma photon is deflected by an electron, which changes its angle with respect to the original direction and transfers a portion of energy to the electron. The probability of Compton scattering depends on the number of the electrons available as scattering targets, therefore increasing linearly with Z ($\sigma \propto Z$). The pair production interaction dominates at high energies, above 1.02 MeV, which is the energy required to create an electron-positron pair. Any excess energy is transformed into kinetic energy used by the positron and electron. This interaction must occur within the coulomb

field of a nucleus. The magnitude of this interaction varies with the square of Z ($\kappa \propto Z^2$). In addition to these three interactions, coherent scattering or Rayleigh scattering is a fourth interaction that can occur. However, this process neither excites nor ionizes atoms and the gamma photon retains its original energy after the scattering.

The "stopping power" of a scintillator to high energy ionizing radiation is described by its density, effective atomic number, and the mass attenuation coefficient. The attenuation coefficient ($\mu$) is the sum of the probabilities $\tau + \sigma + \kappa$. The mass attenuation coefficient accounts for the density ($\rho$) of the material, $\mu/\rho$. Attenuation for gamma rays in a material can be described as $I/I_0 = e^{-(\mu/\rho)\rho t}$, which relates the change in intensity of the gamma ray ($I/I_0$) to the "mass thickness" ($\rho t$) in $mg/cm^2$. The mass attenuation coefficient is energy-dependent, as each of its components is affected.

While a high Z improves gamma ray absorption, it does not necessarily guarantee improved scintillation performance. For example, BGO has very high density and Z of 7.13 g/cc and 83, but a low light yield of 8,200 ph/MeV. In comparison, NaI:Tl has a moderate density of 3.6 g/cc, relatively high Z of 52 and a high light yield of 38,000 ph/MeV [7]. However, a clear benefit is that materials with a higher Z require a lower volume of crystal to achieve the same detection efficiency, making them a more cost-effective option or appropriate when there are spatial limits for the detector. The light yield of the scintillator depends on a number of other factors pertaining to the scintillation mechanism.

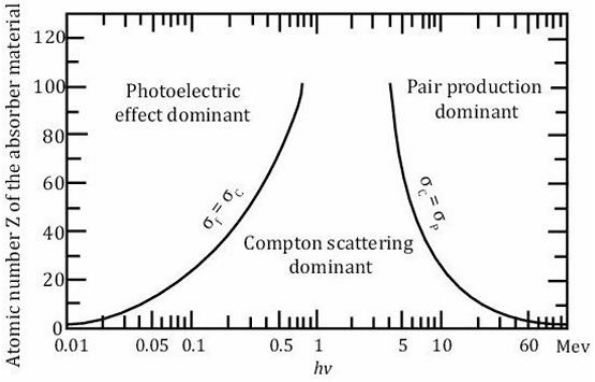


**Figure 1**. The proabability of different interactions with matter according to atomic number Z and incident gamma ray energy (hv), adapted from [7].

The simplest description of the inorganic scintillation mechanism in crystalline materials is that incident radiation excites an electron into the conduction band, and the subsequent relaxation of the electron releases energy in the form of light [4]. In a pure insulating crystal, the large band gap is typically too wide for photon emission to be efficient and for the emission of light to be in the visible range. Therefore, dopants, or activators, are added to the lattice to modify the energy band structure and create a path through which the electron can de-excite back to the valence band, as shown in **Figure 2**. These additional energy states are called luminescence centers or recombination centers.

The scintillation process can be divided into several stages, defined by Rodnyi as [5]:

1. Absorption of ionizing radiation, creation of primary electrons and holes
2. Relaxation of primary electrons and holes (usually non-radiative, or through Auger effect)
3. Thermalization of low-energy secondary electrons, resulting in electron-hole (e-h) pairs with energy ~$E_g$
4. Migration: Energy transfer from e-h pairs to luminesce centers and subsequent excitation
5. Emission from the luminescence centers

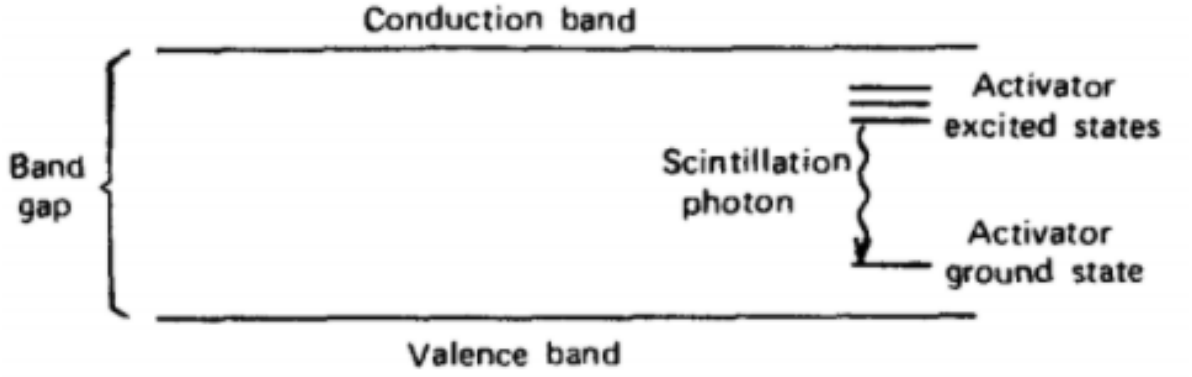


**Figure 2.** Simple depiction of the scintillation process, involving dopant/activator states, reproduced from [4].

Stages 4 and 5 are mostly unique to scintillation. Energy losses in the migration stage depend on the spatial distribution of electrons and holes relative to luminescence centers and traps. Impurities, point defects, surfaces, interfaces, and other material flaws can create energy levels in the band gap, referred to as traps. Deep traps completely remove carriers from the scintillation process, and in ionic crystals, anion vacancies can capture electrons (F centers). Shallow traps in the lattice can capture carriers, which can be released thermally to take part in recombination. This temporary localization of carriers at shallow traps increases the decay time of the crystal and can contribute to afterglow.

Additionally, interaction of electrons, holes, and excitons with phonons can lead to localization, or self-trapping. For high energy excitation in ionic crystals, self-trapped excitons (STE) are formed through the capture of free electrons by $V_k$ centers, sometimes leading to excitonic luminescence. In alkali halides, this intrinsic excitonic luminescence is only effective at room temperature. $V_k$ centers may also be involved in extrinsic luminescence, that is, luminescence involving the energy states of the activator.

Overall, the maximum light yield of an ionic-crystal scintillator is given as:

$$LY_{max} = \frac{S * Q}{\beta * E_g} \times 10^6$$

where S is electron-hole transfer efficiency, Q is luminescence quantum efficiency, $E_g$ is the band gap, and β is a coefficient that is typically 1.5-3 for wide band gap materials and ionic crystals [9, 10]. Therefore, crystals with smaller band gaps are more promising for producing high light yields; however, the band gap must not be so small that the radiative transition of the chosen luminescent dopant(s) cannot be accommodated, and that the emission wavelength produced is optimal for the photodetectors' detection efficiency.

### 1.2 Applications for Inorganic Scintillators

Each application has unique needs in terms of scintillation properties. While this allows for customization and tailoring of a scintillator to specific applications via compositional engineering, the so-called "ideal scintillator" does not exist, inspiring continued research into the discovery and development of novel scintillation materials.

The characteristics of the "ideal inorganic scintillator" were named in the early 2000s [11-14]. With regards to physical characteristics, the detection efficiency, cost, physical form, chemical

stability, and mechanical strength are important. The detection efficiency relates to a high density and effective atomic number, which reduces the amount of scintillator material needed. The crystal growth should be scalable and stable with no phase transitions or decomposition. Ideally, the crystal is insensitive to air, moisture, light, temperature, and it should be mechanically shock resistant. In terms of luminescent characteristics, the emission wavelength should be compatible with the photodetector, the light yield should be high (though the threshold depends on the application), the rise and decay times should be fast, and there should be no afterglow. Additionally, the crystals should be resistant to radiation.

Enormous progress in the state of the art scintillators for gamma ray spectroscopy was made over the next 20 years, where the best energy resolution for commercially available crystals improved from 5-6% at 662 keV improved to then 2.2% at 662 keV [15]. $LaBr_3$:Ce, $LaCl_3$:Eu and inorganic alkali metal halide scintillators doped with europium were some of the major workhorses for these improvements, among others.

Later in 2018, Dujardin et al. formulated three needs, trends, and advances of inorganic scintillators:

1) Energy resolution of 2-3% at 662 keV for energy discrimination in nuclear security and spectroscopy.
2) Sub 100 ps timing resolution of the next generation PET scanners in medical imaging and particle physics experiments.
3) High gamma ray detection efficiency via high density and high effective atomic number.
4) Low cost (materials and production).

This was followed with a 2023 publication by Wang et al., on the needs, trends, and advances in scintillators that was specifically focused on radiographic imaging and tomography. They identified the most important properties to be stopping powder (density, Z, cross sections), light yield, decay time, radiation hardness, size and scalability, cost and fabrication and stability and ruggedness [16].

High energy X-ray radiography (0.5 – 9 MeV) enables high throughput and non-invasive screening of steel cargo containers, and the need for this technology is growing. The 2021 Securing America’s Ports Act calls for the development of a plan to increase the scan rate of commercial and passenger vehicles as well as rail freight entering the U.S. to 100% [17].

1.2.1 *High Energy X-ray Radiography*

High energy X-ray radiography systems consist of an X-ray source, such as a linear accelerator, collimators and beam filters, X-ray detectors, data acquisition electronics, control system, and radiation shielding [18]. The X-rays typically pass through the object to be scanned and interact with detector modules on the other side. The detector modules include a scintillator and a photodetector. The scintillation light induced by the X-rays is collected by an array of photodetectors, like photomultiplier tubes or photodiodes, which convert the light into electrical signals. These signals are then processed to form the X-ray image.

Dual energy (i.e., 6/9 MeV) and dual species systems (i.e., neutrons and X-rays) can provide a contrast between the density of cargo. Examples of a drive-through X-ray inspection system and radiographs acquired from dual energy and dual species systems are in **Figure 3**.

Since cargo imaging systems and radiation portal monitors are typically deployed outdoors across the U.S., several technical standards establish requirements for standard system operation over several environmental conditions, including an ambient temperature range. ANSI 42.46-2008 “Determination of the Imaging Performance of X-Ray and Gamma Ray Systems for Cargo and Vehicle Security Screening” lists a temperature range of +5°C to +35°C, and ANSI 42.35-2016 “Evaluation and Performance of Radiation Detection Portal Monitors for Use in Homeland Security” lists a temperature range −30°C to +55°C [19, 20]. While extreme in comparison to a controlled laboratory benchtop, this range is mild compared to some other applications. For example, down-hole temperature oil well logging applications can reach 375°C [21].

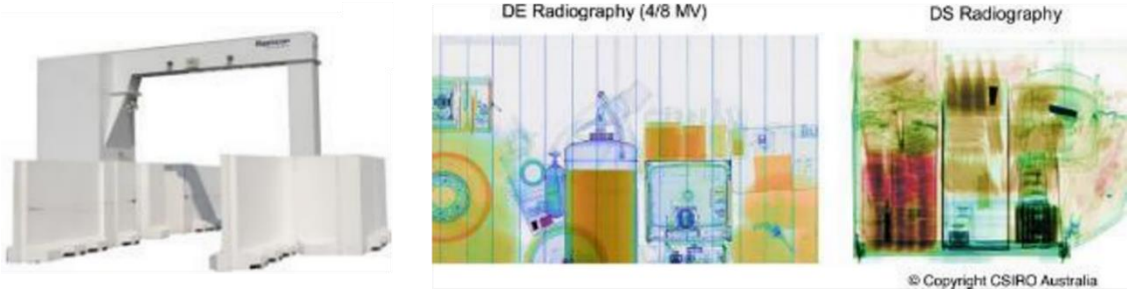


**Figure 3.** Drive through X-ray inspection system and comparison of radiographs acquired with dual energy X-rays (DE) and dual species (DS) inspection system using X-rays and neutrons. Adapted from [22].

Most cargo imaging systems use single crystal scintillators as the X-ray detector. The size of the detector is selected to balance image resolution (pixels of size 5 mm x 5 mm x 30 mm) and the need for a large area to maximize photon capture (array of pixels). The scintillators used in these systems have several requirements for scintillation and physical properties [3, 13, 22-25]. To be able to produce high resolution images quickly, the scintillator should have high light yield (> 30,000 ph/MeV) and low afterglow. High density and effective atomic number are desirable for detection efficiency. Additionally, physical and chemical stability, radiation hardness, and cost of synthesis and fabrication are important considerations.

Currently, $CdWO_4$ single crystals are widely used in high energy X-ray radiography systems. In fact, $CdWO_4$ was the only scintillator used in commercial mobile X-ray radiography systems reported in a U.S. Department of Homeland Security market review [26]. The high density of 7.9 g/cc and effective atomic number of 61 are desirable. Additionally, the crystals have excellent afterglow and radiation hardness, temperature stability, and they are non-hygroscopic [27, 28]. However, the cost of production is high, and their light yield is low (15,000-25,000 ph/MeV). An alternative scintillator is CsI:Tl. Its properties are compared to $CdWO_4$ in **Table 1**. CsI:Tl has high light yield (>50,000 ph/MeV), but it has undesirable high afterglow and is hygroscopic [29]. Co-doped microcolumnar films of CsI:Tl have significantly suppressed afterglow; however, spatial resolution worsens with increasing thickness of the film [30, 31].

**Table 1.** Scintillator properties for high energy X-ray radiography

| | Density (g/cc) ------ Zeff | LY (ph/ MeV) | ER at 662 keV | Decay time (μs) | Afterglow | Radiation hard | Hygro-scopic | Ease of machining | Cost ($/cc) |
|---|---|---|---|---|---|---|---|---|---|
| $CdWO_4$ | 7.9 ------ 64 | 15,000-25,000 | 7.5% | 13 | low | high | No | difficult; cleavage plane | 30 |
| CsI:Tl | 4.5 ------ 54 | 54,000 | 5.3% | 0.98 | high | suitable | Yes | easy | 5 |
| Ideal | > 5 ------ > 65 | >30,000 | < 4% | < 10 | < 1% by 2 ms | high (500 Mrad over 5 years) | No | easy | ≤ 5 |

Other materials under investigation include high light yield polycrystalline ceramics, including Eu-doped $(Gd,Lu)_2O_3$ (GLO) and $Gd_3(Ga,Al)_5O_{12}$:Ce (GGAG:Ce), and $(Gd,Lu)_3(Ga,Al)_5O_{12}$:Ce (GLuGAG) [3, 32, 33]. In recent years, halide perovskites have emerged as potential new materials for X-ray detectors, and their use in radiography applications is under investigation [34, 35].

## 1.3 Metal Halide Perovskites: Materials with Promising Optoelectronic Properties

### 1.3.1 *A Materials Renaissance*

Rapid developments in the power conversion efficiencies of halide perovskite solar cells have led to a burst in research efforts focused on a new generation of photovoltaic devices and "re-discovery" of these materials for other optoelectronic applications, including radiation detection [36, 37]. The record power conversion efficiency for these compounds jumped from 3.8% to 22.1% in 2016 between methylammonium lead bromide ($MAPbBr_3$) and $MAPbI_3$ thin films. Along the way, a number of all organic, inorganic-organic hybrid, and all inorganic compounds have gained attention for promising performance and ease of synthesis in a thin film form. Additionally, there is extensive ongoing research on tracking trends between the bandgap, structural dimensionality, and electronic dimensionality of these compounds [38, 39]. However, the small band gap of several of these materials makes them suitable semiconductors, rather than visible light-emitting scintillators. Another drawback is that many materials suffer from physical, chemical and functional stability, limiting performance and scalability [40, 41].

### 1.3.2 *What is in a name? Perovskite Classification*

The name "Perovskite" has made quite a journey from its original coining to the present day, explored in depth by Katz [42] and summarized here. In 1839, a new mineral was discovered in the Ural Mountains in Russia. The German mineralogist and crystallographer Gustav Rose determined the physical properties and chemical composition of this new mineral, $CaTiO_3$, and named it after a Russian politician and mineralogist Count Lev Alekseyevich Perovski. During his service as the Minister of Internal Affairs, Perovski contributed significantly to the mining industry and mineralogy research in Russia, along with being a personal connoisseur of minerals.

Nearly 100 years later, Swiss-Norwegian mineralogist and geochemist Victor Goldschmidt formulated what is now referred to as the Goldschmidt's tolerance factor to predict stable crystal structures for perovskite materials [43]. Perovskite crystals contain a network of corner-sharing

[$BX_6$] octahedra and crystallize with a general $ABX_3$ stoichiometry. The tolerance factor (*t*) is an empirical dimensionless number calculated from the ratio of the ionic radii in the crystal, described as $t = \frac{R_A + R_X}{\sqrt{2}(R_B + R_X)}$ $R_A$, $R_B$, and $R_X$ are the ionic radii of the A, B, and X atoms. If the tolerance factor is 0.9 – 1, then the structure is likely to be cubic and if it is 0.71 – 0.9, then the structure is likely to be orthorhombic/rhombohedral (distorted perovskite with tilted octahedra). Outside of this range, it is not likely that a perovskite will form. A second empirical index that was created to predict structural stability is the octahedral factor (μ), described as $\mu = \frac{R_B}{R_X}$ [44]. It is expected that a perovskite can form when μ is between 0.442 and 0.895.

Deviations from the $ABX_3$ structure have led to a number of other compounds to be considered as perovskites or perovskite derivatives and analogues [45, 46]. Given the expansive nature of the compositional and structural space, there are investigations to link chemical structure and composition to electronic structure, possibly allowing for tuning of luminescent properties. For example, symmetry within the $ABX_3$ structure impacts electronic properties. Distortion caused by octahedral tilting in $ABX_3$ perovskites with orthorhombic structures has been linked to larger band gaps compared to those in cubic structures [47].

Another example of this structure-property relationship was seen in the cesium lead bromide system, in which the band gap increased with decreasing structural dimensionality [48, 49]. The band gap of "three-dimensional" $CsPbBr_3$ (cubic crystal structure) was 2.35 eV, "two-dimensional" $CsPb_2Br_5$ (tetragonal structure) had a band gap of 3.10 eV, and "zero-dimensional" $Cs_4PbBr_6$ (trigonal structure) had a direct band gap of 3.90 eV. Here, dimensionality refers to the structural arrangement of [$BX_6$] octahedra (**Figure 4**). This "zero dimensional" structure has isolated [$BX_6$] octahedra bridged by monovalent cations, resulting in shorter bond length and higher bond strength, as well as larger band gap and strong exciton localization [48, 49]. It may be possible that these structural-electronic changes can affect scintillation properties.

While there are interesting relationships between the structure and functional properties of these types of materials, the nomenclature of classifying them all as "perovskites" is often misused. Akkerman and Manna have recently reiterated that for a compound to be considered a "perovskite," it must have an $ABX_3$ or equivalent stoichiometry consisting of a cubic network of corner-sharing BX octahedra [45]. This includes orthorhombic and tetragonal $ABX_3$ disordered

perovskites that arise from the tilting of the octahedra. Similarly, Breternitz and Schorr put forth three essential traits for a perovskite, including 1) a stoichiometry in a ratio of 1:1:3, 2) octahedral or distorted octahedra coordination of the B-site cation, and 3) the [$BX_6$] octahedra must be organized in a corner-sharing 3D network [46]. In $A_4BX_6$ structures, the arrangement of the [$BX_6$] octahedra and the presence of two distinct crystallographic sites for A-site cations is inconsistent with the definition of a perovskite. Additionally, $AB_2X_5$ structures do not contain [$BX_6$] octahedra. Nevertheless, the analysis of a family of related compositions and their scintillation properties is valuable.

In this work, the compositions will be referred to as "three-dimensional" and "distorted three-dimensional" perovskites where appropriate ($ABX_3$). Other compositional families will be identified by their stoichiometry ($AB_2X_5$, $A_4BX_6$).

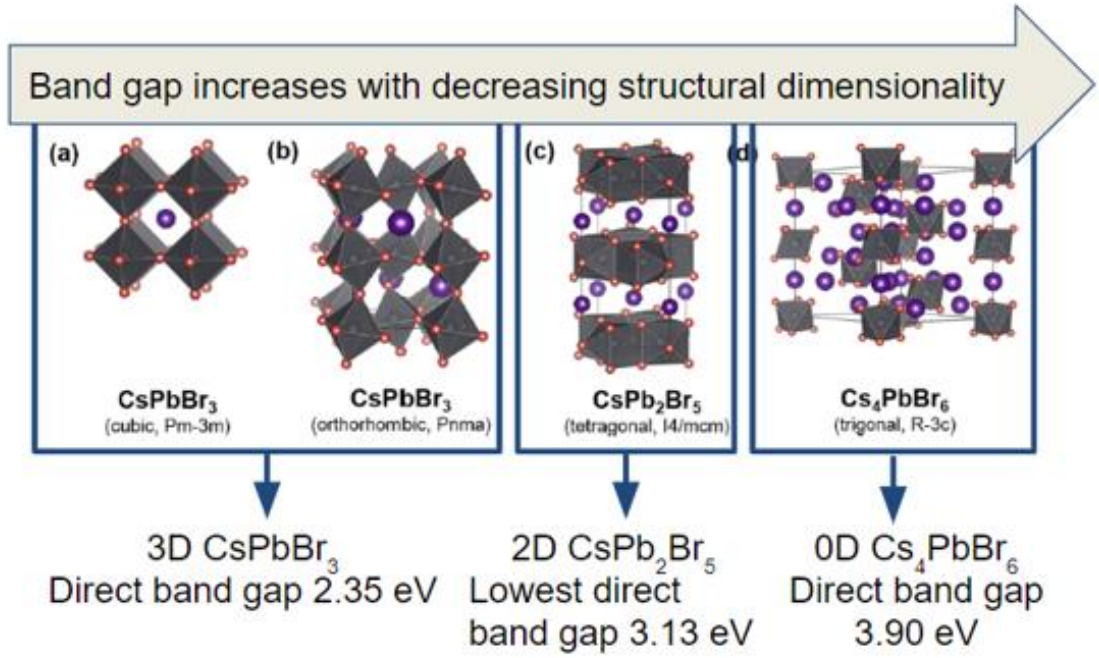


**Figure 4**. Effect of structural dimensionality on the band gap of cesium lead bromide. Adapted from [48].

### 1.3.3 *Inorganic Metal Halide Perovskite Scintillators*

A number of inorganic metal halide perovskites and other compositions with $ABX_3$, $AB_2X_5$, and $A_4BX_6$ stoichiometries have been reported in recent years ($A^+$ = Cs, K; $B^{2+}$ = Ca, Sr, Eu, Yb; $X^-$ = Cl, Br, I) [50-62]. Generally, inorganic metal halide perovskite scintillators are doped with $Eu^{2+}$ and have light yields of 50,000-80,000 ph/MeV, energy resolution of 3 – 6% at 662 keV, and scintillation decay times of 1-4 microseconds. The structural dimensionality may play a role in the performance of these scintillators. The light yield of $Cs_4EuI_6$ was 120% higher than three-dimensional $CsEuI_3$, and that of $Cs_4EuBr_6$ was 255% higher than $CsEuBr_3$ [50, 52, 63].

When considering relevance of these new promising materials for radiation detection applications, the stability, density, and physical form of the materials may pose challenges. The chemical and structural instability of many halide perovskites is a critical limitation and therefore major focus of research. Degradation can occur when the perovskites are exposed to moisture, oxygen, heat, light, and mechanical stress. Their densities are typically 3.5 – 4.5 g/cc and the effective atomic number can vary from ~30-50. These compounds are often hygroscopic. There are limited reports of the afterglow of these scintillators, and radiation hardness has not been studied.

While there are several studies on cesium and potassium-based halide perovskite scintillators, there are only a few studies reported in literature involving growth and characterization of compounds where rubidium occupies the A site. The compounds that have been reported have intense photoluminescence emission when doped with $Yb^{2+}$ and high light yields when doped with $Eu^{2+}$. The light yield of $RbCaBr_3$:Eu was reported to be 55% that of NaI:Tl (LY NaI:Tl ~40,000 ph/MeV) and $RbCaCl_3$:Eu reported to be 77% that of NaI:Tl. Additionally, Rebrova and Grippa demonstrated improvement in light yield and energy resolution of $RbCaBr_3$:Eu and admixed (Cs, Rb)$CaBr_3$:Eu with increasing $Eu^{2+}$ concentration [61, 64-66]. Intense blue emission has been observed for $RbCaCl_3$:Yb and $RbCaCl_3$:Eu [67, 68]. Although their monoclinic structure is different than the “two-dimensional perovskites” with tetragonal $AB_2X_5$ structures, $RbSr_2Br_5$:Eu and $RbSr_2I_5$:Eu have excellent scintillation properties, including light yield of 67,000 and 90,400 ph/MeV, respectively [69].

Advantages and disadvantages in performance with dopant species and concentration warrant exploration of the effects on scintillation properties in new matrices. As mentioned, Both $Eu^{2+}$

and $Yb^{2+}$ were efficient activators in several reported inorganic metal halide perovskites. These dopants also produced desirable performance in the prominent halide scintillator $SrI_2$ [70-73]. In general, $Eu^{2+}$ doping generates higher light yields than $Yb^{2+}$ doping [58, 70]. However, scintillation performance of $Eu^{2+}$ doped crystals can be limited by self-absorption as the crystal size increases [71, 74-76].

While the dopant species is an important decision, the concentration of the luminescent dopant added to the matrix also has significant effects on scintillation properties. Often, increasing the concentration of the dopant increases the light yield, up until a certain point. These increases are not necessarily linear. In the halide perovskite $KCaI_3$:Eu, light yield increased with increasing europium dopant concentration until ~3 mol% Eu. A study in $Cs_4CaI_6$:Yb and $Cs_4SrI_6$:Yb showed increasing light yield with increasing concentration, with a ~13,000 ph/Mev increase between 0.5% and 1% doping, but a smaller ~1,000-5,000 ph/MeV increase between 1% and 3% doping [58]. The optimal $Eu^{2+}$ dopant concentrations in many halide perovskite scintillators have typically been reported in the range of 3-7% [56, 77-83]. However, due to self-absorption and uniformity, the optimal dopant concentration in small crystals may not be the same for larger crystals ( $> 1\ in^3$) [83, 84].

As previously mentioned, three-dimensional $CsEuBr_3$ and zero-dimensional $Cs_4EuBr_6$ are interesting examples of the possible effects of structural dimensionality in scintillators. They are also examples of a type intrinsic, or self-activated scintillator in which the luminescent species is a primary constituent of the crystal rather than just a few mol percent substitution. While europium self-absorption is an issue in these crystals, self-activated scintillators generally have an advantage of improved luminescent distribution throughout the crystal.

In addition to doping to generate desirable luminescence and scintillation performance, doping with multiple elements is one method to further control defects and fine-tune properties [85]. In scintillators, these co-dopants can affect crystal quality, afterglow, light yield, energy resolution, and decay time, among other properties [86-88]. To highlight developments in a material relevant to high energy X-ray radiography, recent co-doping studies with $Eu^{2+}$ and $Sm^{2+}$ in CsI:Tl have shown significant reduction in afterglow [31, 89, 90]. Co-doping with $Sm^{2+}$ (0.05-0.5 mol%) led to suppression of afterglow by a factor of up to 50. It was also shown that ultralow concentrations of $Sm^{2+}$ (0.005 mol%) can reduce afterglow in CsI:Tl by over one order of

magnitude while preserving the initial high light yield of the scintillator [91]. Afterglow intensity in CsI:Tl could also be reduced by almost two orders of magnitude with the addition of 0.2% $Eu^{2+}$. It is thought that both co-dopants introduced deep electron traps, which divert electrons from the shallow traps associated with thallium, the primary luminescent dopant. This diversion suppressed delayed recombination from the shallow traps that led to high afterglow.

Another aspect of rubidium-containing scintillators that should be addressed is their intrinsic radioactivity resulting from the natural radioisotope Rb-87. Rb-87 decays through 100% % β emission to Sr-87 with a maximum energy of 283 keV and half-life of $4.97\times10^{10}$ years [92]. In some applications, like gamma ray spectroscopy, the counts resulting from Rb-87 could be problematic, as they could potentially mask lower energy signatures. However, intrinsic radioactivity could be a less problematic for other homeland security applications, like high energy X-ray radiography, where the detector's intrinsic radioactivity can be subtracted as background [93, 94]. However, the effects on detection efficiency are not clear. There are several commercially successful scintillators that contain radioactive elements, like LSO:Ce (Lu-176) and $LaBr_3$:Ce (La-138). However, the natural abundance of their radioisotopes is much smaller than Rb-87. Lu-176 is 2.6%, and that of La-138 is 0.089%, while that of Rb-87 is 27.83%. The calculated specific activities are 300 Bq/cc for LSO:Ce and 1.44 Bq/cc for $LaBr_3$:Ce.

### 1.4 Vertical Bridgman Crystal Growth

The performance of scintillators can be impacted by the synthesis and quality of the crystals, and it is required that growth and performance can be scalable. Thus, discussion of the crystal growth process is warranted. Metal halide scintillators are typically grown by the Bridgman technique, also commonly referred to as the Bridgman-Stockbarger Method. Chemically compatible compounds with melting points < 1000°C can be grown in sealed quartz ampoules. The ampoule serves both as the growth crucible and containment of hygroscopic materials from ambient moisture.

Percy Williams Bridgman introduced this crystal growth technique in 1924 as a method of growing large single crystals of several different metals [95]. The method involves heating polycrystalline starting material above its melting point and slowly solidifying from the seed end to the tail end of the molten charge. A benefit of this controlled directional solidification is that it

can purify the grown material by segregating impurities to one end of the boule. However, in crystal growth of scintillators, this can also lead to dopant nonuniformity / segregation.

During growth, pulling rate, temperature and temperature gradient, and cooling rate are controlled. The Bridgman furnace can be oriented vertically or horizontally. The ampoule can be translated mechanically through the thermal gradient, or the temperature gradient of the furnace can be changed around the stationary ampoule to reduce mechanical vibrations. Of all the parameters for the growth, Bridgman states that the "most difficult and important is to secure the formation of only one grain at the bottom end." Therefore, growth ampoules often include a specialized grain selector or capillary for this purpose.

Around a decade later, Donald C. Stockbarger modified the Bridgman technique by introducing a thermal baffle between the hot and cold zones of the furnace to increase the temperature gradient [96]. This modification was driven by his investigations on growth of lithium fluoride crystals, which showed that freezing of the melt should occur in a region of the furnace with a high thermal gradient [97].

In the 1970s, Chang, Wilcox, and Fu reported detailed analyses on the most desirable shapes of the interface between the solid and liquid phases of the crystal, including how it can be controlled using insulating material and careful positioning in the furnace [98, 99]. A planar or flat interface minimizes thermal stress, and a slightly convex interface improves grain selection. A slightly convex interface also promotes segregation of unwanted impurities and polycrystalline grains towards the wall of the ampoule, reducing inclusions. The addition of a layer of insulation between the furnace hot zones and cold zones, as done by Stockbarger, decreased dependence of the growth interface shape on thermal conditions.

# CHAPTER 2 SCOPE AND OBJECTIVES

The current scintillators used in X-ray radiography (i.e., $CdWO_4$, CsI:Tl) and other homeland security applications have limitations in performance. While there is ongoing research on many types of scintillators to fulfill the needs of these applications, such as codoping CsI:Tl and testing of new garnet scintillators, many other compounds remain unexplored.

In recent years, potassium and cesium based inorganic metal halide perovskite scintillators activated with divalent europium have shown excellent performance for gamma ray spectroscopy applications, but research into their rubidium-based counterparts is severely limited. Additionally, there are limited reports on the effects of doping these perovskite scintillators with alternative activators, such as divalent ytterbium. Third, many of the properties of these scintillators relevant to X-ray radiography, such as radiation damage and afterglow, have never been tested.

This work focuses on the discovery of new inorganic metal halide scintillators including:

- Explore stability (i.e., phase formation, moisture sensitivity) of new inorganic metal halide perovskites and related compositions.
- Grow, for the first time, single crystals of these new materials via the Bridgman method.
- Test if new compounds scintillate, including investigations on:
    a. the effects of doping with luminescent activators ($Eu^{2+}$, $Yb^{2+}$).
    b. the sensitivity of scintillation properties to dopant concentrations.
- Investigate potential for initial scale up of crystal growth (from Ø7 mm to Ø22 mm size).
- Evaluate application-oriented properties of new materials, like radiation damage.

The outcomes of this work expand the current body of knowledge in terms of 1) compositional space and materials stability, 2) scintillation performance, and 3) suitability of detector materials for applications.

Portions of this work were previously published in peer-reviewed journal articles and presented at conferences. A list of articles and conferences is in **Appendix A**.

# CHAPTER 3 METHODOLOGY

## 3.1 Materials Selection & Doping Studies

Through preliminary experimental screening, several inorganic metal halide candidates were identified. Initial criteria for screening were the reported melt behavior of the compound, density, and effective atomic number, phase purity, and scintillation light yield. Stability was investigated through synthesis of small (2 g) polycrystalline samples, as well as growth of single crystals in Ø7 mm size. X-ray diffraction was done to investigate phase formation and phase purity.

Examining the phase formation, crystal quality, and scintillation properties at this stage led to identification of several candidates for further studies, which are listed in **Table 2**. Of the candidates identified, the scintillation properties as a function of dopant concentration (mol %) were tested. Additionally, different luminescent dopants were explored.

The dopant concentration ranges used in this work were selected based on literature of similar compositions. For example, the optimal $Eu^{2+}$ dopant concentrations in halide compounds are typically in the range of 5-7 mol % [56, 77-83]. Moreover, the optimal europium concentration for small diameter crystals may not be the optimal concentration for larger crystals ( > 1 $in^3$) due to uniformity and europium self-absorption [83, 84]. Some segregation from seed end to tail end of the crystals was expected, due to the differences in ionic radii between the host matrix site and the dopant ion (**Table 3**). To account for this, scintillation properties of samples from the seed end and tail end of the crystals were characterized where applicable.

**Appendix B** summarizes the properties of some compositions that were tested but excluded from further study. The decision to exclude these materials was based on one or more of the following factors: poor raw materials quality, incongruent or unstable melting, poor phase purity, destructive solid-solid phase transitions, low light yield, or no observable radioluminescence. **Table 17** in **Appendix B** summarizes new scintillators with either synthesis or performance limitations. **Table 18** lists unstable compositions and compositions that did not exhibit radioluminescence.

**Table 2.** Scintillator compositions explored in this work.

| Composition | Crystal Structure (Space Group) | Density (g/cc) | Effective Atomic Number | Reported Melt Behavior |
|---|---|---|---|---|
| $CsCaCl_3$ | Cubic (Pm-3m) | 3 | 42 | Congruent [100] |
| $RbSrI_3$ | Orthorhombic (Cmcm) | 4.1 | 49 | Unknown (No published phase diagram) |
| $RbCaBr_3$ | Orthorhombic (Pnma) | 3.4 | 34 | Congruent [101] |
| $RbSr_2Br_5$ | Monoclinic ($P12_1/c1$) | 4.18 | 35 | Congruent [102] |
| $RbSr_2I_5$ | Monoclinic ($P12_1/c1$) | 4.2 | 49 | Unknown (No published phase diagram) |
| $RbBa_2I_5$ | Monoclinic ($P12_1/c1$) | 4.67 | 53 | Unknown (No published phase diagram) |
| $Rb_4CaBr_6$ | Trigonal (R-3hc) | 3.5 | 35 | Peritectic [101] |
| $Rb_4CaI_6$ | Trigonal (R-3hc) | 3.7 | 48 | Peritectic [103] |

**Table 3.** Comparison of ionic radii of dopant and host matrix species.

| Species | Coordination Number | Ionic Radius (Å) [104] |
|---|---|---|
| $Ca^{2+}$ | 6 | 1.00 |
| | 7 | 1.06 |
| $Sr^{2+}$ | 6 | 1.18 |
| | 7 | 1.21 |
| | 8 | 1.26 |
| $Eu^{2+}$ | 6 | 1.17 |
| | 7 | 1.20 |
| | 8 | 1.25 |
| $Yb^{2+}$ | 6 | 1.02 |
| | 7 | 1.14 |
| $Cs^{+}$ | 12 | 1.88 |
| $Tl^{+}$ | 12 | 1.70 |

### 3.2 Crystal Growth

3.2.1 *Sample Preparation and Vertical Bridgman Growth*

Due to the hygroscopic nature of the starting materials and resulting crystals, the Vertical Bridgman crystal growth technique was appropriate for this work. Crystals were grown inside of sealed quartz ampoules. Customized quartz ampoules were created by Bo Bishop at the Glassblowing Shop in the UT Department of Chemistry and Sandfire Scientific, LTD.

Growth began with anhydrous high purity (≥ 99.99% pure, when available) starting materials weighed in stochiometric amounts (**Figure 5**). Note that this quantitative purity refers to the purity level of the material on a metals basis. It typically does not account for the moisture, oxygen, or organic / carbon content that may be present in the raw materials. To maintain the desired stoichiometry, luminescent dopants substituted their constituent site materials (i.e., for $RbSrI_3$:Eu, 5 mol% of $EuI_2$ replaced 5 mol% of $SrI_2$). The raw materials were sensitive to moisture, so samples were prepared inside of a $N_2$ glovebox with controlled oxygen and moisture content. Then, the loaded ampoule was transferred to a vacuum system for drying to remove residual moisture. The samples were dried at 250°C under vacuum of $10^{-7}$ Torr. The time for drying, including ramping up in temperature, was adjusted to be longer for larger samples. After drying, the quartz samples were sealed under vacuum with an oxyhydrogen torch. Prior to growth, the charge was homogenized by melting the ampoule at least ~50°C above the melting point of each of the raw materials comprising the sample for at least 12 hours. This heating cycle was repeated 2-3 times, vertically inverting the ampoule each time to maximize mixing.

A summary of growth parameters is in **Table 4**. Crystals Ø7 mm in diameter were grown for initial evaluation of properties, and for the most promising compositions, crystals were scaled up to Ø12 mm or Ø22 mm. All of the crystals grown in this work were self-seeded in the capillary of the growth ampoules and were therefore randomly oriented. The growth temperatures, translation rates, and cooling rates were tailored to each composition. Three-zone and 24-zone Electrodynamic Gradient Bridgman furnaces (The Mellen Company) were used for synthesis and crystal growth. Additionally, gold-coated transparent Bridgman furnaces (Thoughtventions Unlimited, LLC and ThermCraft, Inc.) were leveraged to observe real-time stability and progression of growth of new compounds. The gold mirror coating reflected infrared radiation and acted as a thermal insulator.

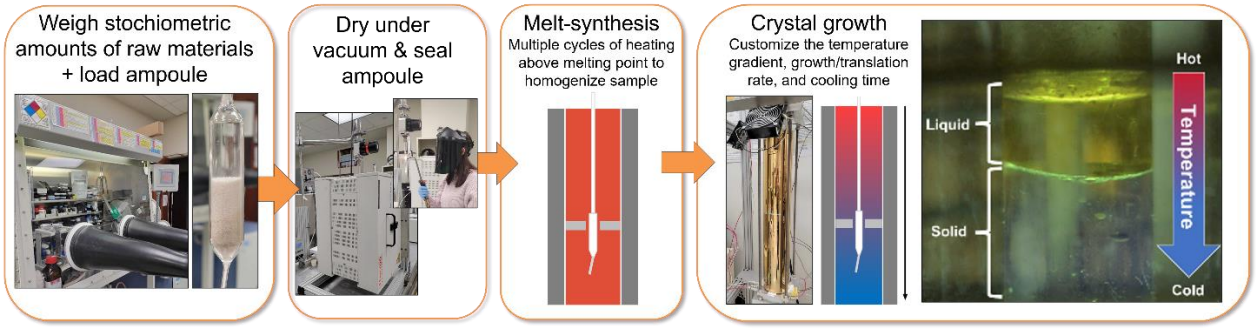


**Figure 5.** Sample preparation for Vertical Bridgman crystal growth.

**Table 4.** Crystal growth parameters.

| Matrix | Diameter (mm) | Ampoule / capillary | Furnace Set Points (°C) | Melting Point (°C) | Translation Rate(s) (mm/hr) | Cooling (hr) |
|---|---|---|---|---|---|---|
| $RbCaBr_3$ | 7 | Bent | 840/640 | 737 | 0.5 | 100 |
| $RbSrI_3$ | 7 | Bent | 600/350 | 453 | 0.5 | 100 |
| $RbSr_2Br_5$ | 7 | Bent, straight | 665/500 | 593 | 0.4 | 100 |
| $RbSr_2I_5$ | 7 | Bent, straight | 585/385 | 490 | 0.4<br>0.5<br>1<br>3<br>5 | 100 |
| $Rb(Sr,Ba)_2I_5$ | 7 | Straight | Various ~655/480 | 526-578 | 0.4 | 90-100 |
| $RbBa_2I_5$ | 7 | Straight | 675/555 | 597 | 0.5 | 100 |
| $Rb_4CaI_6$ | 7 | Bent | 610/510/410 | 544 (peritectic) | 0.5 | 100 |
| $Rb_4CaBr_6$ | 7 | Bent | 680/565/465 | 585 (peritectic) | 0.5 | 100 |
| $CsCaCl_3$ | 12 | Bent, Carbon coated | 980/800 | 910 | 0.8 | 100 |
| $RbSrI_3$ | 22 | Bent | Various, ~600/350 And 580/470/350 | 453 | 0.2 | 150 |
| $Rb_4CaI_6$ | 22 | Bent | 610/510/410 | 544 (peritectic) | 0.2 | 120 |
| $RbSr_2I_5$ | 22 | Straight | 585/385 | 490 | 0.5<br>1.5<br>3.5 | 150 |
| $RbSr_2Br_5$ | 22 | Straight | 665/500 | 593 | 0.5 | 150 |
| $RbCaBr_3$ | 22 | Bent | 840/640 | 737 | 0.25 | 120 |

3.2.2 *Materials Purification / Treatment*

Chemical vendors had limited availability of high purity (> 99.9%), anhydrous raw materials, particularly RbI and RbBr. As such, these materials were purchased in a low-purity form (99.8% or 99.9% pure) and purified in-house. The vendors did not have certificates of analysis available to identify the impurities in the material. To purify the materials, three methods were used:

1) Drying and growth of the material as a single crystal in carbon coated ampoules.
2) Filtering of the melt through quartz filters with controlled porosity.
3) Zone refining at Radiation Monitoring Devices, Inc.

The results of these treatments are shown in **Chapter 7, Scale up of Crystal Growth**.

**3.3 Physical Properties Characterization**

3.3.1 *Powder X-ray Diffraction (XRD)*

To assess phase purity and lattice parameters, powder X-ray Diffraction (XRD) measurements were done. First, small samples were cleaved from the boule of interest while working inside a $N_2$-filled glovebox. The samples were crushed into a fine, uniform powder using an agate mortar and pestle. The powder was loaded onto silicon zero-background sample holders, flattened with a glass slide, and covered with Kapton film, which prevented moisture exposure to the sample during the measurement. The XRD measurements were done at the Institute for Advanced Materials and Manufacturing (IAMM) at the University of Tennessee, Knoxville. The diffraction patterns were collected at room temperature from 15°C-70° 2-theta with a PANalytical Empyrean diffractometer in a Bragg-Brentano geometry. The X-ray source was Cu-K alpha, operated at 45 kV and 40 mA. The sample holder was rotated during the measurements. Initial phase identification was done with High Score Plus, and Rietveld refinements were done using GSAS-II [105].

3.3.2 *High Temperature X-Ray Diffraction (HTXRD)*

For select materials, X-ray diffraction patterns were acquired as a function of increasing temperature. These high temperature X-ray diffraction patterns allowed for the investigation of solid-solid phase changes and determination of the coefficients of thermal expansion (CTE) for $RbSrI_3$, $RbSr_2I_5$, $RbSr_2Br_5$. Samples were crushed into a fine, uniform powder using an agate mortar and pestle inside the $N_2$-filled glovebox. The powder was loaded into a 0.4 mm deep alumina sample holder and flattened with a glass slide. The XRD measurements were done at the

Institute for Advanced Materials and Manufacturing (IAMM) at the University of Tennessee, Knoxville with the assistance of Dr. Michael Koehler. The samples were loaded into the PANalytical Empyrean diffractometer, during which they were exposed to ambient air and moisture for ~10-20 seconds before the sample chamber was closed and $N_2$ gas was flowed. First, the samples were heated to 200°C to dry them before returning to 25°C to acquire the initial pattern. After this, the patterns were acquired between 50°C and 400°C in 50°C increments with a 15 minute dwell between temperature changes. Rietveld refinements were done using HighScore Plus.

3.3.3 *Differential Scanning Calorimetry (DSC)*

To investigate the presence of solid-solid phase changes and measure melting and crystallization temperatures, Differential Scanning Calorimetry (DSC) measurements were done using the Setaram LabSys Evo. For most samples, quartz crucibles were used, which preserved the samples from moisture exposure. A sample ~60 mg in size was sealed under vacuum inside of small quartz crucibles, and an empty, sealed quartz crucible nearly identical in size to the sample crucible was used as the reference. For some samples, alumina crucibles with alumina lids were used. If available, phase diagrams were used to select the maximum temperature used for the measurement; otherwise, the maximum temperature was generally selected as 50-100°C above the melting point of the raw materials used to make the composition. Heat flow curves were collected with a heating rate of 5 K/min with flowing $N_2$ through the sample chamber. The endothermic and exothermic peaks were fit to determine onset temperatures.

3.3.4 *Dynamic Vapor Sorption (DVS)*

Many metal halide scintillators are known to be hygroscopic. To be able to use hygroscopic scintillators in real-world applications, they must be hermetically sealed. For newly discovered scintillators, Dynamic Vapor Sorption (DVS) measurements can help assess the extent to which the materials are hygroscopic, and therefore, their potential needs for hermetic encapsulation. DVS measurements were conducted on samples 30-40 mg in size. The DVS Intrinsic Plus from Surface Measurement Systems was used. The mass change of the sample over time was measured, while the sample was kept at a constant temperature of 25°C and 40% relative humidity, which were meant to mimic ambient conditions. Hygroscopic scintillators $SrI_2$:Eu and NaI:Tl were measured for comparison.

For select compositions, pulse height spectra were collected as a function of time while the sample was exposed to ambient conditions. This was done to investigate how spectroscopic performance changed as the crystal reacted with moisture, similar to work done by Zhuravleva, et al. [106].

### 3.4 Optical, Luminescence & Scintillation Characterization

The crystals' luminescence and scintillation response to UV light, X-rays, and gamma rays was investigated by measuring optical absorbance and transmittance, photoluminescence, radioluminescence, pulse height spectra (light yield and energy resolution), scintillation decay time, and X-ray afterglow.

Right cylinders were cut from Ø7 mm crystals to evaluate luminescence and scintillation properties. Cross-section samples 2-3 mm thick were polished with SiC polishing pads and mineral oil ($C_{15}H_{24}$). The impurity-rich last-to-freeze was either cut or polished away. During most measurements, the samples were submerged in mineral oil to prevent degradation of the samples due to moisture exposure.

#### 3.4.1 *Optical Absorbance and Transmittance and Optical Band Gap*

High optical transmittance can be an indicator of crystal quality, and absorbance can be used to determine optical band gap via the modified Tauc method. Optical transmittance and absorbance were measured from 200-800 nm using the Varian Cary 5000. The absorbance data was used to determine optical band gap using the modified Tauc method [107, 108]. Values of $(\alpha h\nu)^{1/n}$ were plotted against $h\nu$, where $\alpha$ is the absorption coefficient, $h$ is Planck's constant, $\nu$ is the photon's frequency, and $n$ is related to the nature of the electronic transition (i.e., direct, indirect, forbidden, allowed). Then, a linear fit was applied to determine the band gap from intersection with the x-axis. Fits for an indirect band gap (n = 2) and direct band gap (n = ½) were compared.

#### 3.4.2 *Photoluminescence and Radioluminescence*

It is important to determine the emission wavelength of a new scintillator to match the optimal wavelengths for the photodetector to be used. Both photoluminescence and radioluminescence spectra were collected. The crystals were oriented in a reflection geometry, in which the crystal was at an approximately 45 degree orientation to the excitation source and the photodetector. Steady state photoluminescence emission and excitation were collected with the Horiba Jobin

Yvon Flourolog 3 Spectrofluorometer, and radioluminescence was collected under continuous X-ray irradiation (35 kV, 0.1 mA, Cu-target) with a 150-mm focal length Acton SpectraPro-2150i monochromator from 200-800 nm.

3.4.3 *Scintillation Decay Time and X-ray Afterglow*

The scintillation decay time was measured by using the Bollinger and Thomas technique with Cs-137 excitation [2]. The acquired profile was fit with either a single or a multiple exponential decay fit to determine time constants and their proportional contributions.

Of particular importance for high energy X-ray radiography is the characterization of afterglow. Samples with promising afterglow measured in the SMRC laboratories (20 ms minimum time scale) were shipped to RMD, Inc. for characterization of afterglow on shorter time scales (2 ms). At UTK, X-ray induced afterglow was measured after 15 minutes of irradiation with the X-ray tube operated at 35 kV and 0.1 mA. Scintillation light intensity was collected with the Hamamatsu R2059 PMT. Samples were coupled to the PMT window with mineral oil and covered with Teflon tape to aid in light collection. $CdWO_4$ (5x5x5 mm, donated to the University of Tennessee Department of Nuclear Engineering from the U.S. Department of Homeland Security) and CsI:Tl (Ø1", Encapsulated, Amcrys) were measured as references.

3.4.4 *Pulse Height Spectra (Light Yield, Energy Resolution)*

Cs-137 pulse height spectra were collected to measure absolute light yield and energy resolution. A pulse height spectrum is a graphical representation of the energy of the photon interacting with the detector plotted against the counts of pulses at different energy levels. During the measurement, these are binned into different channels. Counts correspond to the energy of a photon emitted by a gamma ray source, and a distinct photopeak forms when many photons of the same energy, such as the gamma rays emitted by a specific source, are absorbed by the detector. The absolute light yield of scintillators is commonly measured with the position of the photopeak corresponding to the 662 keV gamma ray emission of Cs-137. Cs-137 is not a naturally occurring radioisotope; it is produced by nuclear fission of uranium and plutonium and is therefore a byproduct from nuclear reactors and nuclear weapons testing.

During the measurements, a calibrated Hamamatsu R2059 photomultiplier tube (PMT) was used to measure light yield, with the single photoelectron centroid, the PMT quantum efficiency, and the 662 keV photopeak centroid as described in [76]. A Hamamatsu R6231-100 PMT was

used to measure energy resolution and light yield non-proportionality. The energy resolution was determined with a Gaussian fit to the 662 keV photopeak. The full width at half maximum peak intensity was divided by the peak centroid. To test light yield non-proportionality, a set of gamma ray sources with excitation energies from 30.85 – 662 keV were used. For all pulse height spectra measurements, the pulse processing chain consisted of the PMT, a Canberra 2005 preamplifier, an Ortec 672 amplifier with a 10 microsecond shaping time, and a Tukan 8K multi-channel analyzer.

3.4.5 *Temperature-Dependent Light Yield and Radioluminescence*

The temperature-dependent response of samples ~4x4x4 mm in size to X-rays and gamma rays was tested. During these measurements, a sample was attached to the cold finger of a DE202AE cryostat using a Teflon-wrapped copper clamp and held under vacuum (< 20 mTorr). To maximize light collection, a Teflon-wrapped quartz tube covered the sample to guide scintillation light to the photodetector, as shown in **Figure 6**. Temperature was changed and monitored with a Lakeshore 331 Temperature Controller. Radioluminescence measurements (20 K – 600 K) were done with otherwise the same method as previously described. Relative light yield and energy resolution were measured from pulse height spectra collected with a Cs-137 excitation source and a Hamamatsu R2059 PMT. The pulse processing chain consisted of the PMT, a Canberra 2005 preamplifier, an Ortec 672 amplifier with a 10 microsecond shaping time, and a Tukan 8K multi-channel analyzer. The relative light yield was compared by monitoring the change in the channel number position of the 662 keV photopeak. There was at least a 10-15 minute dwell after temperature changes to allow for stabilization.

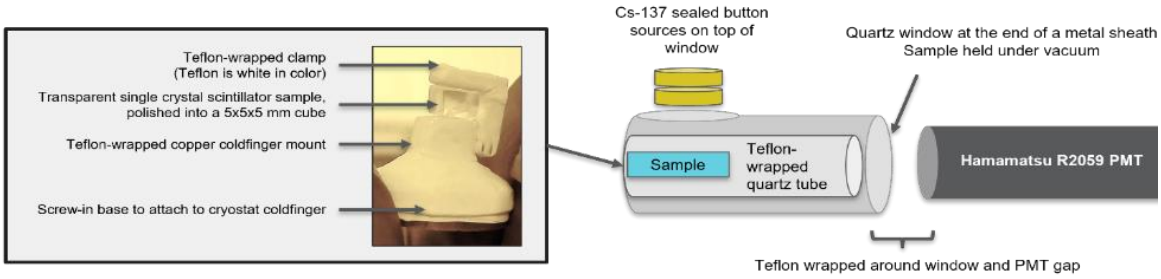


**Figure 6.** Apparatus and sample holder for testing temperature dependence of scintillator light yield.

To maximize light collection during temperature dependent measurements, experiments involving modifications to the measurement configuration were completed while collecting room temperature pulse height spectra for a ~5x5x5 mm LSO:Ce cube.

**Figure 7** shows these configurations and the corresponding pulse height spectra. Teflon was added around the base and around the top of the copper sample holder. The top face of the sample holder was pointed towards the center of the PMT during measurements. It was also tested if including Teflon around the gap between the quartz window of the vacuum chamber and the PMT window affected light collection. The 662 keV photopeak shifted to higher channel numbers with the addition of more Teflon to the sample holder. Changes in pulse height spectra were negligible whether Teflon was included around the gap between the PMT and quartz vacuum chamber or not.

3.4.6 *Irradiation Effects*

Irradiation effects from Co-60 gamma ray exposure and X-ray irradiation with a linear accelerator were investigated for select crystals. The optical transmittance and pulse height spectra were measured before and after irradiation. The details of these experiments are included in **Chapter 8, Radiation Damage.**

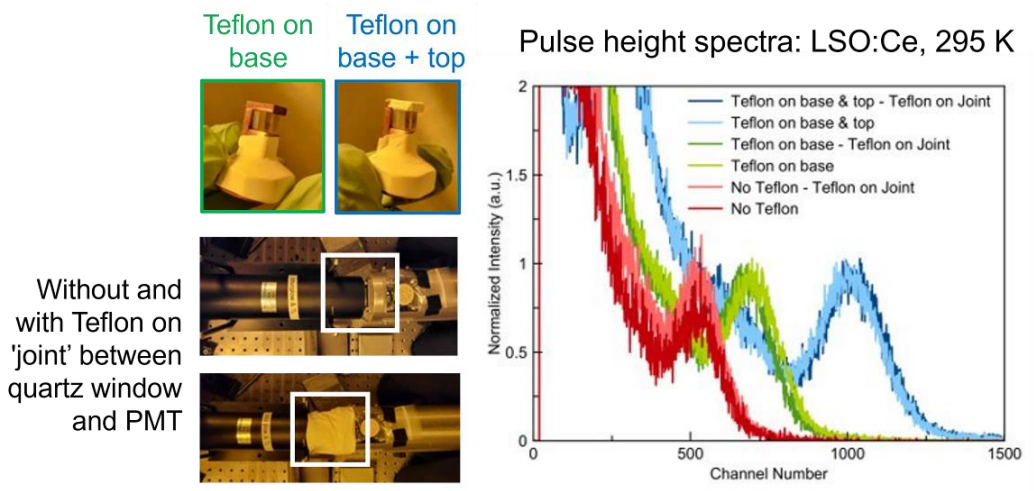


**Figure 7.** Experiments to maximize light collection and improve pulse height spectra for LSO:Ce collected at room temperature.

# CHAPTER 4 $ABX_3$ COMPOSITIONS

Sections of this chapter were originally published in the following peer-reviewed journal articles:

- **K. S. Pestovich**, L. Stand, E. van Loef, C. L. Melcher and M. Zhuravleva, "Crystal Growth of New High Light Yield Halide Perovskite Scintillator $RbSrI_3$," in *Journal of Crystal Growth*, vol. 627, p. 127540 (2024).
- **K. S. Pestovich**, L. Stand, E. van Loef, C. L. Melcher and M. Zhuravleva, "Crystal Growth and Characterization of Europium-Doped Rubidium Calcium Bromide Scintillators," in *IEEE Transactions on Nuclear Science*, vol. 70, no. 7, p. 1370-1377 (2023) © 2023 IEEE.
- **K. S. Pestovich**, L. Stand, K. Joshi, X. Wen, C. L. Melcher, L. S. Pandian, E. van Loef, M. Zhuravleva, "Investigating the Luminescence, Irradiation Effects & Fast Neutron-Gamma Discrimination Characteristics of Cubic Halide Perovskite Scintillator $CsCaCl_3$:($Eu^{2+}$, $Tl^{+}$)" in *Nuclear Instruments and Methods in Physics Research - section A.* Submitted for review.

This chapter describes the crystal growth, physical properties, and scintillation properties on three-dimensional perovskite crystals ($ABX_3$). Two types of studies are discussed: 1) further exploration of known scintillators through dopant studies ($RbCaBr_3$, $CsCaCl_3$) and 2) discovery of a new scintillator composition and tests of its properties ($RbSrI_3$). A summary of the results from this work is included in **Table 5**. While $CsCaCl_3$ is distinct from other compositions in this work in that it is not a rubidium-based halide perovskite, it is one of only a few $ABX_3$ inorganic metal halide perovskite scintillators that have a cubic crystal structure at room temperature. Many of the $ABX_3$ scintillators have an orthorhombic structure at room temperature, with some undergoing solid-solid phase transitions from a cubic structure at high temperatures. Thus, study of $CsCaCl_3$ provided an opportunity to compare differences between cubic and orthorhombic structures, especially in the case of radiation damage (**Chapter 8**).

The structure predicted by Goldschmidt tolerance factors were consistent with the crystal structure measured by XRD. $RbSrI_3$ has a tolerance factor of 0.820 and octahedral factor of 0.536, $RbCaBr_3$ has a tolerance factor of 0.879 and octahedral factor of 0.510, and $CsCaCl_3$ has a tolerance factor of 0.929 and octahedral factor of 0.552 [44]. If the tolerance factor is 0.71 – 0.9,

then the structure is likely to be orthorhombic/rhombohedral (distorted perovskite with tilted octahedra), which was accurate here in the case of $RbSrI_3$ (Orthorhombic, *Cmcm*) and $RbCaBr_3$ (Orthorhombic, *Pnma*). If the tolerance factor is between 0.9 – 1, the crystal is likely to be cubic, which as accurate for $CsCaCl_3$ (Cubic, *Pm-3m*).

High quality single crystals of $RbCaBr_3$, $CsCaCl_3$ and $RbSrI_3$ were grown, undoped and doped with either divalent europium, divalent ytterbium, or monovalent thallium in the case of $CsCaCl_3$. $RbCaBr_3$:Eu had excellent optical transmittance (>70%) and high light yield and energy resolution of 43,000 ph/MeV and 4.0% at 662 keV when doped with 7 mol% Eu. The $CsCaCl_3$:(Eu, Tl) crystals had moderate performance, with the best light yield and energy resolution of $CsCaCl_3$:Tl being 17,000 ph/MeV and 8.6% at 662 keV. Additionally, this crystal had fast neutron-gamma discrimination capabilities, with a FOM of 3.2 between gamma-rays and fast neutron captures that produce protons and a FOM of 1.6 between gamma-rays and fast neutron captures that produce alpha particles. $RbSrI_3$:Eu had excellent scintillation performance, with high light yields up to 83,600 ph/MeV with 7 mol% Eu, and the best energy resolution of 2.8% a 662 keV with 5 mol% Eu.

In both $RbCaBr_3$ and $RbSrI_3$, the dominant radioluminescence emission of $Yb^{2+}$ was its spin-forbidden transition. These crystals had lower light yields of 6,400 ph/MeV and 24,000 ph/MeV, respectively. One limitation here is that the 10 microsecond shaping time used for pulse height spectra measurements may limit the collection of light from the slow decay of $Yb^{2+}$ spin-forbidden emissions, which have been reported to be up to hundreds of microseconds in other compositions. For example, $CsCaBr_3$:Yb 0.1% had decay components of 210 ns and 390 μs [109].

$RbSrI_3$ had several other properties that highlight its suitability of radiography applications. $RbSrI_3$:Eu and $RbSrI_3$:Yb had an X-ray afterglow better than that of CsI:Tl. In particular, $RbSrI_3$:5 mol% Eu had an X-ray afterglow of 1.8% at 2 ms. Additionally, the relative light yield of $RbSrI_3$:Eu changed ≤ 5% over the temperature range relevant to most homeland security applications. Based on promising performance of $RbCaBr_3$:Eu and $RbSrI_3$:Eu in particular, scale up to a Ø22 mm size was pursued, which will be discussed in **Chapter 7, Scale up of Crystal Growth**.

**Table 5.** Properties of $ABX_3$ Scintillators.

| Scintillator (Ø7 mm, 3 mm) | Crystal structure / *Space group* | Density (g/cc) / $Z_{eff}$ | RL $\lambda_{max}$ (nm) | Light Yield (ph/MeV) | Energy Res. at 662 keV | Scint. Decay |
|---|---|---|---|---|---|---|
| $RbCaBr_3$ $E_g$ = 5.5 eV | Ortho-rhombic *Pnma* | 3.46 | 370, 440, 545 | No photopeak | | Not measured |
| $RbCaBr_3$:0.5 mol% Yb | | | 440 | 6,400 | 13.3% | Not measured |
| $RbCaBr_3$:Eu 5% | | 34 | 434 | 37,000 | 7.6% | 2.3 μs |
| $RbCaBr_3$:Eu 7% | | | 436 | 43,000 | 4.0% | 2.8 μs |
| $CsCaCl_3$:1% Eu | Cubic *Pm-3m* | 3 | 450 | 15,800 | 16% | 1.8 μs |
| $CsCaCl_3$:1% Tl *Exhibited γ-n PSD with FOM 1.2 | | | 310, 330, 443 | 17,000 | 8.6% | 2.8 ns (2%), 610 ns (54%), 2.6 μs (45%) |
| $CsCaCl_3$:1% Eu, 1%, Tl | | | 450 | 6,100 | 9.2% | 1.3 μs |
| $CsCaCl_3$ $E_g$ = 5.5 eV | | 42 | Broad 250-400, 450-700 Peak 513 | 2,500 | 24% | 2.5 ns |
| $RbSrI_3$ $E_g$ = 4.9 eV | Ortho-rhombic *Cmcm* | 4.1 | ~447 | 8,000 | 7.9% | 375 ns (71%), 1.3 μs (29%) |
| $RbSrI_3$: 0.5 mol% Yb | | | 457 | 24,000 | 4.9% | 795 ns (Spin allowed) |
| $RbSrI_3$:1 mol% Eu | | 49 | 458 | 50,000 | 3.7% | 0.99 μs |
| $RbSrI_3$:3 mol% Eu | | | 459 | 70,000 | 3.4% | 1 μs |
| $RbSrI_3$:5 mol% Eu | | | 462 | 78,700 | 2.8% | 1.03 μs |
| $RbSrI_3$:7 mol% Eu | | | 463 | 83,600 | 4.4% | 1.14 μs |

### 4.1 Rubidium Calcium Bromide with $Eu^{2+}$ and $Yb^{2+}$ Dopants ($RbCaBr_3$)

The first report on the crystal growth and scintillation properties of $RbCaBr_3$:Eu scintillators was in 2017 [61, 64]. It was found that increased europium dopant concentration from 3 to 8 mol% significantly improved the scintillation performance. The best performance they reported for these crystals was for a crystal doped with 8 mol% $Eu^{2+}$, including a light yield 77% that of NaI:Tl and an energy resolution of 8.2% at 662 keV. The scintillation decay time was 3.56 µs. This performance surpassed that of related compositions that they studied, including $KBaBr_3$:Eu, $CsCaBr_3$:Eu, $KCaCl_3$:Eu, and $RbCaCl_3$:Eu [110]. The density of $RbCaBr_3$ is 3.4 g/cc and the effective atomic number is 35.

To expand upon this work, several Ø7 mm $RbCaBr_3$ crystals were grown and their scintillation properties were tested. For the first time, the properties of undoped and $Yb^{2+}$-doped $RbCaBr_3$ were investigated. Two crystals with 5 mol% Eu and 7 mol% Eu were grown and characterized. Finally, scale up of $RbCaBr_3$:5 mol% Eu to a Ø22 mm size was pursued (**Chapter 7**).

Back-lit photos of the Ø7 mm crystals are shown in **Figure 8**. They were grown using furnace set points of 840/640°C, a translation rate of 0.5 mm/hr and cooled over 100 hours. All the crystals were colorless and highly transparent with excellent crystal quality. One exception is that the $RbCaBr_3$:5 mol% Eu crystal was cracked, which was believed to be related to different thermal gradients experienced during cooling. The uncracked crystals experienced a smaller thermal gradient during cooling due to translation to a lower position in the furnace. A slight improvement in crystal quality was seen between the undoped crystal and those with either $Eu^{2+}$ or $Yb^{2+}$ dopants.

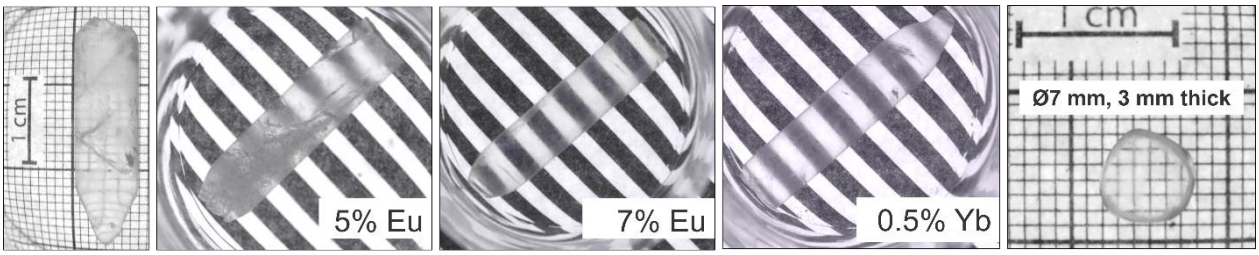


**Figure 8.** Backlit photos of $RbCaBr_3$ crystals 7 mm in diameter size.

To investigate phase purity and phase formation, powder XRD and DSC measurements were done, the results of which are shown in **Figure 9**. Rietveld refinement of the diffraction pattern was done using the room temperature $RbCaBr_3$ structure reported in the Inorganic Solid Phases SpringerMaterials database [111]. The broad peak located 15-25° is from the Kapton film and was included in the background of the refinement. A Goodness of Fit (GOF) of 1.50 was achieved for the $RbCaBr_3$ refinement. The $RbCaBr_3$ crystals were confirmed to be phase-pure with an orthorhombic structure (*Pnma*), consistent with the previous report from Rebrova, et al. [64]. $RbCaBr_3$ contains tilted $[CaBr_6]^{4-}$ corner-sharing octahedra, which were visualized in VESTA [112].

In the DSC heat flow curves, low intensity peaks were observed upon cooling ~170°C below the high intensity crystallization peak at 724°C. These peaks indicate that $RbCaBr_3$ is a congruently melting compound with solid-solid phase transitions upon cooling from the melt to room temperature, which is consistent with the reported phase diagram [101]. The melting point of 737°C was comparable to those previous reports [101, 113].

As shown in **Figure 10**, hygroscopicity was investigated with (A-B) Dynamic Vapor Sorption measurements (DVS) and (C) pulse height spectra measurements. The crystals were deliquescent and had a 50% increase in mass over a five hour period. The rate and maximum moisture intake also showed a slight dependence on the relative humidity. Both increased when the relative humidity increased from 40% to 50%. Based on the DVS measurements, europium doping seemed to minorly reduce hygroscopicity. The hygroscopicity did not show a significant change between samples synthesized with RbBr raw materials used as purchased from the vendor (99.99% purity, APL) versus using the same material treated in-house. The treatment of RbBr raw materials is elaborated on in **Chapter 7, section 7.1.3**.

The relative light yield over time under ambient conditions (50% relative humidity, temperature ~20°C) was compared based on the position of the 662 keV photopeak in the pulse height spectra. The spectra were acquired for the same pre-set amount of time. The light yield of a $RbCaBr_3$:5 mol% Eu crystal remained fairly stable for 2 hours of exposure to ambient conditions. After 4 hours, it declined but remained constant until 10 hours passed. After 10 and 20 hours, the photopeak position did not change much, but the counts under the curve decreased significantly.

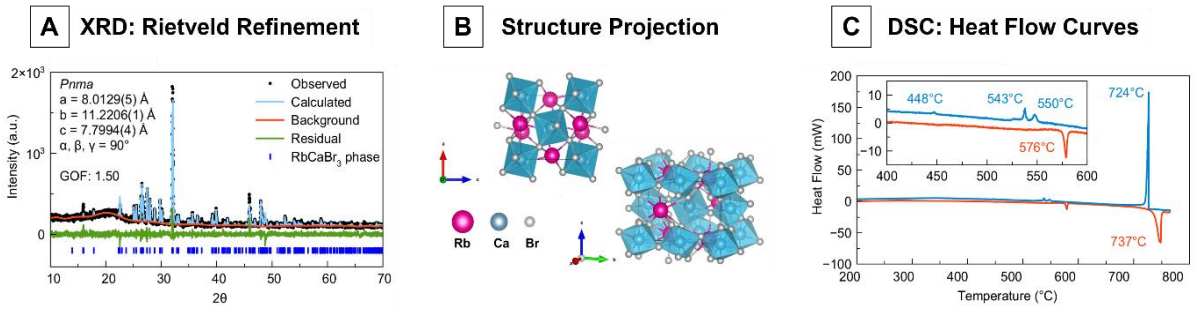


**Figure 9.** A) Powder XRD Rietveld refinement, B) structure projection and C) DSC heat flow curves obtained for $RbCaBr_3$ © 2023 IEEE.

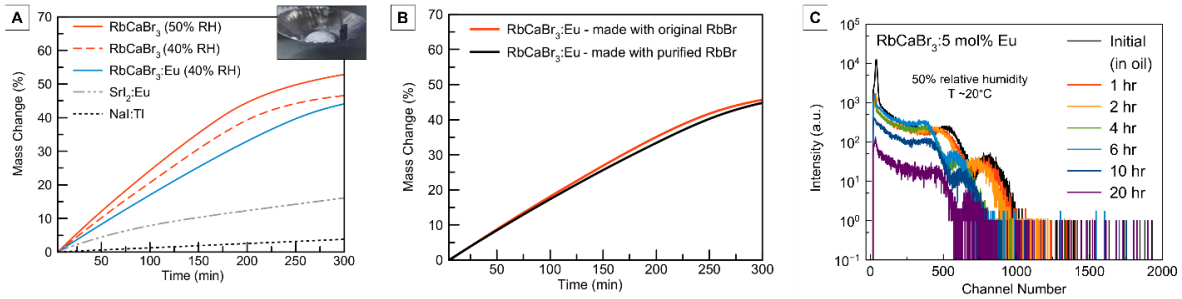


**Figure 10.** Hygroscopicity evaluation of $RbCaBr_3$ including A-B) Dynamic Vapor Sorption measurements and C) pulse height spectra measurements.

Optical absorbance and transmittance of $RbCaBr_3$ are shown in **Figure 11**. The undoped crystal had a high optical transmittance ~60% at high wavelengths, which decreased gradually to ~10% at 200 nm. The optical band gap determined by the Tauc method was 5.5 eV. Assuming that the crystal structure was cubic, the calculated band gap was estimated to be 4.6 [114]. It is common for computational band gaps to be underestimated compared to experimental. The optical transmittance of the europium and ytterbium doped crystal was high, ~80% above the absorption edge for each luminescent dopant.

The photoluminescence and radioluminescence spectra are in **Figure 12**. The excitation and emission of $RbCaBr_3$:Eu were typical of divalent europium. The emission consisted of a narrow peak centered around 435 nm, which slightly redshifted with greater europium dopant concentration. The undoped crystal had several overlapping radioluminescence emission peaks, at approximately 370 nm, 440 nm, and 545 nm. The ytterbium-doped crystal had two photoluminescence peaks, one near 415 nm and one near 440 nm. The 440 nm emission was attributed to the spin-forbidden emission of divalent-ytterbium. This emission was dominant in the radioluminescence emission.

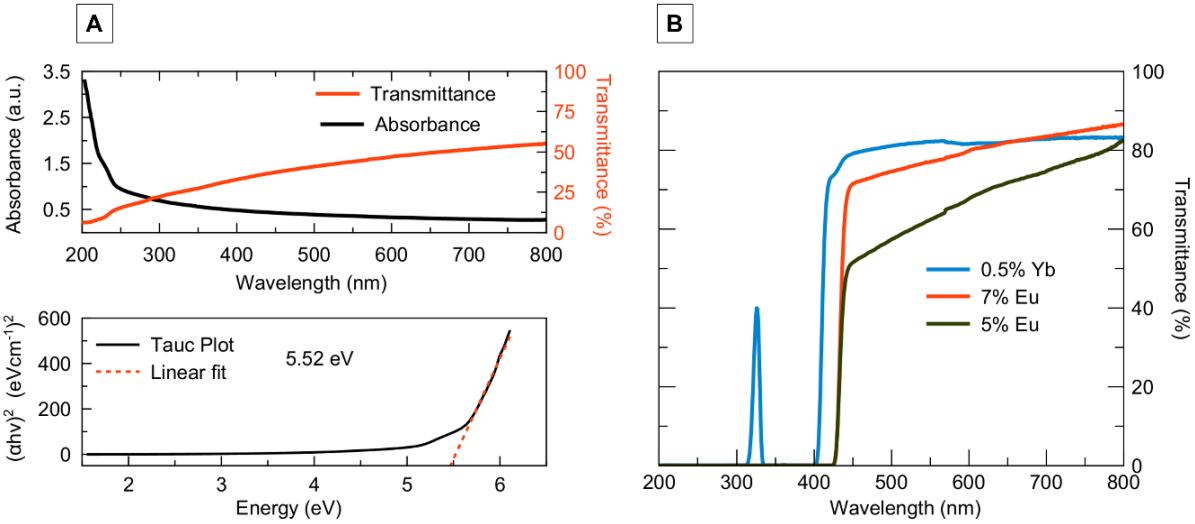


**Figure 11**. Absorbance and transmittance of $RbCaBr_3$ and Tauc plot to determine band gap.

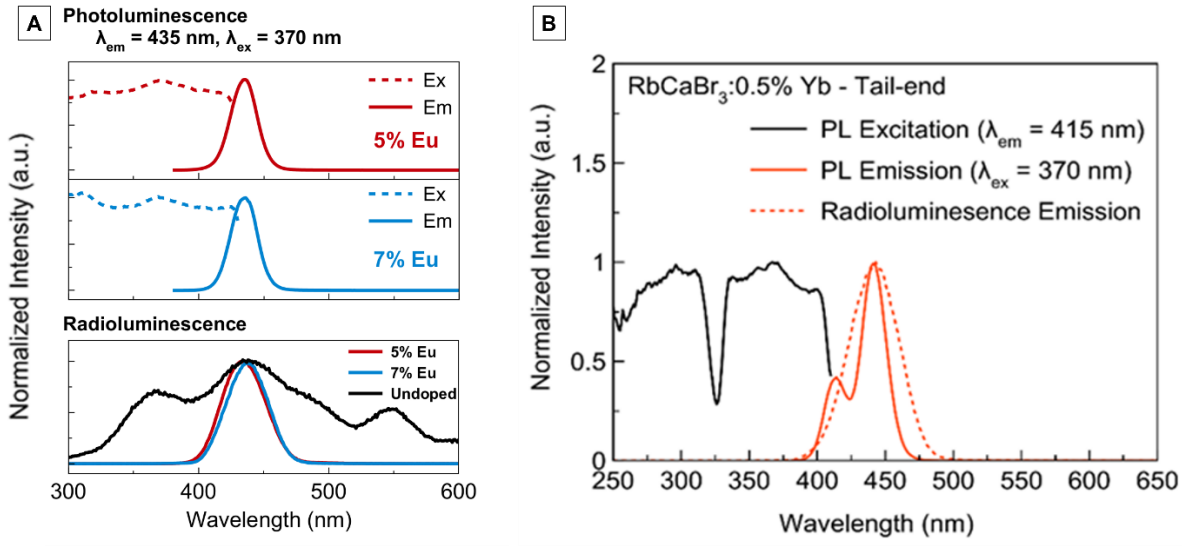


**Figure 12**. Photoluminescence and radioluminescence of A) undoped, europium doped and B) ytterbium doped $RbCaBr_3$.

Pulse height spectra are shown in **Figure 13**. The light yield and energy resolution improved with increased europium dopant concentration. $RbCaBr_3$:7 mol% Eu had a light yield of 43,000 ph/MeV and energy resolution of 4.0% at 662 keV. This is an improvement over properties reported previously, as well as those reported for similar composition $CsCaBr_3$:8 mol% Eu (28,000 ph/MeV, 9.3% at 662 keV) [64, 66, 115]. The light yield and energy resolution of $RbCaBr_3$:Yb were low, 6,400 ph/MeV and 13.3% at 662 keV. This may be due to the spin-forbidden emission of ytterbium being the dominant radioluminescence emission. Undoped $RbCaBr_3$ did not have a measurable photopeak.

The scintillation decay curves and X-ray afterglow profiles are in **Figure 14**. From 5 mol% to 7 mol% Eu, the decay time increased from 2.3 μs to 2.8 μs. This decay time was faster than reported previously for $RbCaBr_3$:8 mol% Eu, which was 3.6 μs [64]. Afterglow improved with increasing dopant concentration but was still higher than CsI:Tl crystal measured for comparison.

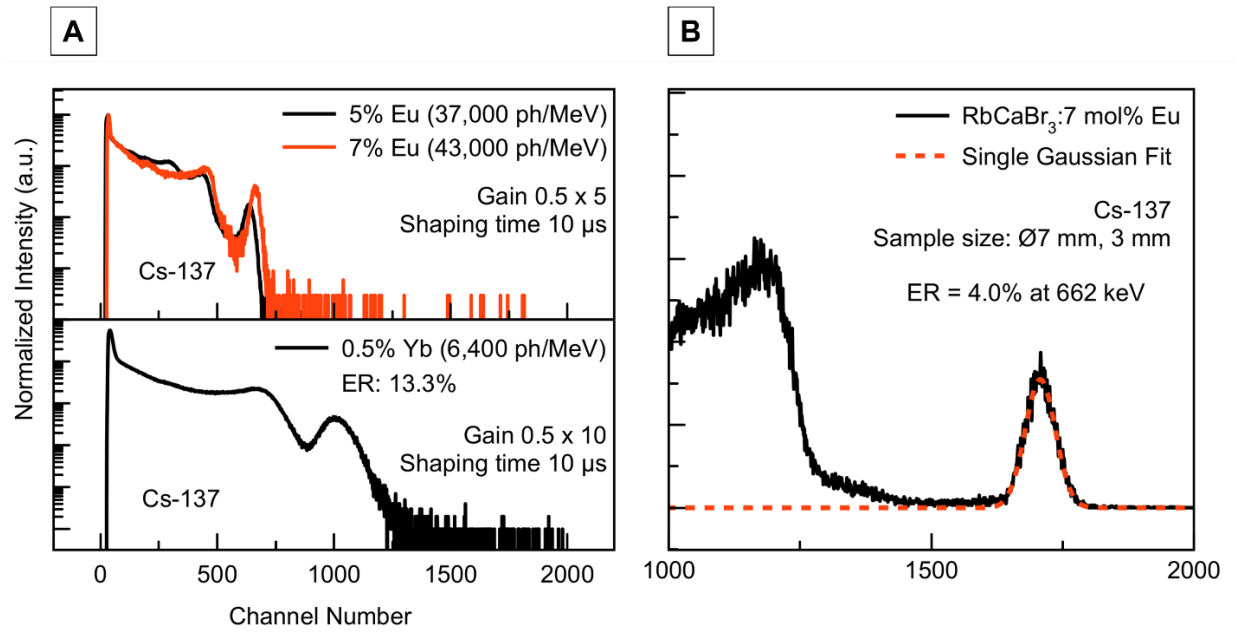


**Figure 13**. A) Cs-137 pulse height spectra of $RbCaBr_3$ crystals and B) Gaussian fit to determine energy resolution of $RbCaBr_3$:7 mol% Eu.

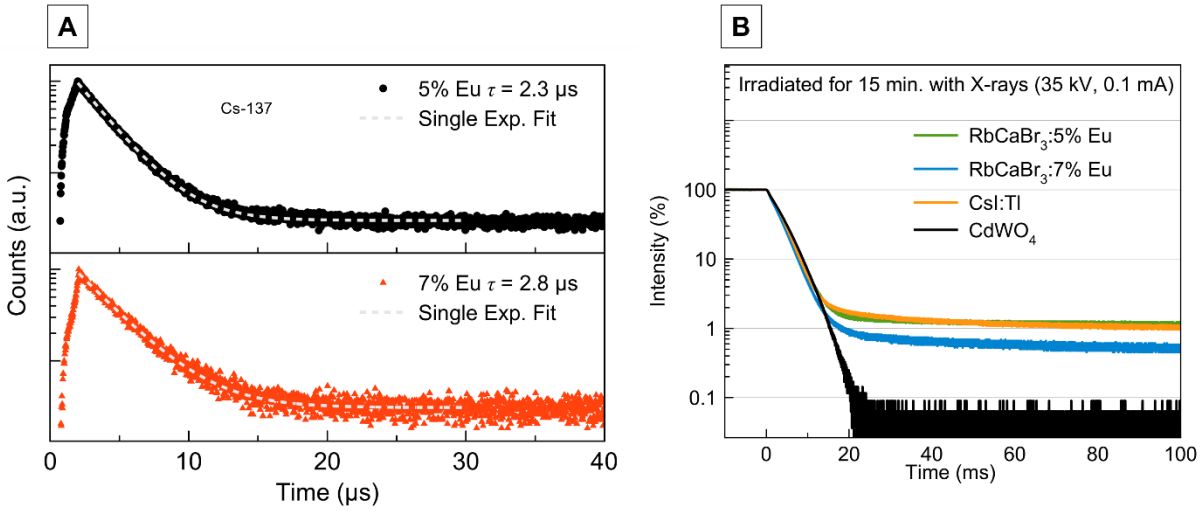


**Figure 14**. Scintillation decay and B) X-ray afterglow of $RbCaBr_3$:Eu crystals.

### 4.2 Cesium Calcium Chloride with $Eu^{2+}$ and $Tl^{+}$ Dopants ($CsCaCl_3$)

The luminescence and scintillation properties of $CsCaCl_3$ have been explored using a wide variety of dopant species (e.g., $Eu^{2+}$, $Yb^{2+}$, $Mn^{2+}$, $Tm^{2+}$, $Ce^{3+}$, $Tl^{+}$, $Cu^{+}$) [116-127]. For instance, the light yield of $CsCaCl_3$:1% Yb is reported to be 3,600-5,200 ph/MeV, limited by the dominant spin-forbidden $Yb^{2+}$ 5d-4f emission with a decay constant of hundreds of microseconds long [109]. Meanwhile, $Eu^{2+}$ doping (10 mol%) led to a significantly higher light yield of 18,000 ph/MeV and a scintillation decay time of 5 microseconds [128]. Doping $CsCaCl_3$ with 0.05-0.1 mol% $Tl^{+}$ resulted in a light yield of ~4,300-5,500 ph/MeV and a two component scintillation decay of 3.2 nanoseconds and 1 microsecond [129]. Furthermore, when fully substituting $Tl^{+}$ for $Cs^{+}$, the scintillator $TlCaCl_3$ exhibits a high light yield of 27,000 ph/MeV and energy resolution of 4.9% at 662 keV, in addition to neutron-gamma Pulse Shape Discrimination (PSD) capabilities with a high Figure of Merit (FOM) of 2.48 [130, 131].

An interesting aspect that has not been investigated is that the chlorine content of $CsCaCl_3$ could lend itself to fast neutron detection, in addition to gamma rays, allowing for neutron-gamma discrimination. Chlorine has two naturally occurring radioisotopes, Cl-35, with a natural abundance of 75.4%, and Cl-37. There are two possible neutron capture reactions, $^{35}Cl(n,p)^{35}S$ and $^{35}Cl(n, \alpha)^{35}p$ [132]. Additionally, undoped $CsCaCl_3$ exhibits ultrafast scintillation decay of ~2.3-2.5 nanoseconds via a Core-Valence Luminescence (CVL) scintillation mechanism, sometimes referred to as Auger-free luminescence (AFL) or cross-luminescence in the literature. Unfortunately, undoped $CsCaCl_3$ was reported to have a low scintillation light yield of 410 to 1,700 ph/MeV [133-135].

The objective of this work was to investigate the scintillation properties of undoped $CsCaCl_3$, $CsCaCl_3$:1% Eu, $CsCaCl_3$:1% Tl, and $CsCaCl_3$:1% Eu, 1% Tl grown from the melt via the Vertical Bridgman method. The motivation of doping simultaneously with $Tl^{+}$ and $Eu^{2+}$ was to leverage a potentially beneficial $Tl^{+} \rightarrow Eu^{2+}$ energy transfer observed in other halide scintillators [136, 137]. In this work, we report on the improved single crystal growth of 12 mm diameter crystals, which resulted in a light yield of 2,500 ph/MeV for undoped $CsCaCl_3$. Additionally, the luminescence and scintillation properties arising from the different dopants are explored. For the first time, the radiation hardness (Co-60, dose points of 100 krad and 1 Mrad) and the neutron-gamma discrimination capabilities of $CsCaCl_3$ crystals were investigated.

At room temperature, $CsCaCl_3$ has a stable cubic crystal structure with a Goldschmidt tolerance factor of 0.89 and space group of Pm-3m. It has a density of 3 g/cc and an effective atomic number of 46. It melts congruently at 910°C, allowing for the growth of high-quality single crystals from the melt [100, 138-140]. One drawback is that $CsCaCl_3$ is slightly sensitive to moisture, though it is not deliquescent.

The $CsCaCl_3$ crystals are shown in **Figure 15**. The photos were taken inside the $N_2$ glovebox, immediately after extraction from the growth ampoules. The crystal diameter was 12 mm and had an isodiametric section ~30 mm tall, excluding the last-to-freeze region. In these experiments, the translation rate (0.8 mm/hr) and cooling rate ( ~9°C/hour) were relatively fast. Yet, all the $CsCaCl_3$ crystals were highly transparent, although the undoped, Eu-doped, and Eu/Tl-doped crystals had texture on the surface that was easily polished away before characterization. Except for the cone of undoped $CsCaCl_3$, the crystals were crack-free.

One difference observed among the crystals was that the $CsCaCl_3$:Eu crystal had voids inside the boule (Fig. 1B), possibly due to the release of gas from the starting materials during growth. Similar voids were seen only on the surface of the $CsCaCl_3$:Eu, Tl crystal, rather than in the bulk (Fig. 1D). Another difference that was observed was the color of the crystals under ambient lighting. While the undoped, Eu- and Tl-doped crystals were colorless, the $CsCaCl_3$:Eu, Tl crystal was yellow. This yellow tint was uniform throughout the boule.

Undoped $CsCaCl_3$ had a high optical transmittance ~75%, indicating high crystal quality (**Figure 16A**). The optical band gap was estimated from experimental absorbance data using the Tauc plot method (**Figure 16B**). Fits were done to Tauc plots assuming a direct and indirect band gap for comparison. Assuming a direct band gap resulted in a higher quality fit, and the band gap was determined to be 5.47 eV. Electronic structure diagrams and simulations reported in the literature report that $CsCaCl_3$ had an indirect band gap of 5.0-5.45 eV, with relatively flat bands comprising the valence band [116, 141-143].

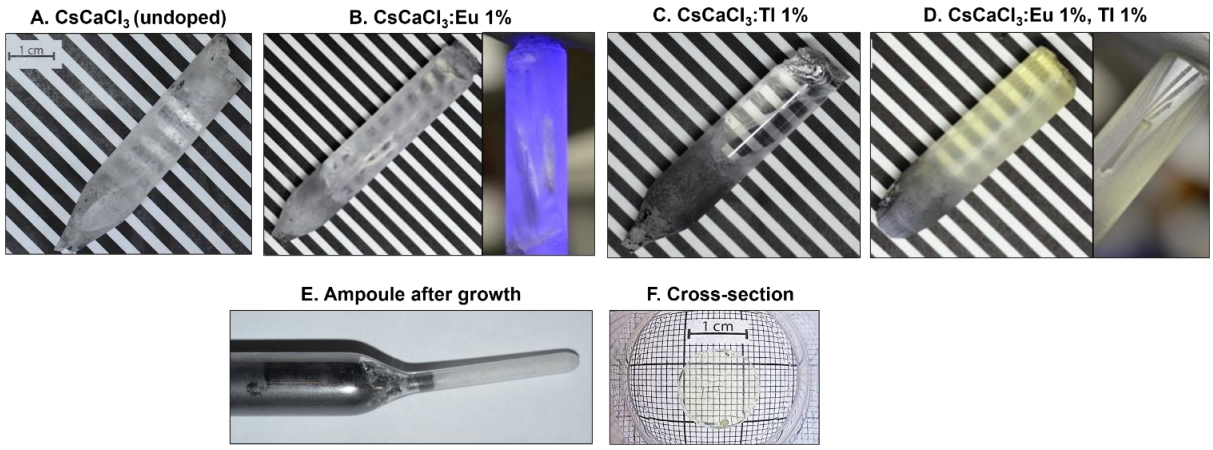


**Figure 15.** $CsCaCl_3$ crystals with $Eu^{2+}$ and $Tl^{+}$ dopants. The black color at the cone is surface residue from the carbon coated growth ampoule. B) $Eu^{2+}$ doped crystal under UV light. D) close up of the textured surface of $CsCaCl_3$:Eu, Tl. E) quartz ampoule after growth. F) backlit photo of cross sectional sample of undoped $CsCaCl_3$.

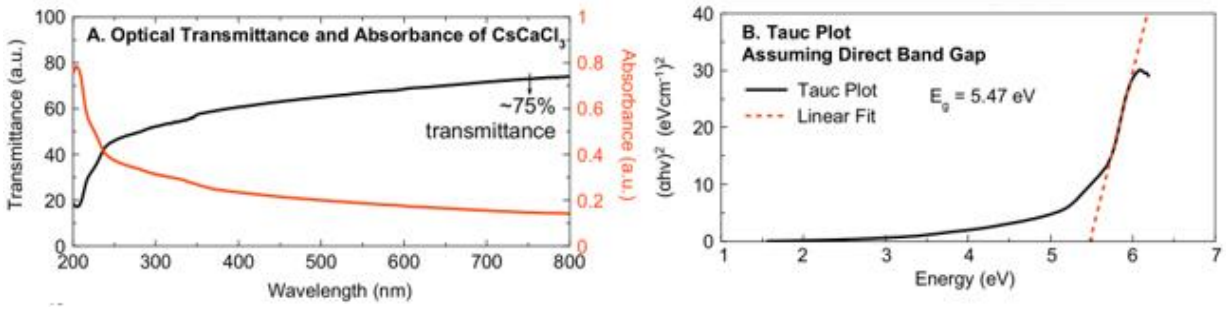


**Figure 16.** A) Optical transmittance and absorbance of $CsCaCl_3$. B) Tauc plot showed that $CsCaCl_3$ had a direct band gap of 5.47 eV.

Photoluminescence emission and excitation and photoluminescence decay times are shown in **Figure 17**. The photoluminescence behavior of $CsCaCl_3$:Eu 1% is typical of the $4f^7$-$4f^65d$ radiative transition of $Eu^{2+}$ [144]. The excitation spectrum consisted of overlapping bands from ~250-430 nm, due to the presence of many states in $4f^65d$ configuration. There was one narrow emission peak at 440 nm. There was an overlap between the excitation and emission bands, as expected from $Eu^{2+}$ self-absorption [74]. The lifetime of the $Eu^{2+}$ $5d_1$ excited state was 1.7 μs for $CsCaCl_3$:Eu.

The photoluminescence behavior of $CsCaCl_3$:Tl was complex. The excitation spectrum had a distinct peak at 265 nm. This excitation resulted in overlapping emissions at 400 nm and 435 nm. When monitoring an emission wavelength of 430 nm, the excitation spectrum had a strong peak at 265 nm, in addition to lower intensity overlapping peaks near 340, 360 and 375 nm. When monitoring with an excitation of 340 nm, low intensity emissions at 360 nm and 394 nm were observed, in addition to the strong emission at 435 nm. When monitoring an excitation of 360 nm, only the emission at 435 nm was seen. The photoluminescence decay consisted of two components, 4.4 ns (11%) and 451 ns (89%) when monitoring the 400 nm emission with a 265 nm excitation.

The luminescence of $CsCaCl_3$:Tl and CsCl:Tl have been studied previously [127, 145, 146]. In CsCl:Tl, photoluminescence emissions were observed at 340 and 360 nm, which were ascribed to trigonal ($A_x$) and tetragonal ($A_T$) Jahn-Teller minima of the $Tl^+$ triplet relaxed excited state, and at 490 nm, which was attributed to a strong off-center STE [146]. Kubota and Kawai found three similar emissions in $CsCaCl_3$:Tl crystals, at 308 nm, 350 nm, and 476 nm, and ascribed them to similar sources [127]. They studied crystals doped with < 0.01 mol% to avoid formation of aggregation centers that could affect luminescence properties, which is significantly different than the 1 mol% concentration used in this present study on scintillation properties. In some Tl-doped alkali halide crystals with high dopant concentrations, new luminescence bands have arisen from dimeric $(Tl^+)_2$ centers, formed by two $Tl^+$ ions located at adjacent positive ion sites [147]. Therefore, to formally assign the transitions of emission and excitation observed in $CsCaCl_3$:Tl 1 mol%, in depth photoluminescence emission, excitation and lifetime studies as a function of temperature could be pursued.

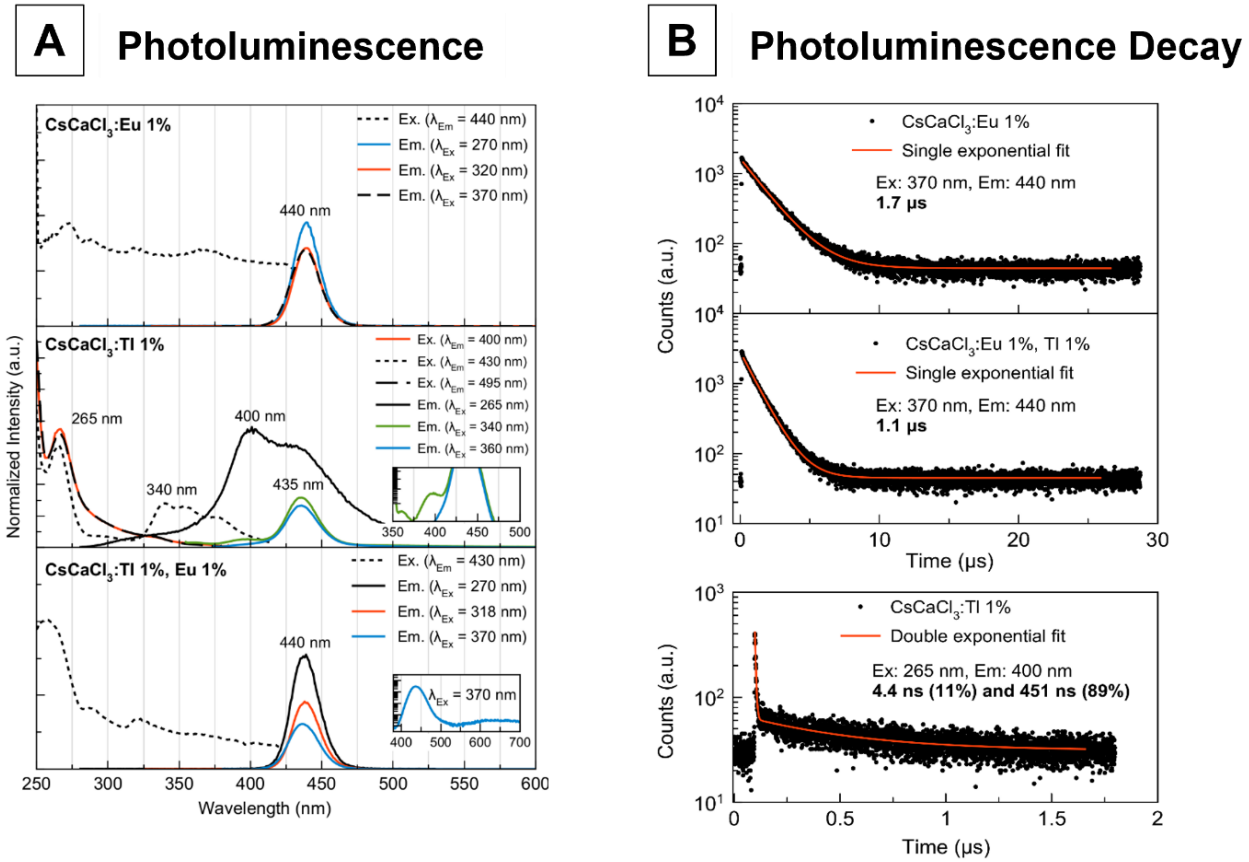


**Figure 17**. $CsCaCl_3$:(Eu, Tl) A) Photoluminescence excitation and emission spectra. The inset graphs show the y-axis in log scale. B) Photoluminescence decay time.

The excitation spectrum of $CsCaCl_3$:Eu, Tl showed overlapping bands from ~250-430 nm, with a peak near 270 nm. Europium self-absorption was also observed, with close excitation and emission bands. There is some overlap between the excitation bands of $CsCaCl_3$:Eu, Tl, and the emission of $CsCaCl_3$:Tl, possibly allowing $Tl^+ \rightarrow Eu^{2+}$ energy transfer. To investigate this, the emission resulting from several different excitation wavelengths was measured. Regardless of the excitation wavelength monitored, the 440 nm emission from $Eu^{2+}$ was observed and the 400 nm emission from $Tl^+$ was suppressed. Additionally, the photoluminescence lifetime was 1.1 μs, which was slightly faster than $Eu^{2+}$ alone and slower than $Tl^+$ alone. To confirm the energy transfer mechanism in $CsCaCl_3$:Eu, Tl, further investigation would be needed, though this is worthwhile to pursue.

If a beneficial energy transfer mechanism exists between $Tl^+$ and $Eu^{2+}$ ions, then altering the ratio of $Eu^{2+}/Tl^+$ dopants could lead to enhancement of the 440 nm emission intensity while maintaining a faster decay time compared to crystals only doped with $Eu^{2+}$. For example, an optimal dopant concentration ratio was found in KCl:Eu 0.1 mol%, Tl 0.05 mol% that increased the intensity of the desired 420 nm emission [148]. One additional emission was observed in the photoluminescence of $CsCaCl_3$:Eu, Tl, which seems to be of a separate origin. When excited with 370 nm, a broad, low intensity emission near 600-700 nm was visible in log scale. A similar emission at 625 nm was observed in RbCl:Eu, Tl photoluminescence emission, which was attributed to an F-center [149].

The radioluminescence emissions are shown in **Figure 18A**. The undoped $CsCaCl_3$ crystal had radioluminescence emissions centered around 250-350 nm, similar to what has been reported in the literature [133]. Like the emissions observed in photoluminescence, $CsCaCl_3$:Eu and $CsCaCl_3$:Eu, Tl showed a narrow, intense emission centered near 447 nm, which result from the $Eu^{2+}$ transitions discussed previously. The crystal doped with both $Eu^{2+}$ and $Tl^+$ also showed low-intensity, broad emission near 700 nm visible in log scale, the origin of which requires further investigation. The $CsCaCl_3$:Tl crystal had overlapping emissions centered near 310 and 330 nm, and another, lower intensity emission near 450 nm. These features were also like those observed in the photoluminescence emission.

Scintillation decay time is plotted in **Figure 18B.** The decay of undoped $CsCaCl_3$ was 2.5 ns. $CsCaCl_3$:Eu and $CsCaCl_3$:Eu, Tl showed similar scintillation decay emissions as their photoluminescence emissions, with a single component of 1.8 μs and 1.3 μs, respectively. However, the scintillation decay time of $CsCaCl_3$:Tl was slightly different. The decay profile was best fit with a three-component exponential decay function: 2.8 ns (2%), 610 ns (54%), and 2.6 μs (45%). For comparison, CsCl:1% Tl had two scintillation decay time constants of similar magnitude and ratios: 5.4 ns (20%) and 220 ns (80%) [146]. In CsCl:1% Tl, the longer decay component was attributed to slow energy transfer from the host to $Tl^+$ ions.

X-ray induced afterglow profiles are shown in **Figure 18C.** $CsCaCl_3$:Eu had high afterglow intensity. The afterglow profiles of CsI:Tl and $CdWO_4$ are also plotted for comparison. Tl-doping reduced the afterglow by an order of magnitude compared to Eu-doping. The combination of both Eu- and Tl-dopants resulted in the lowest afterglow, comparable to CsI:Tl. Investigations on the co-doping of CsI:Tl with $Eu^{2+}$ or $Sm^{2+}$ (0.005 – 0.5 mol%) showed significant reductions in afterglow, and a similar mechanism could be at play in $CsCaCl_3$:Eu 1%, Tl 1% [30, 31, 90, 91, 150, 151]. High afterglow of CsI:Tl is attributed to delayed recombination from shallow traps from $Tl^+$ doping. The $Eu^{2+}$ or $Sm^{2+}$ co-dopants introduced deep electron traps that could divert electrons from the shallow traps.

Pulse height spectra are shown in **Figure 19**. Undoped $CsCaCl_3$ had a light yield of 2,500 ph/MeV, which is a significant improvement from previously reported values (400-1,700 ph/MeV). $CsCaCl_3$:1% Eu had a light yield of 15,800 ph/MeV, and that of $CsCaCl_3$:1% Tl was a slightly higher value of 17,000 ph/MeV. Previously, the light yield of $CsCaCl_3$: 0.05% Tl was reported to be 4,300 ph/MeV, and that of $CsCaCl_3$: 0.1% Tl was 5,500 ph/MeV, showing a significant dependence on the dopant concentration [152]. When $Cs^+$ was fully substituted with $Tl^+$ to create $TlCaCl_3$, the reported light yield was ~30,000 ph/MeV [130, 153]. $CsCaCl_3$:Eu, Tl had a reduced light yield of 6,100 ph/MeV; however, the Eu/Tl dopant ratio may not be optimal. Energy resolution was determined with a single Gaussian fit to the 662 keV photopeak in Cs-137 pulse height spectra. Undoped $CsCaCl_3$ had an energy resolution of 24%, and that of $CsCaCl_3$:Eu was ~16%. $CsCaCl_3$:Tl had the best energy resolution of 8.6%, and that of $CsCaCl_3$:Eu, Tl was similar at 9.2%.

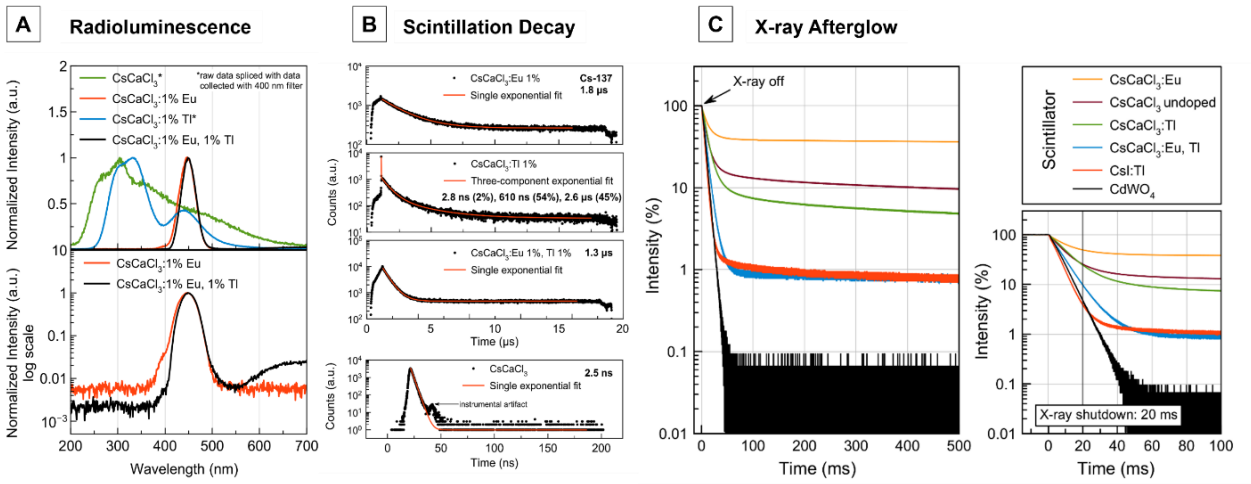


**Figure 18.** $CsCaCl_3$:(Eu, Tl) A) Radioluminescence emission spectra, B) scintillation decay time, and C) X-ray afterglow.

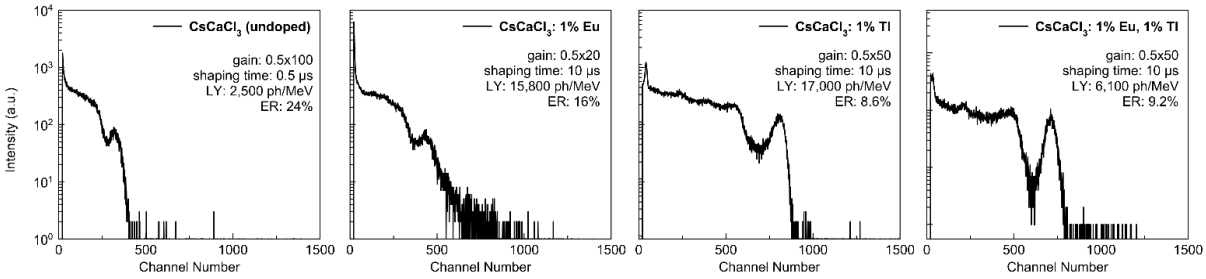


**Figure 19.** $CsCaCl_3$:(Eu, Tl) pulse height spectra (Cs-137).

For Pulse Shape Discrimination (PSD) measurements, a Teledyne-Lecroy HDO6104 oscilloscope (2.5 GS/s with a bandwidth of 1 GHz) was used to digitize the pulses from the PMT. Several thousand traces were collected and analyzed offline to optimize the charge integration parameters to obtain the best discrimination.

$CsCaCl_3$:Tl showed fast neutron and gamma discrimination capabilities, whereas the undoped and Eu-doped crystals did not. **Figure 20A** shows a scatter plot of PSD ratio versus total energy measured under $^{241}$Am/Be source and the generated FOM is in **Figure 20B**. The scatter plot shows three distinct bands. There are two neutron capture reactions in $^{35}$Cl: $^{35}Cl(n,p)^{35}S$ and $^{35}Cl(n, \alpha)^{32}P$, with reaction Q-values of 615 keV and 938 keV, respectively. The events in the bottom band correspond to gamma events, the middle one corresponds to the fast neutron captures in $^{35}$Cl that emit alpha particles and the top band corresponds to fast neutron captures in $^{35}$Cl that produce protons. The FOM plot shows the Y-projection of the scatter plot with a cut between channels 100 to 150. The three bands are well separated with a FOM of 3.2 between gamma-rays and fast neutron captures that produce protons and a FOM of 1.6 between gamma-rays and fast neutron captures that produce alpha particles.

Scintillation decay profiles extracted with gates on corresponding regions of the scatter plot are shown in **Figure 20C**. Gamma and (n.p) events show CVL while the (n, α) events do not show CVL. The fitted values of the decay times are shown in the plot.

Efficient PSD is typically defined by a separation of at least 3 times the standard deviation of the gamma and neutron peaks, which corresponds to a FOM of ~ 1.27 [154]. Several other chloride-based single crystal scintillators show PSD, namely $Cs_2LiYCl_6$:Ce (CLYC), $Cs_2LiLa(Br,Cl_6)$:Ce (CLLBC), $Cs_2HfCl_6$:Ce (CHC), and $LaCl_3$ [155-163]. The FOM of commercially available scintillators CLYC and CLLB are ~3 and ~2, respectively [164]. The best reported FOM for CHC is 0.96 for the $^{35}Cl(n,p)^{35}S$ reaction and 2.6 for the $^{35}Cl(n, \alpha)^{35}P$ reaction for optimum energy windows of 2516-2926 keVee [165]. Studies on CHC and $LaCl_3$ have reported α contamination resulting from actinide contamination in the raw materials, which complicated the analysis of the FOM for the $^{35}Cl(n, \alpha)^{35}P$ band [162, 163]. This is not an issue in $CaCaCl_3$:Tl, which can be an advantage.

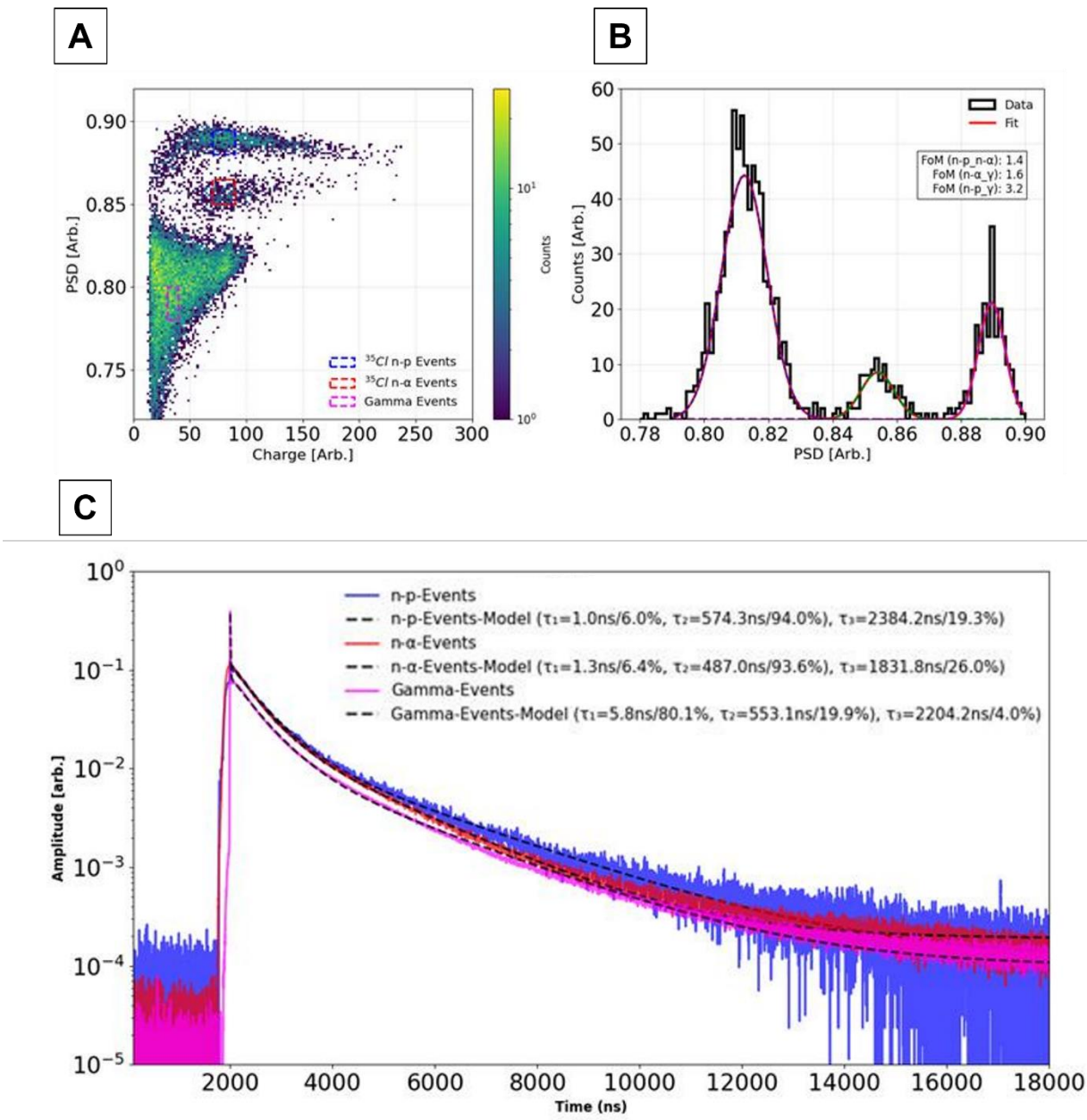


**Figure 20.** A) Pulse shape discrimination scatter plot obtained with $CsCaCl_3$:Tl doped sample under $^{241}$Am/Be neutrons. B) FOM plot generated from the scatter plot shows excellent separation between gamma-rays and fast neutron captures in $^{35}$Cl. The fast neutron capture events that produce protons and alphas can also be separated. C) Scintillation decay profiles (average of several traces) of gamma events and fast neutron capture events in 35 Cl that produce protons and alpha particles.

### 4.3 Rubidium Strontium Iodide with $Eu^{2+}$ and $Yb^{2+}$ Dopants ($RbSrI_3$)

In this work, a new metal halide perovskite scintillator $RbSrI_3$ was grown from the melt via the Vertical Bridgman method for the first time. Physical properties important for scintillator development were evaluated. The scintillation properties intrinsic to $RbSrI_3$ and those resulting from doping with 5 mol% $Eu^{2+}$ and 0.5 mol% $Yb^{2+}$ doping were measured. The crystals were grown with a translation rate of 0.5 mm/hr, thermal gradient ~20°C, and a cooling rate of ~6°/hr. As shown in **Figure 21**, transparent Ø7 mm diameter crystals with high optical quality were grown. The undoped and Yb-doped crystals were colorless, and the crystal doped with 5 mol% Eu had a slightly yellow tint. Overall, a high volume of material free of macroscopic defects was grown. The crystal quality was sensitive to the growth parameters. **Figure 21B** shows improvements to the crystals obtained by using slow translation rates and cooling rates.

Moisture sorption curves for $RbSrI_3$ and two well-known hygroscopic scintillators, $SrI_2$:Eu and NaI:Tl, are shown in **Figure 22**. The rate of moisture sorption indicates sensitivity to ambient moisture. Hygroscopicity was similar to $SrI_2$:Eu, and the sample was deliquescent. Changes due to dopant were minimal.

**Figure 23** shows results from XRD and DSC measurements. A sample from the center of the boule was phase-pure with an orthorhombic structure (*Cmcm*) (Goodness of Fit 1.39). The observed lattice parameters were consistent with previously reported experimental data [166]. A sample from the tail end of the boule contained the $RbSr_2I_5$ phase. In the DSC heat flow curves, there were two endothermic peaks at 453°C and 497°C, and a high intensity exothermic peak at 423°C. Despite this melting behavior, a large transparent single-phase volume of $RbSrI_3$ was grown [69].

Absorbance and transmittance spectra of undoped $RbSrI_3$ are shown in **Figure 24**. At long wavelengths, the optical transmittance was 70%, demonstrating the high optical quality of the crystals. The transmittance decreased significantly between 250 and 400 nm, corresponding with an increase in absorbance. The direct band gap determined by the Tauc method was 4.9 eV, indicated by the linear fit shown in **Figure 24B**. This result is similar to the calculated direct band gap in literature for related compound $CsSrI_3$, which were 3.84 – 4.92 eV, depending on the method used [167].

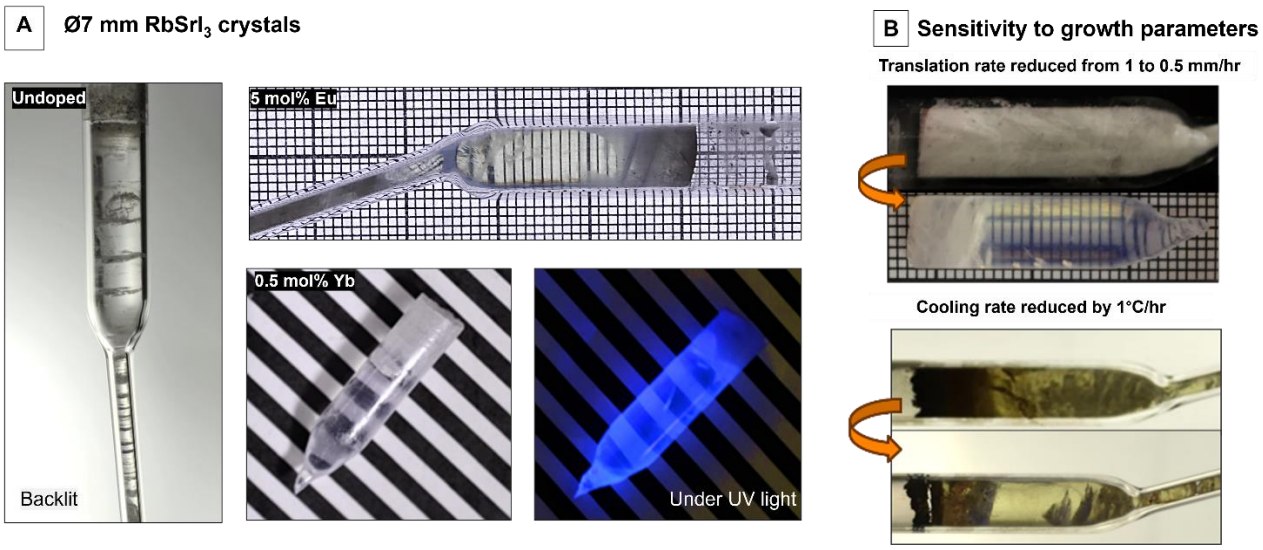


**Figure 21.** A) Ø7 mm crystals of $RbSrI_3$ and B) Improvements in quality of separate Ø7 mm $RbSrI_3$ crystals by reducing translation rate (left) and cooling rate (right).

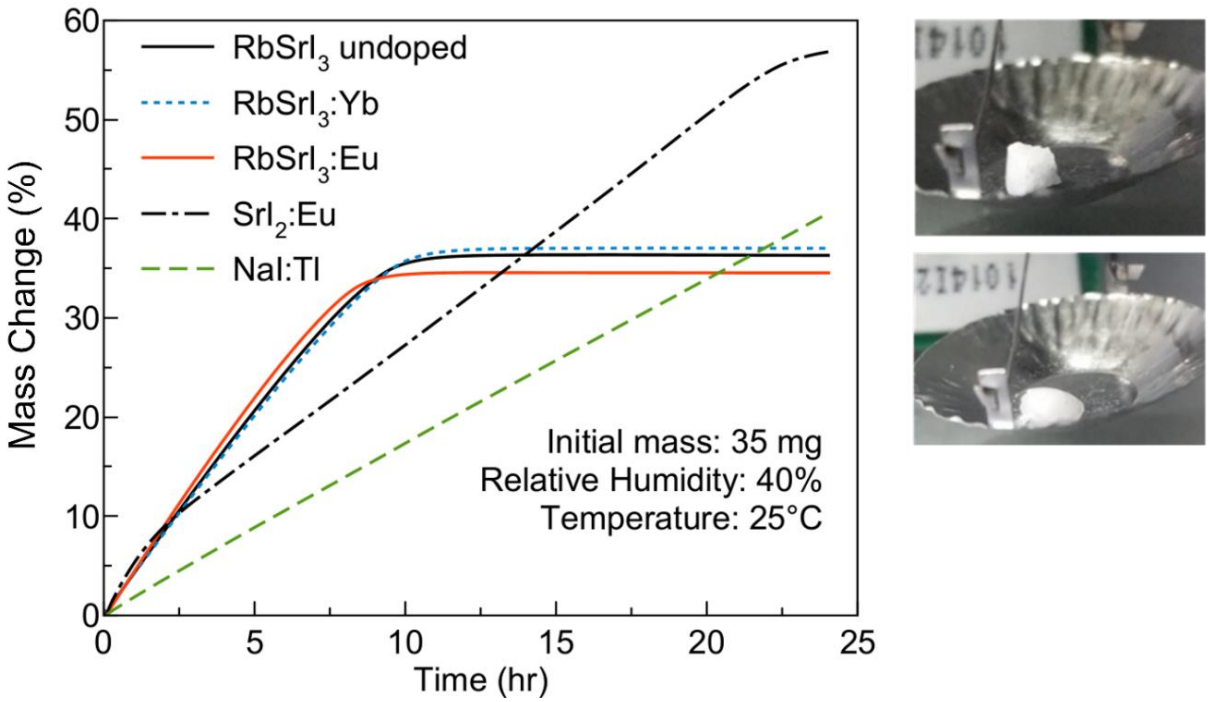


**Figure 22.** Dynamic Vapor Sorption curves comparing moisture sensitivity of $RbSrI_3$ with $SrI_2$:Eu and NaI:Tl. The photos show the sample shortly after the start of the measurement compared to the end.

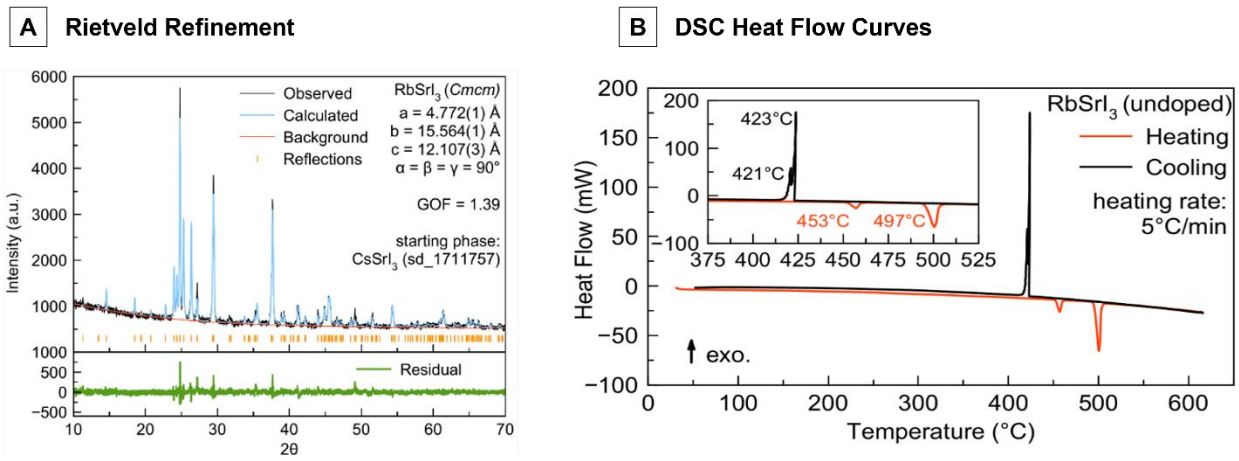


**Figure 23.** A) Powder XRD Rietveld refinement results and B) Differential Scanning Calorimetry heat flow curves for $RbSrI_3$.

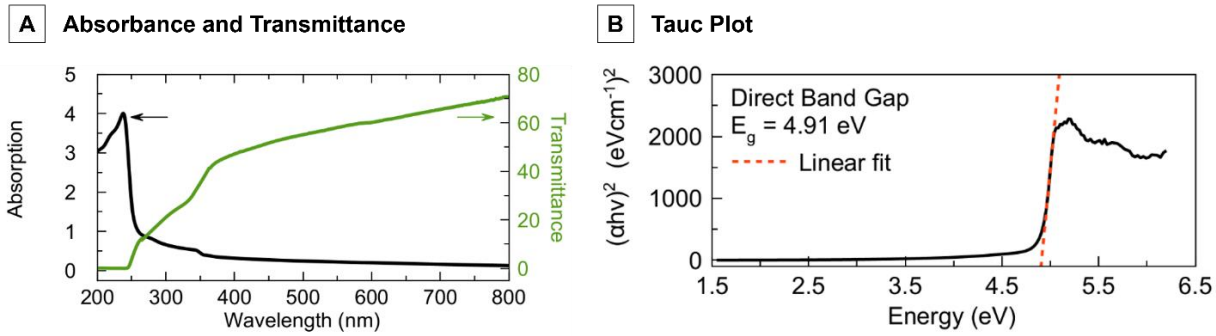


**Figure 24.** A) Optical transmittance and absorbance measurements of 2 mm thick undoped $RbSrI_3$ and B) determination of band gap using the Tauc method.

Photoluminescence and radioluminescence are shown in **Figure 25**. Undoped $RbSrI_3$ had a broad, asymmetric emission from 300-700 nm that peaked at ~445 nm. A similar emission in undoped $SrI_2$ resulted from self-trapped excitons [73]. $RbSrI_3$:Eu had emissions centered at ~460 nm characteristic of the 5d-4f electronic transition of $Eu^{2+}$. The emission leak shifted slightly with increased europium dopant concentration, which was indicative of europium self-absorption. The photoluminescence excitation spectra consisted of several unresolved excitation bands, with maxima located at 273 nm and 370 nm.

$RbSrI_3$:Yb had emissions at 444 nm and 460 nm, corresponding with the spin-allowed and spin-forbidden transitions, respectively. In comparison, the radioluminescence was narrow and symmetric, centered at 458 nm. The photoluminescence excitation spectra contained several overlapping excitation bands (288 nm, 300 nm, 316 nm, 373 nm) with a minimum at 332 nm.

Scintillation decay profiles are shown in **Figure 26**. Undoped $RbSrI_3$ had a primary decay of 375 ns (71%) and secondary component of 1.3 μs (29%). Europium doping resulted in a decay of 1.03 μs, like reports of other $Eu^{2+}$ doped iodide scintillators [69, 168]. The scintillation decay time increased slightly with europium dopant concentration.

The scintillation decay constant of $RbSrI_3$:Yb was 795 ns. For comparison, $SrI_2$:Yb, 0.5% had a 710 ns decay component and a long 77 μs decay component [71]. Similarly, $CsCaBr_3$:Yb 0.1% had decay components of 210 ns and 390 μs [109]. It is often assumed that the long decay component is associated with the spin-forbidden transition. It may be possible that a longer decay component existed for $RbSrI_3$:Yb but was not detected due to the 20 μs time window used for the measurement.

X-ray induced afterglow is compared in **Figure 27** with $SrI_2$:Eu, CsI:Tl and $CdWO_4$ measured with the same parameters. Afterglow of undoped $RbSrI_3$ was lower than $SrI_2$:Eu and comparable to CsI:Tl, and incorporation of $Eu^{2+}$ and $Yb^{2+}$ dopants decreased the afterglow further. The afterglow did not change significantly with different europium concentrations. The crystal doped with 5 mol% Eu was measured at RMD, Inc. using a pulsed X-ray source, which allowed for testing on smaller time scales that at UTK. At 2 ms, the X-ray afterglow was 1.8 %. For comparison, the afterglow of $CdWO_4$ at 2 ms is 0.16%.

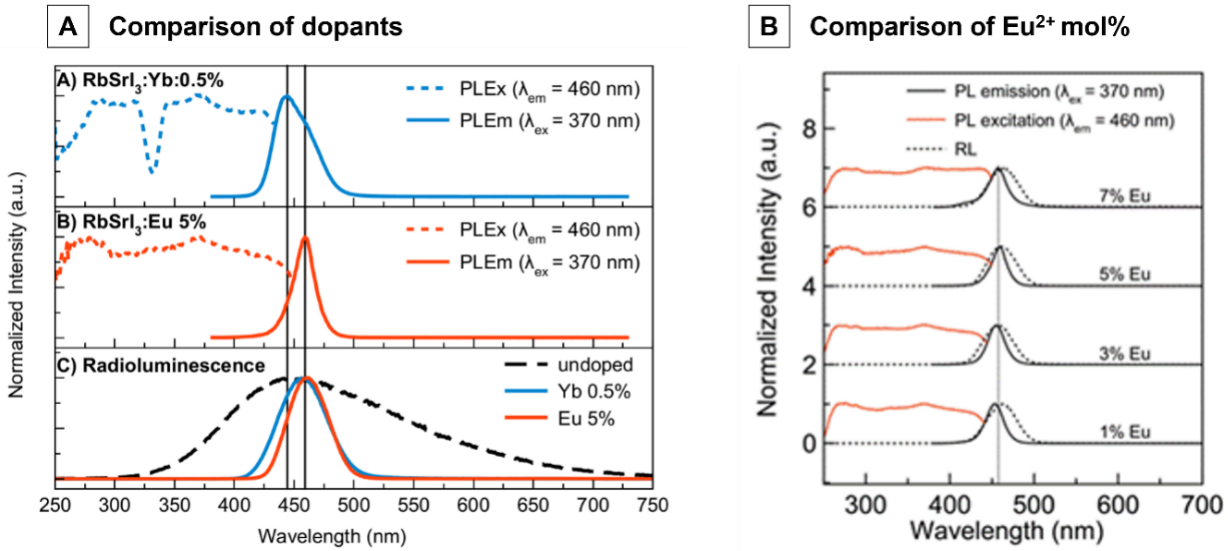


**Figure 25.** A) Photoluminescence and B) radioluminescence of $RbSrI_3$.

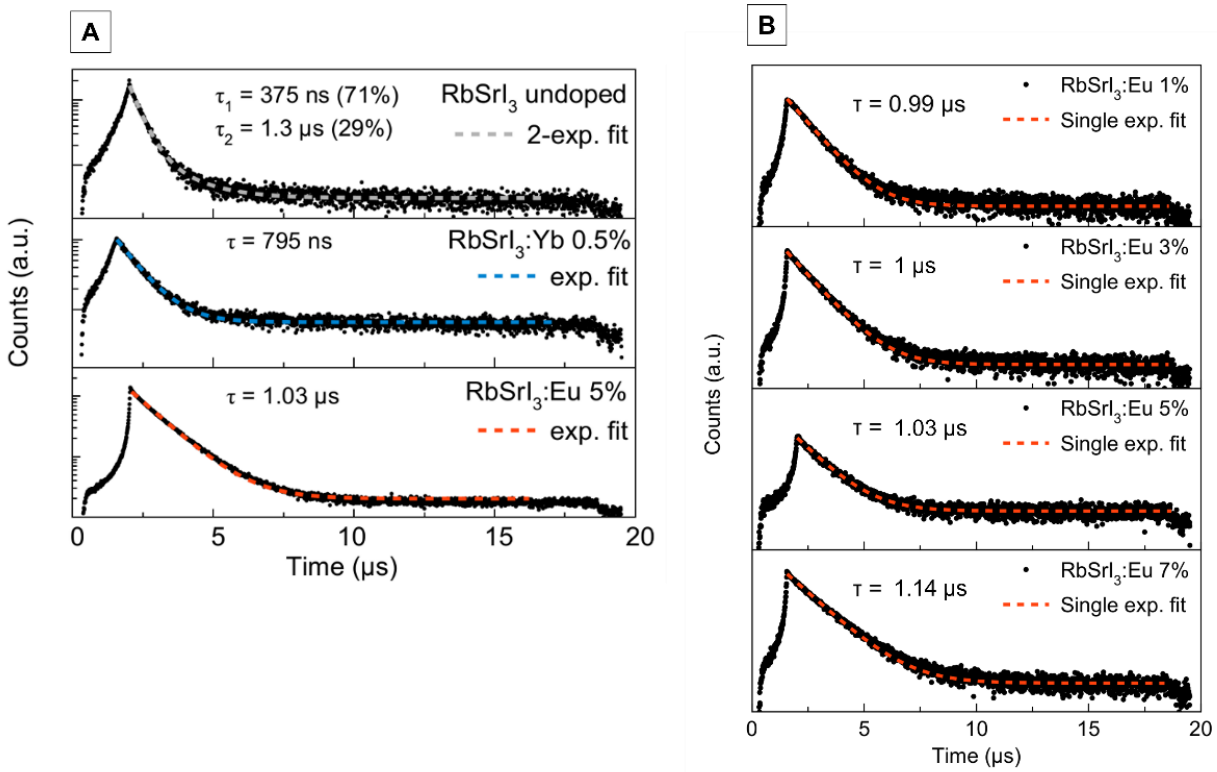


**Figure 26.** Scintillation decay time profiles for $RbSrI_3$.

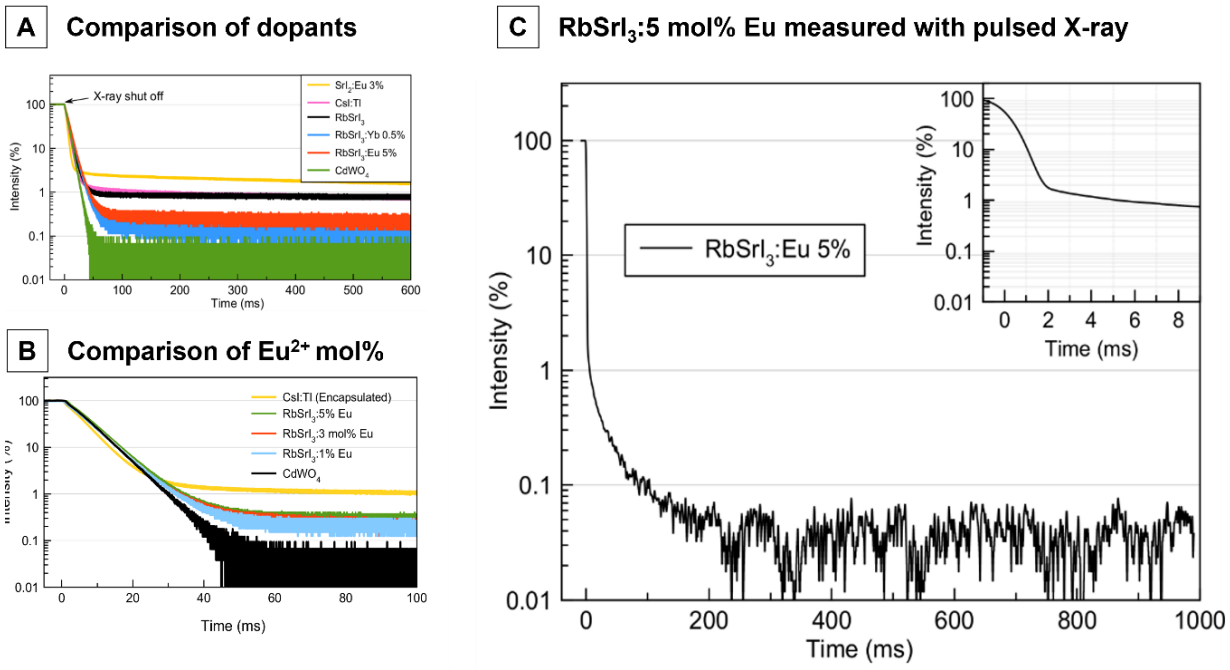


**Figure 27.** X-ray Afterglow of $RbSrI_3$ . $RbSrI_3$:5 mol% Eu had an afterglow of 1.8% at 2 ms.

Pulse height spectra used to determine light yield and energy resolution are plotted in **Figure 28**. Approximate sample size was Ø7 mm, 2 mm. The light yield and energy resolution of undoped $RbSrI_3$ were 8,000 ph/MeV and 7.9% at 662 keV. Both $Yb^{2+}$ and $Eu^{2+}$ dopants produced high light yield and energy resolution. The light yield of $RbSrI_3$:Eu continued to increase with increasing europium dopant concentration. Doping with 5 mol% Eu led to the best energy resolution of 2.8% at 662 keV, with a light yield of 78,700 ph/MeV. In comparison, the related compound $CsSrI_3$:Eu 8% had light yield of 65,000 ph/MeV and energy resolution of 5.9% [168].

The light yield and energy resolution of $RbSrI_3$:Yb were 24,000 ph/MeV and 4.9% at 662 keV, respectively. It may be possible that the light yield of $RbSrI_3$:Yb is higher than as measured. As discussed, a fraction of the $Yb^{2+}$ scintillation light may come from a long spin-forbidden transition with a decay time exceeding the shaping time for this measurement.

Measurements of the light yield of $RbSrI_3$:Eu as a function of temperature were completed. **Figure 29** shows a comparison of the percent change of the centroid position of the 662 keV from its position at room temperature. The results among the three different measurements were similar. The deviation within the temperature range most relevant to the application (±50°C) was < 4%. The deviation was greatest at higher temperatures.

**Figure 30** shows radioluminescence intensity compared to relative light yield and wavelength-resolved radioluminescence of $RbSrI_3$:Eu. Changes in intensity were similar between the two measurements, although light yield showed greater deviations at the temperature extremes. With increasing temperature, there was a redshift and decrease in intensity of the ~460 nm emission peak associated with $Eu^{2+}$ emission. Intensity of a broad peak spanning ~360-400 nm appeared to increase with increasing temperature. No abrupt changes in radioluminescence were seen.

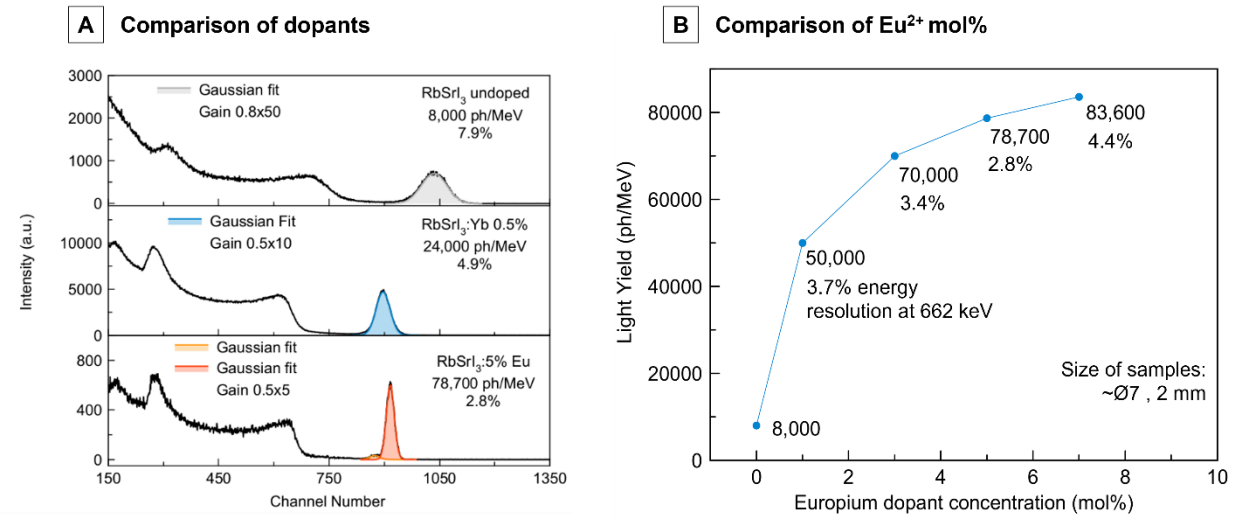


**Figure 28.** $RbSrI_3$ pulse height spectra (Cs-137) and light yield and energy resolution as a function of europium dopant concentration.

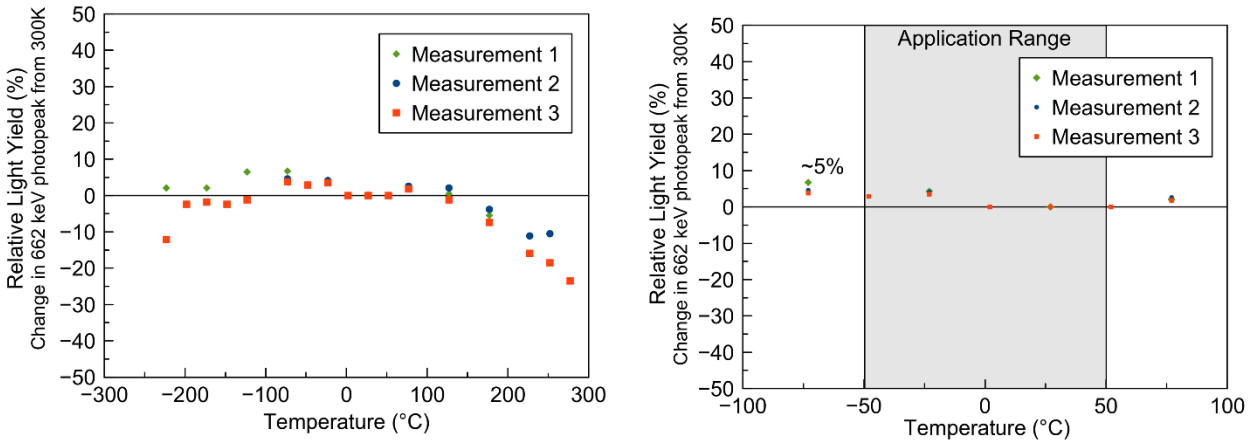


**Figure 29**. Relative light yield of $RbSrI_3$:Eu as a function of temperature. The data is represented as a percent change in the 662 keV centroid position from room temperature.

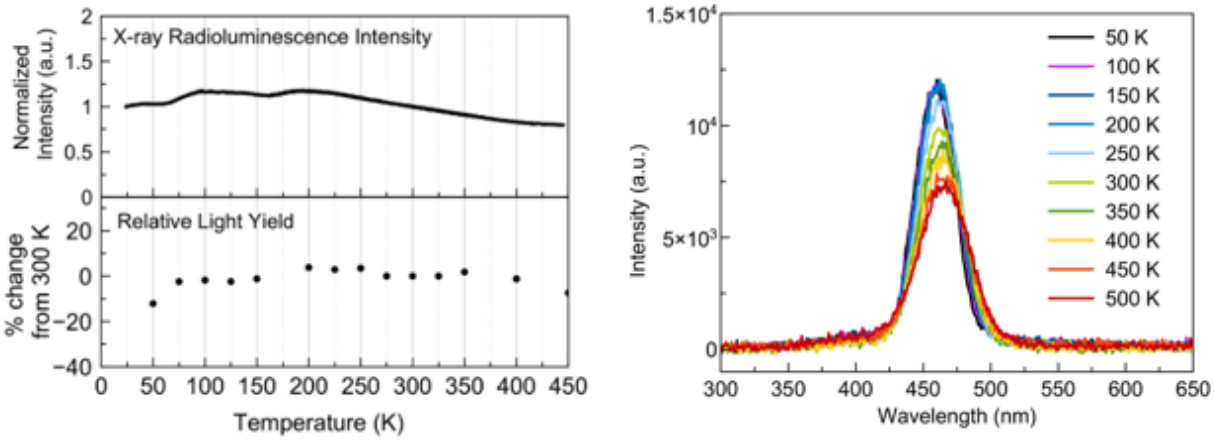


**Figure 30**. X-ray radioluminescence intensity of $RbSrI_3$:Eu as a function of temperature compared to relative light yield. Wavelength-resolved radioluminescence of $RbSrI_3$:Eu collected as a function of temperature.

# CHAPTER 5 $AB_2X_5$ COMPOSITIONS

Sections of this chapter were originally published in the following peer-reviewed journal article:

- **K. S. Pestovich**, L. Stand, N. Anastasi, M. Gillespie, L. S. Pandian, C. L. Melcher, E. van Loef, "Intrinsic scintillation performance & europium concentration effects in $RbSr_2I_5$ and $RbSr_2Br_5$ scintillators," in *Journal of Crystal Growth*, vol. 649, p. 127924 (2025).

A number of inorganic metal halide crystals with the stoichiometry of $AB_2X_5$ ($A^+$ = K, Cs, Rb; $B^{2+}$ = Ca, Ba, Sr, Eu; $X^-$ = I, Br, Cl) have been reported with promising luminescence or scintillation properties, including several with high light yield (>70-90,000 ph/MeV) and energy resolution (2.3-3.3% at 662 keV) [78, 169-188] Owing to their excellent energy resolution, these crystals have primarily been considered for the application of gamma ray spectroscopy.

Among these scintillators, the promising performance and high crystal quality of $RbSr_2Br_5$:Eu 2.5 mol% and $RbSr_2I_5$:Eu 2.5 mol% in a Ø7 mm size warrants further investigation. Initial studies report high performance with europium doping, including a light yield of 64,700 ph/MeV and energy resolution of 4.0% at 662 keV for $RbSr_2Br_5$:Eu 2.5% and 90,400 ph/MeV and energy resolution of 3.0% at 662 keV for $RbSr_2I_5$:Eu 2.5% [69, 189].

Until now, scintillation performance was tested for just one concentration of europium doping (2.5%). However, it is anticipated that the scintillation properties are sensitive to the concentration of luminescent dopant used. Additionally, it is valuable to test the intrinsic scintillation properties of a new material (i.e., without a luminescent dopant), since it is also advantageous to use no or low concentrations of europium, as its self-absorption effects can hinder performance for large (≥ Ø25 mm) crystals [74, 75, 175, 190, 191].

The goals of this work were 1) to investigate, for the first time, the performance of undoped $RbSr_2Br_5$ and $RbSr_2I_5$ scintillators and 2) to test the effects of a range of different europium concentrations on key scintillation properties for high energy X-ray radiography. Nine crystals (Ø7 mm) of $RbSr_2Br_5$:Eu (0, 1, 3, 5, 7 mol% Eu) and $RbSr_2I_5$:Eu (0, 1, 5, 7 mol%) were grown via the Vertical Bridgman method. Lattice parameters, optical band gap, photoluminescence, radioluminescence, light yield, energy resolution, scintillation decay time, and afterglow were measured.

The optical band gap of $RbSr_2Br_5$ was 5.9 eV and that of $RbSr_2I_5$ was 4.7 eV. High scintillation performance was achieved, even with a relatively low europium concentration of 1 mol%. For both $RbSr_2Br_5$:Eu and $RbSr_2I_5$:Eu crystals, light yield of 60–90,000 ph/MeV, energy resolution 2.8–4.0 % at 662 keV, and X-ray afterglow 0.79–1.5 % at 2 ms were obtained.

For $RbSr_2I_5$, cerium ($Ce^{3+}$) was explored as a possible alternative luminescent dopant to $Eu^{2+}$, with the hypothesis that it could produce a faster scintillation decay time and avoid europium self-absorption. Cerium doping was previously found to be a promising dopant in the isostructural scintillator, $KSr_2I_5$ [192]. For this composition, the best light yield and energy resolution were 49,000 ph/MeV and 3.1% at 662 keV with 3.5 mol% Ce, although crystal quality was limited, especially as cerium concentration increased. The scintillation decay time consisted of three components: ~40 ns (~30%), ~250 ns (~30%), and ~1.2 μs (~40%).

In this work, doping $RbSr_2I_5$ with 0.5 mol% Ce resulted in a high light yield of 48,000 ph/MeV and energy resolution of 5.5% at 662 keV. The scintillation decay time consisted of three components, 37 ns (26%), 111 ns (32%), and 1.02 (42%) μs, which was consistent with $KSr_2I_5$:Ce. The decay time was faster than produced with 1% $Eu^{2+}$: 0.7 (59%), 4.0 (41%). While the light yield and decay time were promising, the X-ray afterglow was unfortunately significantly higher than europium-doped crystals. This was possibly due to a charge imbalance introduced by the 3+ valence of cerium, which could be compensated in future experiments by introducing a 1+ valence co-dopant.

In the barium admixture experiments, a balance between highly transparent crystal quality, low hygroscopicity, and high scintillation performance was sought. $RbBa_2I_5$:Eu is an isostructural crystal to $RbSr_2I_5$:Eu. In this work, it was shown to have low hygroscopicity, a high light yield of 102,000 ph/MeV, and an energy resolution of 2.3% at 662 keV. However, it also had low optical transparency. Partial substitution of strontium with barium to make solid solutions of $Rb(Sr, Ba)_2I_5$:Eu led to high scintillation performance, reduced hygroscopicity, and high optical transparency. Additionally, the afterglow of $RbSr_2I_5$:Eu was reduced from 1.73% at 2 ms to 0.13% at 2 ms. While promising, the crystal growth scale up must still be assessed. Small bubbles were seen in the crystals when examined under the optical microscope. It is therefore expected that slow growth rates must be used.

**Table 6.** Properties of $AB_2X_5$ Scintillators.

| Scintillator | Density (g/cc) ---- $Z_{eff}$ | $\lambda_{RL\ max}$ (nm) | Light Yield (ph/MeV) | Energy Resolution at 662 keV | Afterglow (%) at 2 ms | Scintillation Decay (µs) |
|---|---|---|---|---|---|---|
| $RbSr_2Br_5$ $E_g$ = 5.9 eV | 4.2 ---- 35 | 420, 480 | 2,400 | 12.9% | 11.68 | 0.011 (3%). 0.4 (24%), 2.2 (73%) |
| $RbSr_2Br_5$:1% Eu | | 423 | 58,000 | 3.9% | 1.82 | 0.8 (88%), 2.9 (12%) |
| $RbSr_2Br_5$:3% Eu | | 431 | 73,000 | 4.1% | 1.54 | 1 (81%), 2.3 (19%) |
| $RbSr_2Br_5$:5% Eu | | 433 | 73,000 | 3.9% | 1.50 | 1.18 (76%), 2.4 (24%) |
| $RbSr_2Br_5$:7% Eu | | 438 | 71,000 | 4.0% | - | 1.22 (82%), 3.9 (18%) |
| $RbSr_2I_5$ $E_g$ = 4.7 eV | 4.6 ---- 49 | 403, 441, 510 | 14,000 | 7.9% | 22.68 | 0.07 (11%), 0.5 (35%), 1.9 (54%) |
| $RbSr_2I_5$:1% Eu | | 438 | 74,000 | 3.5% | 0.79 | 0.7 (59%) 4.0 (41%) |
| $RbSr_2I_5$:5% Eu | | 444 | 90,000 | 2.9% | 1.73 | 1 (73%), 3.6 (27%) |
| $RbSr_2I_5$:7% Eu | | 445 | 89,000 | 2.8% | 1.22 | 1.1 (75%), 3.7 (25%) |
| $RbSr_2I_5$:0.5% Ce | | 438 | 48,000 | 5.5% | - | 0.037 (26%), 0.111 (32%), 1.02 (42%). |
| $Rb(Sr_{0.5},Ba_{0.5})_2I_5$:5% Eu | 4.7 ---- 51 | 448 | 96,000 | 2.3% | 0.13 | 1 (87%), 3.7 (18%) |
| $RbBa_2I_5$:5% Eu | 4.7 ---- 53 | 445 | 102,000 | 2.3% | - | 0.85 (79%), 2.5 (21%) |

Samples were ~Ø7, 2-4 mm in size.

Crystal structure / Space group : Monoclinic / $P12_1/c1$

$Z_{eff}$ calculated using the equation by Murty [8].

### 5.1 Rubidium Strontium Iodide and Rubidium Strontium Bromide ($RbSr_2I_5$, $RbSr_2Br_5$)

To efficiently and quickly screen the range of europium dopant concentrations studied, quartz boats were used to allow a group of three $RbSr_2I_5$:Eu and a group of three $RbSr_2Br_5$:Eu crystals to each be grown simultaneously. This so-called "boat growth" can subject each crystal to a slightly non-uniform radial thermal gradient and cause cracking or unstable growth interfaces. However, it is also an efficient method to grow several small crystals at once for dopant concentration screening purposes.

Crystal growth in the transparent furnace allowed for visual monitoring of the solid-liquid interface and the cooling process. The solid–liquid interface of each crystal was observed to be stable and relatively flat throughout the growth process.

The resulting $RbSr_2Br_5$:Eu and $RbSr_2I_5$:Eu crystals are shown in **Figure 31**. All crystals were colorless and transparent with high optical quality, regardless of the europium concentration added. Two types of grain selectors (angled, straight) were used, and both produced high quality crystals.

Optical micrographs were taken to examine the crystal quality, shown in **Figure 32**. Images were taken (I) under ambient conditions, (II) with microscope backlighting, (III) with polarized light, and (IV) with flashlights illuminating the sides of the crystals. In images I-III, the crystals were very uniform in appearance. Polarized light showed an absence of high strain and mosaicity in the crystals at this magnification. In image IV, small bubbles were seen within the $RbSr_2Br_5$:Eu 5% crystals. These bubbles lowered the transparency of $RbSr_2Br_5$:Eu crystals compared to $RbSr_2I_5$:Eu. They were uniformly dispersed in the crystals; There was no noticeable radial or axial changes in concentration.

Phase purity was confirmed with powder X-ray diffraction measurements. Rietveld refinement via GSASII was done using crystallographic data retrieved from the Springer Materials database for both compositions [193, 194]. The results are shown in **Figure 33**, and lattice parameters are listed in **Table 7**. A goodness of fit (GOF) of 1.3-1.4 was obtained for the Rietveld refinements. Both $RbSr_2I_5$ and $RbSr_2Br_5$ crystallize in a monoclinic space group ($P12_1/c1$, #14). The lattice parameters coincided well with previously reported data (< 0.1% difference) [69, 102, 166, 195].

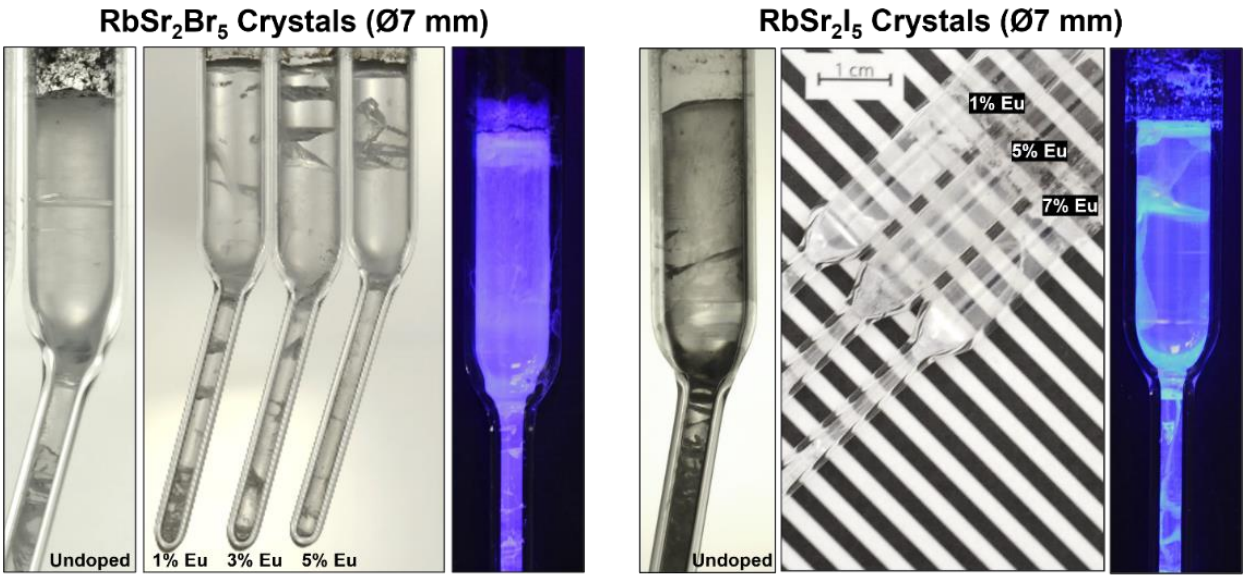


**Figure 31**. Backlit photos of $RbSr_2Br_5$:Eu and $RbSr_2I_5$:Eu single crystals grown via the Vertical Bridgman method in a 7 mm diameter size.

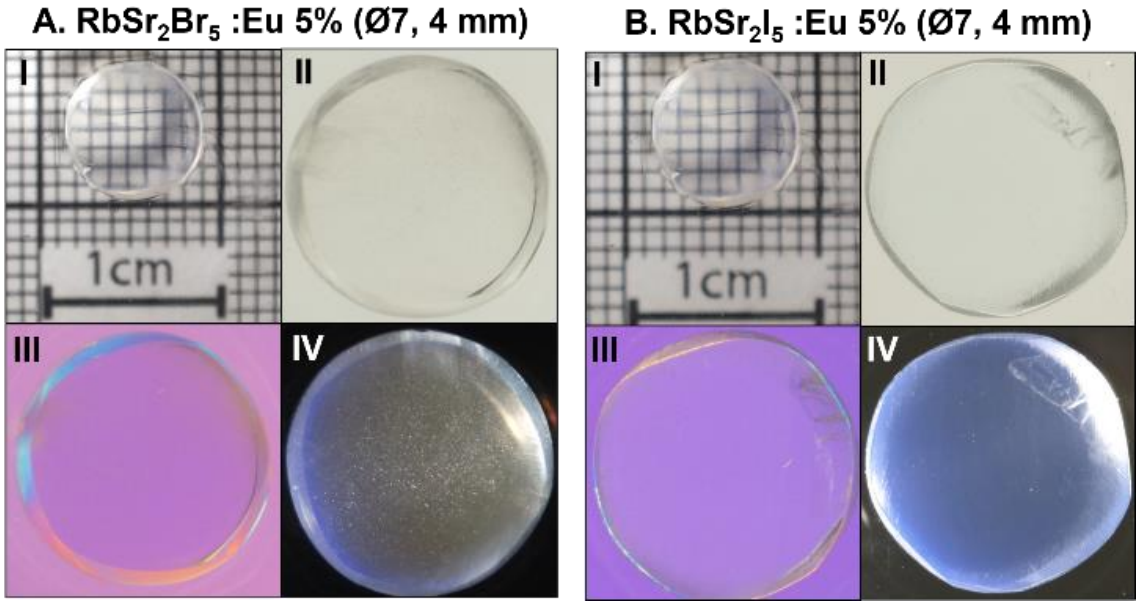


**Figure 32.** Photographs of Ø7, 4 mm cross-sections from $RbSr_2Br_5$:Eu 5% (A) and $RbSr_2I_5$:Eu 5% (B) crystals in mineral oil. Image conditions are as follows: (I) Ambient lighting, (II) Optical microscope backlighting, (III) Optical microscope polarized light, (IV) Optical microscope with flashlights illuminating the sides of the samples.

**Table 7.** Lattice Parameters from Rietveld Refinement

| Parameter | $RbSr_2Br_5$ | $RbSr_2I_5$ |
|---|---|---|
| a (Å) | 9.442(5) | 10.096(3) |
| b (Å) | 8.364(4) | 9.059(1) |
| c (Å) | 13.313(7) | 14.296(4) |
| V ($Å^3$) | 1051.52 | 1307.58 |
| α = γ (°) | 90 | 90 |
| β (°) | 90.258 | 90.236 |

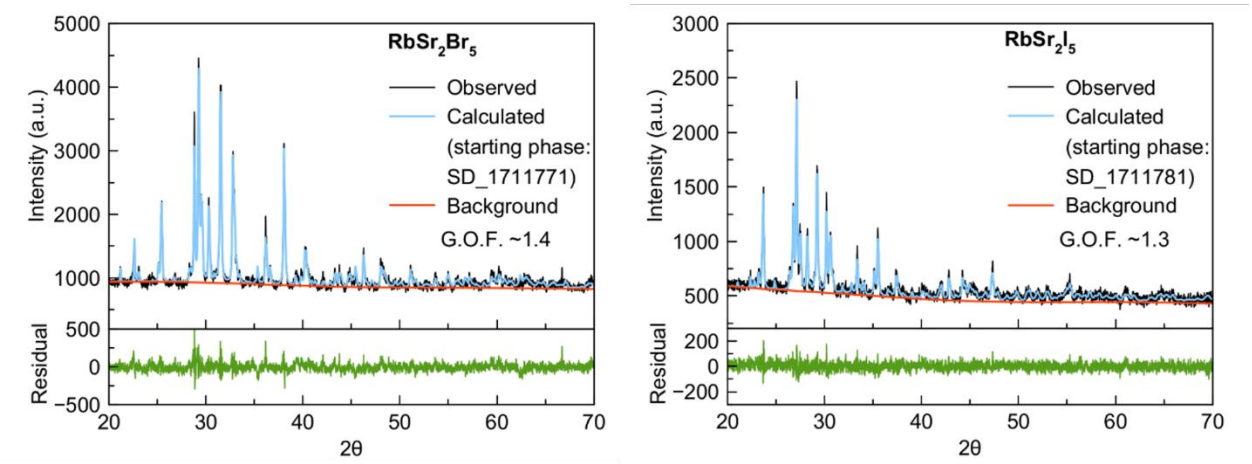


**Figure 33.** Powder X-ray Diffraction patterns and Rietveld refinements with GSASII showed the $RbSr_2I_5$ and $RbSr_2Br_5$ crystals to be phase pure.

The hygroscopicity was tested with Dynamic Vapor Sorption measurements and measuring pulse height spectra under ambient conditions, as shown in **Figure 34**. $RbSr_2Br_5$:Eu was minimally hygroscopic, with a ~3% mass change after 20 hours, and no change in the pulse height spectra acquired under ambient conditions over 16 hours. During the measurement, the crystal surface became hazy and white. . After the measurement, the sample was left on the laboratory benchtop in ambient conditions to test if any changes would occur. It was unchanged for ~20 days with blue luminescence under UV light. After this time period, the sample exhibited deliquescence, which is when a substance absorbs water from the atmosphere and dissolves.

In contrast, $RbSr_2I_5$:Eu was highly hygroscopic, with a mass change of ~43% after 20 hours. This was comparable to NaI:Tl and $SrI_2$:Eu crystals, which had a 33% and 50% change in mass, respectively, and similar rates of moisture sorption after 2 hours. During the DVS measurement, a puddle of liquid formed around the sample, while a solid white piece remained in the center. This deliquescence had an interesting effect on the pulse height spectra measurements. The light yield slightly increased after 1 hour and then remained constant, while the counts slowly declined over the 18 hour period tested. No optical coupling material (i.e. mineral oil or optical grease) was used between the sample and the PMT during the measurement, which usually enhances the light yield by improving the light collection. It is thought that the liquid forming on the surface of the sample improved the coupling of the sample to the PMT, which artificially improved the light yield.

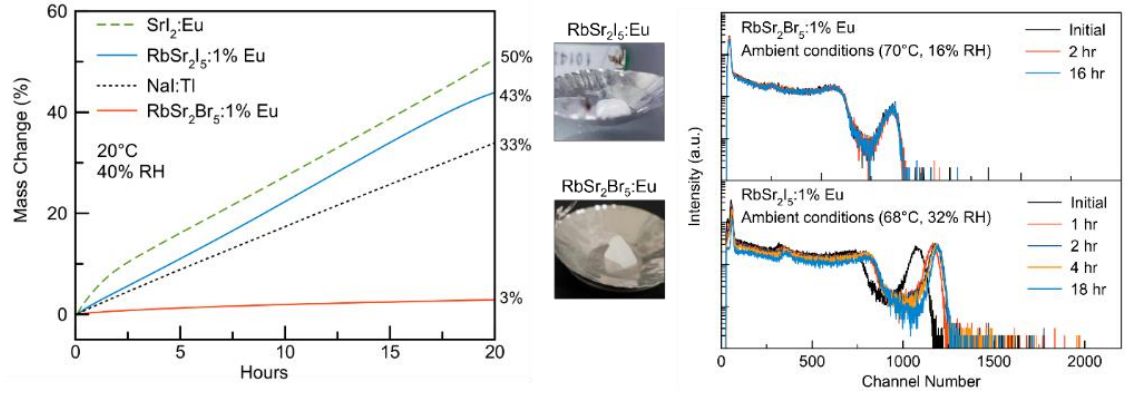


**Figure 34.** Dynamic Vapor Sorption moisture curves and pulse height spectra acquired to assess hygroscopicity of $RbSr_2I_5$:Eu and $RbSr_2Br_5$:Eu scintillators.

Optical absorbance and transmittance of undoped $RbSr_2Br_5$ and $RbSr_2I_5$ are shown in **Figure 35**, along with Tauc plots generated from absorbance data to determine optical band gap. $RbSr_2Br_5$ had high optical transmittance of ~70% near 800 nm, which decreased gradually until ~215 nm, when absorbance increased sharply. $RbSr_2I_5$ had high optical transmittance of ~85% near 800 nm, which gradually decreased around 400 nm until sharply dropping off ~260 nm. The difference in optical transmittance between $RbSr_2Br_5$ and $RbSr_2I_5$ could be due to the small bubbles in the bromide crystals.

Applying a linear fit to the Tauc plot generated from absorbance data, it was found that $RbSr_2Br_5$ and $RbSr_2I_5$ had direct optical band gaps of 5.9 eV and 4.7 eV, respectively. These values correspond well to calculated band gaps for similar compositions $CsBa_2Br_5$ and $CsBa_2I_5$, (4.53-5.77 eV and 3.69-4.49, respectively) [196].

Photoluminescence excitation and emission spectra and radioluminescence emissions are shown in **Figure 36**. The properties were characteristic of 5d-4f transitions from $Eu^{2+}$ [144]. The excitation spectra of $RbSr_2Br_5$:Eu and $RbSr_2Br_5$:Eu crystals consisted of several overlapping bands from ~250-415 nm and ~250-430 nm, respectively. Photoluminescence emissions for all crystals consisted of a single peak. With increasing dopant concentration, the emission of $RbSr_2Br_5$:Eu shifted from 423 nm to 430 nm, and those of $RbSr_2I_5$:Eu shifted from 438 nm to 445 nm. Overlap of photoluminescence excitation and emission spectra increased with increasing $Eu^{2+}$ concentration, consistent with europium self-absorption effects [64-66, 75, 110].

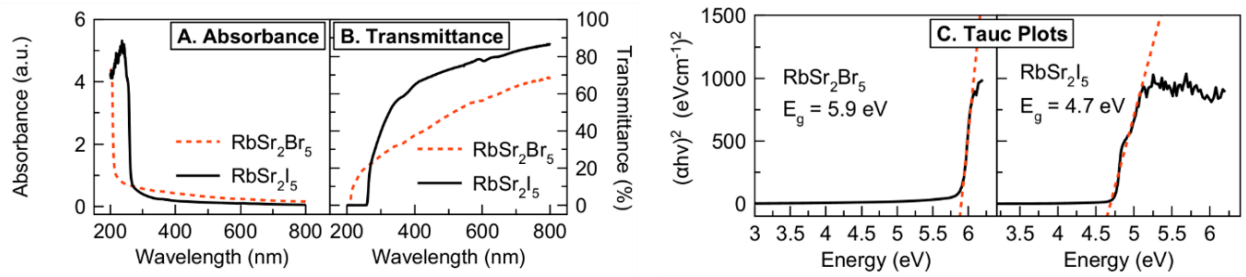


**Figure 35**. A) Optical absorbance and B) transmittance of $RbSr_2Br_5$ and $RbSr_2I_5$, and C) Tauc plots to determine optical band gap.

The radioluminescence emissions were similar to the photoluminescence emissions. With increasing europium concentration, the emission of $RbSr_2Br_5$:Eu redshifted from 423 nm to 438 nm with 7% Eu doping, and the emission of $RbSr_2I_5$:Eu redshifted from 438 nm to 445 nm.

The radioluminescence emission of the undoped crystals had at least one narrow peak and a low intensity broad peak. $RbSr_2Br_5$ crystal had a narrow emission at 420 nm, and a broad emission ~488 nm. $RbSr_2I_5$ had narrow emissions at 403 and 441 nm, and a broad emission centered at 510 nm. The inset of **Figure 36** compares the radioluminescence spectra in log scale. With increasing europium concentration, the intensity of the ~500 nm emission decreased.

These results are similar to radioluminescence studied thoroughly in $CsBa_2I_5$ and $CsBa_2I_5$:Eu [169]. In undoped $CsBa_2I_5$, a broad emission at 390 nm was attributed to a self-trapped exciton (STE), and a narrow emission at 430 nm was attributed to a trace europium impurity in the raw materials. A third, broad emission at 600 nm was attributed to impurity-mediated recombination. This type of emission was also observed in $BaI_2$:Eu. Zone refining and additional purification of $BaI_2$:Eu first reduced and then completely removed the broad emission from the radioluminescence [197]. Further studies on $RbSr_2I_5$ and $RbSr_2Br_5$ crystals may include temperature-dependent luminescence investigations of relationships between trace amounts of impurities, trap structure, and resulting emissions.

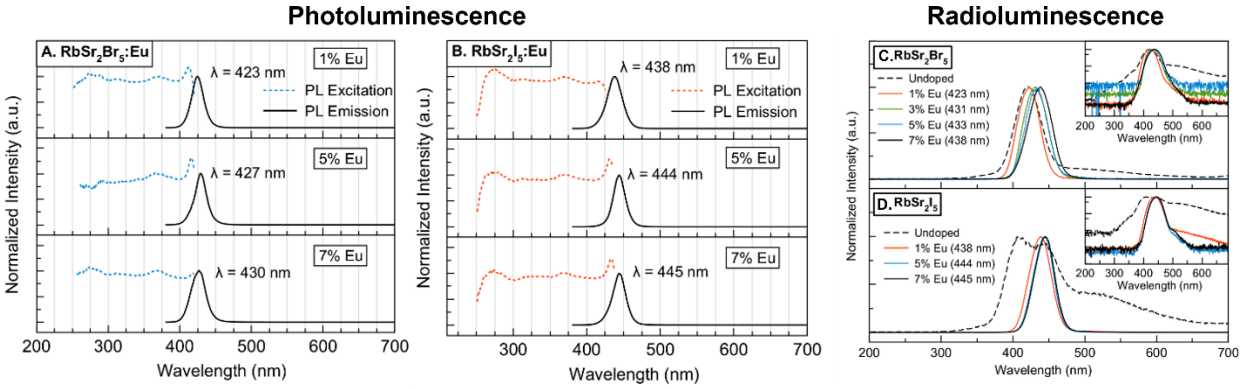


**Figure 36**. A-B) Photoluminescence excitation and emission spectra for $RbSr_2Br_5$:Eu and $RbSr_2I_5$:Eu crystals. C-D) Radioluminescence of $RbSr_2Br_5$:Eu and $RbSr_2I_5$:Eu redshifted with increased europium concentration. The inset shows the spectra in log scale.

A comparison of energy resolution and light yield as a function of europium dopant concentration is plotted in **Figure 37**. The light yield and energy resolution of undoped $RbSr_2I_5$ was 14,000 ph/MeV and 7.6% at 662 keV, while that of undoped $RbSr_2Br_5$ was 2,400 ph/MeV and 12.9% at 662 keV.

Doping with just 1% Eu significantly improved the performance of $RbSr_2Br_5$:Eu and $RbSr_2I_5$:Eu crystals. $RbSr_2Br_5$:Eu 1% had a light yield of 58,000 ph/MeV and an energy resolution of 3.9% at 662 keV. $RbSr_2I_5$:Eu 1% had light yield of 74,000 ph/MeV and energy resolution of 3.5% at 662 keV. Increasing dopant concentrations in both crystals improved the performance further. Between 3-7% Eu, the light yield and energy resolution of $RbSr_2Br_5$:Eu was 73,000 ph/MeV and 4% at 662 keV. The light yield of $RbSr_2I_5$:Eu was 90,000 ph/MeV, and energy resolution incrementally improved to 2.8% at 662 keV. The improvements in light yield likely led to the improved energy resolutions [198].

For these small samples (Ø7, 4 mm), the consistency in the light yield with dopant concentrations above 3% Eu indicates minimal self-absorption or quenching. Overall, the relative change in performance with europium dopant concentration follows similar trends observed in other $AB_2X_5$:Eu scintillators [83, 177].

The difference in the light yield between $RbSr_2Br_5$ and $RbSr_2I_5$ crystals may be attributable to the difference in their band gaps. The maximum light yield of an ionic-crystal scintillator is given as:

$$LY_{max} = \frac{S * Q}{\beta * E_g} \times 10^6$$

where S is electron-hole transfer efficiency, Q is luminescence quantum efficiency, $E_g$ is the band gap, and β is a coefficient that is typically 1.5-3 for wide band gap and ionic crystals [9, 10].

Using the band gap values measured in this study, and assuming that β = 2 and the efficiency terms S and Q are equal to 1, the maximum theoretical light yield estimated for $RbSr_2Br_5$ is ~85,000 ph/MeV and that of $RbSr_2I_5$ is ~106,000 ph/MeV. The highest light yields observed in this study are ~85% the maximum theoretical light yield. Sources of energy loss that reduce the light yield from the theoretical maximum include defects, impurities, self-absorption, and light collection.

Comparing the scintillation performance and crystal growth results, two observations were encouraging for scale up of crystal growth to large diameters (≥ Ø25 mm). First, pulse height spectra were measured for several samples cut along the vertical axis of the crystals to investigate possible effects of europium dopant segregation (Fig. 10). Even for 7% Eu, a relatively high dopant concentration, no significant variation in the performance of the crystals from seed end to tail end was observed. This likely indicates that europium is uniformly distributed along the growth axis. Due to their similar ionic radius and valence (2+), minimal segregation of $Eu^{2+}$ on $Sr^{2+}$ lattice sites was anticipated [104]. For instance, the measured concentration of $EuI_2$ in $SrI_2$:Eu crystals has been reported to be remarkably similar to the nominal concentration added in the melt [199, 200]. Based on reports of zone-refining and crystal growth of co-doped $SrI_2$:Eu, any other alkali and alkali-earth metal impurities may be expected to segregate well to the last-to-freeze, while some metallic and oxygen-bonded impurities could be more difficult to remove [201, 202].

Second, since just 1% Eu generates very promising scintillation performance, the anticipated effects of europium self-absorption with larger crystal size could likely be mitigated with the use of low concentrations of europium. Self-absorption typically worsens with the size of the crystal and dopant concentration.

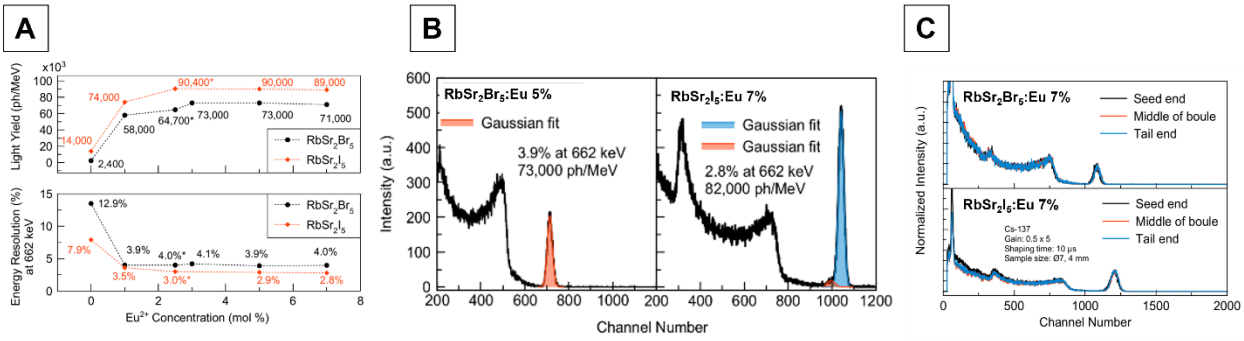


**Figure 37.** A-B) Light yield and energy resolution (at 662 keV) of $RbSr_2I_5$ and $RbSr_2Br_5$ as a function of europium dopant concentration. Samples were Ø7, 4 mm in size. An asterisk (*) marks data reproduced from [69]. C) Pulse height spectra collected for samples from different sections of the boule, showing good uniformity.

Scintillation decay curves are shown in **Figure 38**, along with a comparison of the primary and secondary scintillation decay components as a function of europium concentration. The scintillation decay of the undoped crystals was similar and consisted of three components. $RbSr_2Br_5$ had a minor 11 ns (3%) component, a 0.4 µs (24%) component, and a primary component of 2.2 µs (73%). The scintillation decay of undoped $RbSr_2I_5$ consisted of a minor 70 ns (11%) component, a 0.5 µs (35%) component, and a primary 1.9 µs (54%) component. The europium doped crystals had two decay components, a primary relatively fast component (~0.7-1.2 µs), and a secondary relatively slow component (~2-4 µs).

When considering the secondary decay component, the behavior of $RbSr_2Br_5$ and $RbSr_2I_5$ differed from each other. The secondary decay component of $RbSr_2Br_5$ increased with europium concentration, which may also indicate some self-absorption. However, the secondary decay component of $RbSr_2I_5$ decreased with an increase in $Eu^{2+}$ concentration. This contradicts the expected increase caused by self-absorption.

X-ray induced afterglow profiles are shown in **Figure 39**, and the intensity (%) at several time marks (milliseconds) is listed in **Table 8.** $CdWO_4$ was measured to provide a comparison to the primary scintillator currently used in high energy X-ray radiography systems. The afterglow of $RbSr_2Br_5$ and $RbSr_2I_5$ crystals improved significantly with the addition of europium dopants, approximately by an order of magnitude.

The greatest change in afterglow occurred with 1% Eu doping. At 2 ms, the afterglow of undoped $RbSr_2Br_5$ was 11.68%, and that of $RbSr_2Br_5$:Eu 1% was 1.82%. At 2 ms, the afterglow of undoped $RbSr_2I_5$ was 22.68%, and that of $RbSr_2I_5$:Eu 1% was 0.79%. For comparison, the afterglow of $CdWO_4$ was 0.16% at 2 ms.

While the afterglow of $RbSr_2Br_5$:Eu improved with higher dopant concentrations (3-7%), the magnitude of the changes was smaller. This behavior of afterglow with dopant concentration mirrors those observed for light yield. Meanwhile, the afterglow of $RbSr_2I_5$:Eu did not improve with increasing dopant concentrations. The difference between the trends in $RbSr_2Br_5$:Eu and $RbSr_2I_5$:Eu crystals could be related to their different band gaps and, therefore, the relative differences in energy levels of traps that could be contributing to the afterglow.

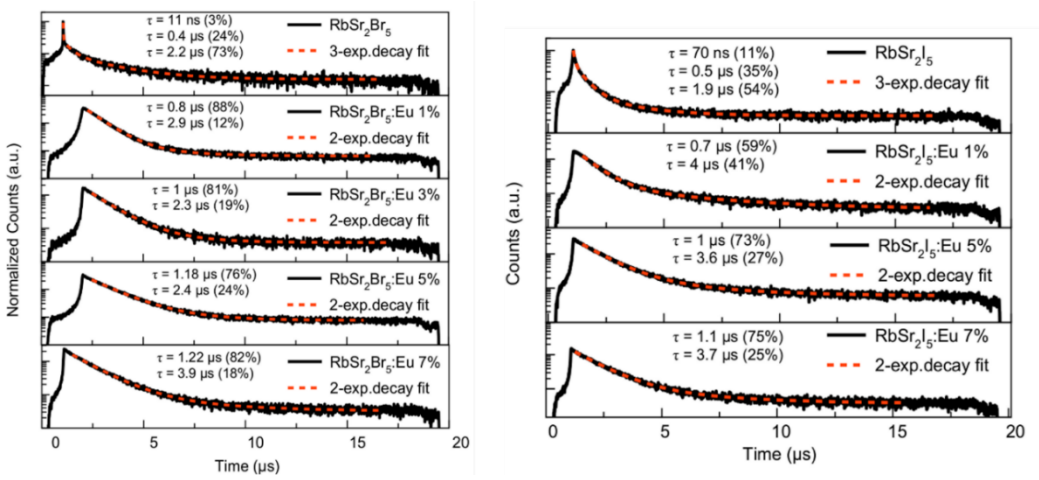


**Figure 38.** Scintillation decay time curves for $RbSr_2Br_5$ and $RbSr_2I_5$ crystals.

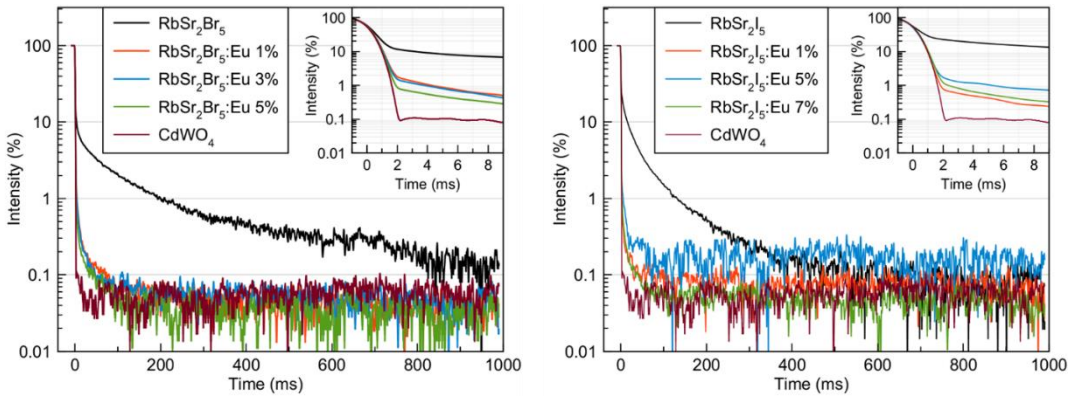


**Figure 39**. X-ray induced afterglow of $RbSr_2Br_5$ and $RbSr_2I_5$ crystals. The inset figures show the first 10 ms after X-rays were shut off.

**Table 8.** Afterglow intensity of $RbSr_2Br_5$ and $RbSr_2I_5$ crystals.

| Scintillator | Intensity at 2 ms | Intensity at 6 ms | Intensity at 20 ms |
|---|---|---|---|
| $RbSr_2Br_5$ | 11.68% | 7.79% | 2.99% |
| $RbSr_2Br_5$:Eu 1% | 1.82% | 0.74% | 0.22% |
| $RbSr_2Br_5$:Eu 3% | 1.54% | 0.68% | 0.21% |
| $RbSr_2Br_5$:Eu 5% | 1.50% | 0.41% | 0.15% |
| $RbSr_2I_5$ | 22.68% | 16.01% | 8.31% |
| $RbSr_2I_5$:Eu 1% | 0.79% | 0.35% | 0.16% |
| $RbSr_2I_5$:Eu 5% | 1.73% | 0.89% | 0.25% |
| $RbSr_2I_5$:Eu 7% | 1.22% | 0.47% | 0.15% |
| $CdWO_4$ | 0.16% | 0.09% | 0.04% |

To investigate the stability of $RbSr_2Br_5$:Eu and $RbSr_2I_5$:Eu, pulse height spectra were acquired at different temperatures. Repeatability was tested first. Results of two tests are plotted in **Figure 40**. A measurement session involving two immediately subsequent temperature cycles from +75°C to -75°C was done on the same sample without repositioning. The relative light yield showed the same behavior. Next, a measurement was done while beginning at 300°C and cooling to -125°C then beginning at -125°C and heating to 300°C. This showed some variation, up to 10%. After this measurement, a thin film was seen on the quartz window of the vacuum chamber, termed here as "fogged." All further measurements were done by first heating to the hottest temperature studied then measuring light yield while decreasing the temperature.

**Figure 41** shows a comparison between the light yield as a function of temperature for $RbSr_2Br_5$:1 mol% Eu and $RbSr_2I_5$:1 mol% Eu. A) shows the pulse height spectra at the highest temperature, room temperature, and lowest temperature. B) shows the relative light yield as a function of temperature, with the top panel showing the entire temperature range measured and the bottom panel showing the temperature range relevant to high energy X-ray radiography.

A distinct photopeak was visible at all temperatures, and generally, $RbSr_2Br_5$:Eu and $RbSr_2I_5$:Eu exhibited similar behavior. The light yield declined rapidly and significantly at colder temperatures. At -75°C, the light yield reduced to ~75% the room temperature value. At -260°C, the light yield was ~40% the room temperature value. Surprisingly, the light yield slightly increased at higher temperatures, ~110% around 100°C.

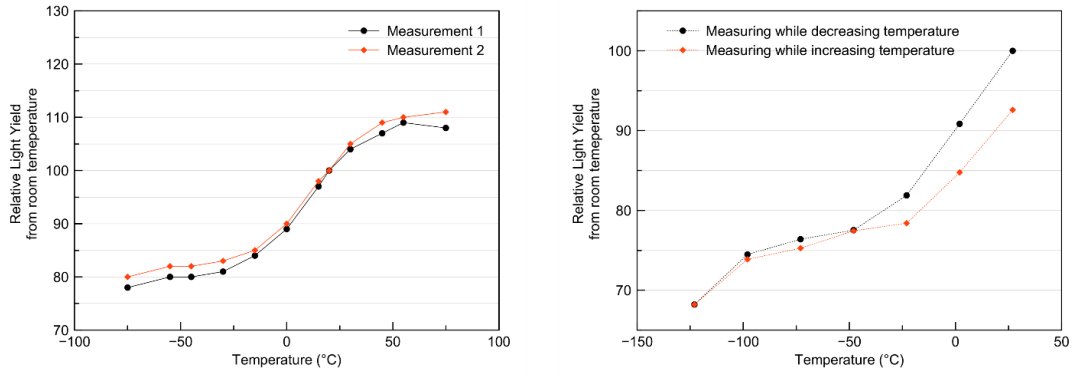


**Figure 40.** Testing repeatability of light yield measurements vs temperature with a $RbSr_2I_5$:Eu crystal. Relative light yield was determined by the change in channel number of the 662 keV photopeak centroid from room temperature.

The temperature range relevant to homeland security applications is −30°C to +55°C. For $RbSr_2Br_5$:Eu, the light yield at -30°C decreased to ~85% the room temperature value and increased to ~101% at +55°C. For $RbSr_2I_5$:Eu, the light yield at -30°C decreased to ~80% of the room temperature value and increased to ~110% at +55°C.

In 2013, Boatner et al. conducted a systematic study of the light yield of 20 different inorganic scintillators versus temperature [21]. The maximum temperature at which a photopeak could be observed was 46°C for $BaF_2$, 151°C for $CdWO_4$, 174°C for CsI:Tl, 277°C for $SrI_2$:Eu, and 395°C for LuAP:Ce.

Among these compositions, only two had a light yield that increased with temperature. The light yield of $Lu_3Al_5O_{12}$:Pr (LuAG:Pr) peaked at 125°C before decreasing. The light yield of $LuAlO_3$:Ce (LuAP:Ce) increased with temperature, and continued to increase at 395°C. In 2015, Tsubota et al. showed that the orthorhombic form of $Gd_2Si_2O_7$:2.5 mol% $Ce^{3+}$ (GPS) had a high light yield at 300°C (573 K) that was 214% the room temperature value, followed by a gradual decrease at higher temperatures [203]. Triclinic GPS with 10% Ce also showed a gradual increase until 150°C (423 K) but rapidly decreased at higher temperatures.

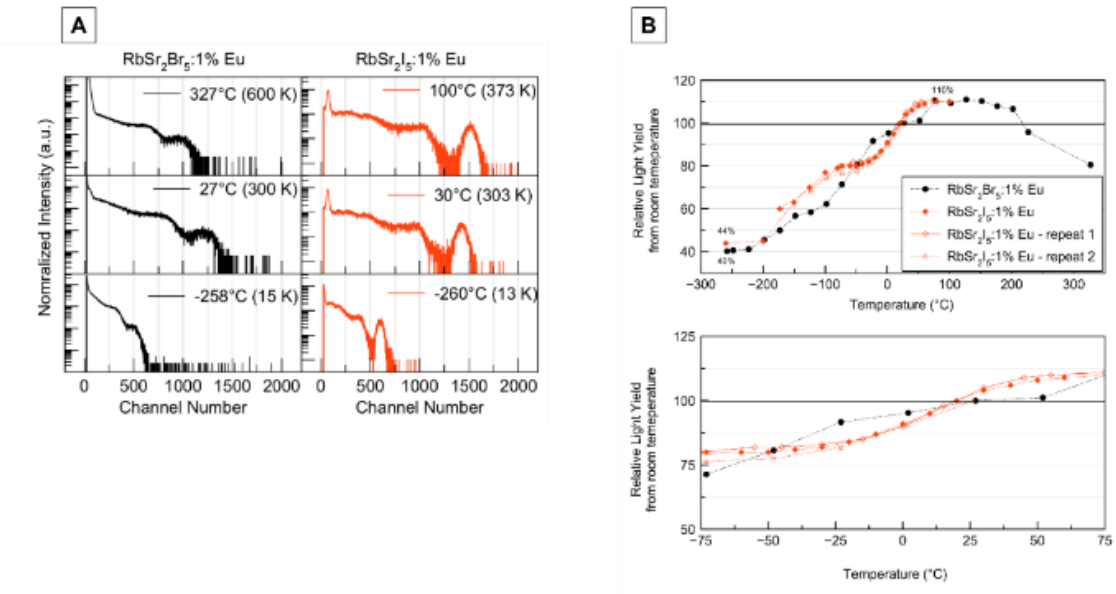


**Figure 41**. Temperature dependent light yield of $RbSr_2Br_5$:Eu and $RbSr_2I_5$:Eu was determined by the change in channel number of the 662 keV photopeak from room temperature.

### 5.2 Rubidium Strontium Iodide with $Ce^{3+}$ dopant ($RbSr_2I_5$:Ce)

As an alternative dopant to divalent europium, trivalent cerium was investigated in $RbSr_2I_5$. The possible advantages included circumventing the issue of europium self-absorption and reaching a faster scintillation decay time while maintaining a high light yield.

Cerium doping was previously found to be a promising alternative dopant in the isostructural scintillator, $KSr_2I_5$ [192]. For this composition, the best light yield and energy resolution were 49,000 ph/MeV and 3.1% at 662 keV with 3.5 mol% Ce, although crystal quality was limited. The scintillation decay time consisted of three components: ~40 ns (~30%), ~250 ns (~30%), and ~1200 ns (~40%).

This experiment aimed to determine if $Ce^{3+}$ was a viable luminescent dopant that would decrease decay time while producing satisfactory light yield as compared to $Eu^{2+}$. In this work, a Ø7 mm crystal of $RbSr_2I_5$:0.5 mol% Ce was grown and its scintillation properties were tested. The dopant concentration was selected to provide an initial indication of performance without sacrificing the crystal quality.

A Ø7 mm $RbSr_2I_5$:0.5 mol% $Ce^{3+}$ was grown with a translation rate of 0.5 mm/hr and furnace set points of 630/530/430°C. The crystal was cooled over 100 hours. As seen in **Figure 42A**, the crystal was highly transparent and mostly colorless. There were small cracks towards the last-to-freeze along with a yellow deposit that was similar in color to cerium iodide raw material.

The scintillation properties are summarized in **Figure 42B-E.** The properties were similar to those reported for $KSr_2I_5$:Ce. The radioluminescence emission consisted of a single, symmetric peak centered near 438 nm, which was the same as produced with 1 mol% Eu. This showed successful incorporation of $Ce^{3+}$ into the $RbSr_2I_5$ matrix.

$RbSr_2I_5$:Ce had a high light yield and energy resolution of 48,000 ph/MeV and 5.5% at 662 keV. While this performance was generally lower than observed with 1 mol% Eu doping, it is also worth noting that the $Ce^{3+}$ concentration was unoptimized.

No significant differences in properties between the seed end and tail end of the crystal were observed, which most likely indicated dopant uniformity throughout the crystal. As an aside, there was a small peak observed in the pulse height spectra near the channel number 70. This was believed to be from Ba-133 contamination of the Cs-137 source used in the measurement.

The scintillation decay time consisted of three components, including two fast components of 30.7 ns (26%), 111 ns (32%) and one longer component of 1.02 µs (42%), which was similar to those observed for $KSr_2I_5$:1 mol% Ce. The decay time components were much faster than those for $RbSr_2I_5$:1% Eu, which were 0.7 µs (59%) and 4.0 µs (41%).

While the light yield, energy resolution, and scintillation decay time were promising, an undesirable property of $RbSr_2I_5$:Ce was the X-ray afterglow. The X-ray afterglow was measured at UTK, using an X-ray tube with a ~20 ms shut down time. For comparison, $KSr_2I_5$:1 mol% $Ce^{3+}$, $RbSr_2I_5$:1 mol% $Eu^{2+}$C, CsI:Tl, and $CdWO_4$ were measured on the same system.

Compared to $KSr_2I_5$:1 mol% $Ce^{3+}$, CsI:Tl, and $RbSr_2I_5$:1 mol% $Eu^{2+}$, the afterglow intensity of $RbSr_2I_5$:0.5 mol% Ce dropped off quickly. However, unlike the other compositions, the X-ray afterglow remained relatively high after ~20 ms.

This exacerbated afterglow may be associated with a charge imbalance from substituting the 2+ Sr site with the 3+ Ce ion. It may be possible that doping with a 1+ valence element could balance the charge and improve the afterglow.

Overall, from these initial experiments, it appeared that $Ce^{3+}$ is a promising luminescent activator for $RbSr_2I_5$, although dopant concentration studies and scale up experiments should be pursued.

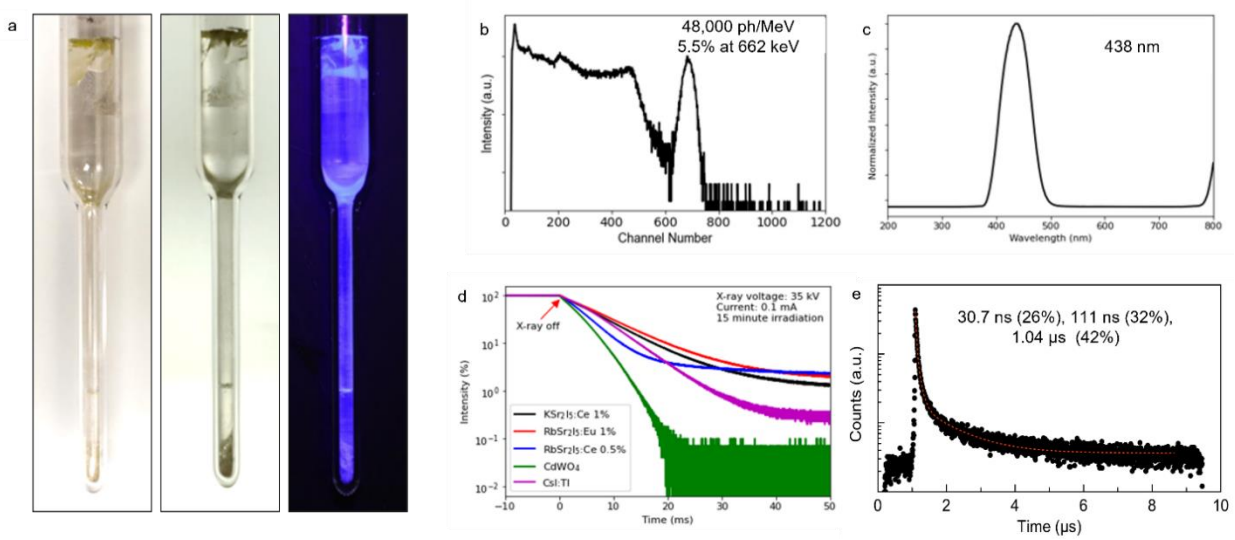


**Figure 42.** $RbSr_2I_5$:0.5 mol% Ce: Ø7 mm crystal and scintillation properties.

### 5.3 Rubidium Strontium-Barium Iodide Mixed Scintillators ($Rb(Sr,Ba)_2I_5$)

While $RbSr_2I_5$ scintillators have already demonstrated very promising performance, there may still be opportunities for further optimization. Anion and cation mixing are two methods to possibly improve scintillation performance or crystal quality even further [56, 204-207]. Specifically for the scintillator $CsSrI_3$:Eu, admixing of $Ba^{2+}$ (0-25%) was pursued to possibly decrease the hygroscopicity of the scintillator, slightly increase the density and effective number, and test its effects on scintillation properties [208]. Higher barium concentrations did, in fact, suppress hygroscopicity and the moisture absorption rate. Unfortunately, however, the light yield also decreased significantly.

Two isostructural compositions, $RbSr_2I_5$:Eu [69] and $RbBa_2I_5$:Eu [178] are interesting candidates for $Ba^{2+}$ admixing within the $AB_2X_5$:Eu scintillator compositional space. While $RbSr_2I_5$:Eu is highly hygroscopic, $RbBa_2I_5$:Eu is not. Additionally, $RbSr_2I_5$:Eu exhibits both excellent scintillation properties and crystal quality, whereas $RbBa_2I_5$:Eu may be limited by its translucent nature.

In this work, admixing $Ba^{2+}$ into $RbSr_2I_5$:Eu 5 mol% was explored via single crystal growth and characterization. Crystals of $Rb(Sr_x, Ba_{1-x})_2I_5$:Eu, x = 0, 0.25, 0.50, 0.75, 1, in a 7 mm diameter were grown by the Vertical Bridgman method. The single crystals' physical properties were characterized, including melt behavior, crystal structure, and hygroscopicity. Luminescence and scintillation properties were investigated, including emission, light yield and energy resolution, light yield proportionality, and decay time.

The crystals are shown in **Figure 43**. They were grown with translation rates of 0.4 and 0.5 mm/hr. The crystals were all colorless, with some cracking observed for higher barium concentrations. This could be mitigated in future experiments by slowing the cooling rate. Some bubble-like inclusions were visible in the crystal with 50% Sr and 50% Ba under the optical microscope. Regardless of the small bubbles, the crystal maintained high optical transmittance, 70-80% above the absorption edge (**Figure 44**). However, the transparency of the crystals worsened with increasing barium concentration. By visual observation in the transparent furnace, it was seen that this translucency formed at high temperatures during cooling.

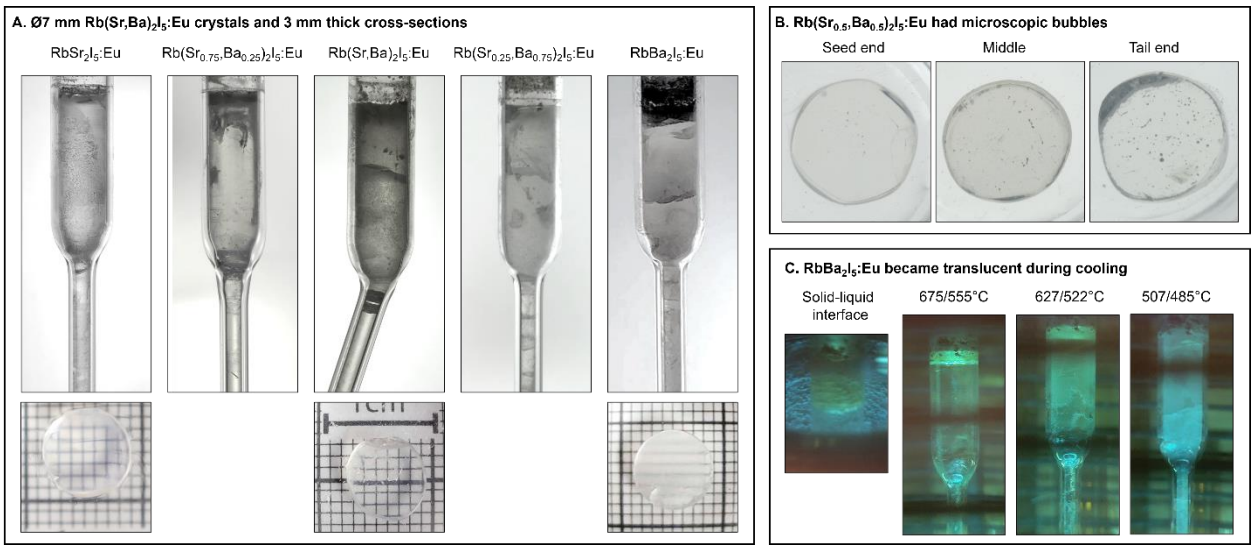


**Figure 43**. A) Backlit photos of $Rb(Sr,Ba)_2I_5$:Eu crystals. The transparency worsened with more than 50% barium concentration. B) Under the optical microscope, small bubbles were visible inside of the $Rb(Sr_{0.5}, Ba_{0.5})_2I_5$:Eu crystal. C) $RbBa_2I_5$:Eu crystal became translucent on cooling.

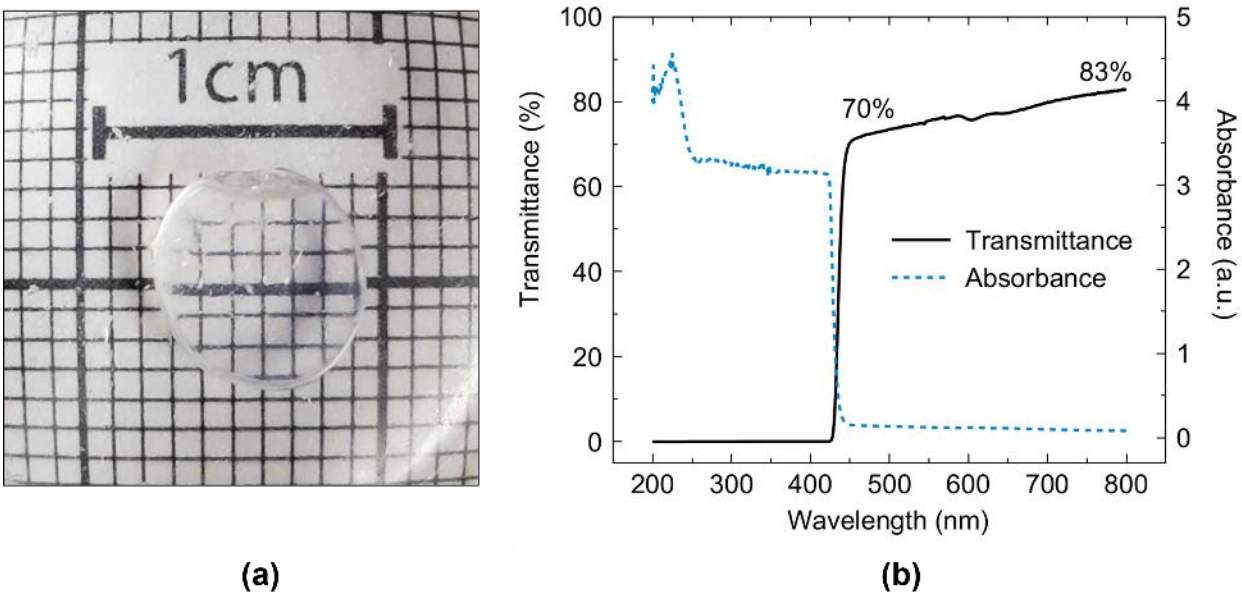


**Figure 44.** A) Cross-section sample of $Rb(Sr_{0.5}, Ba_{0.5})_2I_5$:Eu crystal used for measurements, photographed with ambient lighting. B) Optical transmittance and absorbance spectra.

Rietveld refinement of the powder X-ray diffraction pattern showed that $Rb(Sr_{0.5},Ba_{0.5})_2I_5$:Eu was a single phase and isostructural with $RbSr_2I_5$ and $RbBa_2I_5$. The lattice parameters are listed in **Table 9**. Refinement was done using the reported $RbBa_2I_5$ crystallographic data in the SpringerMaterials database [209]. Compared to $RbSr_2I_5$, the lattice parameters were slightly larger for the admixed composition containing $Ba^{2+}$, and the admixed composition was slightly smaller than $RbBa_2I_5$. This can be expected due to the larger ionic radius of $Ba^{2+}$ compared to $Sr^{2+}$ (~0.17 Å) and approximation from Vegard's law [104, 210]. The effective atomic number (calculated by the equation from Murty) increased from 49 to 53 with barium substitution [8].

**Figure 45** shows the Differential Scanning Calorimetry (DSC) heat flow curves acquired on heating and cooling the $Rb(Sr,Ba)_2I_5$:Eu samples. One pair of endothermic (negative) and exothermic (positive) peaks was observed for each composition, which corresponded to melting and crystallizing. The melting point increased with barium concentration, from 490°C to 568°C for $Rb(Sr_{0.5},Ba_{0.5})_2I_5$:Eu and 597°C for $RbBa_2I_5$:Eu.

**Figure 46** shows the mass change as a function of time during Dynamic Vapor Sorption (DVS) measurements, in addition to the visible changes in the $Rb(Sr_{0.5},Ba_{0.5})_2I_5$:Eu sample. After moisture exposure, the colorless, transparent crystal became pale yellow in color and opaque. In comparison, $RbSr_2I_5$:Eu formed a liquid layer quickly after moisture exposure. Although the visual appearance of $Rb(Sr_{0.5},Ba_{0.5})_2I_5$:Eu crystal changed significantly, the mass change was relatively low. The mass change for $RbSr_2I_5$:Eu after 5 hours of moisture exposure was 16%, comparable to $SrI_2$:Eu. As the barium concentration increased, the hygroscopicity decreased. The mass change for $Rb(Sr_{0.5},Ba_{0.5})_2I_5$:Eu was 7%, and that of $RbBa_2I_5$:Eu was 2.4%

The photoluminescence and radioluminescence spectra are shown in **Figure 47**. Both emissions consisted of one narrow peak at 440-448 nm. This emission is characteristic of the 5d-4f electronic transition of divalent europium [144]. The emission of $Rb(Sr,Ba)_2I_5$:Eu was similar to that of $RbSr_2I_5$:Eu (444 nm) and $RbBa_2I_5$:Eu (436 nm). There was no systematic change in emission wavelength with barium concentration, although the admixed crystals were redshifted by ~5 nm compared to the single component crystals. There was a slight change in the excitation bands between $RbSr_2I_5$:Eu and crystals with barium. All crystals had several overlapping excitation bands from 250-400 nm. In $RbSr_2I_5$:Eu, there is a minimum in these bands near 250 nm, whereas the barium-containing crystals had a peak here.

**Table 9**. Lattice parameters of $Rb(Sr,Ba)_2I_5$:Eu compared to $RbSr_2I_5$ and $RbBa_2I_5$

| Parameter | $RbSr_2I_5$ [166] | $Rb(Sr_{0.5},Ba_{0.5})_2I_5$:Eu | $RbBa_2I_5$ [166] |
|---|---|---|---|
| a (Å) | 10.0975(6) | 10.249(8) | 10.3700(6) |
| b (Å) | 9.0555(4) | 9.173(2) | 9.2577(6) |
| c (Å) | 14.3081(8) | 14.882(8) | 14.7451(8) |
| V ($Å^3$) | 1308.324 | 1399.332 | 1415.589 |
| α = γ (°) | 90 | 90 | 90 |
| β (°) | 90.171(5) | 90.964 | 90.356(4) |

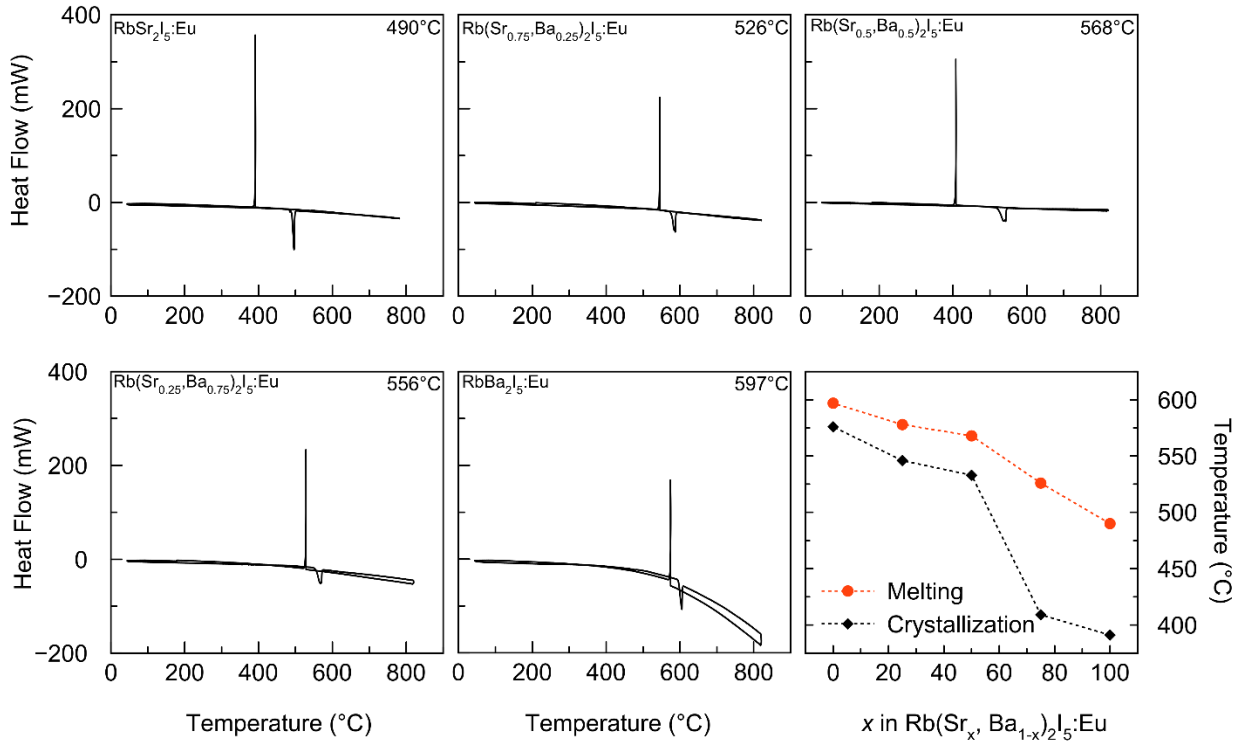


**Figure 45.** DSC curves and comparison of $Rb(Sr,Ba)_2I_5$:Eu melting points.

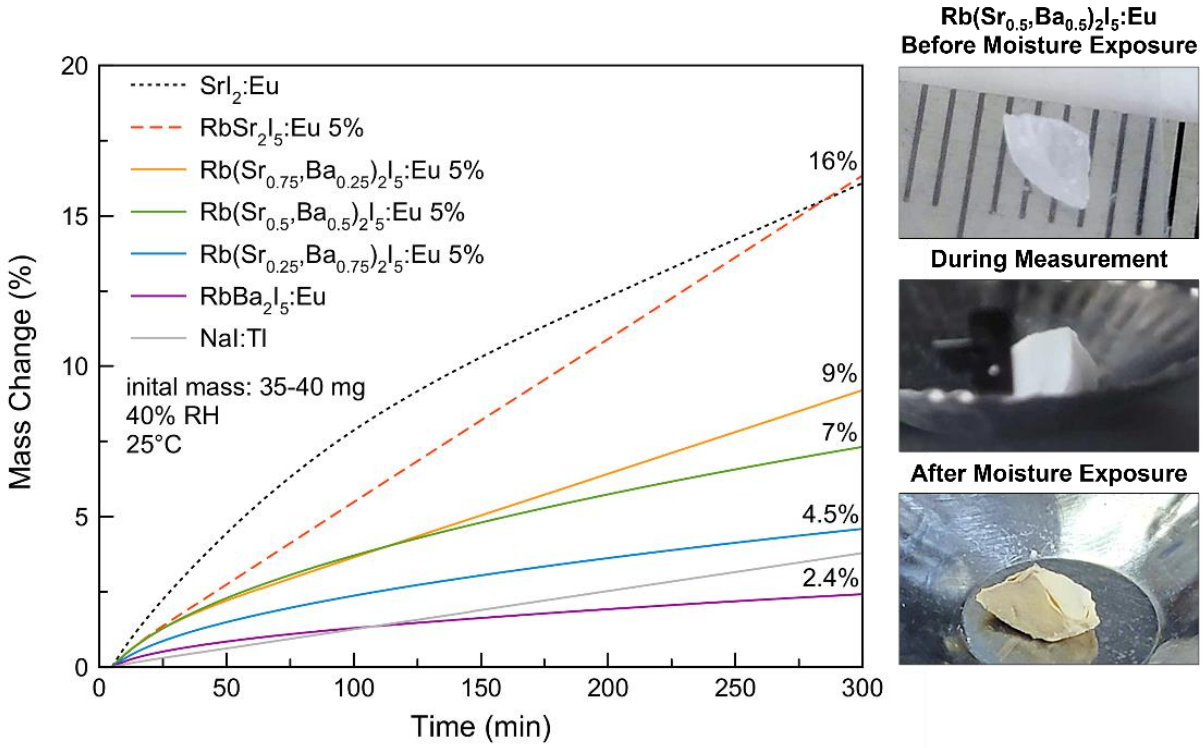


**Figure 46.** DVS curves used to study moisture sensitivity of $Rb(Sr,Ba)_2I_5$:Eu crystals. The sample's surface became pale yellow in color and there was a slight increase in mass (~7%) over time.

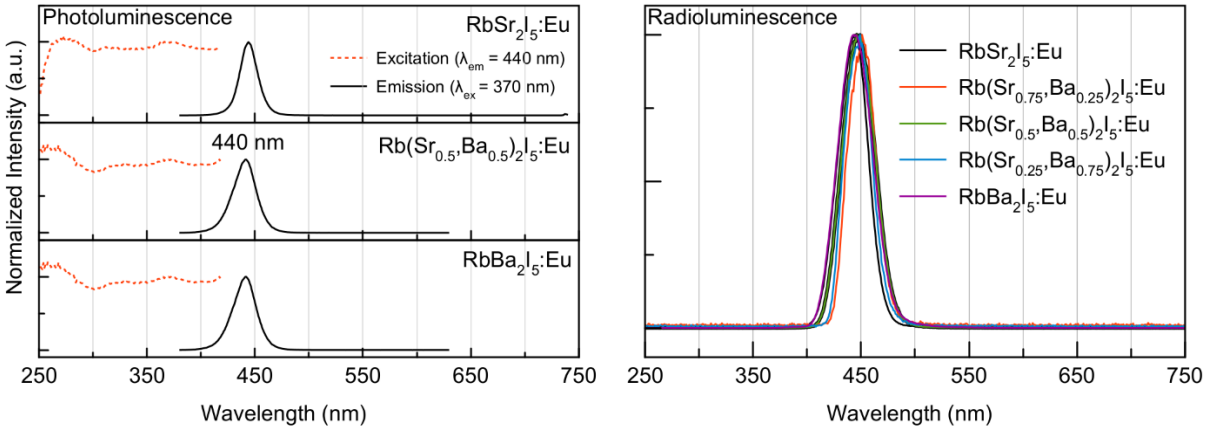


**Figure 47.** Photoluminescence and radioluminescence of $Rb(Sr,Ba)_2I_5$:Eu crystals.

Pulse height spectra and the light yield proportionality plots are shown in **Figure 48**. The light yield proportionality as a function of gamma energy is shown compared to commercial, packaged crystals of NaI:Tl (Harshaw 4D4, Ø1") and $LaCl_3$:Ce (Saint Gobain, Ø13 x 13 mm) measured on the same system. The light yield and energy resolution improved with barium admixing. The highest light yield was 104,000 ph/MeV, measured for the crystal with 75% barium and 25% strontium. It had an energy resolution of 2.3% at 662 keV.

Notably, the performance of $RbBa_2I_5$:Eu far surpasses reported values. The light yield and energy resolution were 58,200 ph/MeV and 8.18% at 662 keV for a crystal doped with 3 mol% Eu. In this work, the light yield and energy resolution were improved to 102,000 ph/MeV and 2.3% at 662 keV for a crystal of approximately the same size doped with 5 mol% Eu. While the slightly higher europium dopant concentration likely plays a role, it is hypothesized that this improvement primarily comes from crystal quality. This work used a translation rate that was 1/3 the speed. Additionally, anhydrous, high purity commercial $BaI_2$ raw materials were used, while the previous work synthesized $BaI_2$ in the laboratory. In this work, the light yield of the 50% Ba and 50% Sr crystal grown at 0.5 mm/hr was slightly lower than the value that may be expected with the trend from crystals grown at 0.4 mm/hr. Thus, we can surmise that the quality and performance of this series of crystals is quite sensitive to raw materials quality and translation rate.

On a different note, one factor likely contributing to the promising energy resolution of $Rb(Sr,Ba)_2I_5$:Eu is its light yield proportionality. The relative light yield was determined by the channel number of measured peaks in gamma spectra and the known gamma ray energies for the sealed sources used during the measurement. The data was normalized with respect to the light yield at 662 keV. The proportionality behavior measured for NaI:Tl and $LaCl_3$:Ce crystals matched well to reported data, with deviations from proportionality of ~17% and ~4%, respectively [211-213]. In comparison, $Rb(Sr,Ba)_2I_5$:Eu and $RbBa_2I_5$:Eu have a relatively linear and proportional response with a ~3% deviation from ideal at lower energies. This response with similar to the reported light yield proportionality of similar halide compositions $RbSr_2I_5$:Eu, $CsBa_2I_5$:Eu, $KSr_2I_5$:Eu, and $CsSrI_3$:Eu within this energy range [52, 63, 69, 81, 172].

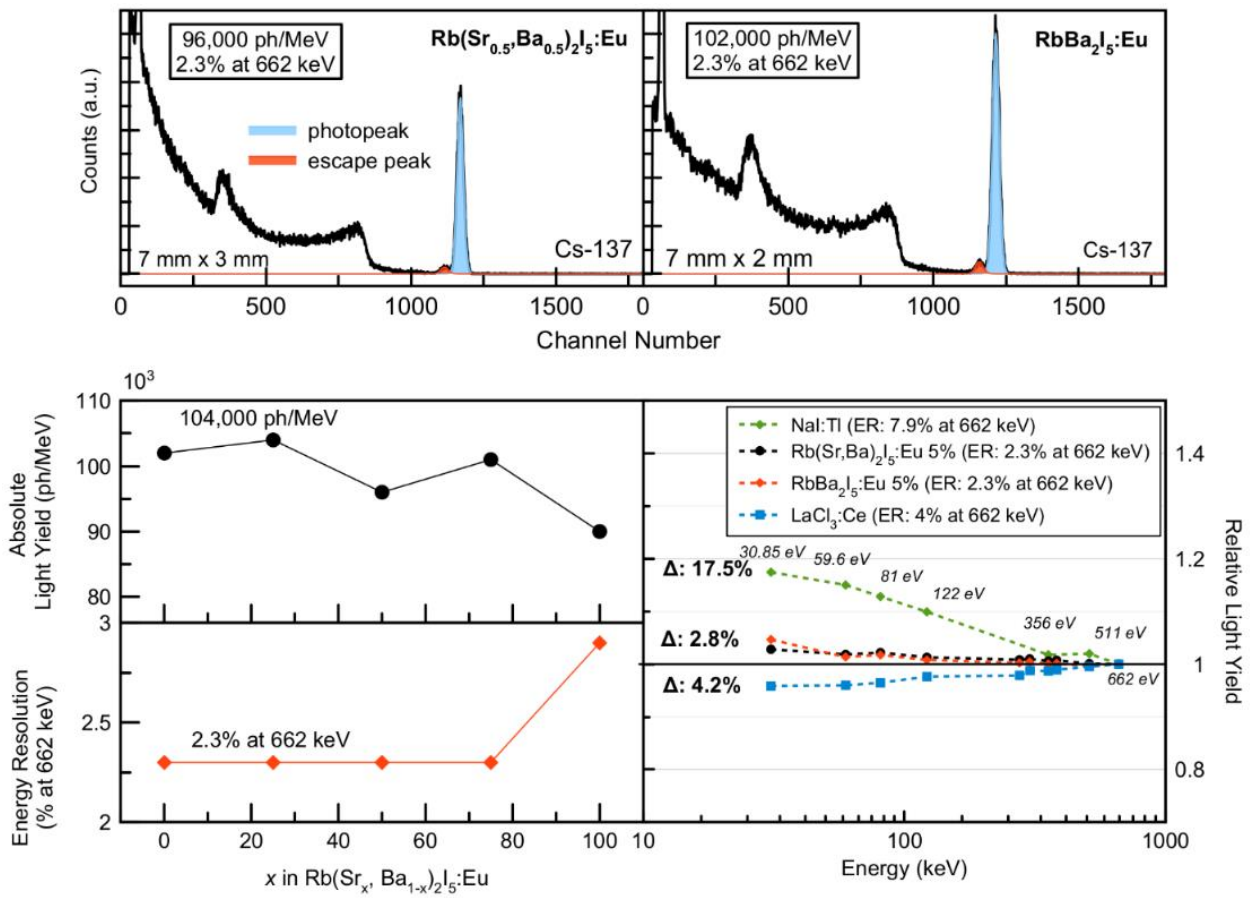


**Figure 48.** Pulse height spectra measured with a Cs-137 gamma source and light yield proportionality measured with a set of gamma sources for $Rb(Sr,Ba)_2I_5$:Eu crystals.

The scintillation decay time profiles are shown in **Figure 49A**. The scintillation decay time of $Rb(Sr_{0.5}, Ba_{0.5})_2I_5$:Eu consisted of two components, 1 µs (87%) and 3.7 µs (18%). These components were similar to $RbSr_2I_5$:Eu, except that the faster component had a higher contribution in the barium admixed composition. The decay time of $RbBa_2I_5$:Eu consisted of two faster components, 0.85 µs (79%) and 2.5 µs (21%).

The X-ray afterglow profiles are shown in **Figure 49B**. It was measured with a traditional X-ray tube (~20 ms shut down, 15 min irradiation) and with a pulsed X-ray source to investigate a long and a short time scale. The afterglow intensities measured with the pulsed X-ray source at different time marks are included in **Table 10**. On a longer time scale, it was seen that the afterglow intensity remained fairly constant over ~200 ms after initial decline. $RbBa_2I_5$:Eu had the lowest afterglow, showing an improvement over CsI:Tl. On the fast time scale with the pulsed X-ray source, the afterglow of $Rb(Sr,Ba)_2I_5$:Eu was shown to be similar to that of $CdWO_4$. The intensity at 2 ms was 0.13%, compared to the 0.16% for $CdWO_4$. The afterglow remained fairly constant, however, declining to 0.10% and 0.09% by 6 ms and 20 ms. This was a significant improvement over $RbSr_2I_5$:5 mol% Eu and $SrI_2$:3 wt% Eu.

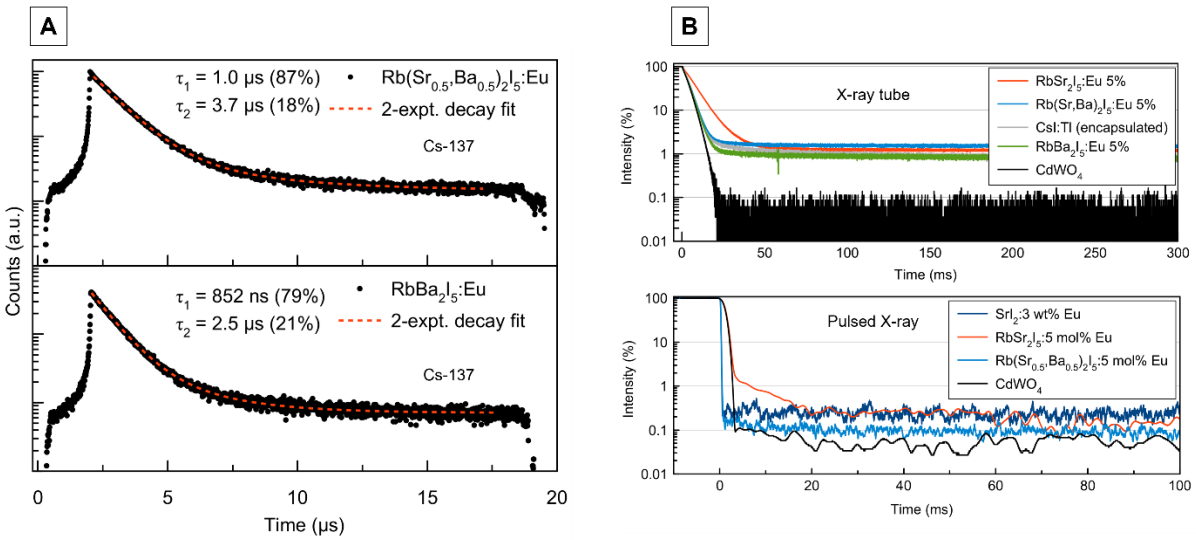


**Figure 49.** A) Scintillation decay time and B) X-ray afterglow of $Rb(Sr,Ba)_2I_5$:Eu crystals.

**Table 10.** X-ray afterglow of $Rb(Sr,Ba)_2I_5$:Eu crystals compared to $SrI_2$:Eu and $CdWO_4$.

| Scintillator | Intensity at 2 ms | Intensity at 6 ms | Intensity at 20 ms |
|---|---|---|---|
| $RbSr_2I_5$:5 mol% Eu | 1.73% | 0.89% | 0.25% |
| $Rb(Sr,Ba)_2I_5$:5 mol% Eu | 0.13% | 0.10% | 0.09% |
| $SrI_2$:Eu | 0.27% | 0.25% | 0.19% |
| $CdWO_4$ | 0.16% | 0.09% | 0.04% |

# CHAPTER 6 $A_4BX_6$ COMPOSITIONS

Sections of this chapter were originally published in the following peer-reviewed journal article:

- **K. S. Pestovich**, L. Stand, E. van Loef, C. L. Melcher and M. Zhuravleva, "Crystal Growth and Characterization of Europium-Doped Rubidium Calcium Bromide Scintillators," in *IEEE Transactions on Nuclear Science*, vol. 70, no. 7, p. 1370-1377 (2023) © 2023 IEEE.

This chapter focuses on two new $A_4BX_6$ scintillators, $Rb_4CaBr_6$ and $Rb_4CaI_6$, doped with $Eu^{2+}$ and $Yb^{2+}$. While their phase diagrams and crystallographic data are available in literature, this is the first report of bulk crystal growth from the melt (Ø7 mm) and the physical and scintillation properties of both compositions [101, 214].

Both $Rb_4CaBr_6$ and $Rb_4CaI_6$ crystallize in a trigonal space group (R-3c), with moderate densities of 3.46 and 3.73 g/cc, respectively. The effective atomic number of $Rb_4CaBr_6$ is 35, and that of $Rb_4CaI_6$ is 49. Doping $Yb^{2+}$ is favorable for uniformity, due to the better match in ionic radius (1.02 Å) to $Ca^{2+}$ (1.00 Å) over that of $Eu^{2+}$ (1.17 Å) for a coordination number of 6 [104]. Their slightly peritectic melt behavior and resulting phase impurities (RbBr, RbI) limited the crystal transparency (< 40% transmittance).

Both crystals had high scintillation performance (**Table 11**). For $Rb_4CaBr_6$, the highest light yield of 71,000 ph/MeV and energy resolution of 6.9% at 662 keV was achieved with 9 mol% Eu doping. However, the undoped and Yb-doped crystals had low light yields (~1,500 ph/MeV) and high afterglow. The highest light yield for $Rb_4CaI_6$ was 70,000 ph/MeV (5 mol% Eu), and the lowest energy resolution was 4.6% at 662 keV (9 mol% Eu). Undoped $Rb_4CaI_6$ had a moderate light yield of 19,000 ph/MeV with energy resolution of 7.9%. Ytterbium-doping was promising in $Rb_4CaI_6$, resulting in a light yield of 49,500 ph/MeV, energy resolution of 4.5% at 662 keV, and an X-ray afterglow lower than CsI:Tl. With dopant-level concentrations of ytterbium, the spin-allowed transition was the dominant radioluminescence emission. As ytterbium concentration increased to 50% and 100%, the spin-forbidden transition dominated.

One possible drawback of $Rb_4BX_6$ was their higher intrinsic radioactive background compared to compositions with different stoichiometries due to their higher concentration of Rb-87. For example, the specific activity of $RbCaBr_3$:Eu 5% was calculated to be 680 Bq/cc and that of $Rb_4CaBr_6$:Eu was 1,184 Bq/cc.

**Table 11.** Properties of $A_4BX_6$ Scintillators

| Scintillator | Density (g/cc) | $Z_{eff}$ | RL $\lambda_{max}$ (nm) | Light Yield (ph/MeV) | Energy Res. (662 keV) | Scintillation Decay (μs) |
|---|---|---|---|---|---|---|
| $Rb_4CaBr_6$ ($E_g$ = 5.4 eV) | 3.46 | 35 | ~420 | 1,300 | - | Not measured |
| $Rb_4CaBr_6$:3% Eu | | | 455 | 21,000 | 7.7% | 2.07 (4%) 8.13 (26%) |
| $Rb_4CaBr_6$:7% Eu | | | 456 | 63,000 | 7.5% | 2.77 (91%) 7.56 (9%) |
| $Rb_4CaBr_6$:9% Eu | | | 457 | 71,000 | 6.9% | 2.83 (79%) 8.52 (21%) |
| $Rb_4CaBr_6$:1% Yb | | | 458 | 1,500 | 33% | Not measured |
| $Rb_4CaI_6$ ($E_g$ = 4.8 eV) | 3.73 | 49 | ~520 | 19,000 | 7.9% | 0.13 (24%), 0.27 (76%) |
| $Rb_4CaI_6$: 3% Eu | | | 470 | 50,000 | 6.3% | 0.25 (5%), 1.91 (95%) |
| $Rb_4CaI_6$: 5% Eu | | | 476 | 70,000 | 5.0% | 0.23 (12%), 1.96 (88%) |
| $Rb_4CaI_6$:7% Eu | | | 477 | 66,000 | 4.8% | 0.34 (4%), 1.9 (96%) |
| $Rb_4CaI_6$:9% Eu | | | 475 | 65.000 | 4.6% | 0.31 (4%), 2.58 (96%) |
| $Rb_4CaI_6$:0.5 % Yb | | | 460 | 35,000 | 5.4% | 0.198 (10%) 1.96 (90%) |
| $Rb_4CaI_6$:1 % Yb | | | 460 | 49,500 | 4.5% | 0.16 (2%), 2.5 (98%) |
| $Rb_4CaI_6$:50 % Yb | 4.2 | 53 | 490 | 2,300 | 16% | Not measured |
| $Rb_4YbI_6$ | | | 490 | 1,500 | 34% | Not measured |

Samples were ~Ø7, 2-4 mm in size.

Crystal structure, *Space group*: Trigonal. *R-3c*

$Z_{eff}$ calculated using the equation by Murty [8].

## 6.1 Rubidium Calcium Bromide with $Eu^{2+}$ and $Yb^{2+}$ Dopants ($Rb_4CaBr_6$)

Although the RbBr-$CaBr_2$ phase diagram shows two compounds, $RbCaBr_3$ and $Rb_4CaBr_6$, the crystal growth and scintillation properties of only $RbCaBr_3$:Eu have been reported previously [101]. In this work, $Rb_4CaBr_6$:Eu was grown from the melt for the first time. Physical properties, including phase formation and hygroscopicity, and the scintillation and luminescence properties were evaluated. The undoped crystal, and crystals doped with $Eu^{2+}$ and $Yb^{2+}$ were grown. Some discussion relates to the results presented in **Chapter 4, section 4.1** on $RbCaBr_3$ crystals.

$Rb_4CaBr_6$ crystals Ø7 mm in size are shown in **Figure 50**. They were grown with a translation rate of 0.5 mm/hr. The growth furnace set points were 680/565/465°C, and the crystals were cooled over 100 hours. The europium-doped crystals were translucent and slightly yellow in color with bright blue luminescence under UV light. While the crystals were transparent after growth, they became translucent while cooling to room temperature, likely the result of a RbBr phase impurity. Additionally, cracking in the crystals seemed to increase slightly with increased europium dopant concentration. While the ytterbium-doped and undoped $Rb_4CaBr_6$ crystals had greater transparency, they also had significant cracking. Under UV light, the capillary of the Yb-doped crystal was bright blue, while the rest of the boule was dim, likely indicating poor incorporation of $Yb^{2+}$ into the boule. The undoped crystal had a dim purple-blue luminescence under UV light.

The quality of $Rb_4CaBr_6$ crystals was sensitive to growth rate and europium concentration. As shown in **Figure 51**, a crystal grown with a faster translation rate of 1 mm/hr had poor uniformity and decreased transparency compared to crystals grown at 0.5 mm/hr. The measured optical transmittance of an ~2 mm thick sample from the crystal grown at 1 mm/hr was ~10%. In comparison, the optical transmittance of the crystals grown at 0.5 mm/hr was 40-60%. The position and shape of the 662 keV photopeak varied significantly from the seed end to the tail end of the crystal. In this case, asymmetry of the photopeak may indicate mixed phases in the crystal. The sample from the tail end had the highest light yield and most symmetric photopeak.

The optical transmittance of the undoped crystal was slightly lower than the europium-doped crystals, as shown in **Figure 52**. It was ~20% from 400-800 nm. The band gap determined from the Tauc plot was 5.4 eV.

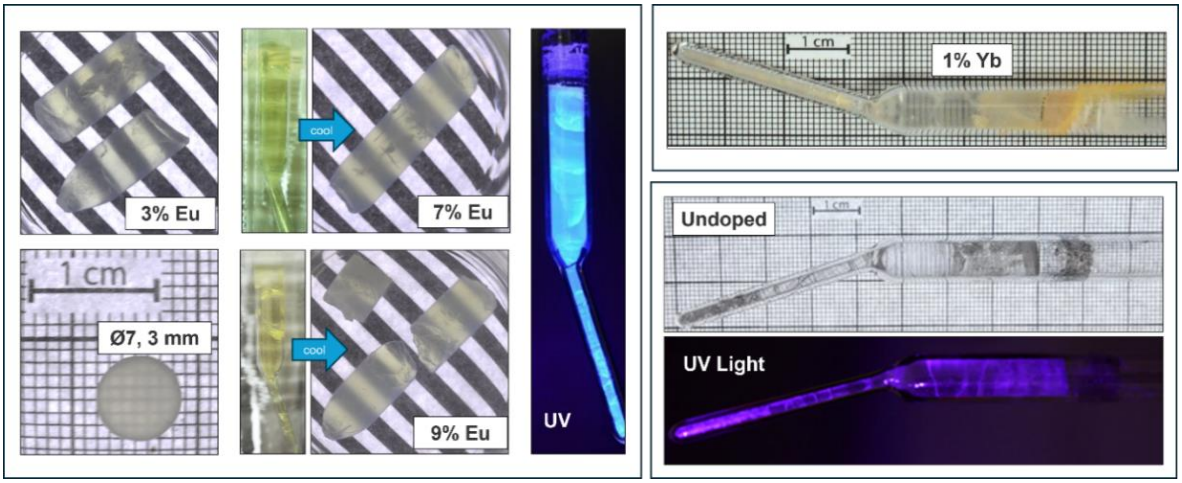


**Figure 50.** $Rb_4CaBr_6$ crystals grown in a Ø7 mm size at 0.5 mm/hr.

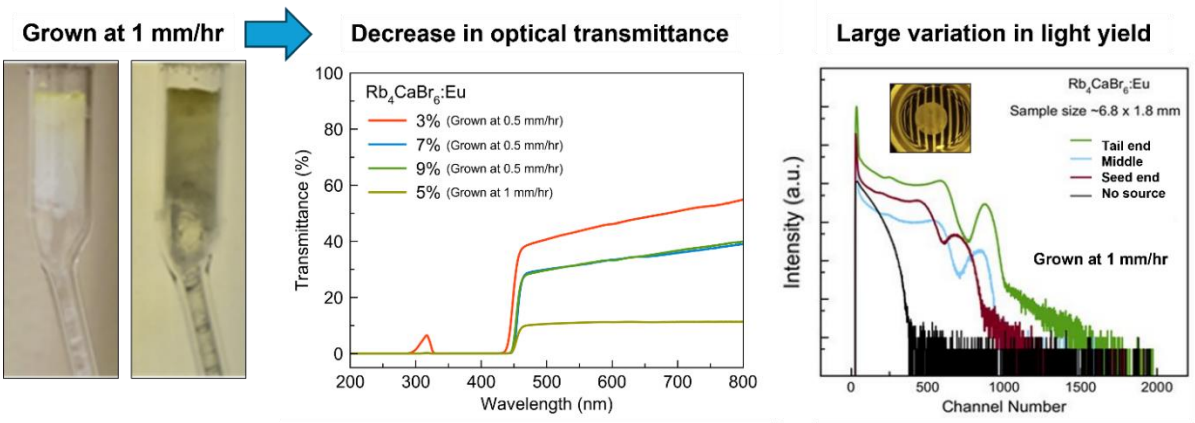


**Figure 51.** $Rb_4CaBr_6$:Eu 5 mol% crystal grown at 1 mm/hr shows decreased transparency and poor uniformity compared to crystals grown at 0.5 mm/hr. Optical transmittance improved with lower europium concentrations.

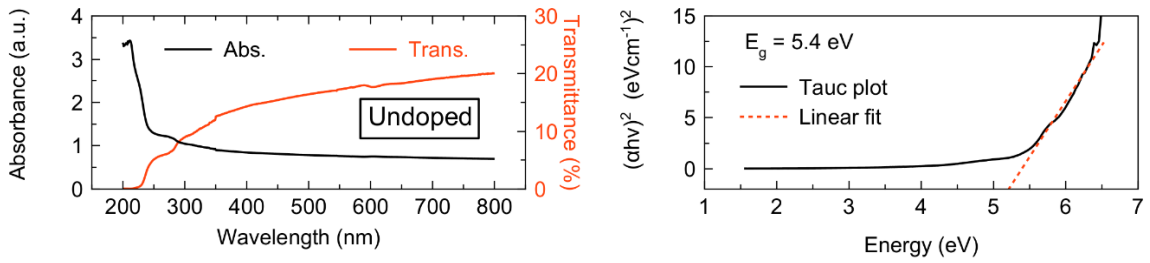


**Figure 52**. Optical absorbance and transmittance of $Rb_4CaBr_6$ and the Tauc plot

Rietveld refinements began with room temperature RbBr and $Rb_4CaBr_6$ structures reported in the Inorganic Solid Phases SpringerMaterials database [215, 216]. Results of Rietveld refinements are plotted in **Figure 53A**. The broad peak located 15-25° is from the Kapton film and was included in the background of the refinement. A Goodness of Fit (GOF) of 2.50 was achieved. The crystals contained both $Rb_4CaBr_6$ (trigonal, *R-3hc*) and RbBr (cubic, *Fm-3m*) phases. The RbBr phase impurity is likely responsible for the translucency of the crystals.

Crystal structure projections produced with VESTA from the refined XRD patterns are in **Figure 53B** [112]. $Rb_4CaBr_6$ contains isolated $[CaBr_6]^{4-}$ octahedra and two distinct $RbBr_n$ polyhedra (n = coordination number), which are a $[RbBr_6]^{5-}$ trigonal prism and a $[RbBr_8]^{7-}$ square antiprism. This structure is similar to other "zero-dimensional" metal halide perovskite scintillators [57, 59]. When comparing the $[CaBr_6]^{4-}$ octahedra both compounds, it was found that the average bond length was 0.0352 Å larger in $RbCaBr_3$ than for $Rb_4CaBr_6$, and the resulting polyhedral volume was larger by 1.1688 $Å^3$.

Heat flow curves from DSC measurements are shown in **Figure 53C**. $Rb_4CaBr_6$ had a broad endothermic peak seen on heating, followed by a low intensity exothermic peak and a high intensity exothermic peak with a temperature difference of 15°C. This behavior is consistent with phase formation behavior indicated by the phase diagram, in which $Rb_4CaBr_6$ was reported to have a peritectic point that lies close to the liquidus [101]. The structure refinement and melt behavior are consistent with several other crystals in the $A_4BX_6$ family [62, 217].

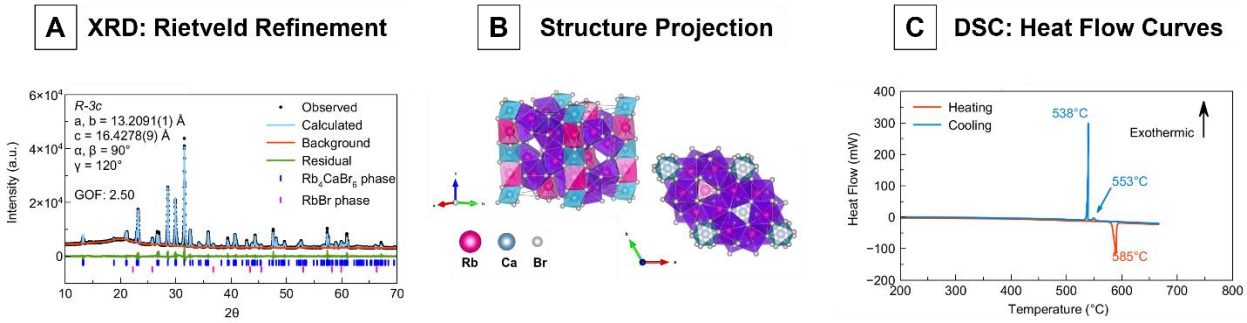


**Figure 53.** A) Powder XRD Rietveld refinement, B) Structure projection and C) DSC heat flow curves for $Rb_4CaBr_6$.

Moisture sorption curves are shown in **Figure 54A**. The inset images show the samples after ~4.5 hours of moisture exposure at 25°C and 40% relative humidity. $RbCaBr_3$ absorbed nearly twice the amount of moisture (47% increase in weight) as $Rb_4CaBr_6$ did (21% increase in weight). $RbCaBr_3$ was also completely deliquescent, while $Rb_4CaBr_6$ was primarily degraded on the surface. One possible reason for the difference in the hygroscopicity of these two compositions could be that the greater bond lengths, and therefore, more open structure of $RbCaBr_3$ could make it more susceptible to moisture absorption.

Pulse height spectra collected under ambient conditions over time (~50% relative humidity, temperature ~20°C) are plotted in **Figure 54B**. The relative light yield over time was compared based on the position of the 662 keV photopeak in the pulse height spectra. The spectra were acquired for the same pre-set amount of time. The light yield of a $Rb_4CaBr_6$:7 mol% Eu crystal remained fairly stable for 6 hours of exposure to ambient conditions. At 6 hours, the counts collected began to decrease, and by 10 hours, the counts under the curve decreased significantly. One artifact in this measurement comes from using a quartz housing for the initial measurement. There was a very slight increase in the position of the photopeak between the initial measurement and the measurement after 1 hour. This was most likely because of better light collection when the crystal was directly coupled to the PMT.

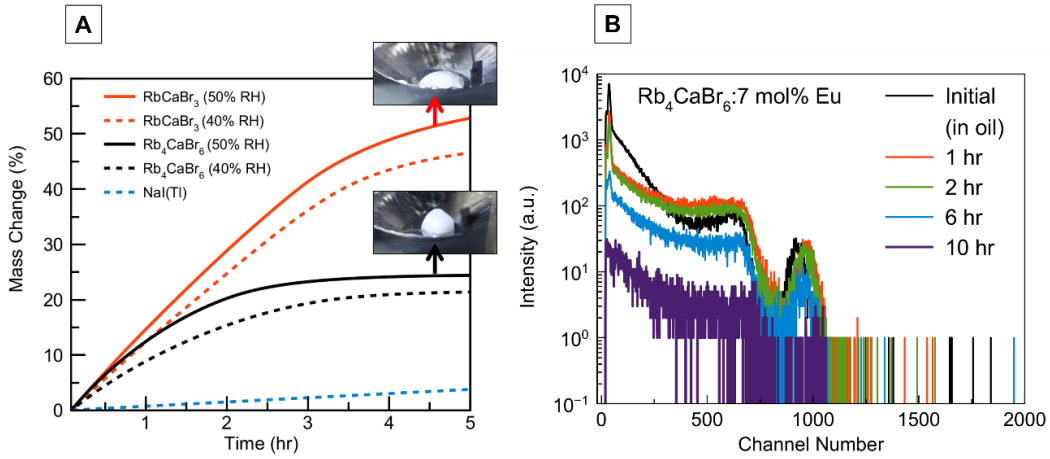


**Figure 54.** A) Dynamic Vapor Sorption (DVS) curves and B) pulse height spectra acquired under ambient conditions for $Rb_4CaBr_6$. The inset figures show the sample during the DVS measurement.

As shown in **Figure 55**, photoluminescence revealed an increase in self-absorption with increasing amounts of $Eu^{2+}$ dopant concentration, evident from increasing overlap in emission and excitation bands. This trend is consistent with that previously observed for other $Eu^{2+}$ dopant concentration studies in halides [74, 80, 218, 219]. Peak radioluminescence emission wavelengths were approximately 455 nm for $Rb_4CaBr_6$:Eu crystals with a continuous redshift of the $Eu^{2+}$ $4f^65d^1$-$4f^7$ emission peak with increasing $Eu^{2+}$ concentration. In comparison, the emission of $RbCaBr_3$:Eu was 435 nm. The larger $[CaBr_6]^{4-}$ octahedron in $RbCaBr_3$:Eu could cause less crystal field splitting than in $Rb_4CaBr_6$:Eu, resulting in a shorter emission wavelength [144, 220].

The radioluminescence of $Rb_4CaBr_6$ consisted of a narrow peak centered at 458 nm, with a low intensity peak near 320 nm and a broad shoulder from 500-600 nm. There was a minor difference between emissions from seed end to tail end, with the 458 nm peak becoming more prominent than the other features at the tail end of the boule.

The radioluminescence of $Rb_4CaBr_6$:Yb primarily consisted of a single, narrow peak centered at 458 nm; however, there was a significant difference between the seed end and tail end of the crystal. The sample from the seed end had pronounced shoulders to the left and the right of the peak. The undoped $Rb_4CaBr_6$ crystal had a broad radioluminescence emission spanning ~350-700 nm centered near 430 nm.

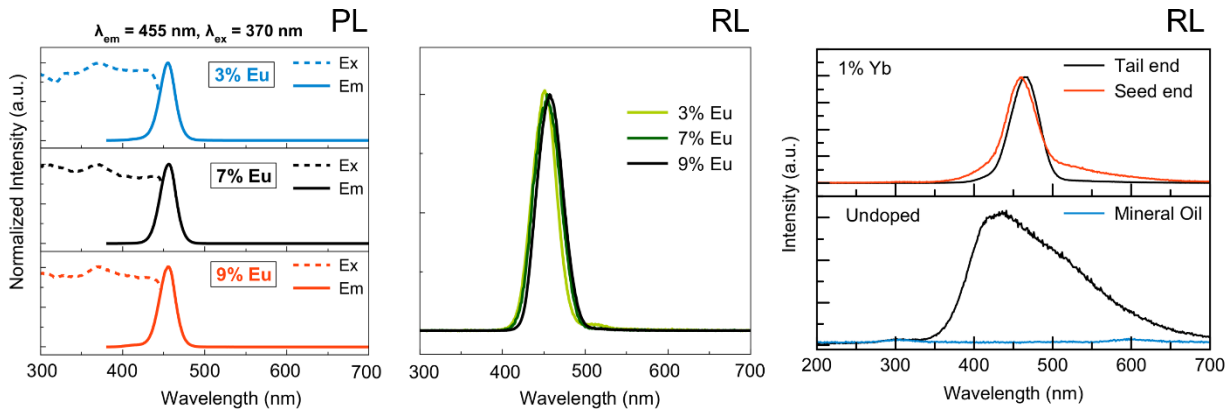


**Figure 55.** Photoluminescence and radioluminescence of $Rb_4CaBr_6$.

Pulse height spectra measured with $Rb_4CaBr_6$ crystals are shown in **Figure 56**. Crystals doped with europium had high light yield and energy resolution, which improved with increased europium concentration. There was some difference between the performance between the seed end and tail end of each boule. The light yield of $Rb_4CaBr_6$:Eu increased significantly (~219%) between 3% Eu and 7% Eu doping and slightly (~6%) between 7% Eu and 9% Eu doping. Despite the high light yield of $Rb_4CaBr_6$:Eu, its energy resolution may have been hindered by the RbBr phase impurity and associated translucency of the crystals. The energy resolution was 7.7%, 7.5% and 6.9% at 662 keV for crystals doped with 3, 7, and 9 mol%, respectively.

The highest light yield of $Rb_4CaBr_6$:Eu was about 65% higher than that of $RbCaBr_3$:Eu, possibly indicating that structural dimensionality of metal halide perovskites could play a role in light yield. In comparison, the light yield of zero-dimensional $Cs_4EuI_6$ was 120% higher than three-dimensional $CsEuI_3$, and $Cs_4EuBr_6$ was 255% higher than $CsEuBr_3$ [50, 52, 63]. The zero-dimensional $A_4BX_6$ structure results in shorter bond length and higher bond strength, as well as larger band gap and strong exciton localization [48, 49]. That being said, the band gaps determined by the Tauc method were similar.

In contrast with europium-doping, ytterbium-doping of $Rb_4CaBr_6$ did not produce desireable performance. It had a light yield of approximately 1,500 ph/MeV and energy resolution of approximately 33% at 662 keV. This was similar to the light yield of the undoped crystal, which was 1,300 ph/MeV, although the photopeak was not well-defined.

The scintillation decay time profiles measured for $Rb_4CaBr_6$:Eu are shown in **Figure 57A.** Decay time of the Yb-doped and undoped crystals were not measured. The scintillation decay time constants for $Rb_4CaBr_6$:Eu were determined from a two-component exponential decay. Scintillation decay time increased with increasing dopant concentration. The primary decay component (> 74%) for $Rb_4CaBr_6$:Eu increased from 2.07 to 2.83 μs across the dopant ranges studied. A second long component exists for $Rb_4CaBr_6$:Eu, which is around 8 μs.

X-ray afterglow is plotted in **Figure 57B.** For crystals doped with europium, afterglow improved with increasing dopant concentration. Notably, these improvements in afterglow mirrored increases in light yield observed for different dopant concentrations within each matrix. In contrast, the crystal doped with ytterbium had very high afterglow. Additionally, this afterglow was visible by eye when exciting the crystal with a UV lamp.

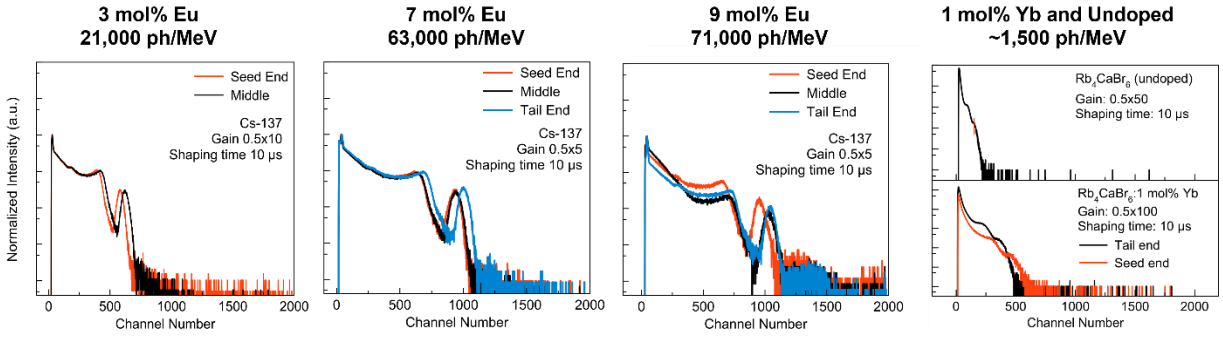


**Figure 56.** Pulse height spectra (Cs-137) measured with $Rb_4CaBr_6$ crystals, showing differences between the seed end and tail end of the crystals.

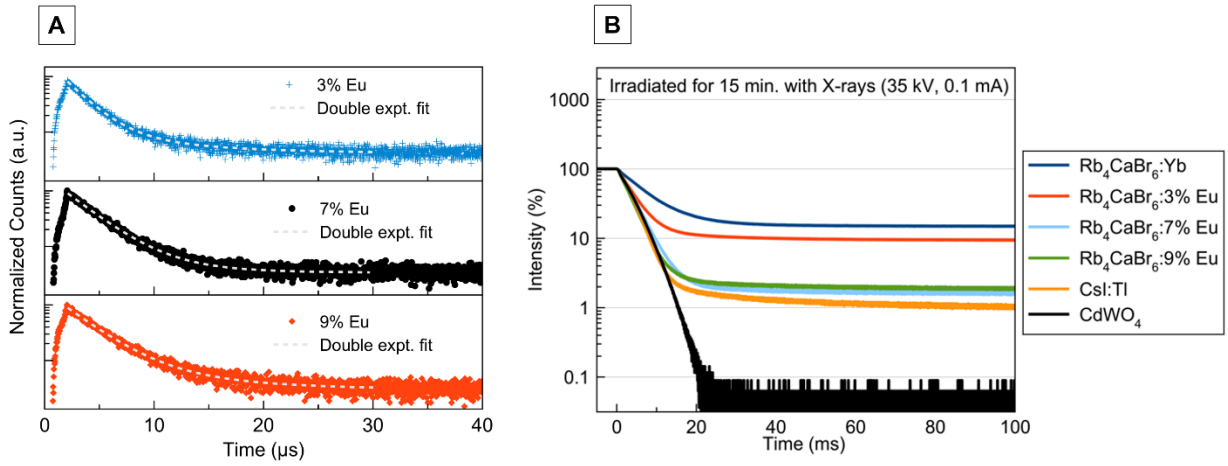


**Figure 57.** A) Scintillation decay time profiles and B) X-ray afterglow of $Rb_4CaBr_6$ crystals.

## 6.2 Rubidium Calcium Iodide with $Eu^{2+}$ and $Yb^{2+}$ Dopants ($Rb_4CaI_6$)

As discussed, inorganic zero-dimensional halide perovskite scintillators of the family $A_4BX_6$ (A = Cs, B = Cs, Sr, Eu, or Yb, X = Br, I) have demonstrated promise for gamma spectroscopy applications, owing to their high light yield and excellent energy resolution [57-59, 221-223]. One example is $Cs_4CaI_6$:Eu 7%, which had a light yield of 69,000 ph/MeV and energy resolution of 3.6% at 662 keV [77]. Incremental substitutions of $Rb^+$ into this matrix were successful, yielding a new scintillator $Cs_3RbCaI_6$:Eu 7 mol% with an even higher light yield of 75,000 ph/MeV and improved energy resolution of 3.3% at 662 keV [62].

$Rb_4CaI_6$ has not yet been explored as a scintillator. This composition is reported to have a peritectic point at 544°C and a trigonal crystal structure (R-3c,167) with a density of 3.73 g/cc and effective atomic number of 49 [214]. While the peritectic nature may prove challenge for growth of high quality crystals, the slightly higher density and effective atomic number are an advantage over the similar composition also studied in this work, $Rb_4CaBr_6$.

To explore the potential of $Rb_4CaI_6$ as a scintillator, Ø7 mm size crystals with different europium concentrations (0, 3, 5, 7, 9 mol%) and ytterbium concentrations (0.5, 1, 50, 100 mol%) were grown via the Vertical Bridgman method. The motivation for studying higher concentrations of ytterbium is because $Rb_4YbI_6$ is isostructural with $Rb_4CaI_6$ but has a higher density of 4.2 g/cc and effective atomic number of 53 [224].

The crystals' physical, luminescence, and scintillation properties were evaluated. Based on the high light yield of $Rb_4CaI_6$:Eu 5%, a Ø22 mm crystal was grown as an initial investigation into scale up of crystal growth, which is presented in **Chapter 7**.

The crystals were grown with a translation rate of 0.5 mm/hr and cooled over 100 hours. Similar to $Rb_4CaBr_6$, the $Rb_4CaI_6$ crystals were transparent prior to cooling, but they each became translucent during cooling. The europium-doped crystals were green-yellow in color, the intensity of which increased with increasing dopant concentration. For high dopant concentrations (7, 9 mol%), the crystals cracked when extracted from their growth ampoules. The crystals doped with ytterbium had a slightly yellow color, which became strong when substituting large amounts of calcium with ytterbium (50 mol%, 100 mol%). Compared to the europium-doped crystals, small concentrations of ytterbium dopant resulted in crystals with improved optical transparency by eye.

The grown crystals are shown in **Figure 58**. Rietveld refinement results of powder X-ray diffraction (XRD) and heat flow curves acquired from Differential Scanning Calorimetry (DSC) measurements are plotted in **Figure 59**. The refinement was done using crystallographic data reported in the SpringerMaterials database for $Rb_4CaI_6$ and RbI [225, 226]. The goodness of fit for the refinement was ~6. The XRD refinement showed a RbI phase impurity. However, one impurity peak at approximately 50 degrees 2-theta was not matched to these patterns and did not seem to correspond to $RbCaI_3$. In the DSC curves, a sharp exothermic/crystallization peak was observed at 435°C, and three endothermic peaks were observed at 470°C, 509°C, and 533°C. The RbI-$CaI_2$ phase diagram by Siefert, et al. reports a peritectic point for $Rb_4CaI_6$ at 544°C, which lies close to the liquidus, in addition to two tie lines at 505°C and 469°C [214].

DVS moisture sorption curves and pulse height spectra acquired under ambient conditions are in **Figure 60**. Moisture sorption curves for $SrI_2$:Eu and NaI:Tl are included for comparison. $Rb_4CaI_6$ absorbed moisture at a higher rate than the two reference scintillators, but the moisture sorption appeared to saturate after about 2 hours of exposure. The final change in mass after 5 hours was ~17% for both $Rb_4CaI_6$ and $SrI_2$:Eu. Compared to the undoped sample, a sample with 5% Eu had a slightly lower change in mass (~15%).

To investigate how this moisture absorption affected scintillation performance, pulse height spectra were acquired for a $Rb_4CaI_6$:Eu 7% single crystal sample over time under ambient conditions. Although moisture sorption saturated after ~2 hours in the DVS curves, the spectroscopic quality of the scintillator continued to degrade over time. After 1 hour of exposure, it appeared that two separate 662 keV photopeaks were forming, which became slightly more distinct after 2 hours. This is possibly from a phase impurity absorbing moisture in addition to the desired $Rb_4CaI_6$ phase.

**Figure 61** shows the optical absorbance and transmittance, along with the Tauc plot made from absorbance data. Based on the Tauc plot from absorbance data, $Rb_4CaI_6$ has a direct band gap of 4.8 eV. Unfortunately, the optical transmittance of these crystals was very low. The undoped crystal had ~3% transmittance at high wavelengths, whereas $Rb_4CaI_6$:3% Eu had ~20% transmittance. This poor transparency is a limitation for this composition.

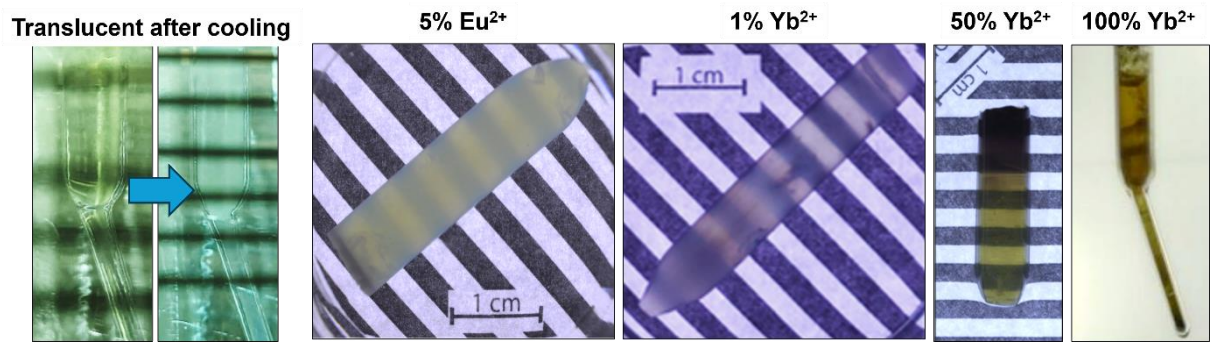


**Figure 58.** Ø7 mm $Rb_4CaI_6$ crystals in the transparent furnace and backlit after cooling.

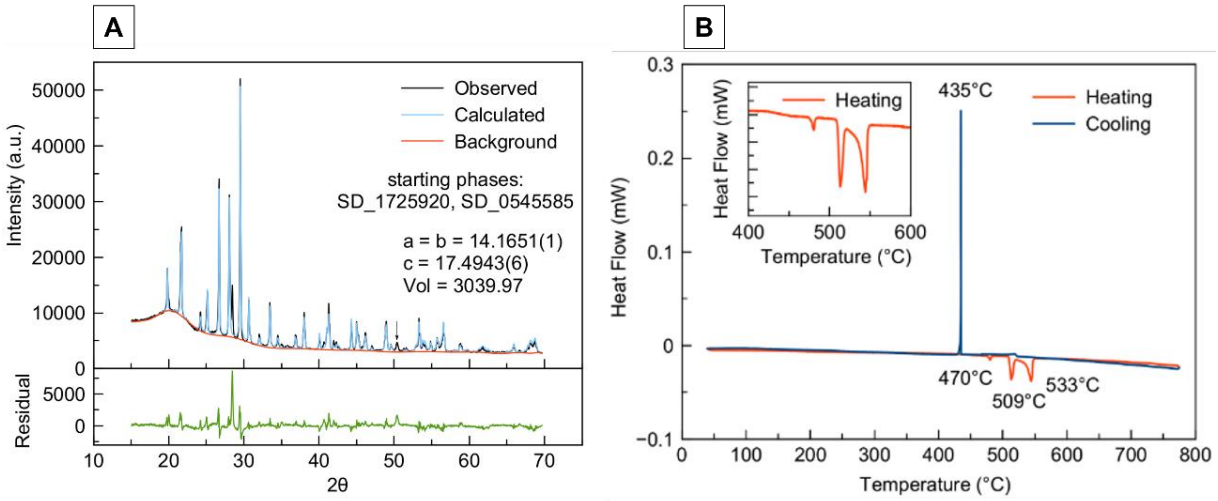


**Figure 59.** A) Powder XRD Rietveld refinement and B) DSC heat flow curves for $Rb_4CaI_6$.

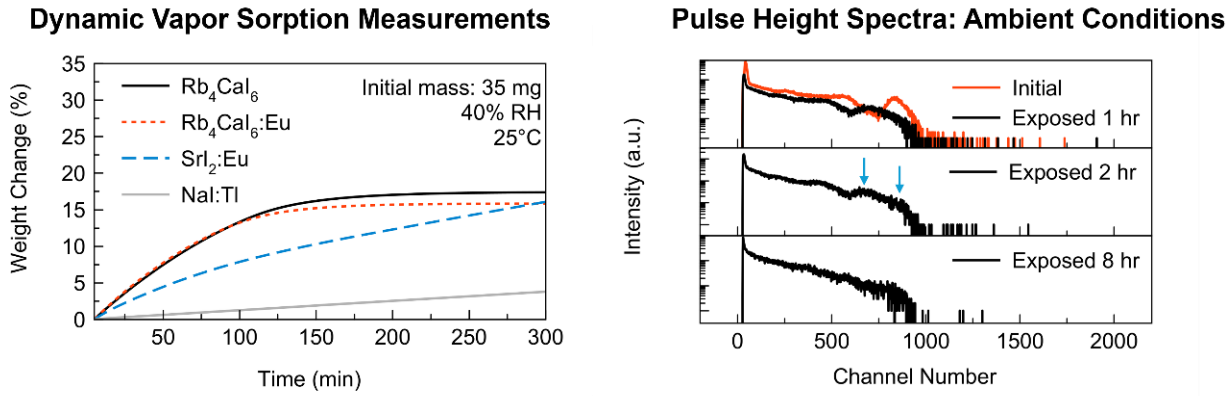


**Figure 60.** Hygroscopicity evaluation of $Rb_4CaI_6$: Dynamic Vapor Sorption measurements and pulse height spectra acquired under ambient conditions.

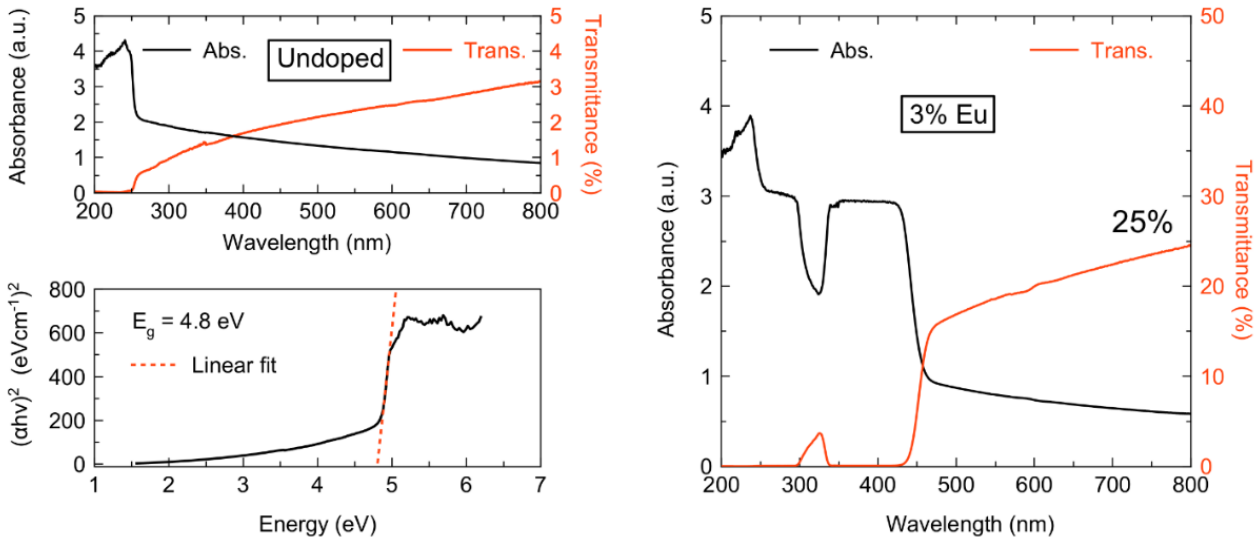


**Figure 61.** Optical absorbance and transmittance of $Rb_4CaI_6$, and the Tauc plot.

Photoluminescence excitation and emission and radioluminescence emission are shown in **Figure 62**. The photoluminescence and radioluminescence of the europium-doped crystal was consistent with the 5d → 4f electronic transition of divalent europium. There were several excitation bands overlapping from 250-440 nm, and the emission consisted of a single, symmetric peak centered around 465 nm. With increased europium concentration, the overlap of the excitation and emission bands increased, indicative of europium self-absorption. The crystals had narrow, symmetric radioluminescence emissions centered at 470 nm, which slightly redshifted to ~475 nm with increasing europium dopant concentration. The radioluminescence peak wavelength of $Rb_4CaI_6$:Eu is comparable to reported emission of $Cs_4CaI_6$:Eu, which was 466 nm [57, 77].

The photoluminescence and radioluminescence of $Rb_4CaI_6$:Yb showed both the spin-allowed and spin-forbidden transitions of divalent ytterbium, and the spin-allowed emission was dominant. This was similar to observations in $Cs_4CaI_6$:Yb [58]. The photoluminescence emission from the spin-allowed transition was centered around 447 nm, and the spin-forbidden emission was centered at ~482 nm. The emissions from the two different transitions were less-defined in $Rb_4CaI_6$:0.5 mol% Yb. The radioluminescence emission was centered at ~460 nm. There was a weak emission from ~530-700 nm in $Rb_4CaI_6$:0.5 mol% Yb, which was suppressed in the crystal doped with 1 mol% Yb. This emission may be related to the radioluminescence of the undoped crystal. Undoped $Rb_4CaI_6$ had a broad radioluminescence emission spanning from ~400 to 700 nm, with a peak intensity near 522 nm. With high concentrations of $Yb^{2+}$, 50% and 100%, the radioluminescence emission shifted to ~490 nm, indicating that the spin-forbidden transition became dominant.

Despite the low transparency of the crystals, $Rb_4CaI_6$:Eu had high light yields and energy resolutions. **Figure 63** compares the light yield and energy resolution of $Rb_4CaI_6$:Eu crystals with different dopant concentrations from 0% - 9% $Eu^{2+}$. Pulse height spectra from the seed end and the tail end of the boules were compared as well. The performance was generally uniform across each crystal, to a greater extent than seen in $Rb_4CaBr_6$.

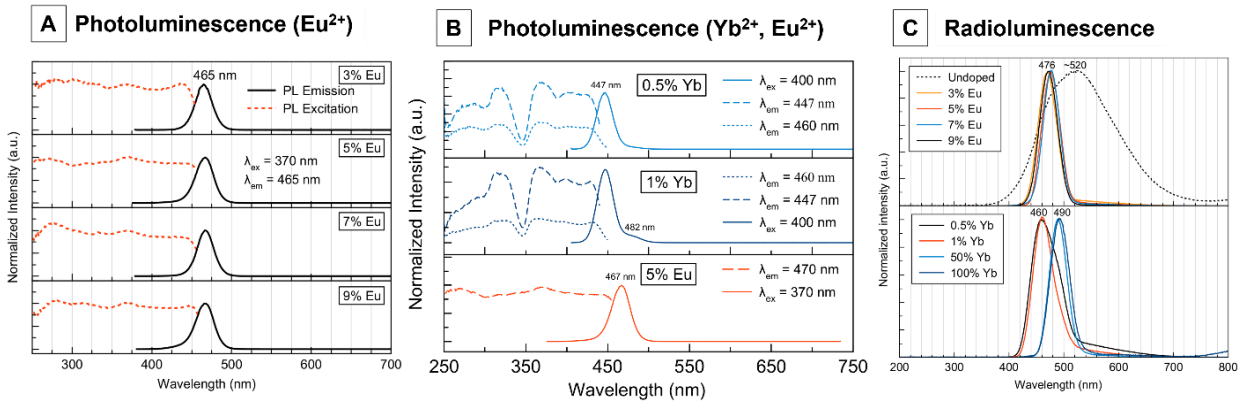


**Figure 62**. A-B) Photoluminescence and B) Radioluminescence of $Rb_4CaI_6$ crystals.

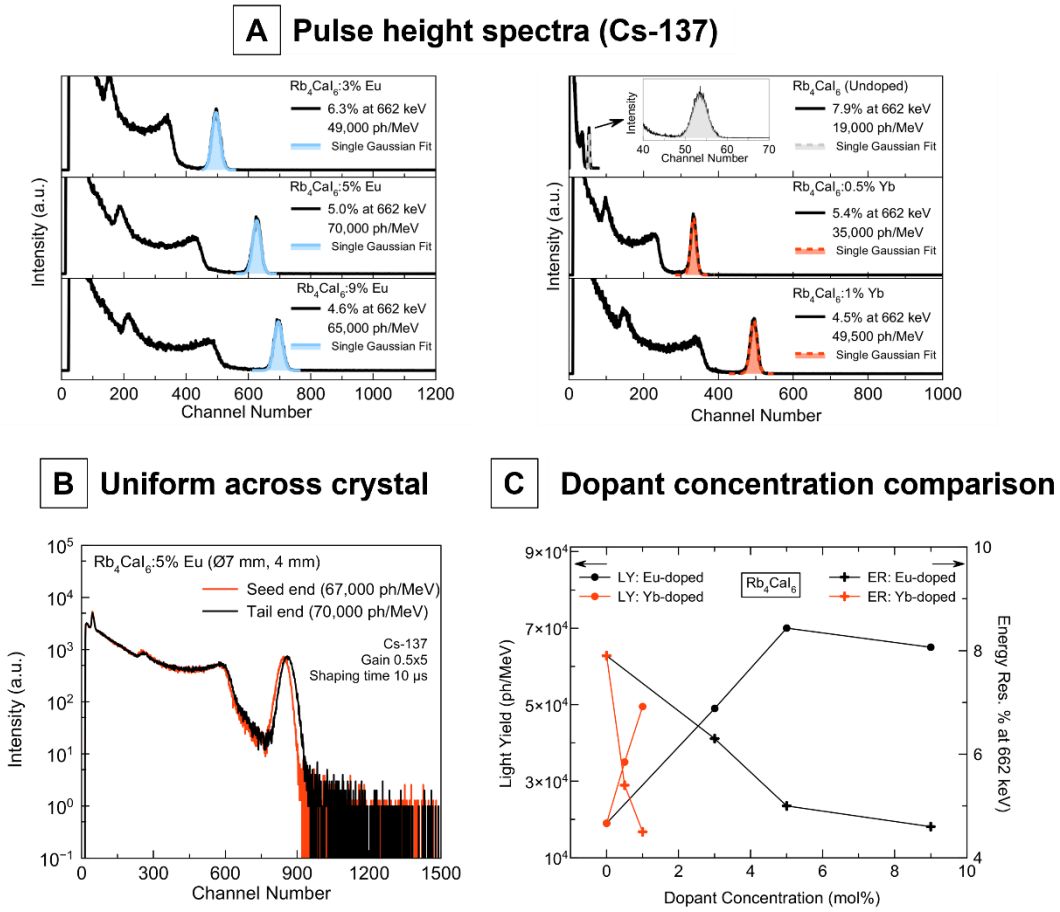


**Figure 63.** Light yield and energy resolution of $Rb_4CaI_6$ crystals.

The light yield and energy resolution of the undoped crystal was 19,000 ph/MeV and 7.9% at 662 keV. Doping with $Eu^{2+}$ increased both properties substantially, up to 70,000 ph/MeV and 5% at 662 keV for $Rb_4CaI_6$:5 mol% Eu. The ytterbium-doped crystals also had promising scintillation performance. The light yield and energy resolution of crystals doped with 0.5 mol% and 1 mol% were 35,000 ph/MeV and 5.4% and 49,500 ph/MeV and 4.5% at 662 keV, respectively. The light yield decreased with large concentrations of ytterbium (50 and 100%) to 2,800 and 1,500 ph/MeV. The energy resolutions were 16% and 34%, respectively. This performance is comparable to that reported for $Cs_4YbI_6$, which had a light yield of 2,700 ph/MeV and emission of 480 nm [60].

The scintillation decay profiles are shown in **Figure 64.** The scintillation decay time of undoped $Rb_4CaI_6$ had two components: 0.l3 µs (24%) and 0.27 µs (76%). Scintillation decay time of $Rb_4CaI_6$:Eu was best fit with a two component exponential fit, consisting of a minor fast component (~0.3 µs, ~5%) and a primary longer component (~2 µs, ~95%). The relative contributions of these components did not change significantly with dopant concentration. The fast component is similar to the primary decay of undoped $Rb_4CaI_6$. The longer component likely corresponds to the europium emission. This component tended to increase slightly with higher europium dopant concentrations, which is typically representative of europium self-absorption.

The scintillation decay time of $Rb_4CaI_6$:Yb crystals was also fit with two components, the first being 198 ns (10%) and 160 ns (2%) and the second being 1.96 µs (90%) and 2.5 µs (98%) for 0.5 mol% and 1 mol%, respectively. The fast component appears to be suppressed with the larger concentration of ytterbium, which is consistent with observations in $Cs_4CaI_6$:Yb [58].

The X-ray afterglow profiles are shown in **Figure 65**. Undoped $Rb_4CaI_6$ had high X-ray afterglow. However, this decreased significantly with the addition of either europium or ytterbium dopants. The X-ray afterglow intensities of all doped crystals were comparable to a commercial sample of CsI:Tl. Among the europium-doped crystals, the afterglow was slightly improved specifically for $Rb_4CaI_6$:3 mol% Eu. Ytterbium-doping led to slightly reduced afterglow. However, full substitution with ytterbium resulted in one of the lowest afterglows observed in this work. $Rb_4YbI_6$ had an afterglow intensity similar to $CdWO_4$.

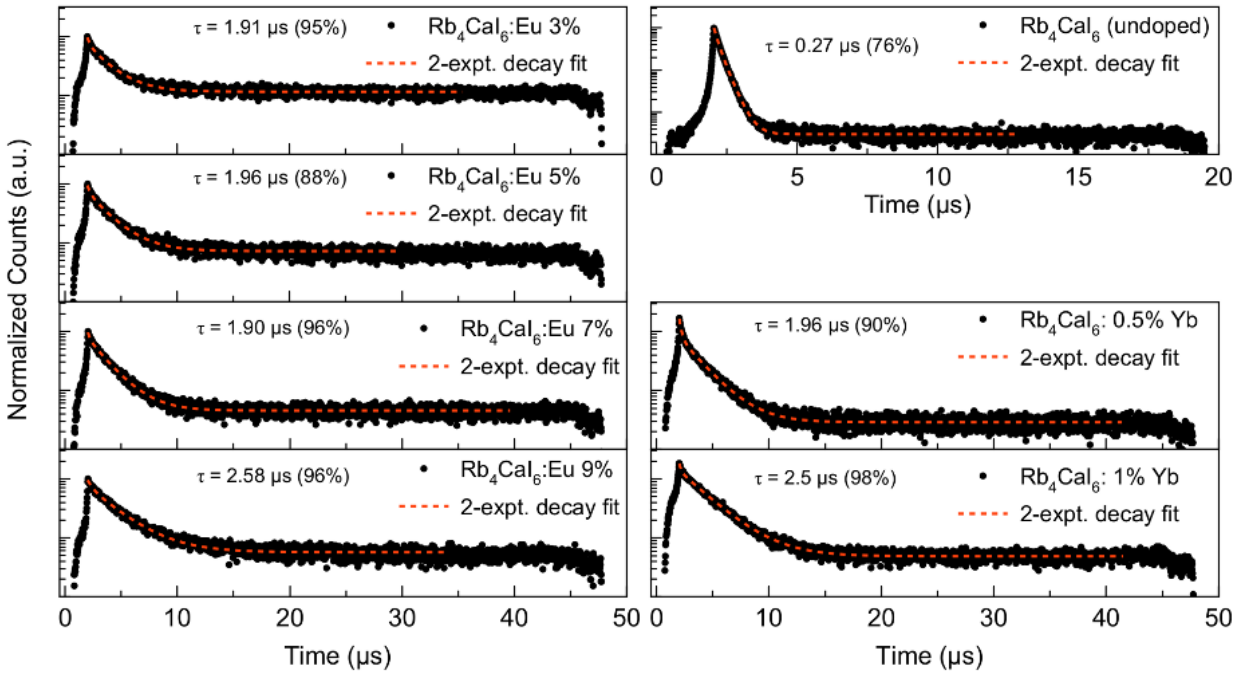


**Figure 64.** Scintillation decay profiles of $Rb_4CaI_6$ crystals.

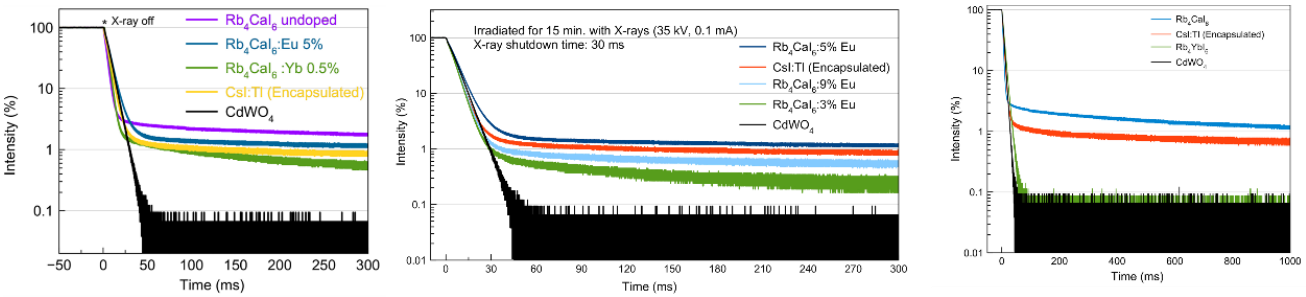


**Figure 65.** X-ray afterglow of $Rb_4CaI_6$ crystals.

# CHAPTER 7 SCALE UP OF CRYSTAL GROWTH

Sections of this chapter were originally published in the following peer-reviewed journal articles:

- **K. S. Pestovich**, L. Stand, E. van Loef, C. L. Melcher and M. Zhuravleva, "Crystal Growth of New High Light Yield Halide Perovskite Scintillator $RbSrI_3$," in *Journal of Crystal Growth*, vol. 627, p. 127540 (2024).
- **K. S. Pestovich**, L. Stand, E. van Loef, C. L. Melcher and M. Zhuravleva, "Crystal Growth and Characterization of Europium-Doped Rubidium Calcium Bromide Scintillators," in *IEEE Transactions on Nuclear Science*, vol. 70, no. 7, p. 1370-1377 (2023) © 2023 IEEE.
- **K. S. Pestovich**, M. Gillespie, L. Stand, C. L. Melcher, E. van Loef, M. Zhuravleva, "Crystal Growth Scale up and Stability of $RbSr_2X_5$:Eu Scintillators" in *Crystal Growth & Design.* Submitted for review.

While extensive research and development efforts focus on the discovery of new scintillators, an essential phase in a materials' initial development is to test their stability with regards to synthesis and performance. For real-world applications, large, uniform crystals are needed, and their synthesis and properties must be scalable. In this work, the crystal growth scale-up to Ø22 mm size was pursued for $RbCaBr_3$:Eu, $RbSrI_3$:Eu, $RbSr_2I_5$:Eu, $RbSr_2Br_5$:Eu, and $Rb_4CaI_6$:Eu. These compositions were selected based on melting behavior, density and effective atomic number, the crystal quality and scintillation properties observed in previous experiments (Ø7 mm), and the availability and quality of the raw materials. $RbCaBr_3$:Eu, $RbSrI_3$:Eu, $RbSr_2I_5$:Eu, $RbSr_2Br_5$:Eu all had excellent crystal quality and scintillation performance in Ø7 mm sizes. Additionally, $RbSrI_3$:Eu, $RbSr_2I_5$:Eu, and $Rb_4CaI_6$:Eu had relatively high densities and effective atomic numbers. Although $Rb_4CaI_6$:Eu was translucent in Ø7 mm sizes due to its peritectic nature, crystal growth in Ø22 mm size was still pursued to investigate stability. The high light yield of this composition warranted this investigation.

While the performance from other luminescent dopants (i.e., $Tl^+$, $Yb^{2+}$, $Ce^{3+}$) was investigated in other parts of this work, all of the Ø22 mm crystals were doped with $Eu^{2+}$ to maximize performance. However, in anticipation of europium self-absorption, the nominal europium concentration for Ø22 mm crystals was reduced from the optimal concentration in some cases.

In addition to the crystal growth experiments, several other investigations were conducted to support scale up. RbBr, RbI, and $CaBr_2$ raw materials were treated in an attempt to improve crystal quality and reduce the costs of the raw materials. High Temperature X-ray Diffraction (HTXRD) was done on $RbSrI_3$, $RbSr_2I_5$, and $RbSr_2Br_5$ to test for low temperature solid-solid phase transitions and determine the coefficients of thermal expansion. Additionally, a translation rate study on the growth of $RbSr_2I_5$:Eu was done up to 3.5 mm/hr.

As mentioned, scintillators containing rubidium have natural intrinsic radioactivity from Rb-87. As the crystal size increases, so do the background counts from Rb-87. While the intrinsic radioactivity was negligible when measuring small Ø7 mm crystals, the counts in pulse height spectra were significant when measuring Ø22 mm crystals. To illustrate this, pulse height spectra measured with and without a Cs-137 source are presented. Compositions with greater fraction of rubidium atoms, such as $Rb_4BX_6$, naturally had greater background counts.

The crystal quality and scintillation properties varied greatly among the different scintillator compositions grown in a Ø22 mm size. Their scintillation properties are summarized in **Table 12**. While the scintillation properties and crystal quality of $RbCaBr_3$:Eu were highly promising, the availability and cost of suitable raw materials and the relatively low density of this material weaken its practical appeal. $RbSrI_3$:Eu showed high scintillation properties and crystal quality in smaller sizes (Ø12 mm), but growth in a Ø22 mm diameter was challenging due to significant cracking. $RbSr_2Br_5$:Eu and $RbSr_2I_5$:Eu crystals had excellent quality and performance. Unfortunately, the density and effective atomic number of $RbSr_2Br_5$:Eu are relatively low, and the crystal quality is limited by the presence of microscopic bubble-like inclusions.

On the other hand, $RbSr_2I_5$:Eu was highly transparent and could be grown at fast translation rates up to 3.5 mm/hr. Finally, the peritectic composition $Rb_4CaI_6$:Eu was grown to investigate stability and scale up potential. The resulting crystal was opaque with moderate scintillation performance. Another drawback for $Rb_4CaI_6$ is its significant intrinsic radioactive background due to a higher Rb-87 concentration in comparison to other compositions with different stoichiometries. Overall, $RbSr_2I_5$:Eu was the most promising among the materials tested.

**Table 12.** Summary of Properties for 22 mm Crystals

| Scintillator | Size (mm) / Geometry | Light Yield (photons/MeV) | Energy Resolution at 662 keV | Scintillation Decay Time (μs) | Crystal Appearance |
|---|---|---|---|---|---|
| $RbCaBr_3$:5 mol% Eu | Ø22, 25 Cylinder | 23,000 | 11-19% | 4.9 (100%) | Highly transparent, colorless, cracks propagating from outside surface. |
| $RbSrI_3$:5 mol% Eu | Ø12, 10 Cylinder | 69,300 | 3.3% | 1.76 (100%) | Highly transparent, slightly yellow, cracking at last-to-freeze. |
| $RbSrI_3$:1 mol% Eu | Ø22, 35 | Not measured | | | Significantly cracked with small transparent areas. Slightly yellow. |
| $RbSr_2I_5$:1 mol% Eu | Ø22, 35 Cylinder with cone | 61,000 | 3.6% | 1.2 (70%), 6.6 (30%) | Highly transparent, colorless, little to no cracking. |
| $RbSr_2Br_5$:1 mol% Eu | Ø22, 35 Cylinder with cone | 46,000 | 5.3% | 1.2 (87%), 6.3 (13%) | Transparent, but hindered by microscopic bubbles. No cracking. |
| $Rb_4CaI_6$:5 mol% Eu | Ø22, 20 Cylinder with cone | 32,000 | 13% | 0.33 (3%), 3.8 (97%) | Opaque, yellow in color, cracking on the surface. |

## 7.1 Rubidium Calcium Bromide ($RbCaBr_3$:Eu)

### 7.1.1 *Crystal Growth of Ø22 mm $RbCaBr_3$:5 mol% Eu*

As discussed, $RbCaBr_3$ is congruently melting (737°C) with two structural phase transitions. Compared to growth of the Ø7 mm crystals of the same composition, the translation rate was reduced by half to 0.25 mm/hr and the cooling time was increased from 100 to 120 hours. The same furnace temperatures were used. As shown in **Figure 66**, the crystal was colorless and transparent, with some cracks that propagated from the tail end and last-to-freeze along the ampoule wall. It had uniform, bright blue luminescence under UV light.

A major difference between growth of 22 and 7 mm diameter crystals was the condition of the ampoule after growth. After growth of the 22 mm crystal, the quartz ampoule was brittle and white in color on the inner walls, which was attributed to corrosion from the raw materials. This was not observed for 7 mm crystals, likely due to the smaller volume of material as well as the significantly shorter growth time that limited how long the quartz was exposed to the material. Use of a carbon coated ampoule could likely improve this, as well as mitigate the cracks on the sides of the crystal. Despite the corrosion, the crystal was easily removed from the growth ampoule. For characterization of scintillation properties, a Ø22, 25 mm cylinder was cut and polished. Due to the high hygroscopicity of the crystal, it was polished inside of the glovebox.

### 7.1.2 *Scintillation Properties of Ø22 mm of $RbCaBr_3$:Eu*

The pulse height spectra and scintillation decay time profile of $RbCaBr_3$:Eu were negatively impacted by $Eu^{2+}$ self-absorption and crystal quality (**Figure 67**). The light yield of the Ø22, 25 mm cylinder was ~23,000 ph/MeV, approximately 14,000 ph/MeV lower than a Ø7 mm, 3 mm crystal. There were differences in the shape of the photopeak depending on which face of the crystal was coupled to the PMT, possibly indicating some dopant inhomogeneity in the crystal. The energy resolution increased from 11% at 662 keV to 19% between the two orientations.

The scintillation decay time consisted of a long single component of 4.9 microseconds, which was approximately double that of the small crystal, 2.3 microseconds. The effects of $Eu^{2+}$ self-absorption could have likely been mitigaed slightly by using a smaller dopant concentration. There was significant overlap between the photolumienence excitation and emission of small $RbCaBr_3$:Eu crystals doped with 5 mol% Eu, indicating a large degree of self-absorption.

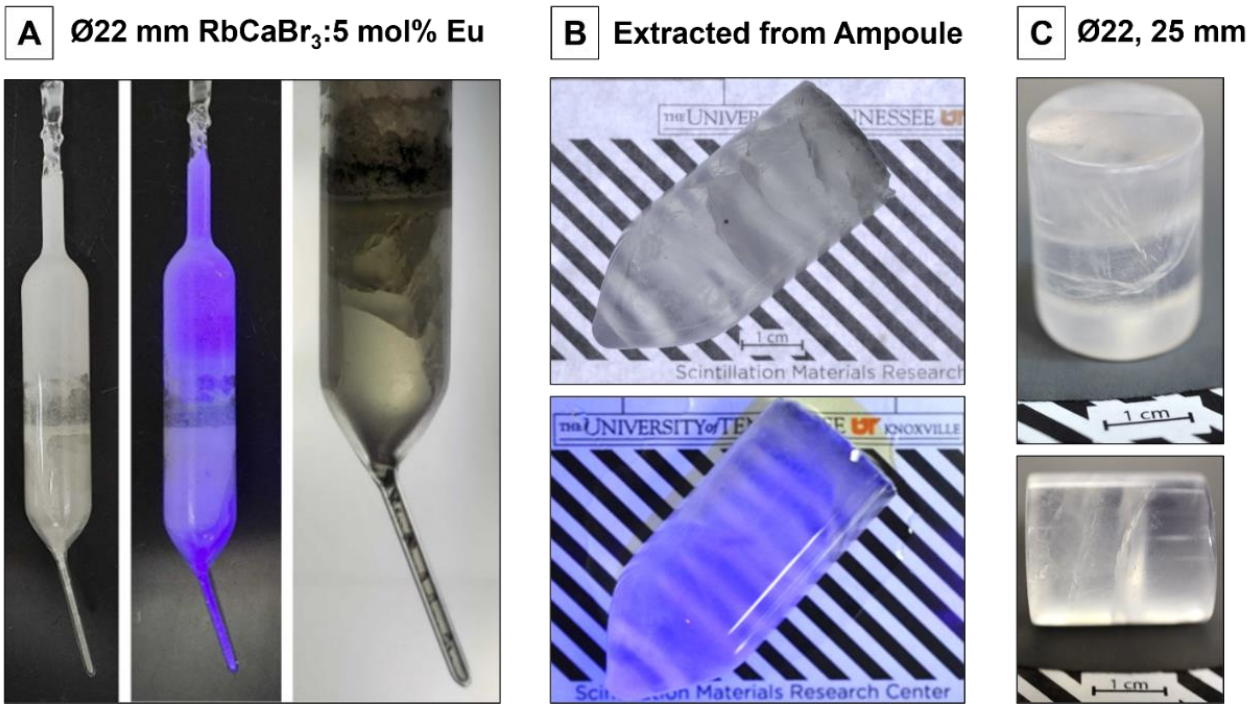


**Figure 66.** Growth of Ø22 mm $RbCaBr_3$:5 mol% Eu. A) shows crystal in ampoule, b) shows crystal extracted from ampoule, C) shows a cut and polished Ø22, 25 thick cylinder used for scintillation characterization.

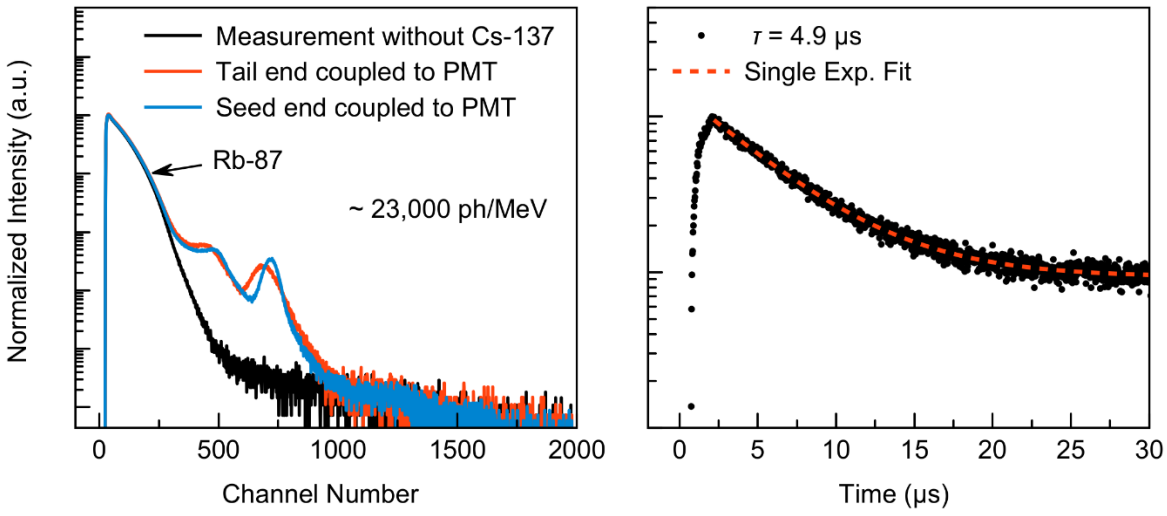


**Figure 67.** Light yield and scintillation decay time measured for a Ø22, 25 mm cylinder of $RbCaBr_3$:5 mol% Eu.

7.1.3 *Treatment of Raw Materials*

While this was a promising initial result, additional scale-up experiments were cost-prohibitive. The raw materials used for the experiment were $20-26 per gram, and at least 50 grams were needed for one crystal. As an alternative, in-house treatment of lower cost raw materials was pursued. A comparison of the raw materials is in **Table 13**. Since $EuBr_2$ was used in just dopant-level quantities, the greater concern was the main constituents of the crystal, RbBr and $CaBr_2$. Clear disadvantages of using the lower cost raw materials include an unknown concentration of unknown impurities (no certificate of analysis available), and possibly moisture or oxygen.

The RbBr raw material was treated via directional solidification. The material (10-100 g) was dried under vacuum in a carbon coated ampoule, heated above the melting point of RbBr, and then translated in a single pass through a controlled thermal gradient at 2-5 mm/hr in a Bridgman furnace. The translation rate was selected based on the size of the charge. After cooling to room temperature, the RbBr material was extracted from the ampoule and the last-to-freeze was removed and discarded. The remainder of the boule was crushed into small pieces using an agate mortar and pestle and stored in the glovebox for future use. This process was qualitatively successful and applied to many different crystal growth experiments and to the treatment of RbI raw material as well. The qualitative impact of RbBr raw materials treatment on the quality of a polycrystalline $Rb_4CaBr_6$ sample is shown in **Figure 68**. However, this method did not appear to work well for $CaBr_2$. It resulted in a dark grey boule that showed dark regions mixed in. The boule was hard and could not be crushed easily to use as raw material.

**Table 13.** Comparison of purity and cost of RbBr and $CaBr_2$ raw materials

| Material | Purity / Vendor / Description | Cost |
|---|---|---|
| RbBr | high purity (99.95%, APL) anhydrous beads | $26/g |
| RbBr | low-purity powder (99.8%, Alfa Aesar; 99.9% Thermo Fisher) treated in-house with a single pass in a Bridgman furnace | $3.45/g + ampoule |
| $CaBr_2$ | high purity anhydrous beads (99.995%, APL) | $20/g |
| $CaBr_2$ | low-purity (99.5%, Alfa Aesar) anhydrous powder treatment attempts with zone refining and melt-filtering | $1.78/g + ampoule |

Two other methods were attempted to treat the $CaBr_2$ raw material. First, zone refining at RMD was attempted. After drying under vacuum with heat tape, a charge of 75 grams was sealed inside of a thick quartz ampoule by sealing the ampoule with a thick plug. Unfortunately, on heating the ampoule in a tube furnace, the quartz of the ampoule failed. This was thought to be due to the large charge size compared the volume of the ampoule and corrosion of the raw material with the ampoule.

The second attempt at treating $CaBr_2$ was melt-filtering. A double chamber melt filtering ampoule with thick quartz tubing was designed. A quartz frit with a 160-250 micrometer porosity was used (**Figure 69**). At UT, a ~22 g charge was dried under vacuum and sealed. Then the ampoule was heated in a furnace to 800°C and allowed to dwell for several days before cooling to room temperature. The quartz ampoule experienced corrosion from the raw material and was very brittle after the experiment. Approximately 15 g of material could be extracted from the ampoule, while some was stuck and reacted with the quartz. The top of the quartz frit showed shiny, black flakes and the bottom of the frit showed solidified droplets of liquid.

A 12 mm diameter $RbCaBr_3$:5 mol% Eu crystal was grown using the treated RbBr and $CaBr_2$ raw materials (**Figure 70**). The crystal had a strong interaction with the quartz ampoule and some yellow coloration. Further treatment of the $CaBr_2$ raw material could have been pursued, including using multiple quartz frits of different porosities and improving the drying program.

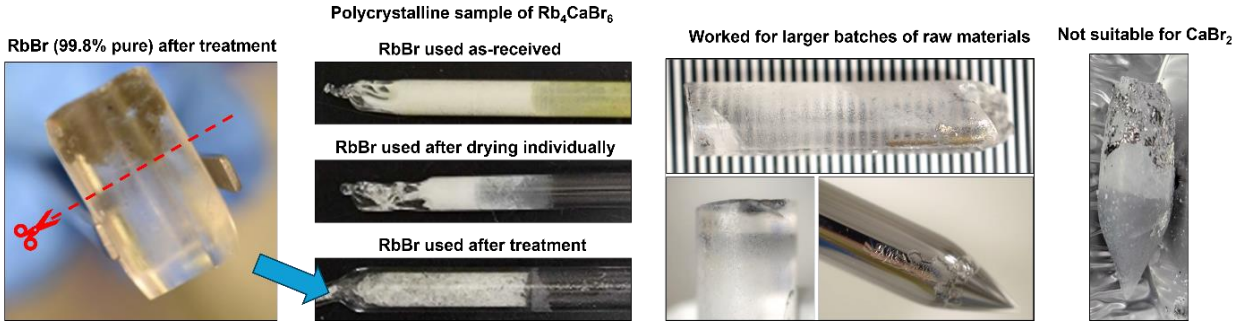


**Figure 68.** Treatment of RbBr by a single pass in a Bridgman furnace and its qualitative impact on polycrystalline $Rb_4CaBr_6$ samples. This method also worked for batches of 10-100 g of RbI and RbBr raw materials, though it did not seem to work well for $CaBr_2$.

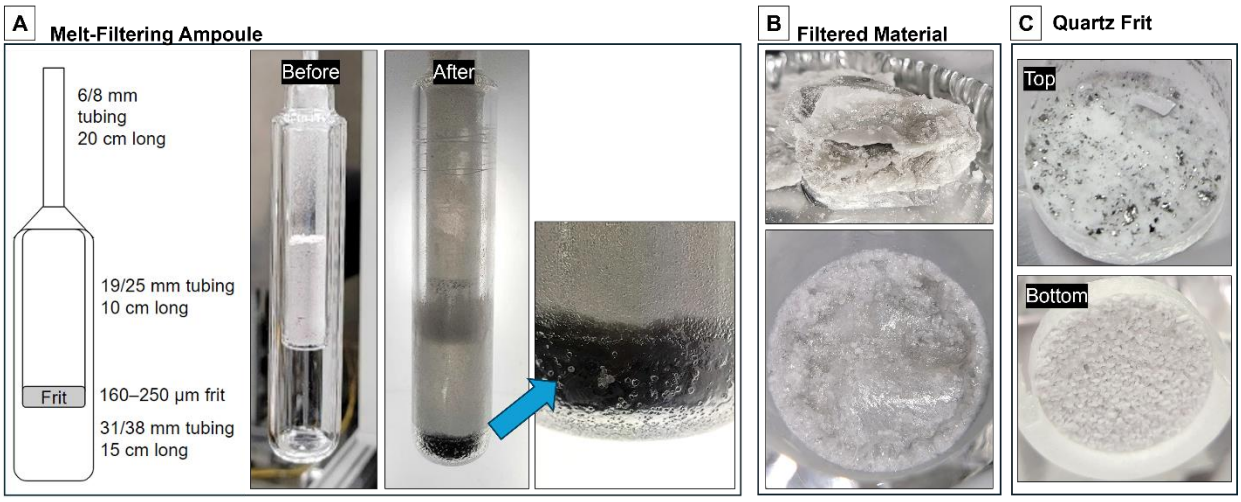


**Figure 69**. Melt-filtering of a 22 g charge of 99.5% pure anhydrous $CaBr_2$ powder led to recovery of ~18 g of material.

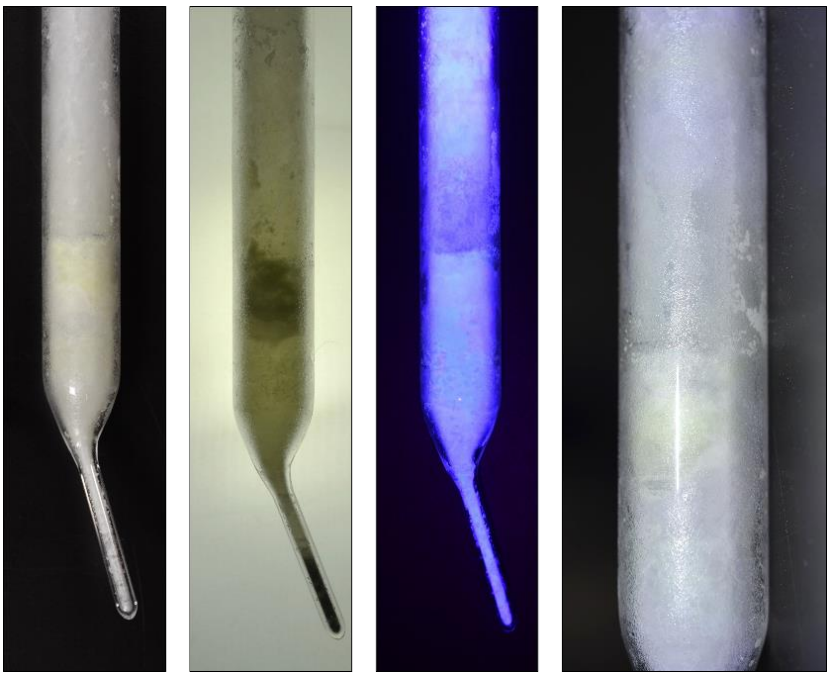

**Figure 70**. 12 mm diameter $RbCaBr_3$:Eu crystal grown using melt-filtered $CaBr_2$ and treated RbBr raw materials.

## 7.2 Rubidium Strontium Iodide ($RbSrI_3$:Eu)

### 7.2.1 *High Temperature XRD and Coefficient of Thermal Expansion of $RbSrI_3$*

Coefficients of thermal expansion were determined from XRD patterns measured as a function of temperature. There were no structural phase transitions observed between 25-350°C. **Figure 71A** shows a gradual shift of diffraction peaks to lower 2θ as temperature increased, coinciding with the increase in lattice parameters and unit cell volume.

The linear coefficients of thermal expansion (CTE, $\overline{\alpha}$) are in **Table 14**, compared with values for orthorhombic crystals $SrI_2$ and $KCaI_3$ and monoclinic $LaCl_3$. These are helpful comparisons, since these scintillators can be grown as high-quality, large diameter crystals (≥ Ø1"), and $KCaI_3$ also has the same space group (*Cmcm*) as $RbSrI_3$ [227-229].

$RbSrI_3$ had large linear CTE and volumetric CTE values, especially in comparison to $LaCl_3$ and $SrI_2$. However, this was similar to $KCaI_3$. The ratios of linear CTE values ($\overline{\alpha}_a/\overline{\alpha}_b$, $\overline{\alpha}_a/\overline{\alpha}_c$, $\overline{\alpha}_b/\overline{\alpha}_c$) inform the magnitude of anisotropy. These ratios for $RbSrI_3$ were similar to $SrI_2$. For an isotropic crystal, the ratios are equal to 1.

### 7.2.2 *Crystal Growth and Scintillation Properties of Ø12 mm $RbSrI_3$:Eu*

A Ø12 mm $RbSrI_3$:5 mol% Eu crystal was grown as an initial test for scale up of crystal growth. The crystal was grown with furnace set points of 620/460/360°C, determined from visual observation of the solid-liquid interface in the furnace. It was translated at 0.5 mm/hr, which was the same speed used for Ø7 mm crystals. It was cooled over 100 hr, which was 15 hours longer than for the smaller crystals.

A highly transparent crystal was grown, as shown in **Figure 72.** There were parallel cracks at the tail end of the boule that formed during cooling. A distinct white last-to-freeze layer was seen, especially visible with backlighting. Some birefringence was also visible, possibly indicating high strain in the crystal resulting from the anisotropic CTE. Even so, a high quality Ø12, 12 mm cylinder could be cut from the boule for scintillation properties characterization.

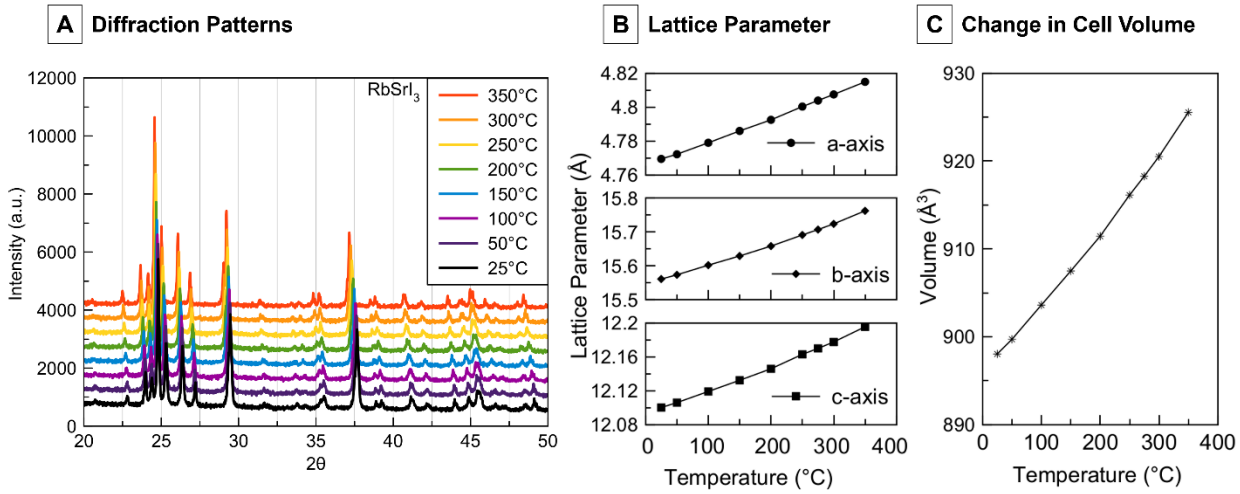


**Figure 71**. A) Peaks shifted to lower 2θ with increased temperature. B) Lattice parameters and C) Cell volume as a function of temperature.

**Table 14.** Coefficient of Thermal Expansion of $RbSrI_3$

| Composition | Linear CTE (x $10^{-5}$ $K^{-1}$) | | | Volumetric CTE (x $10^{-5}$ $K^{-1}$) | Ratios of linear CTE (isotropic ratio = 1) | | |
|---|---|---|---|---|---|---|---|
| | $\overline{\alpha}_a$ | $\overline{\alpha}_b$ | $\overline{\alpha}_c$ | αV | $\overline{\alpha}_a/\overline{\alpha}_b$ | $\overline{\alpha}_a/\overline{\alpha}_c$ | $\overline{\alpha}_b/\overline{\alpha}_c$ |
| $RbSrI_3$ (orthorhombic) | 2.99 | 3.99 | 2.45 | 9.43 | 0.75 | 1.22 | 1.63 |
| $KCaI_3$ [228] (orthorhombic) | 3.51 | 4.126 | 2.873 | 10.61 | 0.9 | 1.2 | 1.4 |
| $SrI_2$:Eu [72] (orthorhombic) | 1.55 | 2.16 | 0.92 | 4.63 | 0.72 | 1.68 | 2.35 |
| $LaCl_3$:Ce [230] (hexagonal) | 2.4 | - | 1.1 | 5.9 | - | 2.18 | - |

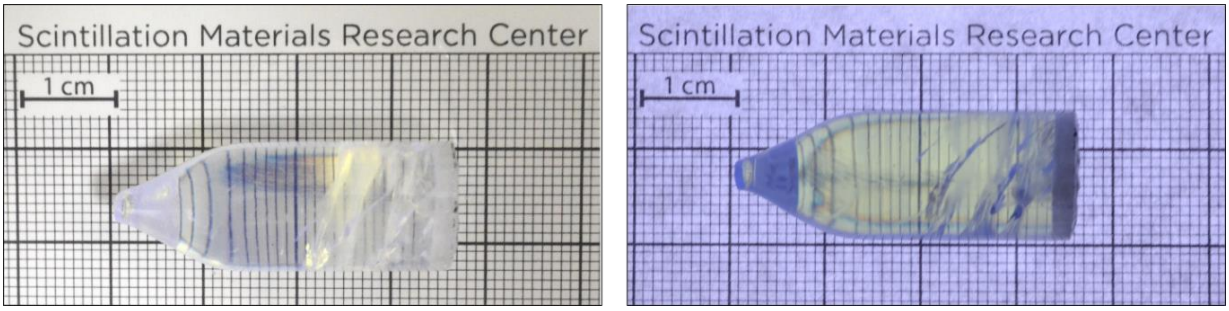


**Figure 72.** Ø12 mm $RbSrI_3$:5 mol% Eu crystal shown with ambient light and backlighting.

Scintillation properties are shown in **Figure 73**. For a Ø12, 12 mm cylinder, the light yield and energy resolution were 69,300 ph/MeV and 3.3% at 662 keV. This was a slight decrease in performance compared to smaller samples. For the Ø7, 3 mm sample, the light yield was 78,700 ph/MeV and the energy resolution was 2.8% at 662 keV. The scintillation decay time of the Ø12, 12 mm cylinder was 1.76 μs, which was a slight increase from the 1.03 μs measured for small crystals. Additionally, the X-ray afterglow intensity of the Ø12 mm crystal increased slightly.

7.2.3 *Crystal Growth of Ø22 mm $RbSrI_3$:Eu*

As shown in **Figure 74**, Ø22 mm $RbSrI_3$:Eu crystals consistently cracked during cooldown between ~200-300°C. HTXRD patterns indicated that there was not a solid-solid phase transition in this region. The use of lower translation (0.2 mm/hr), longer cooling times (175 hours from ~550°C), carbon coated ampoules, and different grain selectors did not lead to improvement.

7.2.4 *Raw Materials Investigations*

For nearly all of the crystal growth experiments using RbI raw materials, the material used was 99.9% pure powder that was treated by a single pass in a Bridgman furnace, as described previously for RbBr. Different sources and treatments of RbI raw materials were also investigated. As a low cost (~$1/g) option, 99% pure powder from Strem was treated by melt filtration and zone refining. Melt filtering of RbI was done with a double chamber ampoule using a coarse and fine frit. Approximately 22 g of RbI was melted and filtered, followed by directional solidification at 5 mm/hr in a carbon coated portion of the ampoule. The raw material reacted severely with the ampoule and frit, as shown in **Figure 75A**.

As an alternative, zone refining at RMD was pursued. A 40 g charge of material was dried under vacuum at 150°C, and the ampoule was sealed with a thick quartz plug. Then, the ampoule was heated to ~50°C above the melting point of RbI. The charge was initially 16 cm in length. The molten zone during zone refining was approximately 2 cm in length. The heating element passed over the charge a total of 18 times with a forward speed of 20 mm/day. As shown in **Figure 75B**, the charge consisted of yellow crystallites prior to zone refining. During the process, a buildup of vapor, presumed to be iodine, was seen at the ends of the ampoule. After zone refining, large, colorless, highly transparent crystallites of RbI were distributed along the length of the ampoule. The ends of the ampoule consisted of smaller crystallites that had a slightly yellow tint, which were discarded.

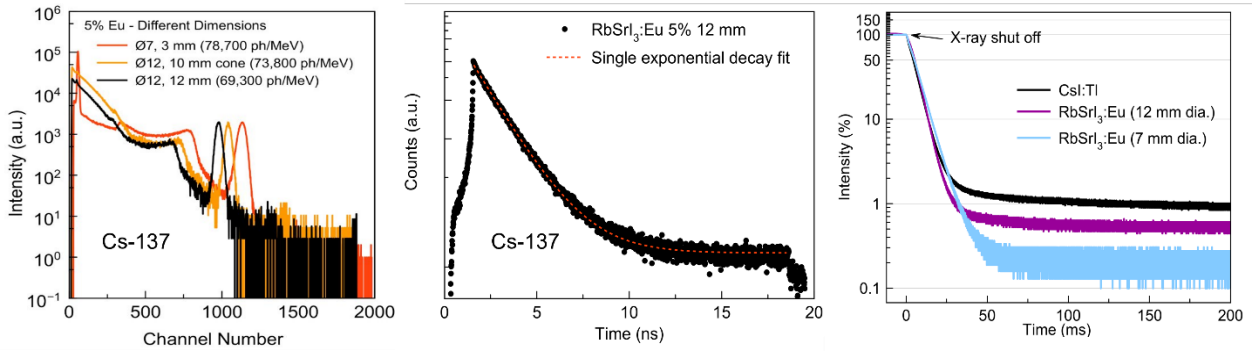


**Figure 73.** Scintillation properties of Ø12 mm $RbSrI_3$:5 mol% Eu crystal.

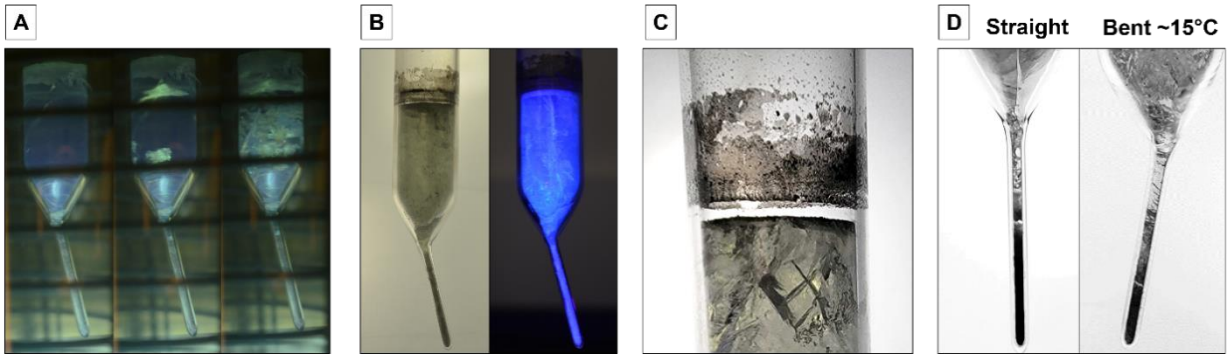


**Figure 74.** Cracking in Ø22 mm $RbSrI_3$:Eu crystals was observed during cooldown, regardless of translation rate, capillary type, cooling time, and use of a carbon coated ampoule.

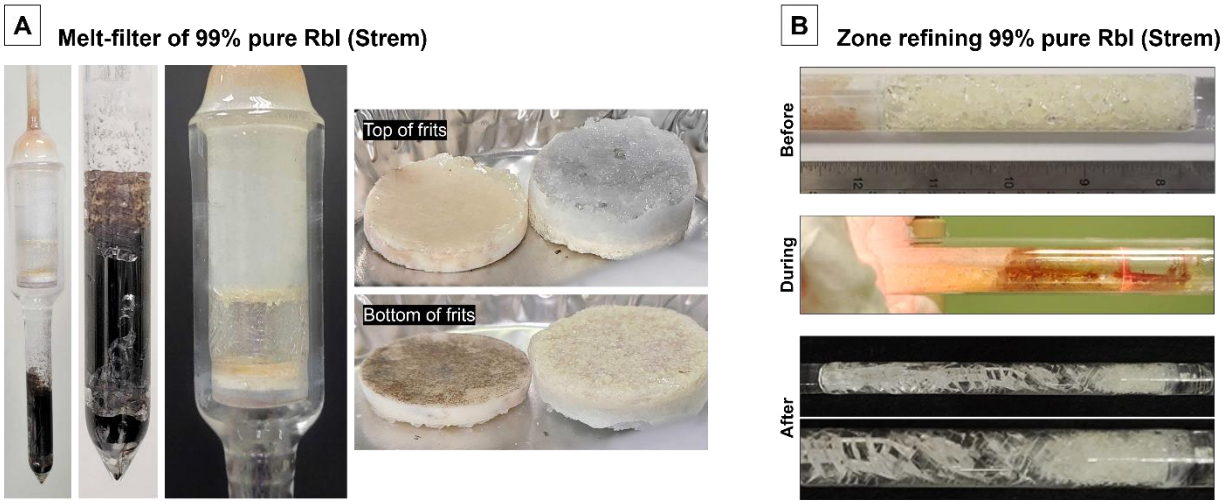


**Figure 75.** A) Melt filtering and B) zone refining of 99% pure RbI powder from the company Strem.

Additionally, two types of RbI raw materials were used to grow Ø22 mm $RbSrI_3$:Eu 1 mol% crystals. The first material was 99.9% pure RbI powder sourced from Sigma-Aldrich, which was used after in-house treatment by a single pass in a Bridgman furnace (~$5/g). The second was 99.9% pure anhydrous RbI beads sourced from APL, which were used as-received (~$35-45/g). Both types of raw materials were used for growths of high-quality Ø7 and Ø12 mm crystals. While the purity of 99.9% was the highest available from any vendor, according to our searches, it was theorized that the anhydrous nature of the APL RbI beads would improve crystal quality.

During drying of the $RbSrI_3$:Eu charge under vacuum preceding crystal growth, the RbI from APL turned grey/brown in color (250°C for 10 hours), and the beads slightly sintered together. The melt-synthesized sample had black specks mixed throughout the white boule. This was investigated with DSC. The observed melting point was consistent with RbI, and there was no evidence of other phase transitions or volatile materials burning off in either the heat flow curve or the thermogravimetric curve. The crystals were grown with nearly identical parameters, including a translation rate of 0.2 mm/hr and cooling over 175 hours.

The crystal grown with purified RbI from Sigma-Aldrich is shown on the left of the photos in **Figure 76** (*1*), and the crystal grown with RbI from APL is shown on the right (*2*). The crystal with the purified RbI had a "shattered" cracking pattern throughout the entire boule, including the capillary; this is consistent with previously observed results. There was also a large amount of black flakes stuck to the inside of the capillary wall. Although severely cracked, the crystal pieces were transparent. Meanwhile, the crystal grown from APL RbI was significantly different. It was grown in a transparent furnace, so growth could be visually monitored. After growth, there was a thick dark yellow liquid layer at the last-to-freeze, which solidified in a brown color. The crystal had one crack in the cone prior to cooling but cracked significantly during the cooling process. The material was somewhat hazy and appeared to react slightly with the quartz ampoule. Additionally, there was a red/orange substance of unknown origin that is unlikely a result of laboratory contamination.

Ultimately, the starting quality of RbI raw materials significantly affected the crystal quality of Ø22 mm $RbSrI_3$:Eu crystals, even if such issues were not experienced in smaller crystals. Unfortunately, the use of anhydrous commercial RbI did not lead to an immediate improvement.

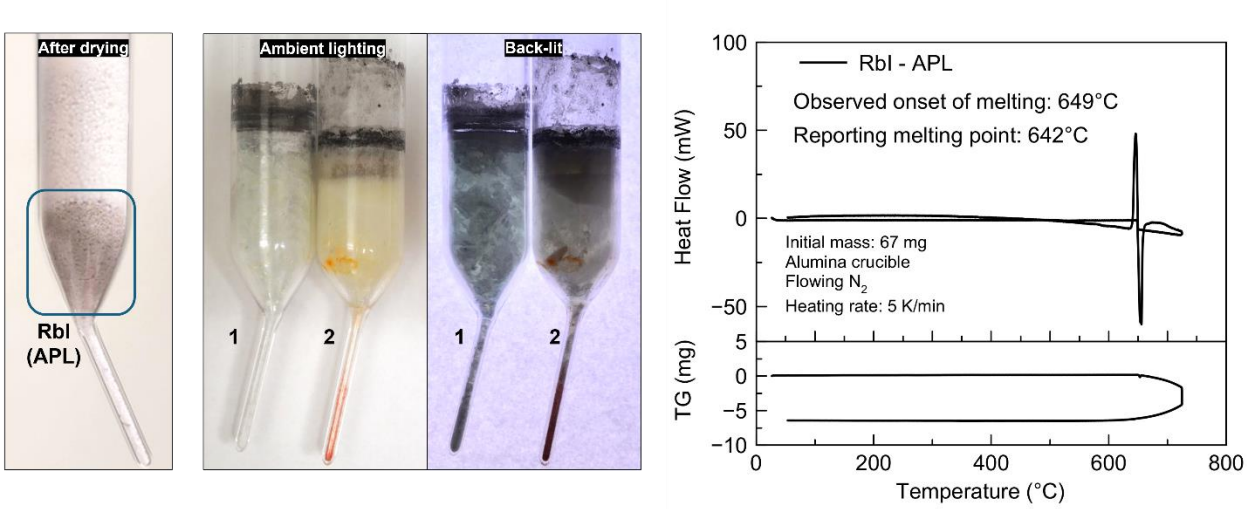


**Figure 76.** RbI from APL turned brown/grey after drying under vacuum. The Ø22 mm $RbSrI_3$:Eu crystal grown from 99.9% pure Sigma-Aldrich material purifed in-house is labeled (1), and the crystal grown from 99.9% pure anhydrous RbI material is labled (2). There was no evidence of impurites in the DSC measurement of RbI.

### 7.3 Rubidium Strontium Bromide, Rubidium Strontium Iodide ($RbSr_2Br_5$:Eu, $RbSr_2I_5$:Eu)

Single crystals of $RbSr_2Br_5$:1% Eu and $RbSr_2I_5$:1% were grown in a Ø22 mm size, and their light yield, energy resolution and scintillation decay time were measured. Based on the promising results with $RbSr_2I_5$:1% Eu, fast translation rates up to 3.5 mm/hr were investigated as well. High Temperature X-ray Diffraction measurements were performed to investigate the coefficients of thermal expansion. Both compositions are reported to be congruently melting without structural phase transitions [69].

#### 7.3.1 *HTXRD and Coefficient of Thermal Expansion of $RbSr_2I_5$ and $RbSr_2Br_5$*

In the HTXRD patterns, as the temperature increased, the peak positions shifted to lower 2θ values with increasing temperature, indicating an expansion of the unit cell. No impurity peaks were observed within this temperature range, indicating structural stability and an absence of solid-solid phase transitions for both compositions. This is an important observation particularly with regards to $RbSr_2Br_5$ crystals, which contained small bubbles. This makes thermal decomposition of the phase and bromine volatility unlikely to be the causes for the bubbles, leaving trapped gases from the raw materials (i.e., moisture, oxygen) as possible sources.

**Figure 77** includes plots of a section of the collected diffraction to highlight changes in the most intense diffraction peaks (~20-55°), and lattice parameters and unit cell volume as a function of temperature for $RbSr_2I_5$ and $RbSr_2Br_5$. Both crystals exhibited a nearly linear increase in lattice parameter with temperature, with no abrupt changes, further confirming the absence of solid-solid phase transitions over this high-temperature region. The volumetric expansion of $RbSr_2Br_5$ was approximately 41 $Å^3$ and that of $RbSr_2I_5$ was 56 $Å^3$.

**Table 15** shows the linear coefficients of thermal expansion (CTE) over a 25°C-400°C temperature range, along with reported values for other non-cubic halide scintillators, including $SrI_2$:Eu and $LaCl_3$:Ce [72, 230]. Both $RbSr_2Br_5$ and $RbSr_2I_5$ had large volumetric CTEs, nearly 2.5 times that of $SrI_2$:Eu. However, $RbSr_2Br_5$ had minimal thermal expansion anisotropy across crystallographic direction, with $\bar{\alpha}_a/\bar{\alpha}_b$, $\bar{\alpha}_a/\bar{\alpha}_c$, and $\bar{\alpha}_b/\bar{\alpha}_c$ values ranging from 0.9-1.1. Meanwhile, the thermal expansion anisotropy of $RbSr_2I_5$ was comparable to that of $SrI_2$:Eu and $LaCl_3$:Ce.

Stronger chemical bonds typically relate to smaller coefficients of thermal expansion. While several factors contribute to bond strength, in general, stronger chemical bonds are shorter in length. The bond lengths in $RbSr_2Br_5$ and $RbSr_2I_5$ were compared to investigate the differences observed their thermal expansion. Bond lengths were sourced from published crystallographic data via VESTA [112, 231, 232]. The maximum bond lengths in $RbSr_2Br_5$ were shorter (Rb-Br: 4.05 Å, Sr-Br: 3.54 Å) than those in $RbSr_2I_5$ (Rb-I: 4.33 Å, Sr-I: 3.74 Å). The higher melting point of $RbSr_2Br_5$ (593°C) also indicates that this composition likely has stronger bonding than $RbSr_2I_5$ (490°C).

One last remark with regards to CTE is how this data can be used to inform future scale-up efforts. The crystal growth experiments in this study were done using randomly oriented, self-seeded grains nucleated in the ampoule capillary. However, the CTE data suggests that crystal quality could benefit from orienting $RbSr_2Br_5$ to grow along the a- or c- axis and $RbSr_2I_5$ to grow along the c- axis. In these orientations, the axis with the lowest CTE would be along the growth direction experiencing the greatest thermal gradient.

**Table 15.** Linear and volumetric coefficients of thermal expansion of $RbSr_2Br_5$ and $RbSr_2I_5$ compared to other scintillators.

| Scintillator (crystal structure) | $\bar{\alpha}_a$ ($10^{-5}$ $K^{-1}$) | $\bar{\alpha}_b$ ($10^{-5}$ $K^{-1}$) | $\bar{\alpha}_c$ ($10^{-5}$ $K^{-1}$) | $\bar{\alpha}_v$ ($10^{-5}$ $K^{-1}$) | $\frac{\bar{\alpha}_a}{\bar{\alpha}_b}$ | $\frac{\bar{\alpha}_a}{\bar{\alpha}_c}$ | $\frac{\bar{\alpha}_b}{\bar{\alpha}_c}$ |
|---|---|---|---|---|---|---|---|
| $RbSr_2Br_5$ (monoclinic) | 3.32 | 3.73 | 3.31 | 10.36 | 0.89 | 1.003 | 1.13 |
| $RbSr_2I_5$ (monoclinic) | 3.53 | 4.86 | 2.79 | 11.18 | 0.73 | 1.27 | 1.74 |
| $SrI_2$:Eu [72] (orthorhombic) | 1.55 | 2.16 | 0.92 | 4.63 | 0.72 | 1.68 | 2.35 |
| $LaCl_3$:Ce [230] (hexagonal) | 2.4 | - | 1.1 | 5.9 | - | 2.18 | - |

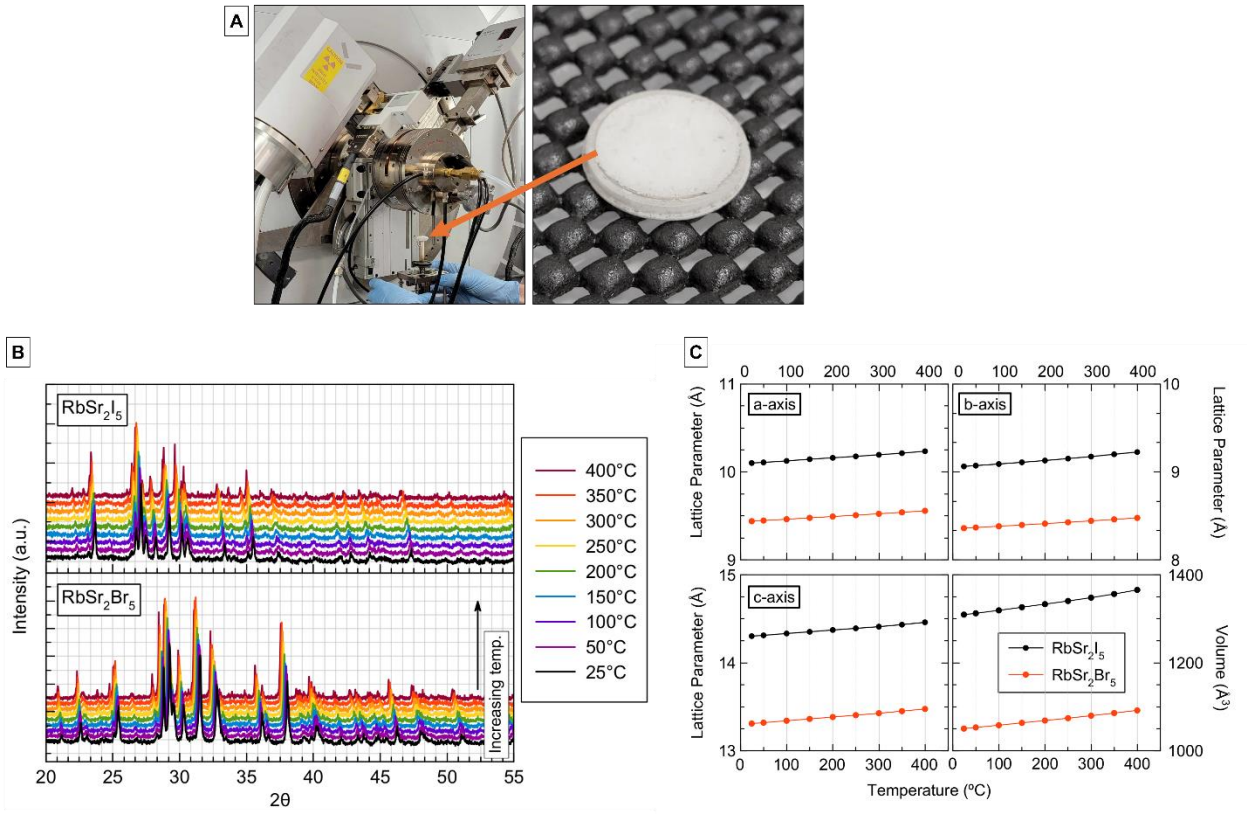


**Figure 77.** A) High temperature X-ray diffraction apparatus and sample. B) Diffraction patterns from 25°C-400°C for $RbSr_2I_5$ and $RbSr_2Br_5$, and C) Changes in lattice parameter and unit cell volume.

7.3.2 *Growth of Ø22 mm $RbSr_2Br_5$:Eu, $RbSr_2I_5$:Eu at 0.5 mm/hr*

Growth of $RbSr_2Br_5$:Eu in a Ø22 mm size yielded a translucent crystal, as shown in **Figure 78, (A-D).** The crystal had a crack along the diameter of the cone that formed during cooling. There were small black flakes on the top of the last-to-freeze, which were attributed to carbon impurities present in the raw materials. Back-lighting of the crystal revealed small bubbles that follow a vertical pathway along the growth direction (**Figure 78D**). These microscopic bubbles were also observed in Ø7 mm samples of this composition.

Growth of $RbSr_2I_5$:Eu in a Ø22 mm size is shown in **Figure 78(E-G).** The crystal was grown at 0.5 mm/hr and only had minor cracks localized to the surface of the crystal and at the last-to-freeze, which seemed to correspond to black impurities present in the raw materials. Otherwise, it had excellent optical quality with no visible macroscopic defects.

The large concentration of black impurities can destabilize the growth, as shown in **Figure 79**. On one occasion, they concentrated on the wall of the ampoule and significantly affected the solid-liquid interface during growth, resulting in a poor quality crystal. Melt-filtration could be one method to remove the impurities.

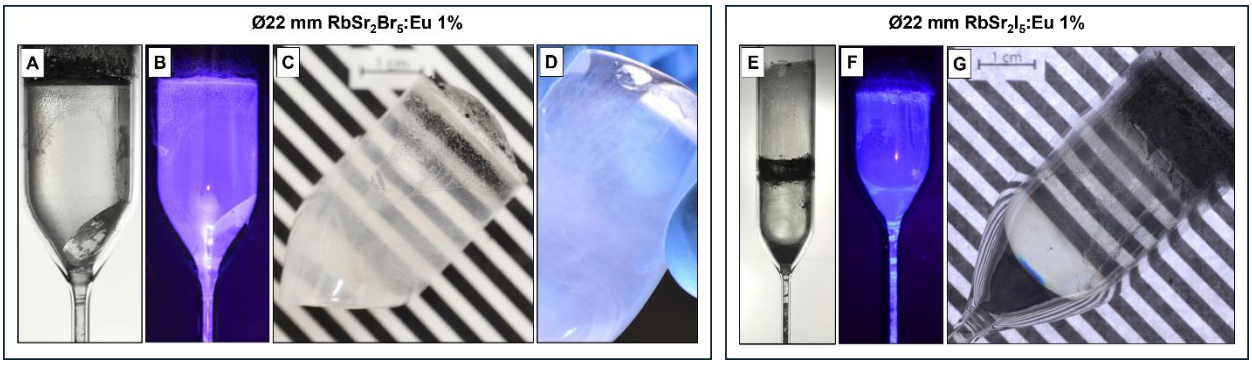


**Figure 78.** Ø22 mm $RbSr_2Br_5$:1% Eu and $RbSr_2I_5$:1% Eu crystals grown at 0.5 mm/hr: (a, e) backlit in the quartz growth ampoule after cooling, (b, f) under UV light excitation, and (c) after extraction from the ampoule with ambient lighting. (d) Small vertical trails of bubbles inside of the $RbSr_2Br_5$:1% Eu were seen.

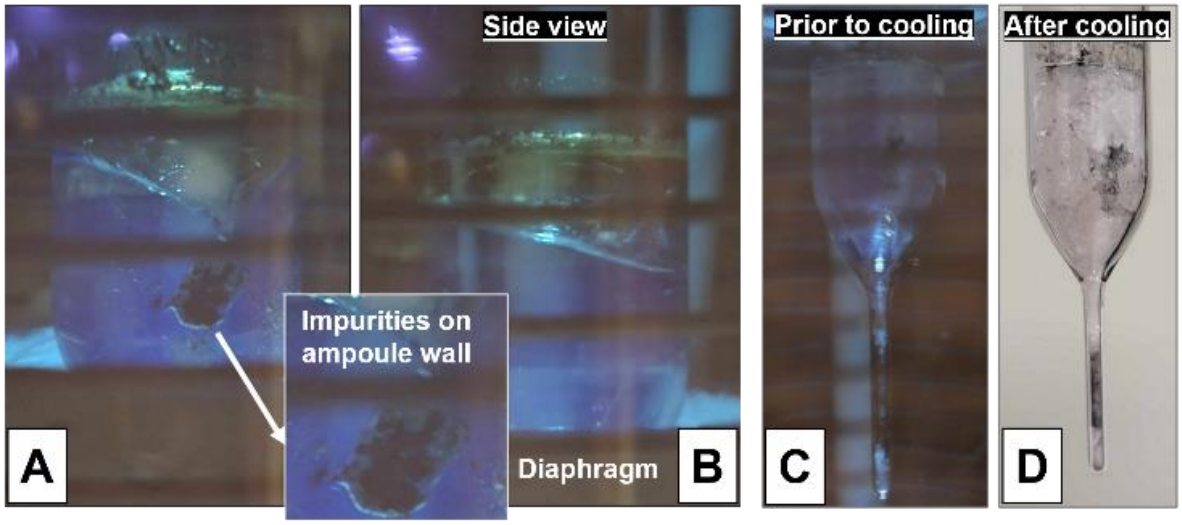


**Figure 79**. When adhered to the ampoule wall, black impurities in the melt destabilized the solid liquid interface, resulting in a poor-quality crystal. However, these impurities typically floated to the surface of the melt.

7.3.3 *Scintillation properties of Ø22 mm $RbSr_2Br_5$:Eu, $RbSr_2I_5$:Eu grown at 0.5 mm/hr*

Pulse height spectra are in **Figure 80**. As crystal size increases, a number of artifacts are expected to reduce light transport and scintillation performance, including compositional inhomogeneities, crystal growth defects, and a greater degree of europium self-absorption [75, 233]. While achieving high performance, the properties of both compositions are less than for observed in small Ø7 mm sizes, most likely due to $Eu^{2+}$ self-absorption. The small bubbles in $RbSr_2Br_5$:Eu may also act as scattering centers, which could further reduce performance as well. The light yield of $RbSr_2Br_5$:Eu was ~26% lower than in small crystals, and that of $RbSr_2I_5$:Eu was ~17% lower.

These results are comparable to other reports of europium-doped halide scintillators; for example, the light yield of isostructural $KSr_2I_5$:2 mol% Eu decreased by ~14% between crystals 0.012 $cm^3$ and 14 $cm^3$ in volume, and the energy resolution changed from 2.9% to 3.4% at 662 keV [177]. One way to alleviate the europium self-absorption effects in large crystals is to reduce the europium dopant concentration even lower than the 1 mol% studied here, depending on the specific properties of interest. In $SrI_2$:Eu, desirable energy resolution could be achieved with 0.1-0.5 mol% Eu, although the optimal light yield was achieved with 5-6 mol% Eu for small crystals [74, 199]. The lower europium concentrations also led to faster decay times and lower costs associated with the $EuI_2$ raw materials.

Pulse height spectra measured with and without a Cs-137 source are shown in **Figure 81,** which demonstrate the intrinsic radioactive background from Rb-87. They show a curve with maximum energy ~283 keV, which coincides with the beta decay of Rb-87 [92]. For some applications, intrinsic radioactivity of large crystals could cause radiation detection efficiency issues from pulse pileup. The extent and factors contributing to this effect require detailed investigation, including crystal volume, packaging, and detector geometry [234].

The scintillation decay curves are plotted in **Figure 82**. For both crystals, the decay time consisted of two components. The $RbSr_2Br_5$:1% Eu crystal had a primary decay component of 1.2 (87%), and a secondary decay component of 6.3 (13%). The decay of the $RbSr_2I_5$:1% Eu crystal was similar: 1.2 (70%), 6.6 (30%). The decay times increased significantly from those of Ø7 mm crystals, which is a behavior typical of europium self-absorption.

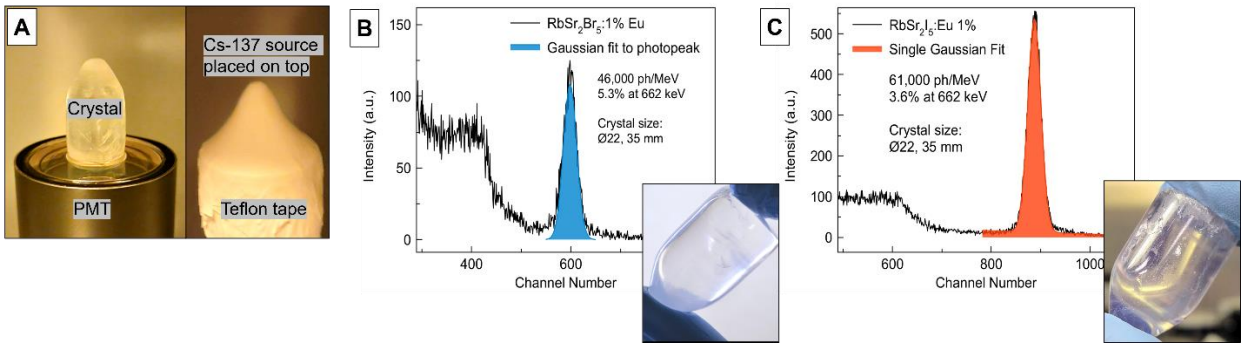


**Figure 80.** A) The crystal was directly coupled to the PMT with mineral oil to measure light yield. B-C) show the Ø22, 35 mm crystals measured and the associated pulse height spectra for $RbSr_2Br_5$:Eu and $RbSr_2I_5$:Eu.

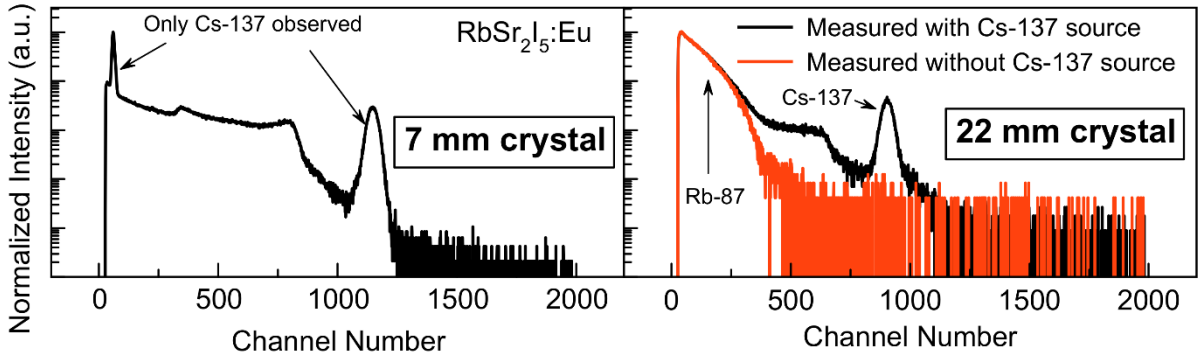


**Figure 81.** Pulse height spectra acquired for a Ø7 mm, 3 mm thick crystal versus a Ø22, 35 mm crystal of $RbSr_2I_5$:1% Eu, showing the intrinsic radioactive background from Rb-87.

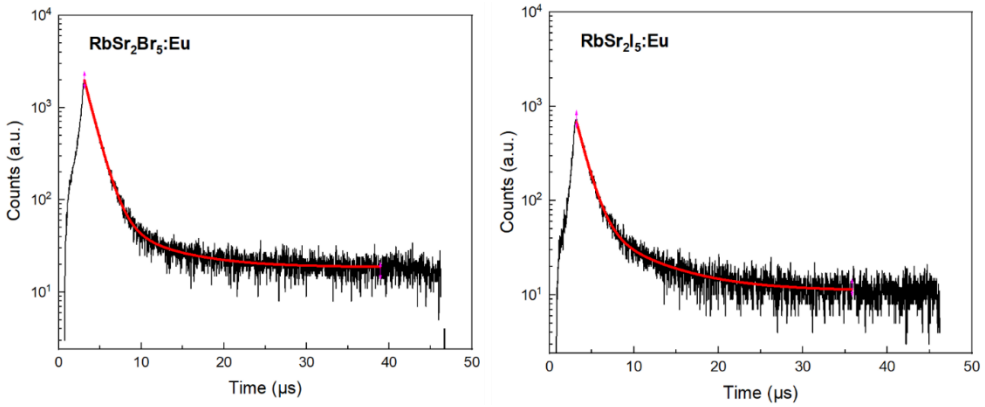


**Figure 82.** Ø22, 35 mm $RbSr_2Br_5$:Eu and $RbSr_2I_5$:Eu crystals had two-component scintillation decays, with a primary component of 1.2 μs and a longer secondary component ~6 μs.

7.3.4 *Crystal Growth Translation Rate Experiments with $RbSr_2I_5$:Eu (Ø7, Ø22 mm)*

Based on the high optical quality of the $RbSr_2I_5$:Eu crystals, growth at faster translation rates was explored. Growths in a Ø7 mm size were done first to investigate a broad range of translation rates and test uniformity of scintillation performance from seed end to tail end of the boules. It was found that transparent, crack-free colorless crystals could be grown with rates of 1, 3, and 5 mm/hr (**Figure 83**). All of the crystals had surface texture that was easily polished away. Under UV excitation, the crystals had a uniform, bright blue luminescence. At 5 mm/hr, some seeding issues in the capillary became noticeable (**Figure 83C**). Additionally, the last-to-freeze of the crystal grown at 5 mm/hr was also slightly slanted, possibly indicative of some instability of the growth interface.

To investigate crystal quality and scintillation properties throughout the boules, scintillation properties were measured for samples cut from the seed end and tail end of each crystal. The light yield and energy resolution showed little variation, likely indicating europium dopant uniformity throughout the boules (**Figure 83D**). Due to the similar ionic radii and compatible valence state of $Eu^{2+}$ and $Sr^{2+}$, it was already expected that dopant segregation would be minimal.

Based on the uniformity and quality of Ø7 mm $RbSr_2I_5$:Eu crystals grown with fast translation rates, similar translation rate experiments were done in a Ø22 mm size. Crystals of $RbSr_2I_5$:1% Eu were grown at 1.5 and 3.5 mm/hr. A comparison between these crystals and one grown at 0.5 mm/hr is shown in **Figure 84**. These back-lit images are helpful for comparing transparency, residue on the ampoules, seeding in the capillary, and any cracking or other macroscopic defects.

The Ø22 mm crystals grown at 0.5 and 1.5 mm/hr were similar in appearance. They were colorless and only had cracks on the surface or at the last-to-freeze. These cracks could be mitigated in future experiments by melt-filtering the charge to remove the black impurities that accumulated on the wall of the ampoule above the last-to-freeze. Additionally, a carbon-coated ampoule could be used, which can prevent sticking of the crystal to the ampoule walls and sometimes serve as a gettering agent for oxygen or water vapor [235]. The crystal grown at 3.5 mm/hr was transparent, but it also showed cracking within the center of the boule. These cracks were parallel to each other. While appearing black in **Figure 84D** due to the backlighting of the photos, the cracks were colorless, and there were no obvious impurity inclusions.

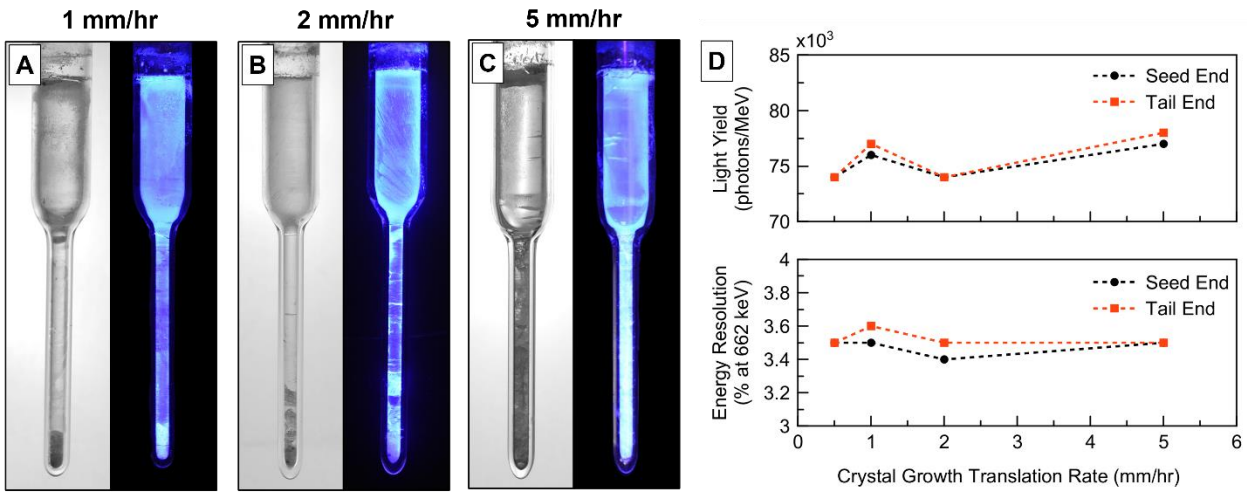


**Figure 83.** High quality Ø7 mm $RbSr_2I_5$:1% Eu crystals could be grown with fast translation rates of 1, 2, and 5 mm/hr. The crystals are shown backlit (left) and glowing under UV light (right). There was little variation in the scintillation properties of the samples from different portions of the boules, indicating uniformity.

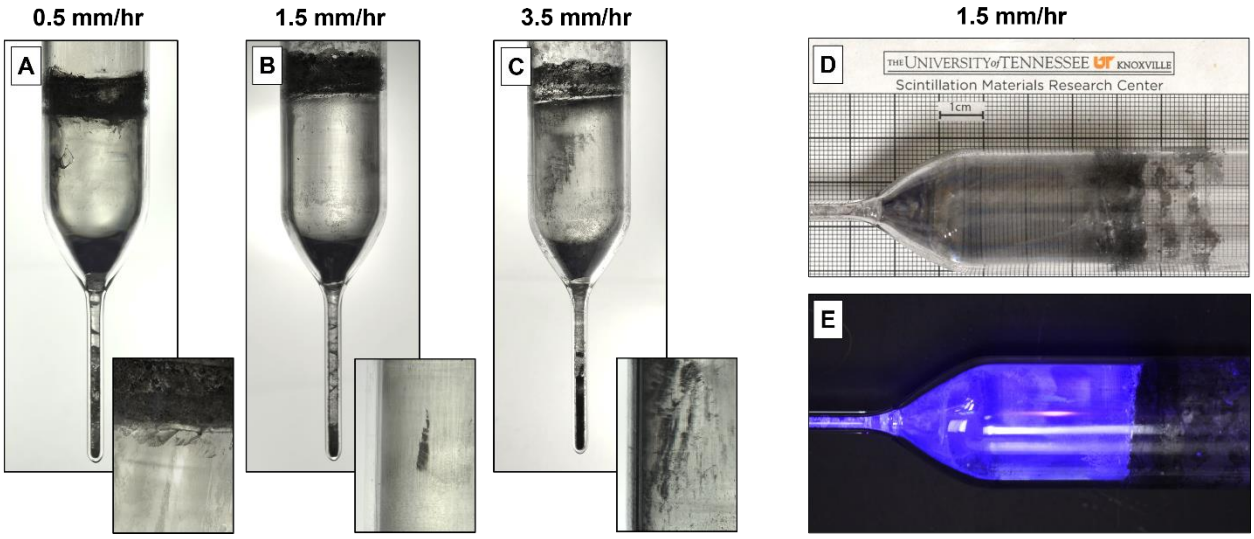


**Figure 84.** Ø22 mm crystals of $RbSr_2I_5$:1% Eu could be grown with fast translation rates. The isodiametric section of the boules was ~35 mm tall. The off-set photos of (a-c) show close ups of unique observations from each crystal. (D) shows the crystal grown at 1.5 mm/hr under ambient lighting on grid paper. (E) shows the same crystal under UV light.

### 7.4 Rubidium Calcium Iodide ($Rb_4CaI_6$:Eu)

Despite challenges with the quality of Ø7 mm $Rb_4CaI_6$ crystals, growth in a Ø22 mm size was pursued to examine the stability of this composition on a larger scale. $Rb_4CaI_6$ is reported to have a peritectic point at 544°C [214]. For this experiment, the crystal was grown with the stochiometric composition.

The crystal and its growth process are shown in **Figure 85**. The crystal was grown with a translation rate of 0.25 mm/hr, which was half the speed as Ø7 mm crystals. It was cooled over 150 hours to room temperature. About midway through the growth process, the crystal looked highly transparent, despite a small crack forming on the side of the crystal where it contacted the ampoule. The capillary looked visually different from the tip to the cone of the crystal, beginning with a seemingly transparent section, followed by a section that looked opaque. These solid and liquid phases of this crystal were also different in color, between a slightly blue section and a dark yellow section, respectively. Prior to cool down, the tail end of the crystal was still liquid. After cooling, the crystal was nearly opaque, and the crack that had started midway through the growth near the ampoule wall propagated along the side the crystal. The tail end of the crystal was more opaque than the seed end and was likely mixed-phase. The crystal had bright blue luminescence under UV light.

The light yield and scintillation decay time of the Ø22, 20 mm boule (**Figure 85D**) were measured and are shown in **Figure 86**. The light yield was measured with the flat, polished tail end side of the crystal coupled to the PMT. It was measured to be ~32,000 ph/MeV with an energy resolution of ~13% at 662 keV. This was a significant deviation from the 70,000 ph/MeV and 5% energy resolution observed for Ø7 mm crystals. Additionally, the 662 keV photopeak was asymmetric, with a long tail on the right side. Notably, the intrinsic radioactive background was higher than observed in other crystals.

The scintillation decay had a primary component of 3.8 microseconds (97%), with a minor contribution from a 0.33 microsecond component (3%). This was consistent with europium self-absorption, which causes scintillation decay time to increase as crystal size and dopant concentration increase. For comparison, the small Ø7, 3 mm crystals doped with 5 mol% Eu had scintillation decay times of 0.23 (12%), 1.96 (88%), and those of the crystal doped with 9 mol% Eu were 0.31 (4%), 2.58 (96%).

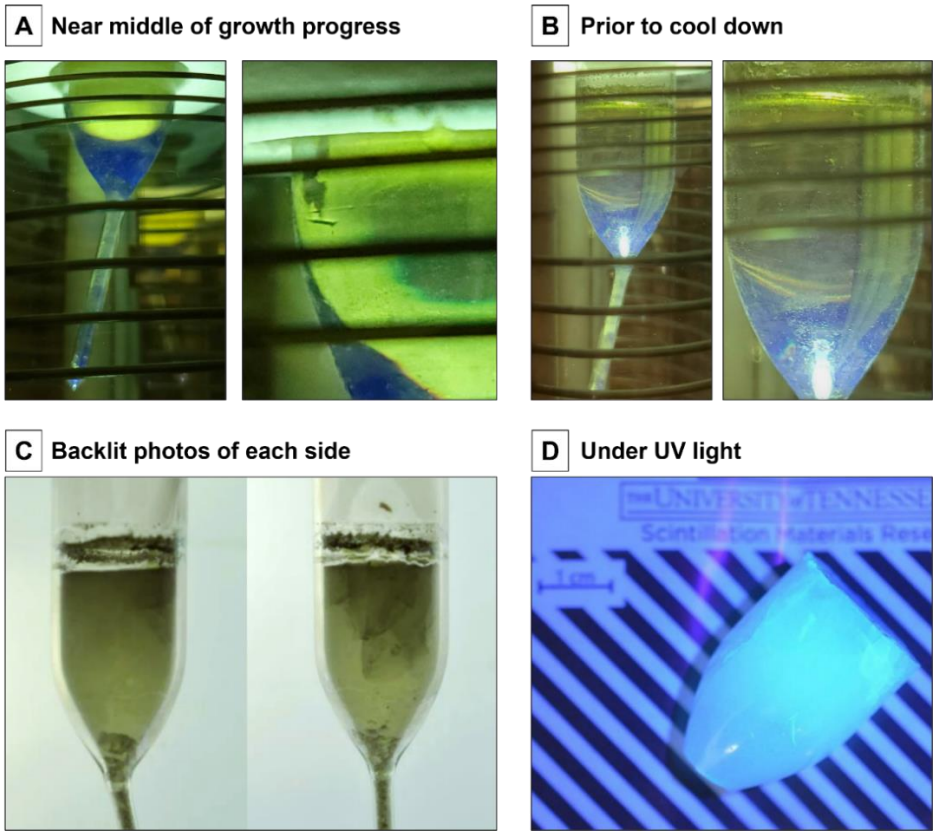


**Figure 85**. Growth of Ø22 mm $Rb_4CaI_6$:5 mol% Eu at 0.25 mm/hr.

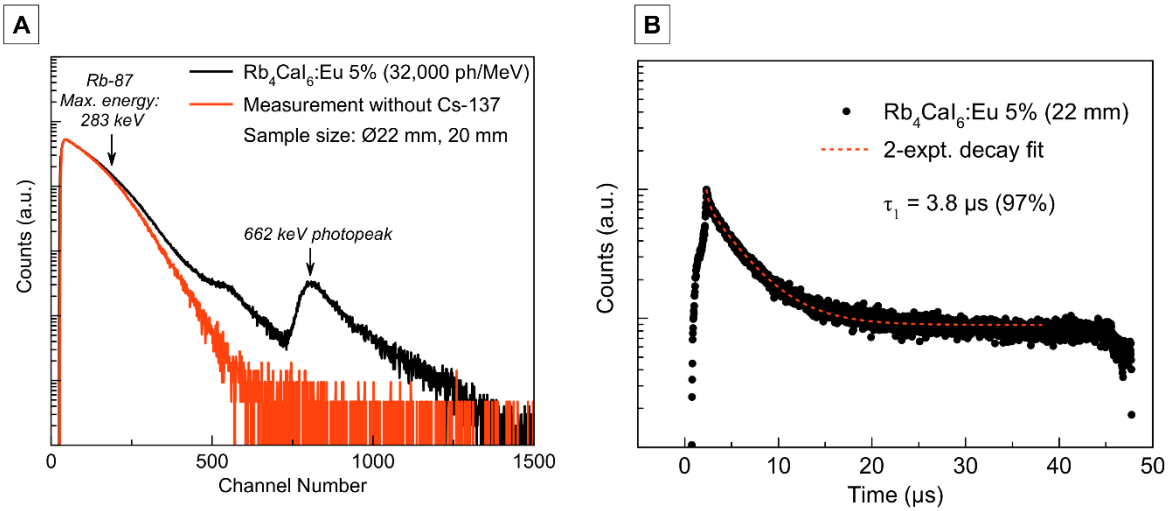


**Figure 86.** A) Pulse height spectra and 2) scintillation decay of a Ø22, 20 mm $Rb_4CaI_6$:5 mol% Eu cylindrical crystal.

# CHAPTER 8 RADIATION DAMAGE

Sections of this chapter were originally published in the following peer-reviewed journal article:

- **K. S. Pestovich**, L. Stand, K. Joshi, X. Wen, C. L. Melcher, L. S. Pandian, E. van Loef, M. Zhuravleva, "Investigating the Luminescence, Irradiation Effects & Fast Neutron-Gamma Discrimination Characteristics of Cubic Halide Perovskite Scintillator $CsCaCl_3$:($Eu^{2+}$, $Tl^{+}$)" in *Nuclear Instruments and Methods in Physics Research - section A.* Submitted for review.

## 8.1 Irradiation Effects

Radiation damage occurs when the absorbed energy is converted into lattice defects. Color centers produce absorption bands (i.e. decreases) in the optical transmission of the crystals, and the light yield will decrease if these absorption bands are in the region of the scintillation emission [10]. There are many types of color centers in alkali halide crystals, the formation and quantity of which depend on a number of factors summarized by Seitz in 1946 [236]. One prevalent type of color center is an F-center (from the German *Farbzentrum*), which results from an anion vacancy trapping an electron. Typically, the creation of color centers dominates over damage to the scintillation mechanism [7]. In addition to color centers, irradiation can produce shallow traps which can worsen the afterglow.

Mechanisms and tolerances for radiation damage differ greatly between alkali halide and oxide scintillators. Damage in alkali halides has been observed to be coupled with the presence of oxygen contamination leading to formation of hydroxyl species. For instance, clearly identifiable radiation-induced absorption bands attributed to different types of F centers (F, F', F'', and F''') were suppressed in a CsI:Tl crystal grown with a scavenger to remove oxygen contamination from the melt [237]. Meanwhile, radiation damage in oxide scintillators is often related to structural defects, such as oxygen vacancies in the crystalline lattice [7]. The radiation damage of some crystals may recover at room temperature, which can cause a non-uniform detector response and lead to a calibration requirement for a detector. Interestingly, scintillators BGO and $PbWO_4$ recover within a few hours to a few weeks, while damage in $BaF_2$ and CsI:Tl is long-lasting and may not occur at room temperature on its own. Annealing and optical bleaching, such as with UV light, are often pursued as a means of healing the induced defects to recover the initial performance.

A comparison of the optical transmittance of $CdWO_4$ and CsI:Tl as a function of dose with Co-60 is shown in **Figure 87**, reproduced from Kobayashi, et al. [28, 238]. $CdWO_4$ is considered a radiation-hard material. The optical transmittance essentially shows no change after $10^8$ rad. Additionally, no change in the visual appearance of the crystals was observed. The behavior of CsI and CsI:Tl crystals is quite different. Noticeable damage occurs in these crystals at doses of 1-10 krad, although undoped CsI crystals had greater radiation resistance than CsI:Tl [239, 240]. After exposure to $10^3$ rad, the optical transmittance of CsI:Tl decreased from a normalized intensity of 0.8 to 0.5 near the absorption edge ~320 nm. Defect formation became significant above $10^5$ rad, at which point distinct absorbance bands were observed. While the decreased optical transmittance led to lower light yield, the scintillation mechanism was only affected at higher doses (5 x $10^7$ rad) in CsI:Tl [241]. It should also be noted that the extent of radiation damage in CsI:Tl crystals depends on crystal quality, raw materials, oxygen impurities, and the size of the crystals as well [242].

While there are a number of important considerations for evaluating the radiation hardness of single crystal scintillators, this initial study focuses on observing the changes in the visual appearance of the crystals, changes in the optical transmittance, and testing the light yield by measuring pulse height spectra. Future investigations should include effects of dose rate, possible recovery time and methods, and any effects on the scintillation mechanism, especially as it relates to afterglow.

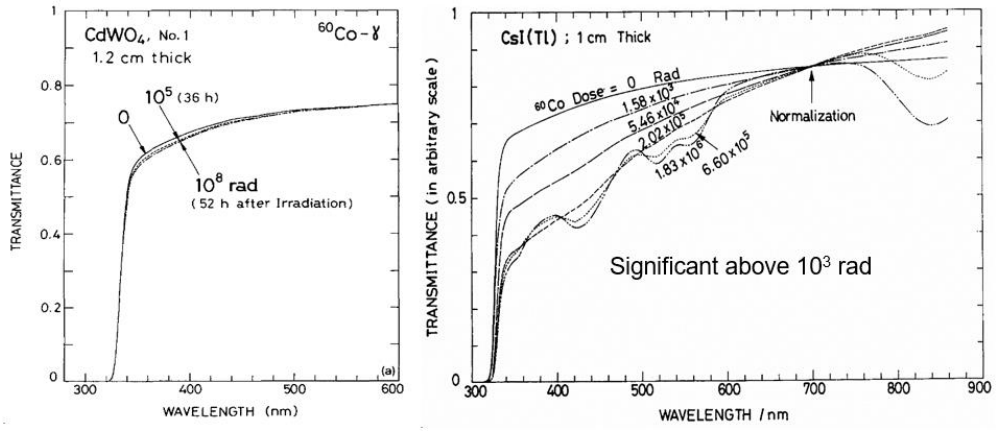


**Figure 87.** Transmittance of $CdWO_4$ and CsI:Tl vs dose with Co-60. Adapted from [28, 238].

## 8.2 Methodology

An initial assessment of the irradiation effects from Co-60 and high energy 9 MV X-rays was carried out up to a 10 Mrad dose. Samples were irradiated with Co-60 at the Gamma Cave Facility and Submersible Chamber at the University of Massachusetts, Lowell and with 9 MV X-rays at the Accelerator Research Center at the University of Tennessee. The crystals tested with Co-60 included: $RbCaBr_3$, $Rb_4CaBr_6$, $CsCaCl_3$, $RbSrI_3$, $RbSr_2Br_5$, $RbSr_2I_5$ and $Rb_4CaI_6$. Only $RbSrI_3$:5 mol% Eu and $RbSr_2I_5$:1 mol% Eu were tested with the X-ray linac. Before and after irradiation, the optical transmittance and the light yield were measured. Samples were ~Ø7 mm, 2-4 mm in size. Small samples were tested in these initial experiments to favor optical transmittance measurements and to fit several samples into a uniform irradiation area.

Measurement of transmittance (200-800 nm) and pulse height spectra (Cs-137) before irradiation showed that performance was uniform and consistent among the samples. At least three transmittance spectra were acquired after repositioning the crystal to ensure consistent results. Quartz sample holders with mineral oil were used to prevent surface degradation from moisture during the measurement.

At the Gamma Cave Facility, dose points from 100 krad to 10 Mrad were investigated. Samples were shipped and irradiated in mineral oil ($C_{15}H_{24}$) filled amber-colored glass vials with molecular sieve. Molecular sieve has small uniform pores intended to adsorb and trap water molecules. The amber color of the vials was intended to reduce any possible effects from optical bleaching of the samples over time. Since there were several weeks between irradiation and measurements, the crystals were re-polished. The dose was controlled by changing the distance from the source and/or the exposure length. The maximum dose rate was $6.93 \times 10^5$ Rad/hr, and the longest exposure was 72.25 hours.

At the Accelerator Research Center at UTK, dose points of 2 Mrad and 10 Mrad were tested. The samples were irradiated in food-storage vacuum-sealable bags. These bags are made of a thick, thermoplastic polymer (Polyethylene $(C_2H_4)_n$ and Nylon/polyamide $(C_6H_{11}NO)_n$) that is a strong barrier to moisture and air. They are also cost effective and easy to customize the size. For some longer irradiation times, molecular size was included inside a second sealed bag around the samples. The dose rate at 1 meter was 3,108 Rad/minute for 9 MV X-rays. The samples were placed 15 cm away from the source, which corresponded to a dose rate of $1.38 \times 10^5$ Rad/minute

or 8.29 x $10^6$ Rad/hr (**Figure 88)**. This was a higher dose rate than tested at the Gamma Cave. The accumulated dose was controlled by the irradiation time (14.48 minutes for 2 Mrad and 72.39 minutes for 10 Mrad). Two samples per dose were tested for repeatability. The pulse height spectra were acquired approximately 24 hours after irradiation and then again 3 weeks after irradiation. The crystals were not re-polished during this period and were stored in mineral oil in a room with yellow lighting.

Another difference to note between the Co-60 and linac irradiation experiments is that photoneutrons are also emitted during the operation of the linac. These are neutrons generated by reaction of the high energy X-rays with the nuclei of the high atomic number materials in the linac components. It is estimated that the intensity could be as high as 1 x $10^{10}$ neutrons/second.

The energy dependence of the various gamma ray interaction processes was calculated using the NIST XCOM Photon Cross Sections Database [243]. The plots are shown in **Figure 89**, compared to $CdWO_4$ and CsI:Tl. In addition to promising preliminary results with the Co-60 gamma irradiation experiments, $RbSr_2I_5$:Eu and $RbSrI_3$:Eu were tested with the X-ray linac. They had somewhat comparable mass attenuation coefficients to CsI:Tl and $CdWO_4$ at high energies (1-10 MeV). The lower density and lower Z crystals $CsCaCl_3$ and $RbCaBr_3$ showed worsened attenuation.

**Figure 88.** Samples in front of the linac in a vacuum sealed bag.

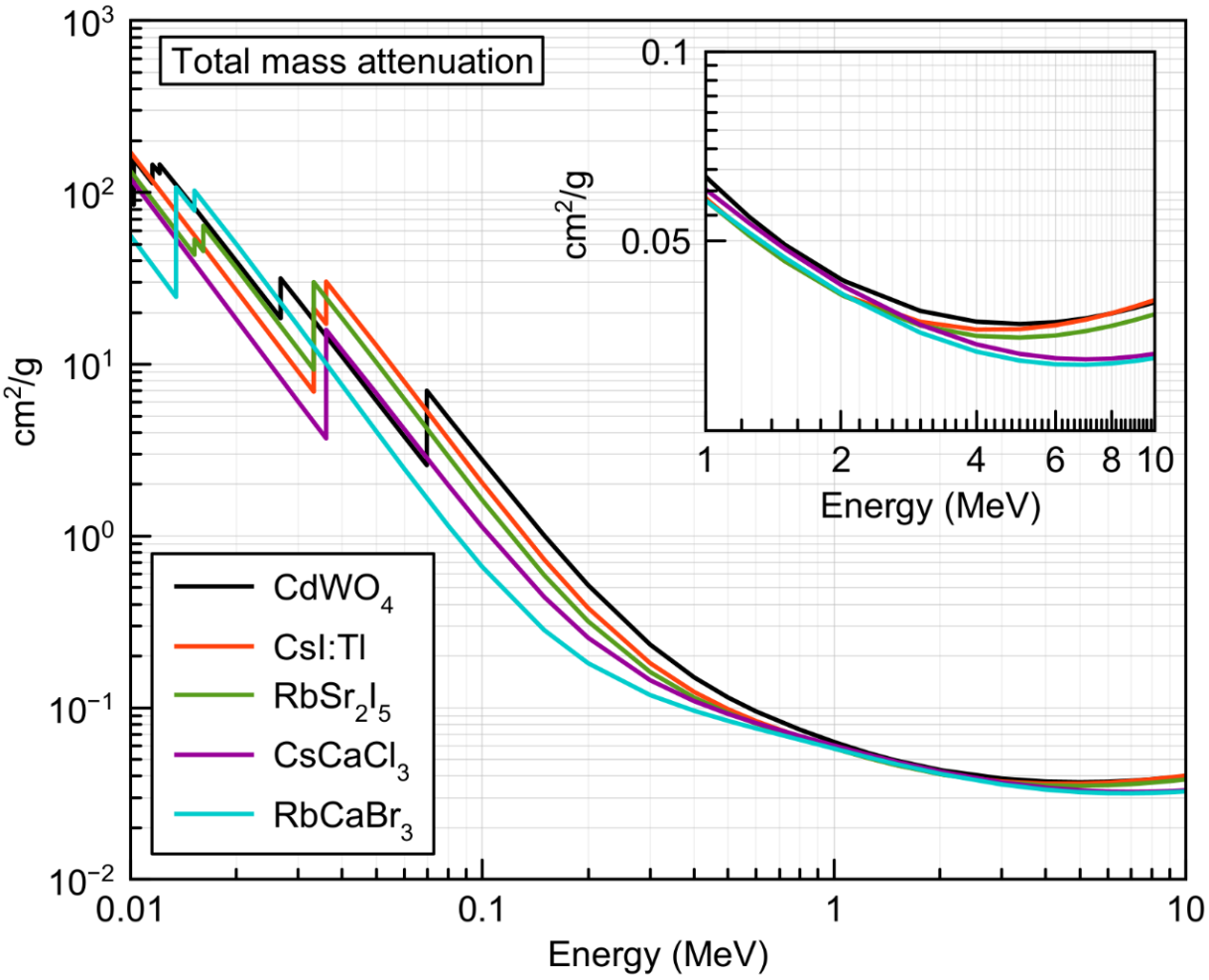


**Figure 89.** Mass attenuation versus energy for different scintillators calculated with the NIST XCOM Photon Cross Section Database [243]. $RbSr_2I_5$ and $RbSrI_3$ were nearly equivalent, so only $RbSr_2I_5$ is shown here.

### 8.3 Rubidium Calcium Bromide ($RbCaBr_3$ and $Rb_4CaBr_6$)

$RbCaBr_3$ and $Rb_4CaBr_6$ crystals were irradiated at the Gamma Cave with 100 krad and 1 Mrad doses. For $RbCaBr_3$, the visual appearance and optical transmittance of the crystals were compared before and after irradiation, shown in **Figure 90A**. The crystals' visual appearance did not change significantly before and after irradiation. The crystal doped with 7 mol% Eu showed slight darkening in color. This coincided with a slight decrease in the optical transmittance from ~450 nm to 600 nm. Otherwise, there were no well-defined absorption bands in the transmittance spectra. Unfortunately, there were inconsistencies in the pulse height spectra measurements preventing a reliable comparison.

Given the low transmittance of the $Rb_4CaBr_6$ crystals, only the visual appearance of the crystals and the pulse height spectra were compared. These are shown in **Figure 90B**. While the undoped crystal became slightly orange tinted, there was no obvious change in the appearance of the europium-doped crystals. The crystal doped with 9 mol% is shown, but the properties were the same for crystals with other concentrations. The photopeak position in the pulse height spectra showed little change, except for a slight decrease for the europium-doped crystals after 1 Mrad.

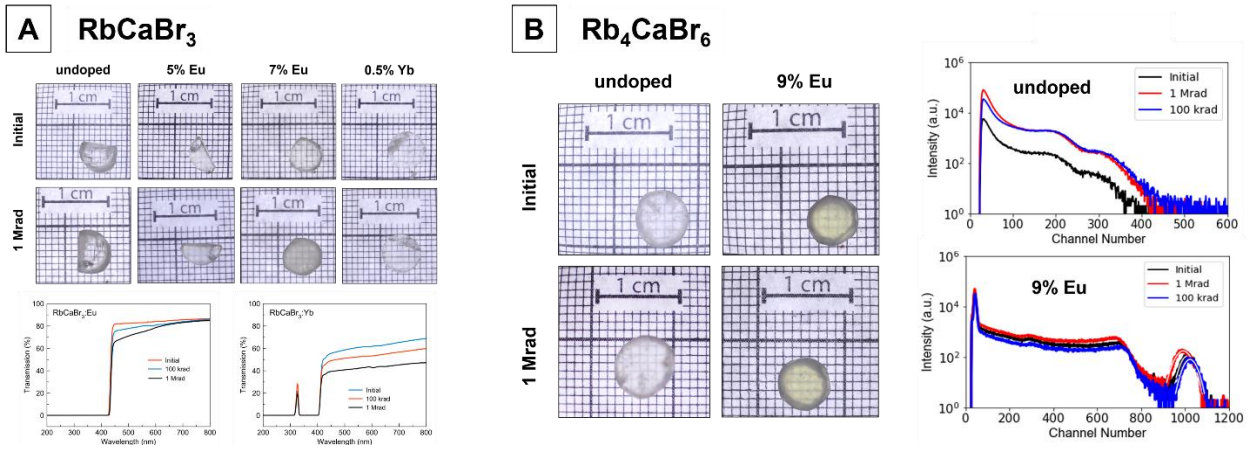


**Figure 90.** A) $RbCaBr_3$ crystals and B) $Rb_4CaBr_6$ crystals before and after irradiation with Co-60 to 100 krad and 1 Mrad.

### 8.4 Cesium Calcium Chloride ($CsCaCl_3$:(Eu, Tl)) – 100 krad and 1 Mrad, Co-60

Visual changes in the color of the undoped $CsCaCl_3$ crystal, $CsCaCl_3$:Eu, $CsCaCl_3$:Tl, and $CsCaCl_3$:Tl, Eu as a function of dose is shown in **Figure 91**. Changes in the optical transmittance and pulse height spectra are shown in **Figure 92**. The positions of the 662 keV photopeak resulting from Cs-137 excitation were compared to evaluate the relative light yield.

The visual appearance, optical transmittance, and pulse height spectra of undoped $CsCaCl_3$ changed significantly with dose point. After exposure to 100 krad, the colorless crystals became purple, which darkened in intensity after exposure to 1 Mrad. The transmittance of the undoped crystal decreased in the region 200-800 nm, with a dip around 370-470 nm and a more intense dip at 525 nm (~25% reduction in transmittance).

Noda et al. previously studied electron and hole trap states of undoped and Eu-doped $CsCaCl_3$ polycrystalline ceramics for storage phosphor applications using optical absorption spectra and thermoluminescence glow curves. Their dose range was from 65-2000 krad. In undoped $CsCaCl_3$, they found that two absorption bands formed with increased radiation exposure, ascribed to a Vk' center (370-450 nm) and an F-center (480-550 nm) [244]. In the present study, the pulse height spectra acquired with the undoped $CsCaCl_3$ crystals did not have a photopeak after exposure to both dose points.

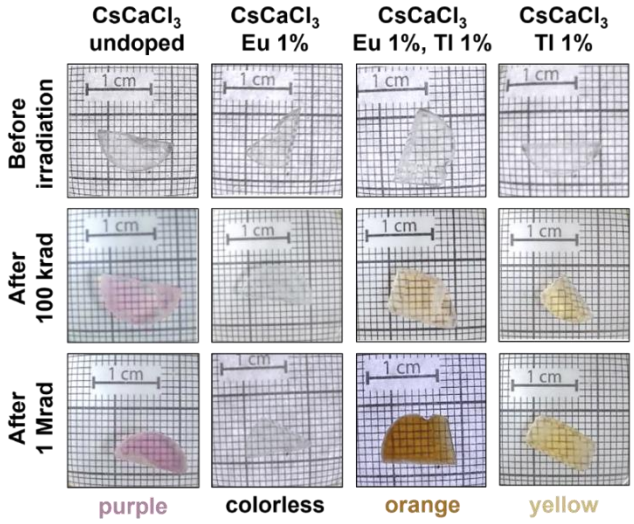


**Figure 91.** Changes in visual appearance of $CsCaCl_3$:(Eu, Tl) crystals after exposure to 100 krad ($10^5$ rad or 1 x $10^3$ Gy) and 1 Mrad ($10^6$ rad or 1 x $10^4$ Gy) dose points.

In contrast, the $CsCaCl_3$:Eu crystals exhibited no significant changes in appearance or in their pulse height spectra. The optical transmittance of $CsCaCl_3$:Eu decreased in the region of 425 to 750 nm, above the absorption edge of $Eu^{2+}$. Near 450 nm, the transmittance decreased by ~10% with increasing dose. Noda et al. ascribed an absorption band near 480-550 nm to an F-center that formed with increased radiation exposure. In this work, the light yield of the $CsCaCl_3$:Eu crystal changed just slightly (~4%) after exposure to the 100 krad dose. However, the photopeak was less defined. After exposure to the 1 Mrad dose, the light yield decreased by ~27%.

The $CsCaCl_3$:Tl crystal became yellow with radiation exposure, which deepened in intensity with increased dose. Two distinct dips in the optical transmittance of $CsCaCl_3$:Tl were found at ~325 nm and ~475 nm. Butterworth et al. studied the formation of color centers in KCl:Tl from Co-60 irradiation [245]. In KCl:Tl, an absorption from an F-center increased steadily with dose with a peak centered near 550 nm. Meanwhile, the $Tl^+$ absorption band became less distinct with increased dose. This was somewhat similar to behavior observed in $CsCaCl_3$:Tl, in which the 500 nm band increased in intensity and the 275 nm band decreased in intensity with dose. The position of the 662 keV photopeak of the thallium-doped crystals changed significantly after exposure to both dose points. The light yield of $CsCaCl_3$:Tl decreased by ~16% after 100 krad and by ~50% after 1 Mrad.

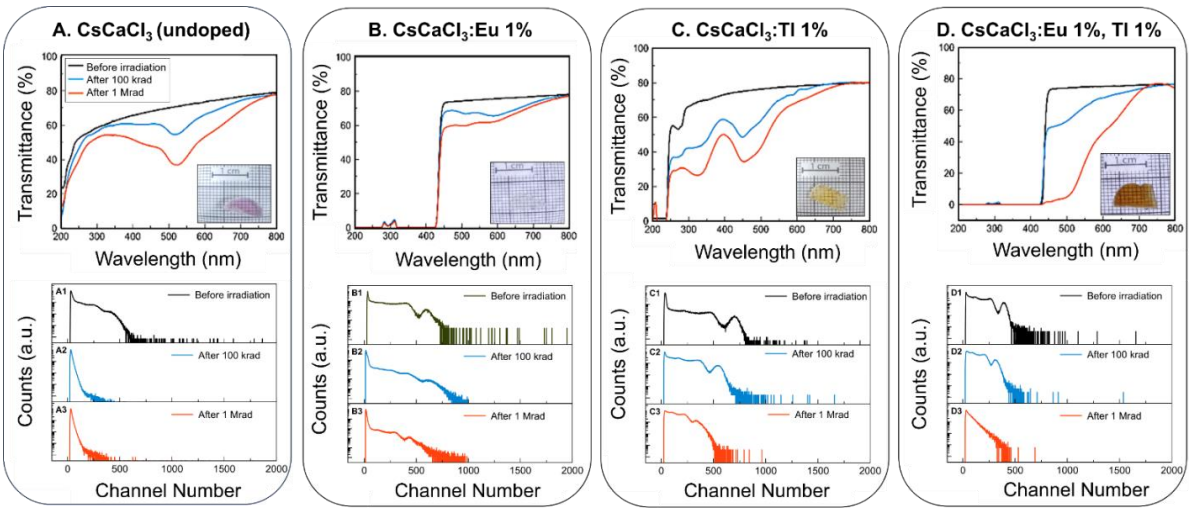


**Figure 92.** Changes in optical transmittance (top) and pulse height spectra (bottom) with dose (pre-irradiation in black, 100 krad in blue, and 1 Mrad in red) for $CsCaCl_3$ crystals.

The $CsCaCl_3$:Eu, Tl crystal showed the greatest change in visual appearance, becoming dark orange after 1 Mrad. Accordingly, the transmittance of $CsCaCl_3$:Eu, Tl decreased significantly with dose in the region 425-700 nm, coinciding with a 25% decrease after 100 krad and a 75% decrease after 1 Mrad at 500 nm. After exposure to 100 krad, the light yield of $CsCaCl_3$:Eu, Tl decreased by ~20%, and the pulse height spectrum for the sample exposed to 1 Mrad did not have a photopeak.

### 8.5 Rubidium Strontium Iodide ($RbSrI_3$) – 100 krad to 10 Mrad, Co-60 and X-ray linac

Pulse height spectra measured before and after irradiation with 100 krad and 1 Mrad doses at the Gamma Cave are compared in **Figure 93** for undoped $RbSrI_3$ and $RbSrI_3$:Eu 5 mol%. It appears that Eu-doping improved radiation hardness of $RbSrI_3$ crystals. The undoped crystal experienced a ~36% reduction in light yield after 1 Mrad, whereas the crystal doped with 5 mol% Eu only experienced a ~3% reduction.

Based on the promising performance of $RbSrI_3$:Eu up to 1 Mrad, the effect of higher dose points up to 10 Mrad were explored. **Figure 94** shows the crystals before and after irradiation, their optical transmittance spectra, and relative light yield as a function of dose. While there was a slight slope change in the optical transmittance spectra, distinct absorbance bands were not observed in the optical transmittance. Overall, there was a less than 2% change in light yield of $RbSrI_3$:Eu up to 10 Mrad.

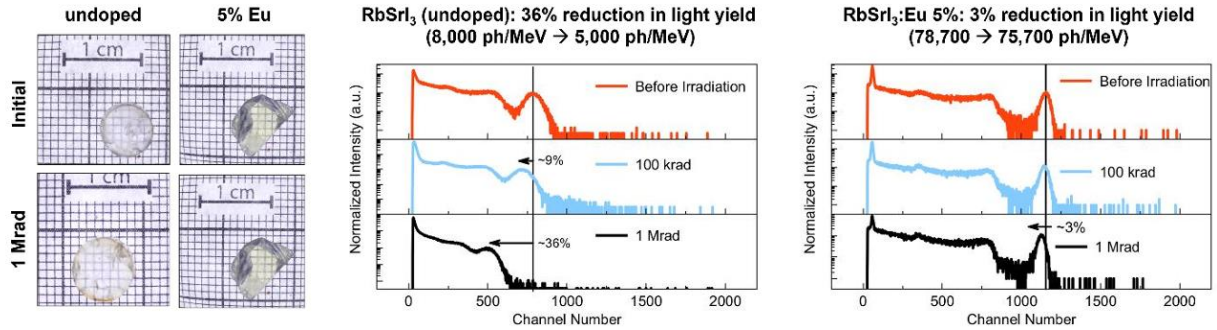


**Figure 93.** Comparison between pulse height spectra acquired with $RbSrI_3$ scintillators before irradiation and after irradiation with 100 krad and 1 Mrad doses (Co-60). Eu-doping appears to improve radiation hardness of $RbSrI_3$.

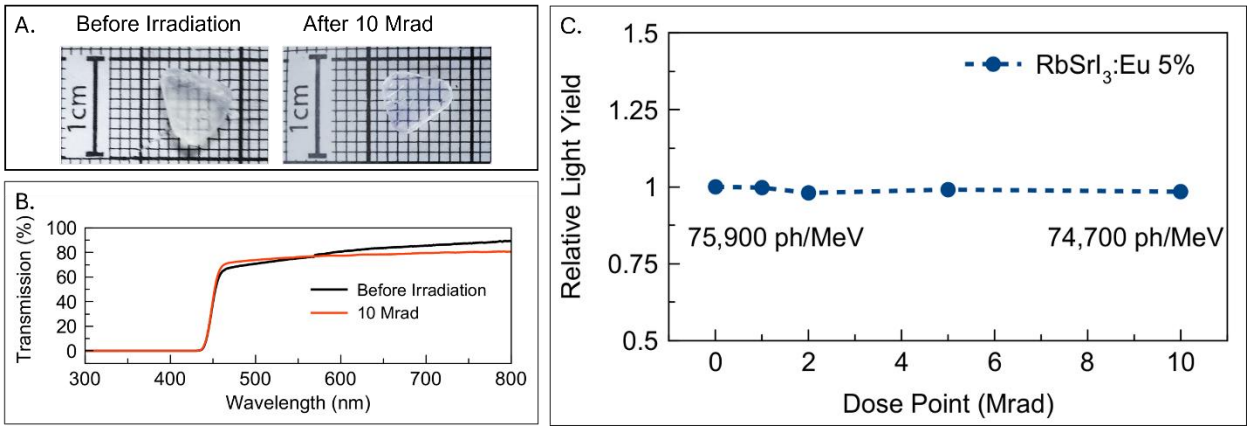


**Figure 94.** Characterization of $RbSrI_3$:Eu crystals before and after 10 Mrad Co-60 irradiation at the Gamma Cave, including A) visual inspection of the crystals, B) optical transmittance measurements, and C) light yield as a function of dose point.

Based on these promising results with Co-60, additional tests were done with the X-ray linac at UTK. The four samples tested were cut from the same cross-section of a Ø12 mm boule. The crystals and their properties before and after irradiation are shown in **Figure 95**. Immediately after irradiation at 10 Mrad, the crystals had a dim blue color that faded after a few minutes. The cause is not currently known, but it was hypothesized to relate to afterglow, since the scintillation emission wavelength is a similar blue color, 460 nm.

After irradiation, the crystals turned slightly yellow in color, especially after the 10 Mrad dose. The optical transmittance of the crystals before irradiation and after 2 Mrad did not show significant differences. However, the transmittance of the 10 Mrad crystal decreased by ~10% above the absorption edge, which was consistent with the yellow color of the crystals. Additionally, an absorbance peak near 310 nm increased. No other evidence of absorbance band formation was seen.

The position of the 662 keV photopeak decreased in the pulse height spectra before and after irradiation. After 2 Mrad, there was an ~8% decrease in light yield, and after 10 Mrad, there was an ~14% decrease in light yield. **Figure 96** shows the pulse height spectra acquired 24 hours after irradiation and ~3 weeks after irradiation. These showed activation of the crystals, especially after 10 Mrad.

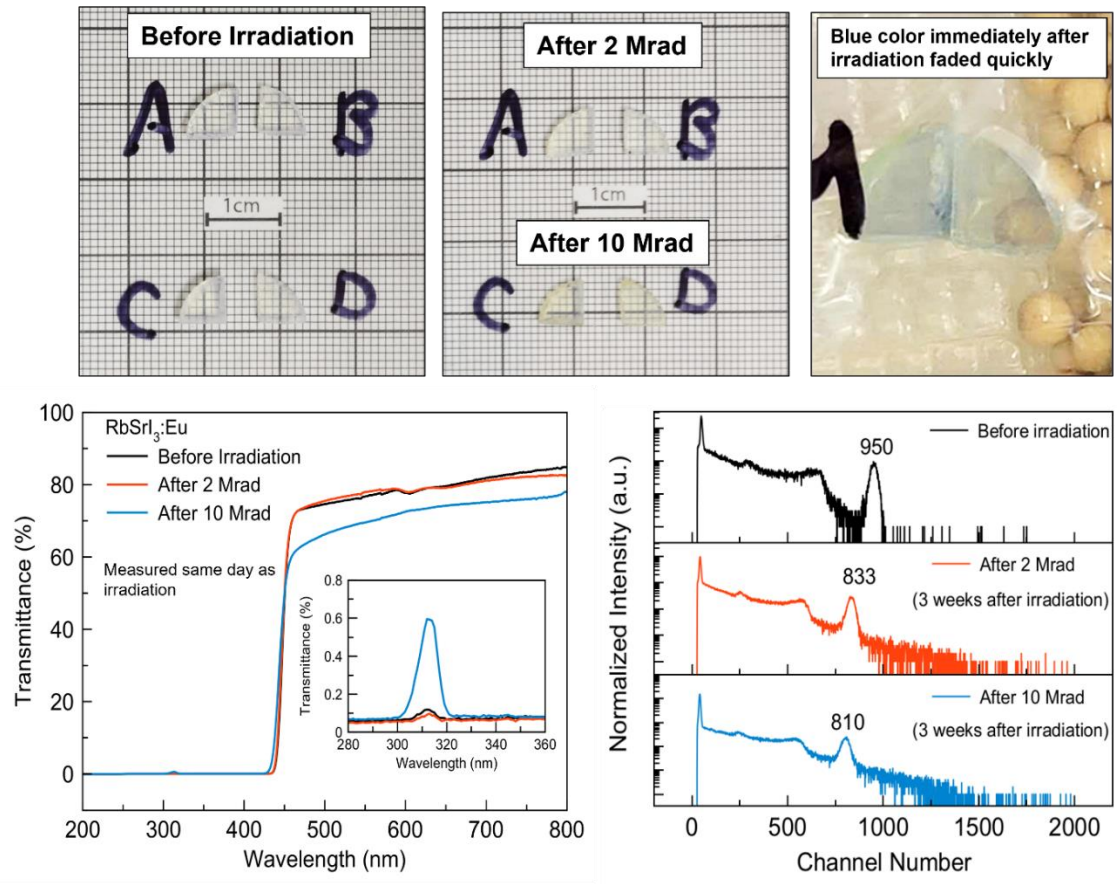


**Figure 95.** Eu-doped $RbSrI_3$ crystals before and after 2 and 10 Mrad doses with the Varian M9A linear accelerator. Immediately after irradiation, they had a dim blue color that faded after a few minutes.

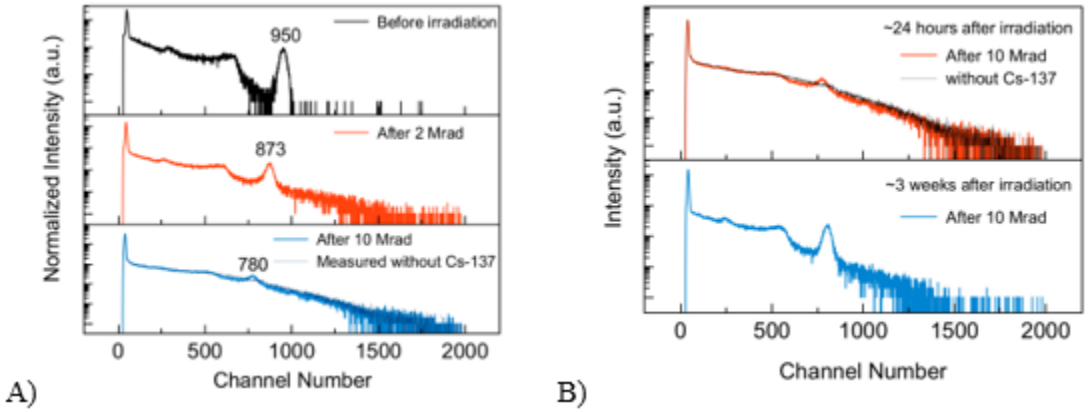


**Figure 96.** A) Pulse height spectra acquired approximately 24 hours after linac irradiation showed activation of the crystals at both dose points. B) After 3 weeks, this activation had decreased significantly.

### 8.6 Rubidium Strontium Bromide ($RbSr_2Br_5$) – 2 Mrad, 10 Mrad, Co-60

As an initial assessment of radiation hardness, $RbSr_2Br_5$ crystals were irradiated at the Gamma Cave Facility. The $RbSr_2Br_5$:Eu crystals before and after irradiation and their optical transmittance and pulse height spectra are shown in **Figure 97**.

The crystals became somewhat hazy once returned to UTK. This is thought to be associated with moisture degradation, rather than radiation damage. The $RbSr_2Br_5$ crystals had small bubbles within the crystal, which could have allowed moisture to infiltrate the crystal volume rather than degrading only the surface, which can be easily polished away. There was a decrease in optical transmittance of $RbSr_2Br_5$:Eu, which may relate to the hypothesized moisture degradation as well.

Like $RbSrI_3$, it appears that Eu-doping improved radiation hardness of $RbSr_2Br_5$ compared to the undoped crystal. The europium-doped crystals had a ~1% decrease in light yield. In contrast, the undoped crystal decreased by ~13% after 10 Mrad. Additionally, samples with different Eu-concentrations were tested (1-7 mol% Eu). Each crystal showed similar changes in optical transmittance and pulse height spectra. There was no obvious trend with dopant concentration.

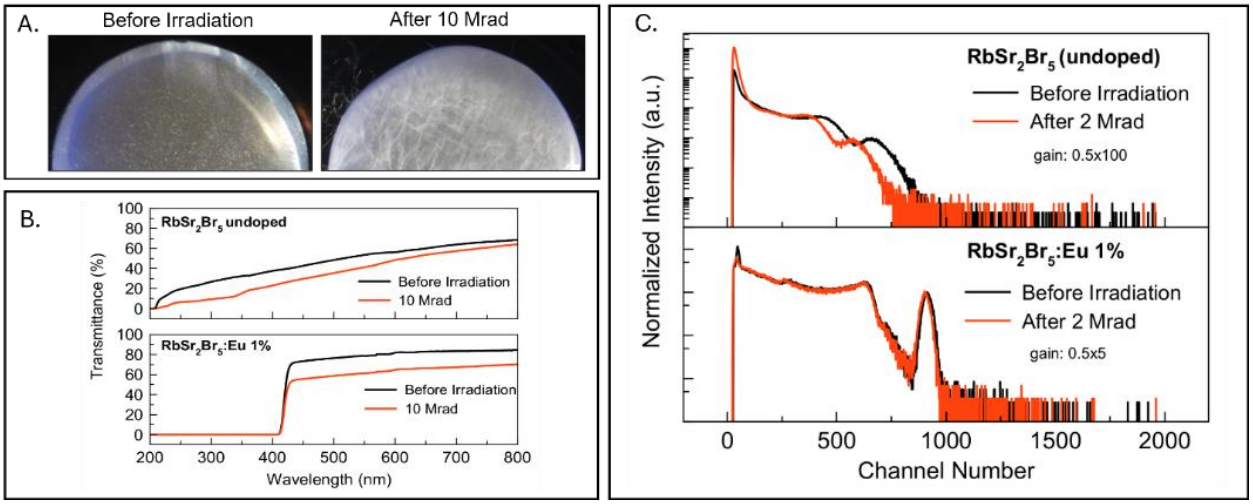


**Figure 97.** Characterization of $RbSr_2Br_5$:Eu crystals before and after Co-60 irradiation at the Gamma Cave, including A) visual inspection of the crystals under the optical microscope, B) optical transmittance measurements, and C) pulse height spectra measurements.

### 8.7 Rubidium Strontium Iodide ($RbSr_2I_5$) – 2 Mrad, 10 Mrad, Co-60 and X-ray linac

As an initial assessment of radiation hardness, $RbSr_2I_5$:Eu crystals were irradiated at the Gamma Cave Facility. The $RbSr_2I_5$:Eu crystals before and after irradiation and their optical transmittance and pulse height spectra are shown in **Figure 98** . There was very little change in their visual appearance, optical transmittance spectra, and pulse height spectra. There was a 1-4% decrease in light yield for the Eu-doped crystals after exposure to 10 Mrad.

Based on these promising results, crystals of $RbSr_2I_5$:1 mol% Eu were irradiated with the Varian M9A linear accelerator. The crystals, optical transmittance, and pulse height spectra acquired before and after irradiation to 2 and 10 Mrad dose points are shown in **Figure 99**. The crystals were Ø7, 2 mm and were cut from the same Ø7 mm boule.

Before irradiation, the crystals were colorless and highly transparent. After 2 Mrad, there was little change in the visual appearance of the crystals by eye. After 10 Mrad, the crystals became slightly yellow in color. This change in color was consistent with a 5-10% decrease in the optical transmittance of the crystals that was observed above the absorption edge, ~450-800 nm.

The relative light yield was compared by the channel number at the center of the 662 keV photopeak in the Cs-137 pulse height spectra measured ~24 hours after the irradiation. The light yield of the crystals had decreased by ~12% after 2 Mrad and by ~30% after 10 Mrad.

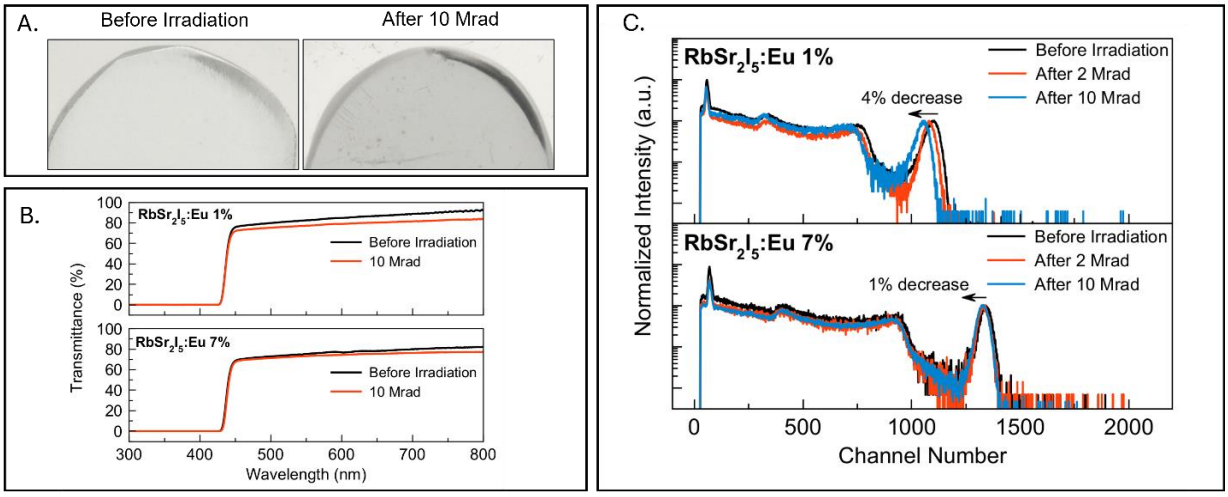


**Figure 98.** Characterization of $RbSr_2I_5$:Eu crystals before and after Co-60 irradiation at the Gamma Cave, including A) visual inspection of the crystals under the optical microscope, B) optical transmittance measurements, and C) pulse height spectra measurements

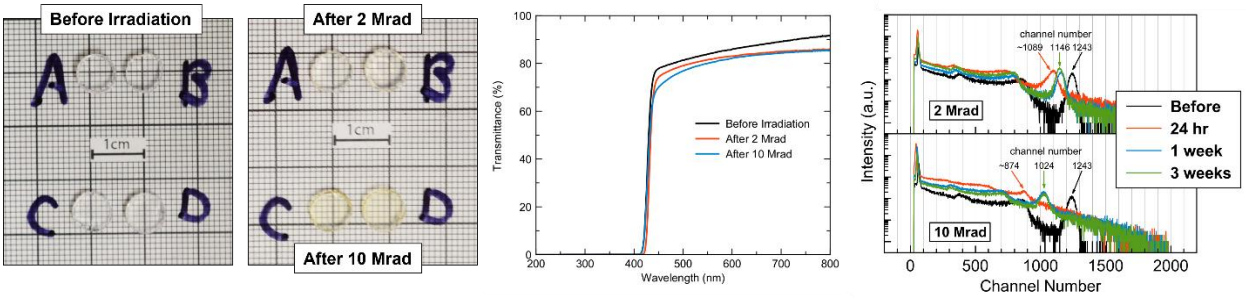


**Figure 99.** $RbSr_2I_5$:1% Eu crystals before and after 2 and 10 Mrad doses with the Varian M9A linear accelerator.

The crystals also showed activation from the irradiation, which contributed significant background counts in the pulse height spectra. After 1 and 3 weeks, the light yield had improved and the background counts had decreased. At this point, the decrease in light yield after 2 Mrad was ~8% and the decrease after 10 Mrad was ~18%.

### 8.8 Rubidium Calcium Iodide ($Rb_4CaI_6$) – 100 krad and 1 Mrad, Co-60

$Rb_4CaI_6$ crystals showed little change before and after irradiation, as shown in **Figure 100** and **Figure 101**. The crystals showed no significant changes in appearance by eye. Unfortunately, the already low optical transmittance of $Rb_4CaI_6$ crystals made comparison of the change in optical transmittance unviable. Instead, evidence of defect formation was investigated by measuring the optical absorbance for an undoped and a europium-doped crystal. Both crystals showed an increase in optical absorbance between 500-800 nm; however, there were no distinct absorbance bands that formed.

Their pulse height spectra were measured to investigate changes in light yield. For all $Rb_4CaI_6$ crystals tested, including the undoped crystal, Yb-doped, and Eu-doped crystals, the light yield did not show changes as a function of dose. One exception was $Rb_4CaI_6$:1 mol% Yb, which showed a decrease in light yield after 1 Mrad exposure. While this is overall a promising result, the poor transparency and phase purity of these crystals needs to be addressed.

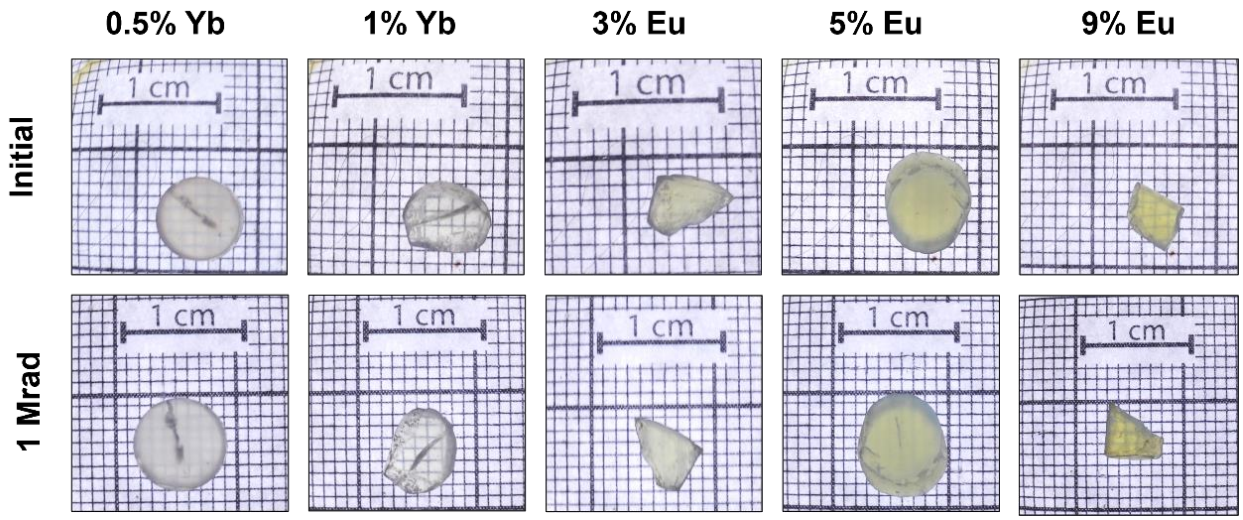


**Figure 100.** Backlit photos of $Rb_4CaI_6$ before and after irradiation.

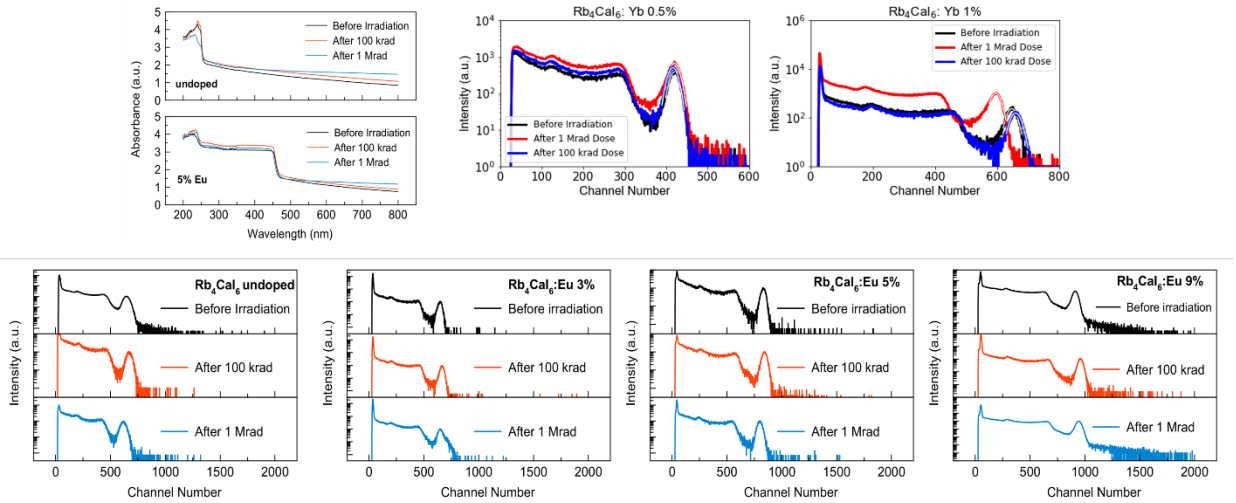


**Figure 101.** Optical absorbance and pulse height spectra measured for $Rb_4CaI_6$ crystals before and after 100 krad and 1 Mrad doses (Co-60).

# CHAPTER 9 SUMMARY AND OUTLOOK

Initially discovered in 1839, perovskite materials are experiencing a renaissance due to their promising optoelectronic properties almost two centuries later. For perovskite solar cells, the record power conversion efficiency jumped from 3.8% to 22.1% in 2016. In recent years, interest has grown in use of these materials for radiation detection. In the last decade, a large number of high-performance inorganic metal halide scintillators with excellent properties have been reported, including "three-dimensional" perovskites ($ABX_3$), $AB_2X_5$ compositions, and $A_4BX_6$ compositions ($A^+$ = Cs, K; $B^{2+}$ = Ca, Sr, Eu, Yb; $X^-$ = Cl, Br, I) materials. With light yields of 50,000 – 80,000 ph/MeV and energy resolutions of 3-6% at 662 keV, these materials were well-suited for gamma ray spectroscopy. This present work further expanded the compositional space, with a focus on rubidium-containing perovskites, and tested their properties oriented towards high-energy X-ray radiography applications.

High-energy X-ray radiography (0.5 – 9 MeV) enables high throughput and non-invasive screening of steel cargo containers, and the need for this technology is growing. The 2021 Securing America's Ports Act calls for the development of a plan to increase the scan rate of commercial vehicles, passenger vehicles, and rail freight entering the U.S. to 100%. In addition to testing the scintillation and luminescence properties, the X-ray afterglow, temperature stability, and radiation damage were explored in this work, in addition to crystal growth scale up in a 22 mm diameter size.

While different luminescent dopants were tested ($Eu^{2+}$, $Yb^{2+}$, $Tl^+$, $Ce^{3+}$) for some matrices, overall, $Eu^{2+}$ produced the highest scintillation performance. For the $ABX_3$ compositions, the slow spin-forbidden transition of $Yb^{2+}$ was dominant over the fast spin-allowed transition, which limited the measured light yield.

While overall interesting scintillators with some strong properties, less-promising materials for the application of interest were $CsCaCl_3$, $Rb_4CaBr_6$, and $Rb_4CaI_6$. Although they had scale up potential (12 mm diameter), the $CsCaCl_3$(Eu, Tl) crystals had relatively low scintillation performance (10,000 ph/MeV), high afterglow, and poor radiation tolerance. Additionally, they had the lowest density of all materials studied. One interesting finding, however, was that $CsCaCl_3$:Tl showed fast-neutron gamma discrimination with a FOM of 3.2 between gamma-rays and fast neutron captures that produce protons and a FOM of 1.6 between gamma-rays and fast

neutron captures that produce alpha particles. $Rb_4CaBr_6$:Eu and $Rb_4CaI_6$:Eu both had high light yields (> 70,000 ph/MeV), but their peritectic nature hindered the optical quality of the crystals. Another disadvantage of these $A_4BX_6$ crystals was their higher intrinsic radioactivity from Rb-87, due to a higher fraction of rubidium in their stoichiometry compared to the others.

Four promising materials were $RbCaBr_3$:Eu, $RbSrI_3$:Eu, $RbSr_2I_5$:Eu, and $RbSr_2Br_5$:Eu. $RbCaBr_3$:Eu had high scintillation performance, decent radiation resistance with Co-60, and crystal growth scale up potential to 22 mm diameter size. However, its low density and effective atomic number are a limitation, in addition to having an afterglow greater than CsI:Tl. On the other hand, $RbSrI_3$:Eu had higher density and effective atomic number, excellent scintillation performance (78,700 ph/MeV and 2.8% at 662 keV), and a low afterglow of 1.8% at 2 ms. It also had promising radiation tolerance with Co-60 and with 9 MV X-rays with the linear accelerator. The light yield decreased by ~3% with 10 Mrad via Co-60 and ~14% with 10 Mrad via the 9 MV X-rays. The mass attenuation coefficient was comparable to CsI:Tl at high energies (1-10 MeV). One major challenge for this material, however, is scaling up crystal growth. Despite an absence of structural phase-transitions on cooling (400°C to 25°C), congruent melting, and moderately anisotropic coefficients of thermal expansion, it consistently experienced significant cracking in a Ø22 mm size. However, high quality Ø12 mm crystals could be grown.

Two crystals that had excellent crystal growth scale up potential were $RbSr_2Br_5$:Eu and $RbSr_2I_5$:Eu. High quality crystals could be grown in Ø22 mm size, including at fast translation rates of 3.5 mm/hr for $RbSr_2I_5$:Eu. The scintillation properties, X-ray afterglow, and radiation tolerance were promising. In fact, the X-ray afterglow of $RbSr_2I_5$:1 mol% Eu was 0.79% at 2 ms. $RbSr_2Br_5$:Eu had an advantage in terms of hygroscopicity; after several hours in ambient conditions, the pulse height spectra remained constant. After more than a week in ambient conditions, the physical appearance of the crystal did not change, beyond fogging of the surface. $RbSr_2I_5$:Eu, however, was deliquescent. Overall, between the two, $RbSr_2I_5$:Eu was more promising due to higher density and effective atomic number and improved scintillation properties. Its mass attenuation coefficient was like CsI:Tl at high energies (1 – 10 MeV). After exposure to 9 MV X-rays with the linear accelerator, the light yield decreased by ~18% at 10 Mrad.

Barium-admixing of $RbSr_2I_5$:Eu led to improved scintillation performance, achieving light yields of 104,000 ph/MeV and an energy resolution of 2.3% at 662 keV. $Rb(Sr_{0.5},Ba_{0.5})_2I_5$:5 mol% Eu also had the lowest afterglow among the samples in this study, reaching 0.13% at 2 ms. However, dopant concentration effects, radiation tolerance, and scale up potential are unknown, so further investigations should still be pursued.

Properties of select scintillators from this work are shown in **Table 16,** compared to the ideal properties for high energy X-ray radiography. Based on these results, $RbSrI_3$:Eu and $RbSr_2I_5$:Eu were the most promising candidates, despite the scale up challenges of $RbSrI_3$:Eu. Their light yield stability versus temperature were investigated. In real-world applications, the detector system must function uniformly over a temperature range of ±55°C. $RbSrI_3$:Eu showed better stability, experiencing just a ~5% change, while the light yield of $RbSr_2I_5$:Eu changed by ~30% over this range, including a slight 10% increase at higher temperatures.

Future areas of work for these materials can include:

1) Fabricating rectangular pixels and examining their uniformity, as this will be the final form of a radiography detector array.
2) Investigating methods to encapsulate the crystals from moisture, and possibly thermal and mechanical shock.
3) Co-doping to further reduce the X-ray afterglow, supported by thermoluminescence measurements to understand trap structure.

**Table 16.** Properties of select scintillators from this work compared to requirements for high energy X-ray radiography.

| Scintillator | Density (g/cc) | $Z_{eff}$ | LY (ph/ MeV) | ER at 662 keV | Decay time (μs) | Afterglow | Hygro scopic | Scalable |
|---|---|---|---|---|---|---|---|---|
| $RbCaBr_3$:Eu 7 mol% Eu | 3.46 | 34 | 43,000 | 4% | 2.8 | > CsI:Tl | Yes, severe | Ø22 mm |
| $RbSrI_3$:5 mol% Eu | 4.1 | 49 | 78,700 | 2.8% | 1 | Low 1.8% at 2 ms | Yes, severe | Ø12 mm |
| $RbSr_2I_5$:5 mol% Eu | 4.6 | 49 | 90,000 | 2.9% | 1 (73%), 3.6 (27%) | Low 0.79% at 2 ms (1% Eu) 1.73% at 2 ms (5% Eu) | Yes, severe | Ø22 mm, fast growth |
| $Rb(Sr_{0.5},Ba_{0.5})_2I_5$: 5 mol% Eu | 4.7 | 51 | 96,000 | 2.3% | 1 (87%), 3.7 (18%) | Low 0.13% at 2 ms | Yes, minor | Unknown |
| $RbSr_2Br_5$:5 mol% Eu | 4.2 | 35 | 73,000 | 3.9% | 1.18 (76%), 2.4 (24%) | Low 1.50% at 2 ms | Yes, minor | Ø22 mm |
| $CdWO_4$ | 7.9 | 64 | 15,000 | 7.5% | 13 | Low 0.16% at 2 ms | No | Yes |
| CsI:Tl | 4.5 | 54 | 54,000 | 5.3% | 0.98 | High | Yes, minor | Yes |
| Ideal | > 5 | > 65 | > 30,000 | < 4% | < 10 | < 1% by 2 ms | No | Yes |

## LIST OF REFERENCES


1. Melcher, C., *Scintillators for well logging applications.* Nuclear Instruments and Methods in Physics Research Section B: Beam Interactions with Materials and Atoms, 1989. **40**: p. 1214-1218.
2. Lecoq, P., *Development of new scintillators for medical applications.* Nuclear Instruments and Methods in Physics Research Section A: Accelerators, Spectrometers, Detectors and Associated Equipment, 2016. **809**: p. 130-139.
3. Glodo, J., et al., *New developments in scintillators for security applications.* Physics Procedia, 2017. **90**: p. 285-290.
4. Kim, C., et al., *A review of inorganic scintillation crystals for extreme environments.* Crystals, 2021. **11**(6): p. 669.
5. van Blaaderen, J.J., et al., *Guidelines for the Selection of Scintillators for Indirect Photon-Counting X-ray Detectors.* Chemistry of Materials, 2025.
6. Lecoq, P., M. Schussler, and M. Schneegans, *Progress and prospects in the development of new scintillators for future high energy physics experiments.* Nuclear Instruments and Methods in Physics Research Section A: Accelerators, Spectrometers, Detectors and Associated Equipment, 1992. **315**(1-3): p. 337-343.
7. Knoll, G.F., *Radiation detection and measurement*. 2010: John Wiley & Sons.
8. Murty, R., *Effective atomic numbers of heterogeneous materials.* Nature, 1965. **207**(4995): p. 398-399.
9. Rodnyi, P., P. Dorenbos, and C. Van Eijk, *Energy loss in inorganic scintillators.* Physica Status Solidi (b), 1995. **187**(1): p. 15-29.
10. Rodnyi, P.A., *Physical processes in inorganic scintillators*. 2020: CRC press.
11. Derenzo, S., et al., *The quest for the ideal inorganic scintillator.* Nuclear Instruments and Methods in Physics Research Section A: Accelerators, Spectrometers, Detectors and Associated Equipment, 2003. **505**(1-2): p. 111-117.
12. Melcher, C., *Perspectives on the future development of new scintillators.* Nuclear Instruments and Methods in Physics Research Section A: Accelerators, Spectrometers, Detectors and Associated Equipment, 2005. **537**(1-2): p. 6-14.

13. Nikl, M., *Scintillation detectors for x-rays.* Measurement Science and Technology, 2006. **17**(4): p. R37.
14. Weber, M.J., *Inorganic scintillators: today and tomorrow.* Journal of Luminescence, 2002. **100**(1-4): p. 35-45.
15. Dorenbos, P., *The quest for high resolution γ-ray scintillators.* Optical Materials: X, 2019. **1**: p. 100021.
16. Wang, Z., et al., *Needs, trends, and advances in scintillators for radiographic imaging and tomography.* IEEE Transactions on Nuclear Science, 2023.
17. *Securing America's Ports Act*, in *116-299*. 2021, H.R. 5273 - 116th Congress of the United States. p. 4906-4908.
18. Chen, G., *Understanding X-ray cargo imaging.* Nuclear Instruments and Methods in Physics Research Section B: Beam Interactions with Materials and Atoms, 2005. **241**(1-4): p. 810-815.
19. Standard, A.N., *Determination of the Imaging Performance of X-Ray and Gamma-Ray Systems for Cargo and Vehicle Security Screening*. 2017, Institute of Electrical and Electronics Engineers, Inc.
20. Institute, A.N.S., *Evaluation and Performance of Radiation Detection Portal Monitors for Use in Homeland Security*. 2016, Institute of Electrical and Electronics Engineers, Inc.
21. Boatner, L.A., et al., *The characterization of scintillator performance at temperatures up to 400 degrees centigrade.* Nuclear Instruments and Methods in Physics Research Section A: Accelerators, Spectrometers, Detectors and Associated Equipment, 2013. **709**: p. 95-107.
22. Bendahan, J., *Review of active interrogation techniques.* Nuclear Instruments and Methods in Physics Research Section A: Accelerators, Spectrometers, Detectors and Associated Equipment, 2020. **954**: p. 161120.
23. Bendahan, J., *Vehicle and cargo scanning for contraband.* Physics Procedia, 2017. **90**: p. 242-255.
24. Siewerdsen, J. and D. Jaffray, *A ghost story: Spatio-temporal response characteristics of an indirect-detection flat-panel imager.* Medical physics, 1999. **26**(8): p. 1624-1641.

25. Qiu, X., et al., *Mechanical properties and machinability of GYGAG:Ce ceramic scintillators.* Ceramics International, 2020. **46**(4): p. 4550-4555.
26. (NUSTL), N.U.S.T.L., *Mobile X-ray Systems for Search and Inspection Market Survey Report*. 2012, Department of Homeland Security.
27. Burachas, S.P., et al., *Large volume $CdWO_4$ crystal scintillators.* Nuclear Instruments and Methods in Physics Research Section A: Accelerators, Spectrometers, Detectors and Associated Equipment, 1996. **369**(1): p. 164-168.
28. Kobayashi, M., et al., *Cadmium tungstate scintillators with excellent radiation hardness and low background.* Nuclear Instruments and Methods in Physics Research Section A: Accelerators, Spectrometers, Detectors and Associated Equipment, 1994. **349**(2-3): p. 407-411.
29. Lutz, S.S. and S.A. Baker, *Scintillator evaluation for high-energy X-ray diagnostics*. 2001, Bechtel Nevada Corporation (US).
30. Nagarkar, V.V., et al., *Suppression of Afterglow in Microcolumnar CsI:Tl by Codoping With $Sm^{2+}$Recent Advances.* IEEE Transactions on Nuclear Science, 2009. **56**(3): p. 565-569.
31. Brecher, C., et al., *Suppression of afterglow in CsI:Tl by codoping with $Eu^{2+}$*. Nuclear Instruments and Methods in Physics Research Section A: Accelerators, Spectrometers, Detectors and Associated Equipment, 2006. **558**(2): p. 450-457.
32. Cherepy, N., et al. *Transparent ceramic scintillators for gamma spectroscopy and MeV imaging*. in *Hard X-ray, Gamma-ray, and neutron detector physics XVII*. 2015. SPIE.
33. Duclos, S.J., et al., *Development of the HiLightTM scintillator for computed tomography medical imaging.* Nuclear Instruments and Methods in Physics Research Section A: Accelerators, Spectrometers, Detectors and Associated Equipment, 2003. **505**(1): p. 68-71.
34. Zhou, F., et al., *Halide Perovskite, a potential scintillator for X-ray detection.* Small Methods, 2020. **4**(10): p. 2000506.
35. Zhou, Y., et al., *Metal halide perovskites for X-ray imaging scintillators and detectors.* ACS Energy Letters, 2021. **6**(2): p. 739-768.

36. Stoumpos, C.C. and M.G. Kanatzidis, *The renaissance of halide perovskites and their evolution as emerging semiconductors.* Accounts of Chemical Research, 2015. **48**(10): p. 2791-2802.
37. Stoumpos, C.C. and M.G. Kanatzidis, *Halide Perovskites: poor man's high-performance semiconductors.* Advanced Materials, 2016. **28**(28): p. 5778-5793.
38. Xiao, Z. and Y. Yan, *Progress in theoretical study of metal halide perovskite solar cell materials.* Advanced Energy Materials, 2017. **7**(22): p. 1701136.
39. Tian, J., et al., *Inorganic halide perovskite solar cells: progress and challenges.* Advanced Energy Materials, 2020. **10**(23): p. 2000183.
40. Boyd, C.C., et al., *Understanding degradation mechanisms and improving stability of perovskite photovoltaics.* Chemical Reviews, 2018. **119**(5): p. 3418-3451.
41. Wang, D., et al., *Stability of perovskite solar cells.* Solar Energy Materials and Solar Cells, 2016. **147**: p. 255-275.
42. Katz, E.A., *Perovskite: name puzzle and German-Russian odyssey of discovery.* Helvetica Chimica Acta, 2020. **103**(6): p. e2000061.
43. Goldschmidt, V.M., *Die gesetze der krystallochemie.* Naturwissenschaften, 1926. **14**(21): p. 477-485.
44. Tanaka, H., T. Oku, and N. Ueoka, *Structural stabilities of organic–inorganic perovskite crystals.* Japanese Journal of Applied Physics, 2018. **57**(8S3): p. 08RE12.
45. Akkerman, Q.A. and L. Manna, *What defines a halide perovskite?* ACS Energy Letters, 2020. **5**(2): p. 604-610.
46. Breternitz, J. and S. Schorr, *What defines a perovskite?* Advanced Energy Materials, 2018. **8**(34): p. 1802366.
47. Prasanna, R., et al., *Band Gap Tuning via Lattice Contraction and Octahedral Tilting in Perovskite Materials for Photovoltaics.* Journal of the American Ceramic Society, 2017. **139**(32): p. 11117-11124.
48. Almutlaq, J., et al., *The benefit and challenges of zero-dimensional perovskites.* The Journal of Physical Chemistry Letters, 2018. **9**(14): p. 4131-4138.
49. Guo, Y., et al., *Recent Advances in All-Inorganic Zero-Dimensional Metal Halides.* ChemPlusChem, 2021. **86**(12): p. 1577-1585.

50. Wen, X., et al., *Synthesis and Characterization of All-Inorganic Perovskite CsEuBr3 Single-Crystal Scintillator.* Physica Status Solidi (RRL)–Rapid Research Letters, 2023. **17**(3): p. 2200341.
51. Wu, Y., et al., *Quaternary iodide K(Ca,Sr)$I_3$:$Eu^{2+}$ single-crystal scintillators for radiation detection: crystal structure, electronic structure, and optical and scintillation properties.* Advanced Optical Materials, 2016. **4**(10): p. 1518-1532.
52. Yang, K., et al. *Optical and scintillation properties of single crystal $CsSr_{1-x}Eu_xI_3$.* in *IEEE Nuclear Science Symposuim & Medical Imaging Conference*. 2010. IEEE.
53. Grippa, A.Y., et al., *Crystal growth and scintillation properties of $CsCaBr_3$:$Eu^{2+}$ ($CsCa_{1-x}Eu_xBr_3$, $0 \leq x \leq 0.08$).* Journal of Crystal Growth, 2013. **371**: p. 112-116.
54. Cherginets, V., et al., *Scintillation properties of $CsSrX_3$:$Eu^{2+}$($CsSr_{1-y}Eu_yX_3$, X= Cl, Br; $0 \leq y \leq 0.05$) single crystals grown by the Bridgman method.* Materials Chemistry and Physics, 2014. **143**(3): p. 1296-1299.
55. Sun, S., et al., *0D perovskites: unique properties, synthesis, and their applications.* Advanced Science, 2021. **8**(24): p. 2102689.
56. Stand, L., et al., *Characterization of mixed halide scintillators: $CsSrBrI_2$:Eu, $CsCaBrI_2$:Eu and $CsSrClBr_2$:Eu.* Journal of Luminescence, 2019. **207**: p. 70-77.
57. Stand, L., et al., *Crystal growth and scintillation properties of $Eu^{2+}$ doped $Cs_4CaI_6$ and $Cs_4SrI_6$.* Journal of Crystal Growth, 2018. **486**: p. 162-168.
58. Rutstrom, D., et al., *Crystal growth and scintillation properties of new ytterbium-activated scintillators $Cs_4CaI_6$: Yb and $Cs_4SrI_6$:Yb.* Optical Materials, 2020. **110**: p. 110536.
59. Wu, Y., et al., *Zero-dimensional $Cs_4EuX_6$ (X= Br, I) all-inorganic perovskite single crystals for gamma-ray spectroscopy.* Journal of Materials Chemistry C, 2018. **6**(25): p. 6647-6655.
60. Wu, Y., et al., *Crystal structure, electronic structure, optical and scintillation properties of self-activated $Cs_4YbI_6$.* Journal of Luminescence, 2018. **201**: p. 460-465.
61. Rebrova, N., et al., *Scintillation properties of crystals based on ternary bromides of calcium and alkali metals activated with europium.* Crystal Research and Technology, 2017. **52**(6): p. 1600404.

62. Johnson, J.A., et al., *Discovery of new compounds and scintillators of the $A_4BX_6$ family: crystal structure, thermal, optical, and scintillation properties.* Crystal Growth & Design, 2018. **18**(9): p. 5220-5230.
63. Yang, K., M. Zhuravleva, and C.L. Melcher, *Crystal growth and characterization of $CsSr_{1-x}Eu_xI_3$ high light yield scintillators.* Physica Status Solidi (RRL)–Rapid Research Letters, 2011. **5**(1): p. 43-45.
64. Rebrova, N., et al., *Crystal growth and characterization of $Eu^{2+}$ doped $RbCaX_3$ (X= Cl, Br) scintillators.* Journal of Crystal Growth, 2017. **466**: p. 39-44.
65. Rebrova, N., et al., *Effects of europium concentration on luminescent and scintillation performance of $Cs_{0.2}Rb_{0.8}Ca_{1-x}Eu_xBr_3$ ($0 \leq x \leq 0.08$) crystals.* Journal of Rare Earths, 2022. **40**(1): p. 29-33.
66. Rebrova, N., et al., *Crystal growth and characterization of $Eu^{2+}$ doped $Cs_{1-x}Rb_xCaBr_3$.* Journal of Alloys and Compounds, 2020. **816**: p. 152594.
67. Raipurkar, J., et al., *Luminescence of some 3d activators in $RbCaCl_3$.* Journal of Luminescence, 2013. **136**: p. 365-368.
68. Raipurkar, J., et al., *Luminescence of $Yb^{2+}$ in $RbCaCl_3$.* Journal of Luminescence, 2013. **134**: p. 456-458.
69. Stand, L., et al., *New high performing scintillators: $RbSr_2Br_5$: Eu and $RbSr_2I_5$: Eu.* Optical Materials, 2017. **73**: p. 408-414.
70. Rowe, E., et al., *A New Lanthanide Activator for Iodide Based Scintillators: $Yb^{2+}$*. IEEE Transactions on Nuclear Science, 2013. **60**(2): p. 1057-1060.
71. Alekhin, M.S., et al., *Optical and scintillation properties of $SrI_2$:$Yb^{2+}$*. Optical Materials, 2014. **37**: p. 382-386.
72. Cherepy, N., et al. *$SrI_2$ scintillator for gamma ray spectroscopy*. in *Hard X-Ray, Gamma-Ray, and Neutron Detector Physics XI*. 2009. SPIE.
73. Cherepy, N.J., et al., *Scintillators with potential to supersede lanthanum bromide.* IEEE Transactions on Nuclear Science, 2009. **56**(3): p. 873-880.
74. Glodo, J., et al., *Concentration effects in Eu doped $SrI_2$.* IEEE Transactions on Nuclear Science, 2010. **57**(3): p. 1228-1232.

75. Alekhin, M.S., et al. *Scintillation properties and self absorption in $SrI_2:Eu^{2+}$*. in *IEEE Nuclear Science Symposuim & Medical Imaging Conference*. 2010. IEEE.
76. De Haas, J.T. and P. Dorenbos, *Advances in yield calibration of scintillators.* IEEE Transactions on Nuclear Science, 2008. **55**(3): p. 1086-1092.
77. Rutstrom, D., et al., *Europium concentration effects on the scintillation properties of $Cs_4SrI_6$: Eu and $Cs_4CaI_6$: Eu single crystals for use in gamma spectroscopy.* Journal of Luminescence, 2019. **216**: p. 116740.
78. Stand, L., et al., *Scintillation properties of $Eu^{2+}$-doped $KBa_2I_5$ and $K_2BaI_4$.* Journal of Luminescence, 2016. **169**: p. 301-307.
79. Zhuravleva, M., et al., *New single crystal scintillators: $CsCaCl_3$:Eu and $CsCaI_3$:Eu.* Journal of Crystal Growth, 2012. **352**(1): p. 115-119.
80. Wu, Y., et al., *$Eu^{2+}$ concentration effects in $KCa_{0.8}Sr_{0.2}I_3:Eu^{2+}$: A novel high-performance scintillator.* Nuclear Instruments and Methods in Physics Research Section A: Accelerators, Spectrometers, Detectors and Associated Equipment, 2016. **820**: p. 132-140.
81. Alekhin, M.S., et al., *Optical and scintillation properties of $CsBa_2I_5:Eu^{2+}$*. Journal of luminescence, 2014. **145**: p. 723-728.
82. Stand, L., et al., *Gamma-ray spectroscopic characterization of long, rapidly-grown $KSr_2I_5$:Eu crystals.* Nuclear Instruments and Methods in Physics Research Section A: Accelerators, Spectrometers, Detectors and Associated Equipment, 2020. **962**: p. 163700.
83. Stand, L., et al., *Exploring growth conditions and $Eu^{2+}$ concentration effects for $KSr_2I_5$: Eu scintillator crystals.* Journal of Crystal Growth, 2016. **439**: p. 93-98.
84. Stand, L., et al., *Exploring growth conditions and $Eu^{2+}$ concentration effects for $KSr_2I_5$:Eu scintillator crystals II: Ø 25 mm crystals.* Journal of Crystal Growth, 2018. **483**: p. 301-307.
85. Zhang, J., et al., *A brief review of co-doping.* Frontiers of physics, 2016. **11**: p. 1-21.
86. Kamada, K., et al., *Co-doping effects on luminescence and scintillation properties of Ce doped $Lu_3Al_5O_{12}$ scintillator.* Nuclear Instruments and Methods in Physics Research Section A: Accelerators, Spectrometers, Detectors and Associated Equipment, 2015. **782**: p. 9-12.

87. Spurrier, M.A., et al., *Effects of $Ca^{2+}$ Co-Doping on the Scintillation Properties of LSO:Ce.* IEEE Transactions on Nuclear Science, 2008. **55**(3): p. 1178-1182.
88. Quarati, F., et al., *Co-doping of $CeBr_3$ scintillator detectors for energy resolution enhancement.* Nuclear Instruments and Methods in Physics Research Section A: Accelerators, Spectrometers, Detectors and Associated Equipment, 2014. **735**: p. 655-658.
89. Nagarkar, V.V., et al., *Suppression of Afterglow in Microcolumnar CsI:Tl by Codoping With $Sm^{2+}$ Recent Advances.* IEEE Transactions on Nuclear Science, 2009. **56**(3): p. 565-569.
90. Ovechkina, E., et al., *Multiple doping of CsI:Tl crystals and its effect on afterglow.* Radiation Measurements, 2007. **42**(4-5): p. 541-544.
91. Wu, Y., et al., *Ultralow-concentration Sm codoping in CsI:Tl scintillator: A case of little things can make a big difference.* Optical Materials, 2014. **38**: p. 297-300.
92. Johnson, T.D. and W.D. Kulp, *Nuclear Data Sheets for A = 87.* Nuclear Data Sheets, 2015. **129**: p. 1-190.
93. Yao, R., T. Ma, and Y. Shao. *Effects of LSO detector intrisic radioactivity on SPECT imaging*. in *2007 IEEE Nuclear Science Symposium Conference Record*. 2007. IEEE.
94. Alva-Sánchez, H., et al., *Understanding the intrinsic radioactivity energy spectrum from $^{176}Lu$ in LYSO/LSO scintillation crystals.* Scientific Reports, 2018. **8**(1): p. 1-7.
95. Garandet, J. and T. Alboussiere, *Bridgman growth: modelling and experiments.* Progress in Crystal Growth and Characterization of Materials, 1999. **38**(1-4): p. 133-159.
96. Stockbarger, D.C., *The production of large single crystals of lithium fluoride.* Review of Scientific Instruments, 1936. **7**(3): p. 133-136.
97. Stockbarger, D.C., *Improved crystallization of lithium fluoride of optical quality.* Discussions of the Faraday Society, 1949. **5**: p. 299-306.
98. Chang, C.E. and W.R. Wilcox, *Control of interface shape in the vertical Bridgman-Stockbarger technique.* Journal of Crystal Growth, 1974. **21**(1): p. 135-140.
99. Fu, T.-W. and W.R. Wilcox, *Influence of insulation on stability of interface shape and position in the vertical Bridgman-Stockbarger technique.* Journal of Crystal Growth, 1980. **48**(3): p. 416-424.

100. Seifert, H. and U. Langenbach, *Thermoanalytische und röntgenographische untersuchungen an systemen alkalichlorid/calciumchlorid.* Zeitschrift für anorganische und allgemeine Chemie, 1969. **368**(1-2): p. 36-43.
101. Seifert, H.J. and D. Haberhauer, *Über die Systeme Alkalimetallbromid/Calciumbromid.* Zeitschrift für anorganische und allgemeine Chemie, 1982. **491**(1): p. 301-307.
102. Paul, M. and H. Seifert, *EMF-measurements with galvanic bromine cells in the systems $RBr/MBr_2$ (M= Sr, Ba).* Journal of Thermal Analysis, 1989. **35**(2): p. 585-593.
103. Seirfert, H.J., *Thermochemische Und Strukturelle Untersuchungen An Systemen Aus Alkalimetalliodid Und $MgI_2$ (1) Bzw. $CaI_2$ (2).* 1980.
104. Shannon, R.D., *Revised effective ionic radii and systematic studies of interatomic distances in halides and chalcogenides.* Acta Crystallographica Section A: crystal physics, diffraction, theoretical and general crystallography, 1976. **32**(5): p. 751-767.
105. Toby, B.H. and R.B. Von Dreele, *GSAS-II: the genesis of a modern open-source all purpose crystallography software package.* Journal of Applied Crystallography, 2013. **46**(2): p. 544-549.
106. Zhuravleva, M., et al. *Hygroscopicity evaluation of halide scintillators*. in *2013 IEEE Nuclear Science Symposium and Medical Imaging Conference (2013 NSS/MIC)*. 2013. IEEE.
107. Viezbicke, B.D., et al., *Evaluation of the Tauc method for optical absorption edge determination: ZnO thin films as a model system.* Physica Status Solidi (b), 2015. **252**(8): p. 1700-1710.
108. Tauc, J., R. Grigorovici, and A. Vancu, *Optical properties and electronic structure of amorphous germanium.* Physica Status Solidi (b), 1966. **15**(2): p. 627-637.
109. Mizoi, K., et al., *Photoluminescence and scintillation properties of $Yb^{2+}$-doped $ACaCl_3$ (A= Cs, Rb, K) crystals.* Journal of Luminescence, 2020. **227**: p. 117521.
110. Grippa, A.Y., et al., *Scintillation properties of $ACa_{1-}$ $yEuyX_3$ (A= K, Rb, Cs, X= Cl, Br) crystals.* Functional Materials, 2018.
111. *T-$RbCaBr_3$ ($RbCaBr_3$ rt) Crystal Structure: Datasheet from "PAULING FILE Multinaries Edition – 2022" in SpringerMaterials*, P. Villars and K. Cenzual, Editors.,

Springer-Verlag Berlin Heidelberg & Material Phases Data System (MPDS), Switzerland & National Institute for Materials Science (NIMS), Japan.

112. Momma, K. and F. Izumi, *VESTA: a three-dimensional visualization system for electronic and structural analysis.* Journal of Applied Crystallography, 2008. **41**(3): p. 653-658.

113. Emons, H., G. Bräutigam, and W. Horlbeck, *Untersuchungen zum Phasengleichgewicht fest—flüssig in binären Mischungen aus Erdalkalimetall-und Alkalimetallbromiden.* Chem. zvesti, 1976. **30**: p. 748.

114. Okumura, R., T. Oku, and A. Suzuki, *Electronic structures and properties of lead-free cesium-or rubidium-based perovskite halide compounds by first-principles calculations.* Nano Trends, 2023. **4**: p. 100020.

115. Grippa, A.Y., et al., *Crystal growth and scintillation properties of $CsCaBr_3:Eu^{2+}$ ($CsCa_{1-x}Eu_xBr_3$, $0 \leq x \leq 0.08$).* Journal of Crystal Growth, 2013. **371**: p. 112-116.

116. Tyagi, M., M. Zhuravleva, and C. Melcher, *Theoretical and experimental characterization of promising new scintillators: $Eu^{2+}$ doped $CsCaCl_3$ and $CsCaI_3$.* Journal of Applied Physics, 2013. **113**(20).

117. Zhang, Y., et al., *$Eu^{2+}$: $CsCaX_3$ (X= Cl, Br, I) perovskite nanocrystals in glasses for blue light-emitting applications.* Journal of Materials Chemistry C, 2023. **11**(30): p. 10389-10397.

118. Rebrova, N., et al., *Scintillation properties of $Eu^{2+}$ activated $CsCaCl_{3-x}Br_x$ (x= 1, 1.5, 2).* Journal of Luminescence, 2017. **182**: p. 172-176.

119. Mizoi, K., et al., *Evaluation of photoluminescence and scintillation properties of Yb2+-doped $CsMX_3$ (M= Ca, Sr; X= Cl, Br) crystals.* Journal of Luminescence, 2022. **245**: p. 118797.

120. Rahman, A.U., et al., *Electronic and Thermoelectric Properties of $Yb^{2+}$-Doped Cubic Perovskite $CsCaCl_3$: A First-Principles Study.* Journal of Electronic Materials, 2024. **53**(1): p. 312-321.

121. Suta, M., et al., *Photoluminescence properties of $Yb^{2+}$ ions doped in the perovskites $CsCaX_3$ and $CsSrX_3$ (X= Cl, Br, and I)–a comparative study.* Physical Chemistry Chemical Physics, 2016. **18**(19): p. 13196-13208.

122. Suta, M. and C. Wickleder, *Spin Crossover of $Yb^{2+}$ in $CsCaX_3$ and $CsSrX_3$ (X= Cl, Br, I)–A Guideline to Novel Halide-Based Scintillators.* Advanced Functional Materials, 2017. **27**(2): p. 1602783.

123. Fujimoto, Y., et al., *Photoluminescence and radiation response properties of $Ce^{3+}$-doped $CsCaCl_3$ crystalline scintillator*. Physica Scripta, 2016. **91**(9): p. 094002.

124. Grimm, J., E. Beurer, and H.U. Güdel, *Crystal Absorption Spectra in the Region of 4f− 4f and 4f−5d Excitations in $Tm^{2+}$-Doped $CsCaCl_3$, $CsCaBr_3$, and $CsCaI_3$.* Inorganic Chemistry, 2006. **45**(26): p. 10905-10908.

125. Grimm, J., et al., *Light-emission and excited-state dynamics in $Tm^{2+}$ doped $CsCaCl_3$, $CsCaBr_3$, and $CsCaI_3$.* The Journal of Physical Chemistry B, 2006. **110**(5): p. 2093-2101.

126. Liu, Z., et al., *The unique luminescent properties and enhanced thermal stability of a novel all-inorganic perovskite $CsCaCl_3$: $Mn^{2+}$ for solid-state lighting applications.* Journal of Materials Chemistry C, 2024. **12**(4): p. 1309-1316.

127. Kubota, K. and T. Kawai, *Optical characteristics of $Tl^+$ centers in $CsCaCl_3$, $KCaCl_3$, and CsCl crystals.* Journal of Physics and Chemistry of Solids, 2022. **163**: p. 110592.

128. Zhuravleva, M., et al., *New single crystal scintillators: $CsCaCl_3$:Eu and $CsCaI_3$:Eu.* Journal of Crystal Growth, 2012. **352**(1): p. 115-119.

129. 佐伯啓一郎, et al. *$Tl^+$ 添加 $CsCaCl_3$ 結晶のシンチレーション特性*. in *応用物理学会学術講演会講演予稿集 第 76 回応用物理学会秋季学術講演会*. 2015. 公益社団法人応用物理学会.

130. Van Loef, E., et al., *Crystal Growth, Density Functional Theory, and Scintillation Properties of $TlCaX_3$ (X= Cl, Br, I).* IEEE Transactions on Nuclear Science, 2023.

131. Edgar Van Loef, J.G., Pijush Bhattacharya, Lakshmi Soundara Pandian, Kanai S. Shah, *Halide-based scintillator materials*. 2023, Radiation Monitoring Devices, Inc.: United States.

132. Durham, R. and F. Girardi, *Effective neutron activation cross-sections of some chlorine and sulphur reactions in NRX.* Il Nuovo Cimento (1955-1965), 1961. **19**: p. 4-17.

133. Vaněček, V., et al., *Ultraviolet cross-luminescence in ternary chlorides of alkali and alkaline-earth metals.* Optical Materials: X, 2021. **12**: p. 100103.
134. Koshimizu, M., et al., *Scintillation and luminescence properties of a single $CsCaCl_3$ crystal.* Optical Materials, 2014. **36**(12): p. 1930-1933.
135. Takahashi, K., et al., *Auger-free luminescence characteristics of $Cs(Ca_{1-x}Mg_x)Cl_3$.* Nuclear Instruments and Methods in Physics Research Section A: Accelerators, Spectrometers, Detectors and Associated Equipment, 2020. **954**: p. 161842.
136. Gridin, S., et al., *Energy transfer in co-doped NaI:(Tl, Eu) crystals.* Functional Materials, 2014.
137. Shiran, N.V., et al., *Eu doped and Eu, Tl co-doped NaI scintillators.* IEEE Transactions on Nuclear Science, 2010. **57**(3): p. 1233-1235.
138. Perry, G.S. and K.N. Moody, *CsCl-$CaCl_2$ phase diagram.* Thermochimica Acta, 1992. **198**(1): p. 167-172.
139. Midorikawa, M., Y. Ishibashi, and Y. Takagi, *Optical and dilatometric studies of $KCaCl_3$ and $RbCaCl_3$ Crystals.* Journal of the Physical Society of Japan, 1979. **46**(4): p. 1240-1244.
140. Vaills, Y., et al., *X-ray investigations of the cubic to tetragonal phase transition in $CsCaCl_3$ at Tc= 95 K.* Solid State Communications, 1986. **60**(2): p. 139-141.
141. Chornodolskyy, Y., et al., *Features of the core–valence luminescence and electron energy band structure of $A_{1-x}Cs_xCaCl_3$ (A= K, Rb) crystals.* Journal of Physics: Condensed Matter, 2007. **19**(47): p. 476211.
142. Ephraim Babu, K., et al., *Structural, elastic, electronic, and optical properties of cubic perovskite $CsCaCl_3$ compound: An ab initio study.* Acta Physica Polonica A, 2014. **125**(5): p. 1179-1185.
143. Jellil, Z. and H. Ez-Zahraouy, *Pressure-induced band gap engineering and enhanced optoelectronic properties of non-toxic Ca-based perovskite $CsCaCl_3$: Insights from density functional theory.* Computational Condensed Matter, 2024. **38**: p. e00879.
144. Dorenbos, P., *Energy of the first $4f^7 \rightarrow 4f^6 5d$ transition of $Eu^{2+}$ in inorganic compounds.* Journal of Luminescence, 2003. **104**(4): p. 239-260.

145. Nagirnyi, V., S. Zazubovich, and N. Jaanson, *Luminescence of CsCl:Tl single crystals.* Physica Status Solidi (b), 1993. **175**(1): p. 155-164.
146. Sakai, T., et al., *Luminescence and scintillation properties of Tl-and In-doped CsCl crystals.* Japanese Journal of Applied Physics, 2017. **56**(6): p. 062601.
147. Pascual, J., Z. Barandiarán, and L. Seijo, *Ab initio model potential embedded-cluster calculation of the geometric structure of $Tl^+$ monomer and dimer centers in KCl.* Journal of Molecular Structure: THEOCHEM, 2001. **537**(1-3): p. 151-161.
148. Nagarajan, S. and R. Sudarkodi, *Luminescence in KCl: $Eu^{2+}$, $Tl^+$ X-ray storage phosphors.* Journal of Alloys and Compounds, 2009. **468**(1-2): p. 558-562.
149. Nagarajan, S. and R. Sudarkodi, *Luminescence characteristics of $Tl^+$ ions co-doped RbCl: $Eu^{2+}$ crystals.* Nuclear Instruments and Methods in Physics Research Section B: Beam Interactions with Materials and Atoms, 2008. **266**(16): p. 3595-3601.
150. Bartram, R., et al., *Suppression of afterglow in CsI:Tl by codoping with $Eu^{2+}$—II: Theoretical model.* Nuclear Instruments and Methods in Physics Research Section A: Accelerators, Spectrometers, Detectors and Associated Equipment, 2006. **558**(2): p. 458-467.
151. Wu, Y., et al., *CsI:$Tl^+$, $Yb^{2+}$: ultra-high light yield scintillator with reduced afterglow.* CrystEngComm, 2014. **16**(16): p. 3312-3317.
152. Saeki, K., et al. *$Tl^+$ Additive $CsCaCl_3$ Scintillation properties of crystals*. in *The 76th Japan Society of Applied Physics*. 2016.
153. Khan, A., et al., *Intrinsically activated $TlCaCl_3$: A new halide scintillator for radiation detection.* Radiation Measurements, 2017. **107**: p. 115-118.
154. Zaitseva, N., et al., *Plastic scintillators with efficient neutron/gamma pulse shape discrimination.* Nuclear Instruments and Methods in Physics Research Section A: Accelerators, Spectrometers, Detectors and Associated Equipment, 2012. **668**: p. 88-93.
155. Glodo, J., et al., *$Cs_2LiYCl_6$:Ce Scintillator for Nuclear Monitoring Applications.* IEEE Transactions on Nuclear Science, 2009. **56**(3): p. 1257-1261.
156. Shirwadkar, U., et al. *Novel scintillation material $Cs_2LiLaBr_{6-x}Cl_x$:Ce for gamma-ray and neutron spectroscopy*. in *2012 IEEE Nuclear Science Symposium and Medical Imaging Conference Record (NSS/MIC)*. 2012. IEEE.

157. Guss, P., et al., *Novel deployment of Elpasolites as a dual gamma–neutron directional detector.* Site Directed Research & Development, 2013.
158. Hawrami, R., et al., *$Cs_2LiLa(Br,Cl)_6$ Crystals for Nuclear Security Applications.* IEEE Transactions on Nuclear Science, 2016. **63**(2): p. 509-512.
159. Song, R., et al., *Simultaneous detection of energy and flux for neutron and gamma by CLYC scintillator.* IEEE Transactions on Nuclear Science, 2023.
160. Cardenas, C., et al., *Pulse-shape discrimination with $Cs_2HfCl_6$ crystal scintillator.* Nuclear Instruments and Methods in Physics Research Section A: Accelerators, Spectrometers, Detectors and Associated Equipment, 2017. **869**: p. 63-67.
161. Nagorny, S., *Novel $Cs_2HfCl_6$ crystal scintillator: recent progress and perspectives.* Physics, 2021. **3**(2): p. 320-351.
162. Davis, H., et al., *Systematic evaluation of fast neutron sensing with Cesium Hafnium Chloride.* Nuclear Instruments and Methods in Physics Research Section A: Accelerators, Spectrometers, Detectors and Associated Equipment, 2023. **1052**: p. 168247.
163. Vuong, P.Q., et al., *Neutron spectroscopy using pure $LaCl_3$ crystal and the dependence of pulse shape discrimination on Ce-doped concentrations.* Nuclear Engineering and Technology, 2021. **53**(11): p. 3784-3789.
164. Jin, T., et al., *Recent trends in elpasolite single crystal scintillators for radiation detection.* Crystals, 2022. **12**(7): p. 887.
165. Taggart, M., et al., *Fast-neutron response of the novel scintillator caesium hafnium chloride.* Nuclear Instruments and Methods in Physics Research Section A: Accelerators, Spectrometers, Detectors and Associated Equipment, 2021. **1012**: p. 165224.
166. Schilling, G. and G. Meyer, *Ternäre Bromide und Iodide zweiwertiger Lanthanide und ihre Erdalkali-Analoga vom Typ $AMX_3$ und $AM_2X_5$.* Zeitschrift für anorganische und allgemeine Chemie, 1996. **622**(5): p. 759-765.
167. Mousa, A.A., et al., *Stability, elastic and electronic properties of the $CsSrI_3$ halid perovskite.* Computational Condensed Matter, 2022. **32**: p. e00724.
168. Yang, K., M. Zhuravleva, and C.L. Melcher, *Crystal growth and characterization of $CsSr_{1-x}Eu_xI_3$ high light yield scintillators.* Physica Status Solidi (RRL)–Rapid Research Letters, 2011. **5**(1): p. 43-45.

169. Alekhin, M.S., et al., *Optical and scintillation properties of $CsBa_2I_5:Eu^{2+}$*. Journal of Luminescence, 2014. **145**: p. 723-728.
170. Bizarri, G., et al., *Scintillation and Optical Properties of BaBrI:Eu and $CsBa_2I_5:Eu^{2+}$*. IEEE Transactions on Nuclear Science, 2011. **58**(6): p. 3403-3410.
171. Borade, R., E. Bourret-Courchesne, and S. Derenzo, *Scintillation properties of $CsBa_2Br_5:Eu^{2+}$*. Nuclear Instruments and Methods in Physics Research Section A: Accelerators, Spectrometers, Detectors and Associated Equipment, 2011. **652**(1): p. 260-263.
172. Stand, L., et al., *Growth and characterization of potassium strontium iodide: A new high light yield scintillator with 2.4% energy resolution.* Nuclear Instruments and Methods in Physics Research Section A: Accelerators, Spectrometers, Detectors and Associated Equipment, 2015. **780**: p. 40-44.
173. Stand, L., et al., *Crystal growth and scintillation properties of potassium strontium bromide.* Optical Materials, 2015. **46**: p. 59-63.
174. Raja, A., et al., *Growth difficulties and growth of crack free $Eu^{2+}$ activated $KSr_2I_5$ scintillator single crystal by vertical bridgman-stockbarger technique for radiation detection applications.* Results in Chemistry, 2024. **7**: p. 101346.
175. Gahane, D., et al., *Luminescence of some $Eu^{2+}$ activated bromides.* Journal of Alloys and Compounds, 2009. **484**(1-2): p. 660-664.
176. Stracuzzi, L.M.S., *Discovery and Development of Potassium-based Metal Halide Scintillators for Radiation Detection Application*. 2018, University of Tennessee, Knoxville.
177. Stand, L., et al., *Exploring growth conditions and $Eu^{2+}$ concentration effects for $KSr_2I_5$: Eu scintillator crystals II: Ø 25 mm crystals.* Journal of Crystal Growth, 2018. **483**: p. 301-307.
178. Rebrova, N., et al., *Growth and luminescent properties of new $Eu^{2+}$ doped $RbBa_2I_5$ scintillator*. Nuclear Instruments and Methods in Physics Research Section A: Accelerators, Spectrometers, Detectors and Associated Equipment, 2020. **978**: p. 164463.
179. Rebrov, A., et al., *$K(Sr_{1-x}Eu_x)_2Cl_5$ scintillation material obtained using $Eu_2O_3$ dissolution in the growth chloride melt.* Journal of Crystal Growth, 2020. **543**: p. 125706.

180. Wolszczak, W., K.W. Krämer, and P. Dorenbos, *$CsBa_2I_5:Eu^{2+}$, $Sm^{2+}$—The First High-Energy Resolution Black Scintillator for γ-Ray Spectroscopy.* Physica Status Solidi (RRL)–Rapid Research Letters, 2019. **13**(9): p. 1900158.
181. Fang, C. and K. Biswas, *Preferential Eu site occupation and its consequences in the ternary luminescent halides $AB_2I_5$:$Eu^{2+}$ (A= Li–Cs; B= Sr, Ba).* Physical Review Applied, 2015. **4**(1): p. 014012.
182. Fu, X., et al., *Cerium Ion Promoting the Emission of Self-Trapped Excitons of Quasi-2D Europium Halide Perovskites for Self-Activated White Light-Emitting.* The Journal of Physical Chemistry C, 2023. **127**(17): p. 8159-8166.
183. Kang, B., et al., *Emerging new pseudobinary and ternary halides as scintillators for radiation detection.* IEEE Transactions on Nuclear Science, 2016. **64**(7): p. 1817-1824.
184. Edgar, A., G. Williams, and G. Appleby, *Photo-stimulated luminescence from europium-doped rubidium barium bromide in fluorozirconate glass ceramics.* Journal of Luminescence, 2004. **108**(1-4): p. 19-23.
185. Appleby, G., A. Edgar, and G. Williams, *Structure and photostimulated luminescent properties of Eu-doped $M_2BaX_4$ (M= Cs, Rb; X= Br, Cl).* Journal of Applied Physics, 2004. **96**(11): p. 6281-6285.
186. Tumram, P.V., S. Wankhede, and S. Moharil. *Wet chemical synthesis of $KSr_2I_5:Eu^{2+}$ phosphor*. in *AIP Conference Proceedings*. 2019. AIP Publishing.
187. Kim, H., et al., *Scintillation performance of the $TlSr_2I_5$ ($Eu^{2+}$) single crystal.* Optical Materials, 2018. **82**: p. 7-10.
188. Pandian, L.S., et al., *$TlSr_2I_5:Eu^{2+}$-A new high density scintillator for gamma-ray detection.* Nuclear Instruments and Methods in Physics Research Section A: Accelerators, Spectrometers, Detectors and Associated Equipment, 2021. **988**: p. 164876.
189. Mungmode, C., D. Gahane, and S. Moharil. *Luminescence characteristics of $Eu^{2+}$ activated $RbSr_2Br_5$ phosphor*. in *Proceeding of National Conference on "Advanced Materials"*. 2014.
190. Hawrami, R., et al., *Bridgman bulk growth and scintillation measurements of $SrI_2:Eu^{2+}$*. Journal of Crystal Growth, 2013. **379**: p. 69-72.

191. van Loef, E.V., et al., *Crystal growth and scintillation properties of strontium iodide scintillators.* IEEE Transactions on Nuclear Science, 2009. **56**(3): p. 869-872.
192. Comer, E.P., *Improving the Scintillation Performance of $KSr_2I_5:Ce^{3+}$ through Exploration of Activator Concentration and Growth Conditions.* 2019. Master's Thesis, University of Tennessee, Knoxville.
193. *$RbSr_2I_5$ Crystal Structure: Datasheet from "PAULING FILE Multinaries Edition – 2022" in SpringerMaterials* P. Villars and K. Cenzual, Editors., Springer-Verlag Berlin Heidelberg & Material Phases Data System (MPDS), Switzerland & National Institute for Materials Science (NIMS), Japan.
194. *$RbSr_2Br_5$ Crystal Structure: Datasheet from "PAULING FILE Multinaries Edition – 2022" in SpringerMaterials* P. Villars and K. Cenzual, Editors., Springer-Verlag Berlin Heidelberg & Material Phases Data System (MPDS), Switzerland & National Institute for Materials Science (NIMS), Japan.
195. Riccardi, R., et al., *Binary systems formed by alkali bromides with barium or strontium bromide.* Zeitschrift Für Naturforschung A, 1970. **25**(5): p. 781-785.
196. Singh, D.J., *Structure and optical properties of high light output halide scintillators.* Physical Review B, 2010. **82**(15): p. 155145.
197. Cherepy, N.J., et al., *Strontium and barium iodide high light yield scintillators.* Applied Physics Letters, 2008. **92**(8).
198. Dorenbos, P., *Fundamental Limitations in the Performance of $Ce^{3+}$, $Pr^{3+}$, $Eu^{2+}$ Activated Scintillators.* IEEE Transactions on Nuclear Science, 2010. **57**(3): p. 1162-1167.
199. Smerechuk, A., et al., *Growth and scintillation performances of $SrI_2$: Eu with low activator concentration.* Journal of Crystal Growth, 2019. **521**: p. 41-45.
200. Galenin, E., et al., *Growth and characterization of $SrI_2$: Eu crystals fabricated by the Czochralski method.* IEEE Transactions on Nuclear Science, 2017. **65**(8): p. 2174-2177.
201. Swider, S., et al., *Impurity segregation in zone-refined precursors for crystalline halide scintillators.* Nuclear Instruments and Methods in Physics Research Section A: Accelerators, Spectrometers, Detectors and Associated Equipment, 2015. **784**: p. 5-8.

202. Lam, S., et al. *Impact of impurities $Cs^{+}$, $Mg^{2+}$, $Fe^{2+}$, and $Sn^{2+}$ on scintillation performance of $SrI_2$ (Eu)*. in *2014 IEEE Nuclear Science Symposium and Medical Imaging Conference (NSS/MIC)*. 2014. IEEE.
203. Tsubota, Y., et al., *High-temperature scintillation properties of orthorhombic $Gd_2Si_2O_7$ aiming at well logging.* Applied Physics Express, 2015. **8**(6): p. 062602.
204. Gektin, A.V., A.N. Belsky, and A.N. Vasil'ev, *Scintillation efficiency improvement by mixed crystal use.* IEEE Transactions on Nuclear Science, 2013. **61**(1): p. 262-270.
205. Sidletskiy, O., *Trends in search for bright mixed scintillators.* Physica Status Solidi (a), 2018. **215**(13): p. 1701034.
206. Sidletskiy, O., A. Gektin, and A. Belsky, *Light-yield improvement trends in mixed scintillation crystals.* Physica Status Solidi (a), 2014. **211**(10): p. 2384-2387.
207. Li, Q., et al. *Search for improved-performance scintillator candidates among the electronic structures of mixed halides*. in *Hard X-Ray, Gamma-Ray, and Neutron Detector Physics XVI*. 2014. SPIE.
208. Wei, H., et al., *Effect of Ba substitution in $CsSrI_3$:$Eu^{2+}$*. Journal of Crystal Growth, 2013. **384**: p. 27-32.
209. *$RbBa_2I_5$ Crystal Structure: Datasheet from "PAULING FILE Multinaries Edition – 2022" in SpringerMaterials*, P. Villars and K. Cenzual, Editors., Springer-Verlag Berlin Heidelberg & Material Phases Data System (MPDS), Switzerland & National Institute for Materials Science (NIMS), Japan.
210. Denton, A.R. and N.W. Ashcroft, *Vegard's law*. Physical Review A, 1991. **43**(6): p. 3161-3164.
211. Balcerzyk, M., M. Moszyński, and M. Kapusta, *Comparison of $LaCl_3$:Ce and NaI (Tl) scintillators in $\gamma$-ray spectrometry.* Nuclear Instruments and Methods in Physics Research Section A: Accelerators, Spectrometers, Detectors and Associated Equipment, 2005. **537**(1-2): p. 50-56.
212. Moszyński, M., et al., *Intrinsic energy resolution of NaI(Tl).* Nuclear Instruments and Methods in Physics Research Section A: Accelerators, Spectrometers, Detectors and Associated Equipment, 2002. **484**(1-3): p. 259-269.

213. Shah, K., et al., *$LaCl_3$:Ce scintillator for γ-ray detection.* Nuclear Instruments and Methods in Physics Research Section A: Accelerators, Spectrometers, Detectors and Associated Equipment, 2003. **505**(1-2): p. 76-81.
214. Seifert, H.J., B. Muller, and E. Stotzel, *Thermochemische und Strukturelle Untersuchungen An Systemen Aus Alkalimetalliodid Und $MgI_2$ (1) bzw. $CaI_2$ (2).* Revue de Chimie Minerale, 1980. **17**: p. 147-157.
215. *RbBr Crystal Structure: Datasheet from "PAULING FILE Multinaries Edition – 2022" in SpringerMaterials,* P. Villars and K. Cenzual, Editors., Springer-Verlag Berlin Heidelberg & Material Phases Data System (MPDS), Switzerland & National Institute for Materials Science (NIMS), Japan.
216. *$Rb_4CaBr_6$ Crystal Structure: Datasheet from "PAULING FILE Multinaries Edition – 2022" in SpringerMaterials,* P. Villars and K. Cenzual, Editors., Springer-Verlag Berlin Heidelberg & Material Phases Data System (MPDS), Switzerland & National Institute for Materials Science (NIMS), Japan.
217. Beck, H. and W. Milius, *Study on $A_4BX_6$ compounds. I. structure refinement of ternary Cd halides $A_4CdX_6$ (A= NH4, K, Rb, In, Tl; X= Cl, I).* Zeitschrift für anorganische und allgemeine Chemie, 1986. **539**(8): p. 7-17.
218. Lindsey, A.C., et al., *Effects of increasing size and changing europium activator concentration in $KCaI_3$ scintillator crystals.* Journal of Crystal Growth, 2016. **449**: p. 96-103.
219. Shirwadkar, U., et al., *Promising alkaline earth halide scintillators for gamma-ray spectroscopy.* IEEE Transactions on Nuclear Science, 2013. **60**(2): p. 1011-1015.
220. Dorenbos, P., *Crystal field splitting of lanthanide 4fn−15d-levels in inorganic compounds.* Journal of Alloys and Compounds, 2002. **341**(1): p. 156-159.
221. Pestovich, K.S., et al., *Crystal Growth & Characterization of Europium-Doped Rubidium Calcium Bromide Scintillators.* IEEE Transactions on Nuclear Science, 2023. **70**(7): p. 1370-1377.
222. van Aarle, C., K.W. Krämer, and P. Dorenbos, *Avoiding concentration quenching and self-absorption in $Cs_4EuX_6$ (X= Br, I) by $Sm^{2+}$ doping.* Journal of Materials Chemistry C, 2023. **11**(6): p. 2336-2344.

223. Wen, X., et al., *Near-Infrared Emitting of Zero-Dimensional Europium (II) Halide Scintillators: Energy Transfer Engineering via $Sm^{2+}$ Doping.* ACS Applied Electronic Materials, 2023. **5**(6): p. 3507-3514.
224. Meitian, W. and W. Shihua, *$Rb_4YbI_6$ Synthesis and Crystal Structure.* Journal of Solid State Chemistry, 1997. **128**(1): p. 66-68.
225. *$Rb_4CaI_6$ Crystal Structure: Datasheet from "PAULING FILE Multinaries Edition – 2022" in SpringerMaterials*, P. Villars and K. Cenzual, Editors., Springer-Verlag Berlin Heidelberg & Material Phases Data System (MPDS), Switzerland & National Institute for Materials Science (NIMS), Japan.
226. *RbI Crystal Structure: Datasheet from "PAULING FILE Multinaries Edition – 2022" in SpringerMaterials*, P. Villars and K. Cenzual, Editors., Springer-Verlag Berlin Heidelberg & Material Phases Data System (MPDS), Switzerland & National Institute for Materials Science (NIMS), Japan.
227. Boatner, L.A., et al., *Bridgman growth of large $SrI_2:Eu^{2+}$ single crystals: A high-performance scintillator for radiation detection applications.* Journal of Crystal Growth, 2013. **379**: p. 63-68.
228. Lindsey, A.C., et al., *Determination of thermal expansion of $KCaI_3$ using in-situ high temperature powder X-ray diffraction.* Materials Chemistry and Physics, 2018. **212**: p. 161-166.
229. Hawrami, R., et al., *Bridgman bulk growth and scintillation measurements of $SrI_2:Eu^{2+}$.* Journal of Crystal Growth, 2013. **379**: p. 69-72.
230. Iltis, A., et al., *Lanthanum halide scintillators: Properties and applications.* Nuclear Instruments and Methods in Physics Research Section A: Accelerators, Spectrometers, Detectors and Associated Equipment, 2006. **563**(2): p. 359-363.
231. *$RbSr_2Br_5$ Crystal Structure: Datasheet from "PAULING FILE Multinaries Edition – 2022" in SpringerMaterials*, P. Villars and K. Cenzual, Editors., Springer-Verlag Berlin Heidelberg & Material Phases Data System (MPDS), Switzerland & National Institute for Materials Science (NIMS), Japan.
232. *$RbSr_2I_5$ Crystal Structure: Datasheet from "PAULING FILE Multinaries Edition – 2022" in SpringerMaterials*, P. Villars and K. Cenzual, Editors., Springer-Verlag Berlin

Heidelberg & Material Phases Data System (MPDS), Switzerland & National Institute for Materials Science (NIMS), Japan.

233. Lam, S., et al., *Microscale luminescence imaging of defects, inhomogeneities, and secondary phases in halide scintillators.* Nuclear Instruments and Methods in Physics Research Section A: Accelerators, Spectrometers, Detectors and Associated Equipment, 2015. **784**: p. 23-28.

234. Rust, M., C. Melcher, and E. Lukosi, *Intrinsic radioactivity of $KSr_2I_5:Eu^{2+}$*. Nuclear Instruments and Methods in Physics Research Section A: Accelerators, Spectrometers, Detectors and Associated Equipment, 2016. **833**: p. 33-37.

235. Yip, L., I. Shih, and C. Champness, *Method of avoiding ampoule adhesion of ingots in Bridgman growth of $CuInSe_2$.* Journal of Crystal Growth, 1993. **129**(1-2): p. 102-106.

236. Seitz, F., *Color centers in alkali halide crystals.* Reviews of Modern Physics, 1946. **18**(3): p. 384.

237. Zhu, R., *Radiation damage in scintillating crystals.* Nuclear Instruments and Methods in Physics Research Section A: Accelerators, Spectrometers, Detectors and Associated Equipment, 1998. **413**(2): p. 297-311.

238. Kobayashi, M. and S. Sakuragi, *Radiation damage of CsI(Tl) crystals above $10^3$ rad.* Nuclear Instruments and Methods in Physics Research Section A: Accelerators, Spectrometers, Detectors and Associated Equipment, 1987. **254**(2): p. 275-280.

239. Zhu, R.-y., *Radiation damage in scintillating crystals.* Nuclear Instruments and Methods in Physics Research Section A: Accelerators, Spectrometers, Detectors and Associated Equipment, 1998. **413**(2-3): p. 297-311.

240. Woody, C.L., et al., *Radiation damage in undoped CsI and CsI (Tl).* IEEE Transactions on Nuclear Science, 1992. **39**(4): p. 524-531.

241. Hamada, M.M., et al., *Radiation damage of CsI(Tl) scintillators: blocking of energy transfer process of $V_k$ centers to $Tl^+$ activators.* Nuclear Instruments and Methods in Physics Research Section A: Accelerators, Spectrometers, Detectors and Associated Equipment, 2002. **486**(1-2): p. 330-335.

242. Beylin, D., et al., *Study of the radiation hardness of CsI(Tl) scintillation crystals.* Nuclear Instruments and Methods in Physics Research Section A: Accelerators, Spectrometers, Detectors and Associated Equipment, 2005. **541**(3): p. 501-515.
243. Berger, M.J.H., J.H.; Seltzer, S.M.; Chang, J.; Coursey, J.S., Sukumar, R., Zucker, D.S.; Olsen, K., *XCOM: Photon Cross Sections Database NIST Standard Reference Database 8 (XGAM)*, P. NIST, Radiation Physics Division, Editor. 2010.
244. Noda, S., et al., *Analysis of electron and hole trap states in novel storage phosphors: Undoped, Eu-doped, and Ce-doped $CsCaCl_3$ ceramics.* Nuclear Instruments and Methods in Physics Research Section B: Beam Interactions with Materials and Atoms, 2018. **435**: p. 43-49.
245. Butterworth, J., P. Esser, and P. Levy, *Formation of color centers in KCl:Tl by gamma irradiation at 21°C.* Physical Review B, 1970. **2**(8): p. 3340.

# APPENDICES

**Appendix A.** First-Author Manuscripts and Conference Presentations

**Appendix B.** Compositional Screening – Materials excluded from further study

## Appendix A. First-Author Manuscripts and Conference Presentations

Manuscripts

1. **K. S. Pestovich**, L. Stand, N. Anastasi, M. Gillespie, L. S. Pandian, C. L. Melcher, E. van Loef, "Intrinsic scintillation performance & europium concentration effects in $RbSr_2I_5$ and $RbSr_2Br_5$ scintillators," in *Journal of Crystal Growth*, vol. 649, p. 127924 (2025).
2. **K. S. Pestovich**, L. Stand, E. van Loef, C. L. Melcher and M. Zhuravleva, "Crystal Growth of New High Light Yield Halide Perovskite Scintillator $RbSrI_3$," in *Journal of Crystal Growth*, vol. 627, p. 127540 (2024).
3. **K. S. Pestovich**, L. Stand, E. van Loef, C. L. Melcher and M. Zhuravleva, "Crystal Growth and Characterization of Europium-Doped Rubidium Calcium Bromide Scintillators," in *IEEE Transactions on Nuclear Science*, vol. 70, no. 7, p. 1370-1377 (2023).
4. **K. S. Pestovich**, L. Stand, K. Joshi, X. Wen, C. L. Melcher, L. S. Pandian, E. van Loef, M. Zhuravleva, "Investigating the Luminescence, Irradiation Effects & Fast Neutron-Gamma Discrimination Characteristics of Cubic Halide Perovskite Scintillator $CsCaCl_3$:($Eu^{2+}$, $Tl^{+}$)" in *Nuclear Instruments and Methods in Physics Research - section A.* Submitted for review.
5. **K. S. Pestovich**, M. Gillespie, L. Stand, C. L. Melcher, E. van Loef, M. Zhuravleva, "Crystal Growth Scale up and Stability of $RbSr_2X_5$:Eu Scintillators" in *Crystal Growth & Design.* Submitted for review.

Presentations

*Professional Conferences*

1. **July 2024:** “Radiation hardness of new halide perovskite scintillators.” [Presentation]. CAARI-SNEAP 2024: 7th International Conference on the Application of Accelerators in Research and Industry and the 55th Symposium of Northeastern Accelerator Personnel, Fort Worth, TX.
2. **June 2024:** “Dopant Studies in Inorganic Halide Scintillators Grown via the Vertical Bridgman Method.” [Invited Presentation]. CGCT-9: 9th Asian Conference on Crystal Growth and Crystal Technology, Jeju Island, South Korea.
3. **August 2023:** “First Bridgman Growth of $RbSrI_3$:Eu Scintillator for High Energy X-ray Radiography” [Presentation]. 23rd American Conference on Crystal Growth and Epitaxy, Tucson, AZ.
4. **November 2022:** "New High Light Yield Rubidium Halide Perovskite Scintillators." [Poster]. IEEE Nuclear Science Symposium, Medical Imaging Conference and Room Temperature Semiconductor Detector Conference, Virtual.
5. **October 2022:** “Scintillators for Accelerator Science” [Invited Presentation Substitute]. CAARI-SNEAP 2022: 6th International Conference on the Application of Accelerators in Research and Industry and the 55th Symposium of Northeastern Accelerator Personnel, Denton, TX.
6. **September 2022:** “Crystal growth and characterization of high light yield rubidium calcium bromide scintillators” [Presentation]. 17th International Conference on Scintillating Materials and their Applications, Santa Fe, NM.

*Student Conferences & Posters*

1. **February 2025**: “Crystal Growth and Scintillation Performance of 22 mm Diameter $RbSr_2Br_5$:Eu and $RbSr_2I_5$:Eu” [Poster]. *Oak Ridge Chapter of ASMI, UT Center for Materials and Manufacturing, and East Tennessee ACeRS Student Night*, Knoxville, TN.
2. **February 2024:** “Investigating Performance of $CsCaCl_3$:X Scintillators (X = Tl, Eu)” [Poster]. *Oak Ridge Chapter of ASM and UT Center for Materials and Manufacturing Student Night*, Knoxville, TN.

3. **April 2023:** Comparison of Two Dopant Species in the New Scintillator $Rb_4CaI_6$" [Lightning Talk]. *American Nuclear Society Student Conference*, Knoxville, TN.
4. **October 2023**: "X-ray Vision: Discovering New Scintillators for Improved Cargo Screening" [Rapid Fire Presentation]. *We23, Society of Women Engineers Conference*, Los Angeles, CA.
5. **February 2023:** "This or That? Comparing Eu and Yb doping in $Rb_4CaI_6$ scintillator" [Poster]. *Oak Ridge Chapter of ASM and UT Center for Materials Processing Student Night*, Knoxville, TN.
6. **February 2023:** "This or That? Comparing Eu and Yb doping in $Rb_4CaI_6$ scintillator" [Poster]. *Japanese Business Roundtable, Center for Global Engagement and Women in Engineering Program at UT*, University of Tennessee, Knoxville, TN.
7. **August 2022:** "Bright Ideas: Luminescent dopant concentration studies to optimize light yield in $Rb_4CaI_6$*"* [Poster]. *Center for Materials Processing End of Summer Student Poster Competition*, Knoxville, TN.
8. **June 2022:** "Novel High Light Yield Rubidium Halide Perovskite Scintillators" [Poster]. *National Nuclear Security Administration Defense Nuclear Nonproliferation R&D University Program Review*, Ann Arbor, MI.
9. **February 2022:** "Seeing Through Steel: Discovery of $Eu^{2+}$ doped Rubidium Calcium Bromide Scintillators" [Poster]. *Oak Ridge Chapter of ASM and UT Center for Materials Processing Student Night Poster Session*, Knoxville, TN, virtual.
10. **September 2021:** "Compositional Screening of Rubidium Halide Perovskite Scintillators" [Poster]. *National Nuclear Security Administration Defense Nuclear Nonproliferation R&D University Program Review*, Atlanta, GA.
11. **October 2020:** "Making a good thing better: Preliminary evaluation of Li codoping on the scintillation performance of $Cs_4SrI_6$:Eu" [Poster]. *Oak Ridge Chapter of ASM, UT Center for Materials Processing and the Southeast section of American Association for Crystal Growth, Student Night Poster Session*, virtual.

## Appendix B. Compositional Screening – Materials excluded from further study

**Table 17.** New scintillators with synthesis or performance limitations

| Crystal | Melting Habit | Melting Point (°C) | Crystal Structure | Density (g/cc) | $Z_{eff}$ | RL Emission (nm) | Light Yield | Concern |
|---|---|---|---|---|---|---|---|---|
| $CsEuCl_3$ | Congruent | 800 | Tetragonal (P4mm) | 3.7 | 56 | 460, 540 | 15,700 | Non-uniform performance |
| $RbEuI_3$ | Congruent | 480 | Orthorhombic (Pmmm) | 4.8 | 55 | 480 | 22,000 | Non-uniform performance |
| $RbMgCl_3$ | Congruent | 559 | Hexagonal (P63/mmc); Several known polytypes | 2.78 | 35 | 300, 450, 610 | No photopeak observed | |
| $RbMgCl_3$:Eu | Congruent | 559 | | 2.78 | 35 | 450 | 15,000 | Non-uniform performance |
| $RbCaI_3$ | Congruent | 582 | Orthorhombic (Pnam) | 4.04 | 48 | | | Destructive phase transition on cooling |
| $RbCaI_3$:Eu | Congruent | 582 | | 4.04 | 48 | 476 | 72000 | |
| $RbCaI_3$:Yb | Congruent | 582 | | 4.04 | 48 | 478 | 33200 | |
| $Cs_2NaTbCl_6$ | Incongruent | 772 | Cubic | 3.52 | 58 | 500, 550, 625 | No photopeak observed | |
| $Rb_2NaCeBr_6$ | Incongruent | Unknown | | | 42 | 400 | No photopeak observed | |

**Table 18.** Unstable compositions or compositions without radioluminescence

| Crystal | Melting Habit | Melting Point (°C) | Crystal Structure | Density (g/cc) | Concern |
|---|---|---|---|---|---|
| $RbCu_2Br_3$ | Congruent | 260 | Orthorhombic (Cmcm) | 4.28 | No radioluminescence |
| $CsCrCl_3$ | Congruent | 709 | Hexagonal (P63/mmc) | 3.41 | |
| $CsCoCl_3$ | Congruent | 547 | Hexagonal (P63/mmc) | 3.66 | |
| $CsCoBr_3$ | Congruent | 470 | Hexagonal (P63/mmc) | 4.62 | |
| $RbMgBr_3$:Eu | Congruent | 465 | Trigonal (P-3c1) | 3.7 | Raw materials reacted with quartz ampoule before growth – crystals were not grown |
| $RbMgI_3$:Eu | Unknown | Unknown | Unknown | Unknown | |
| $Rb_4MgI_6$:Eu | Unknown | Unknown | Unknown | Unknown | |
| $RbCaCl_3$ | Congruent | 854 | Orthorhombic (Pnma) | 2.56 | |
| $RbSrCl_3$:Eu | Unstable < ~350°C | 690 | - | - | Unstable or unsuccessful growth / multiple phases |
| $RbSrBr_3$:Eu | | 604 | - | - | |
| $RbEuCl_3$ | | 664 | - | - | |
| $Rb_4EuCl_6$ | Incongruent | Unknown | - | - | |
| $RbBaI_3$ (Undoped, Eu, Yb) | Incongruent | Unknown | - | - | |
| $Rb_4BaI_6$ (Undoped, Eu, Yb) | Incongruent | Unknown | - | - | |
| $Rb_4SrI_6$ (Undoped, Eu, Yb) | Incongruent | Unknown | - | - | |

## VITA

Kimberly S. Pestovich was born in Colorado, USA. She earned a Bachelor of Science degree in Chemical Engineering from New Mexico State University in 2019. Following graduation, she continued an internship at Los Alamos National Laboratory as a post-baccalaureate appointee. Here, her research focused on multicomponent rare-earth aluminum garnet scintillator development. In 2020, Kimberly moved to Knoxville, Tennessee to pursue doctoral research at the Scintillation Materials Research Center. She worked as a Graduate Research Assistant and Graduate Teaching Assistant in the Department of Materials Science and Engineering. Her research focused on discovery of new inorganic metal halide scintillators via Vertical Bridgman crystal growth. During this time, she also earned a Master of Science in Materials Science and Engineering (Summer 2022) and a Graduate Certificate in Engineering Management (Fall 2022). Following graduation with her PhD, Kimberly is continuing her career in radiation detection with applications in homeland security.